IAEA-TECDOC-1438

# *Emerging applications of radiation in nanotechnology*

*Proceedings of a consultants meeting held in Bologna, Italy, 22–25 March 2004*

IAEA
International Atomic Energy Agency

March 2005

IAEA-TECDOC-1438

# *Emerging applications of radiation in nanotechnology*

*Proceedings of a consultants meeting held in Bologna, Italy, 22–25 March 2004*

IAEA
International Atomic Energy Agency

March 2005

The originating Section of this publication in the IAEA was:

Industrial Applications and Chemistry Section
International Atomic Energy Agency
Wagramer Strasse 5
P.O. Box 100
A-1400 Vienna, Austria

EMERGING APPLICATIONS OF RADIATION IN NANOTECHNOLOGY
IAEA, VIENNA, 2005
IAEA-TECDOC-1438
ISBN 92–0–100605–5
ISSN 1011–4289



Printed by the IAEA in Austria
March 2005

## FOREWORD

Nanotechnology is one of the fastest growing new areas in science and engineering. The subject arises from the convergence of electronics, physics, chemistry, biology and material sciences to create new functional systems of nanoscale dimensions. Nanotechnology deals with science and technology associated with dimensions in the range of 0.1 to 100 nm. Nanotechnology is predicted to have a major impact on the manufacturing technology 20 to 30 years from now.

The ability to fabricate structures with nanometric precision is of fundamental importance to any exploitation of nanotechnology. Nanofabrication involves various lithographies to write extremely small structures. Radiation based technology using X rays, e-beams and ion beams is the key to a variety of different approaches to micropattering.

Other studies concern formation and synthesis of nanoparticles and nanocomposites. Radiation synthesis of copper, silver and nanoparticles of other metals is studied. Metal and salt–polymer composites are synthesized by this method. Metal sulphide semiconductors of nanometric matrices are prepared using gamma irradiation of a suitable solution of monomer, sulphur and metal sources. These products find application in photoluminescent, photoelectric and non-linear optic materials.

An interesting field of radiation nanotechnological application concerns the development of PC-controlled biochips for programmed release systems. Nano-ordered hydrogels based on natural polymers as polysaccharides (hyaluronic acid, agrose, starch, chitosan) and proteins (keratin, soybean) are potential responsive materials for such biochips and sensors. The nano approach to these biological materials should be developed further. Studies on natural and thermoplastic natural rubber-clay composites have given promising results. Nanomaterials with high abrasion and high scratch resistance will find industrial applications.

The International Atomic Energy Agency is promoting the new development in radiation technologies through its technical cooperation programmes, coordinated research projects, consultants and technical meetings and conferences.

The Consultants Meeting on Emerging Applications of Radiation Nanotechnology was hosted by the Institute of Organic Synthesis and Photochemistry in Bologna, Italy, from 22 to 25 March 2004. The meeting reviewed the status of nanotechnology worldwide. Applications of radiation for nanostructures and nanomachine fabrication, especially drug delivery systems, polymer based electronic, solar energy photovoltaic devises, etc., were discussed during the meeting. The opportunities of radiation technology applications were amply demonstrated.

This report provides basic information on the potential of application of radiation processing technology in nanotechnology. Development of new materials, especially for health care products and advanced products (electronics, solar energy systems, biotechnology, etc.) are the main objectives of R&D activities in the near future. It is envisaged that the outcome of this meeting will lead to new programmes and international collaboration for research concerning the application of various radiation techniques in nanotechnology.

The IAEA acknowledges the valuable contribution of all the participants in the consultants meeting. The IAEA officer responsible for this publication was A.G. Chmielewski of the Division of Physical and Chemical Sciences.

## *EDITORIAL NOTE*

*This publication has been prepared from the original material as submitted by the authors. The views expressed do not necessarily reflect those of the IAEA, the governments of the nominating Member States or the nominating organizations.*

*The use of particular designations of countries or territories does not imply any judgement by the publisher, the IAEA, as to the legal status of such countries or territories, of their authorities and institutions or of the delimitation of their boundaries.*

*The mention of names of specific companies or products (whether or not indicated as registered) does not imply any intention to infringe proprietary rights, nor should it be construed as an endorsement or recommendation on the part of the IAEA.*

*The authors are responsible for having obtained the necessary permission for the IAEA to reproduce, translate or use material from sources already protected by copyrights.*

**CONTENTS**

# SUMMARY

## 1. INTRODUCTION

Nanotechnology is one of the fastest growing new areas in science and engineering. The subject arises from the convergence of electronics, physics, chemistry, biology and materials science to create new functional systems of nanoscale dimensions. Nanotechnology deals with science and technology associated with dimensions in the range of 0.1 to 100 nm.

Coal and diamonds are a good example on how changes in the atoms' arrangement may alter substance properties. Man knows how to use these changes technologically, e.g. the different role of silicone in sand and in computer chips. Nature knows this process better than man, sometimes not in a profitable manner for mankind as in the case of cancerous and healthy tissue: throughout history, variations in the arrangement of atoms have distinguished the diseased from the healthy.

The ability to arrange atoms lies in the foundation of this technology. Nowadays, science and industry made progress in atom arranging, but primitive methods are still being used. With our present technology, we are still forced to handle atoms in unruly groups.

Ordinarily, when chemists make molecular chains of polymers, they feed molecules into a reactor where they collide and join together in a statistical manner. The resulting chains have varying lengths and molecular mass. Genetic engineers are already showing the way. The protein machines, called restriction enzymes, "read" certain DNA sequences as "cut here". They read these genetic patterns by touch, by sticking to them and they cut the chain by rearranging a few atoms. Other enzymes splice pieces together, reading matching parts as "glue here", likewise "reading" chains by selective stickiness and splicing chains by rearranging a few atoms. By using gene machines to write and restriction enzymes to cut and paste, genetic engineers can write and edit whatever DNA message they choose.

Nanotechnology is predicted to have a major impact on the manufacturing technology 20 to 30 years from now. However, it has been implemented in the manufacturing of products as diverse as novel foods, medical devices, chemical coatings, personal health testing kits, sensors for security systems, water purification units for manned space craft, displays for hand-held computers and high resolution cinema screens. New products that can be foreseen in the nearest future include the following: sensors, transducers, displays, active and passive electronic components, energy storage/conversion systems, biomedical devices, etc. In addition, many technological developments are being reported. Firstly, the underpinning core science will need to be established. An interdisciplinary approach is required, bringing together key elements of biology, chemistry, engineering and physics. The development of appropriate interdisciplinary collaboration is expected to present challenges no less demanding than the science itself. Therefore, such collaboration from the side of radiation chemists and physicists is needed as well. They are not newcomers in the field, arrangement of atoms and ions has been performed using ion or electron beams and radiation for many years. Talking about nanotechnology, we have in mind materials (including biological ones) and nanomachines. Molecular nanotechnology is perceived to be an inevitable development not to be achieved in the near future. In this context, self assembly and self organization are recognized as crucial methodologies.

If we look into the dictionary's definition of a machine, it is "any system, usually of rigid bodies, formed and connected to alter, transmit, and direct applied forces in a predetermined manner to accomplish a specific objective, such as the performance of useful work". Biochemists dream of designing and building such devices, but there are difficulties to overcome. Engineers use beams of light, electrons and ions to design patterns onto silicon chips, but chemists must build much more indirectly than that. When they combine molecules in various sequences, they have only limited control over how the molecules join. When biochemists need complex molecular machines, they still

have to borrow them from cells. Nevertheless, advanced molecular machines will eventually let them build nanocircuits and nanomachines as easily and directly as engineers now build microcircuits or washing machines. Then progress will become swift and dramatic.

Regarding materials processing, radiation chemists presented in the past a similar approach as did chemists, namely, treatment in bulk. However, new trends concerning a more precise treatment technology were observed. Surface curing, ion track membranes and controlled release drug delivery systems are very good examples of such developments. The last two products from this list may even fit into the definition of nanomachine: they control substance transport rate by their own structure properties. The fabrication of nanostructures yields materials with new and improved properties; both approaches, "top-down" and "bottom-up" can be studied.

The ability to fabricate structures with nanometric precision is of fundamental importance to any exploitation of nanotechnology. Nanofabrication involves various lithographies to write extremely small structures. Radiation based technology using X rays, e-beams and ion beams is the key to a variety of different approaches to micropattering. Radiation effect on resists occurs through bond breaking (positive resist) or crosslinking between polymer chains (negative resist). Polymer is becoming better or less soluble in developer. This technique has already been commercialized. Due to the small wavelength of the 30–100 keV electrons, the resolution of electron beam nanolithography is much higher than that of optical lithography. To improve resolution, electron direct writing systems applying electrons with the energy as low as 2 keV are proposed to reduce electron scattering effects.

Other studies concern formation and synthesis of nanoparticles and nanocomposites. Radiation synthesis of copper, silver and other metals' nanoparticles is studied. The solution of metal salts is exposed to gamma rays and formed reactive species reduce metal ion to zero valent state. Formation of aqueous bimetallic clusters by gamma and electron irradiation was studied as well. Metal and salt–polymer composites are synthesized by this method. Metal sulphide semiconductors of nanometric matrices are prepared using gamma irradiation of a suitable solution of monomer, sulphur and metal sources. These products find application in photo-luminescent, photoelectric and non-linear optic materials.

An interesting field of radiation nanotechnological application concerns the development of PC controlled biochips for programmed release systems. Nano-ordered hydrogels based on natural polymers as polysaccharides (hyaluronic acid, agrose, starch, chitosan) and proteins (keratin, soybean) being pH and electric potential responsive materials for such biochips and sensors. To avoid the regress in further developments concerning radiation processing of natural polymers, the nano approach to these biological materials should be developed further. Their self organization and functionalism depend on the basic fundamentals of the discussed science. The studies on natural rubber-clay composites and thermoplastic natural rubber-clay composites have given interesting results. Nanomaterials with high abrasion and high scratch resistance will find industrial application.

## 2. PURPOSE OF THE MEETING

The IAEA is promoting the peaceful use of nuclear and radiation technologies through its Technical Cooperation Programmes, Coordinated Research Projects, Consultants and Technical Meetings, Conferences, etc. Due to the IAEA's support, some new technologies were developed and transferred to Member States during the past years.

At the beginning of the 21st century, new science and technology development programmes are being elaborated and implemented, including UN resolutions concerning sustainable development, Johannesburg Protocol, 6$^{th}$ EU Thematic Framework, and others. Therefore, the IAEA's Industrial Applications and Chemistry Section of the Division of Physical and Chemical Sciences, Department of Nuclear Sciences and Applications, organized a Technical Meeting (TM) at its Headquarters in

Vienna, Austria, from 28 to 30 April 2003, to review the present situation and possible developments of radiation technology to contribute sustainable development. The meeting gathered the most eminent experts in the field and future programmes were discussed and recommendations elaborated. This meeting provided the basic input to launch others on the most important fields of radiation technology applications. The first one on "Advances in Radiation Chemistry of Polymers" was held in Notre Dame, USA, in September 2003, the second on "Status of Industrial Scale Radiation Treatment of Wastewater" in Taejon, Republic of Korea, in October 2003 and the third on "Radiation Processing of Polysaccharides" in Takasaki, Japan, in November 2003. During the meetings in Vienna and Notre Dame, papers on application of radiation in nanotechnology have already been presented. Therefore, since the new activities undertaken by the IAEA are based on the recommendations of the experts representing Member States and are closely related to the progress in the science and technology, organization of the Consultants Meeting on the subject has been decided, in the frame of the programme run by Industrial Applications and Chemistry Section.

All applications of radiation for nanostructures and nanomachines' fabrication were discussed during the meeting. The participants tried to categorize these applications and discuss observed trends. The opportunities of radiation technology applications, based on needs and advantages of the technique, were reviewed as well.

This was the first meeting on the subject organized by IAEA, therefore its importance can not be overestimated. The IAEA hopes that the outcome of this meeting will initiate a new programmes and international collaboration for research concerning application of various radiation techniques in the nanotechnology field. This should bridge radiation specialists with other research groups in the field and make connections between programmes of the IAEA and big international and national projects.

## 3. MAIN TOPICS REPORTED AND DISCUSSED DURING THE MEETING

### 3.1. Recent Trends in nanotechnology

Nanoscience and nanotechnology are cross-interdisciplinary areas involving materials and functional systems whose structures and components, due to their nanoscale size, exhibit unusual and/or enhanced properties. Since the science is a new, recently developed field, the meeting started with overview of general trends. This information gives ideas concerning possible radiation applications. In particular the covered topics were:

- Organic light emitting diodes whose possible applications are in the market for displays, will replace liquid crystals in next generation of displays for portable devices,
- Organic photovoltaic cells containing blends of regioregular poly(3-alkylthiophenes) and soluble fullerene derivatives,
- The use of scanning probe microscopy to explore the nanoscale world,
- The CVD synthesis of carbon nanotubes, their structure characterization by SEM and TEM, and their electronic application,
- A bottom-up way to produce nanostructures assembling a discrete number of molecular components (supramolecular system) in order to form artificial molecular machines,
- Synthesis of nanocrystalline Si and SiC thin films of thickness in the nanometer range by the plasma enhanced chemical vapour deposition technique and the application of *p* nc-Si films in heterojunction solar cells,
- Next generation lithographies using extreme ultraviolet, projection lithography in order to overcome the physical limits of optical lithography,
- Preparation by dispersion polymerization of nano/microspheres for in *vivo* delivery of biologically active proteins,
- Formation of Si/SiC nanostructures on Si wafers by annealing at high temperature in ultra high vacuum and possible future application in the field of lithography and photoluminescence.

Since radiation has already broad applications in materials processing, the developments and procedures concerning three topics were reported, as examples of process commercialisation methodologies:

- the use of ionizing radiation for curing of epoxy resin for high performance composites, dispersion polymerization of methylmethacrylate in dense $CO_2$ and synthesis of microgels for active release,
- radiation effects on semiconductor devices for radiation tolerance studies,
- studies of the radiolytic effect of γ irradiation during preparation of polyester microspheres containing drugs.

### 3.2. Fundamental issues in the effects of radiation on nanostructures

The study of materials in the nano size regime is still in its infancy, therefore, there are many fundamental issues that need to be addressed when irradiation is applied to the production or utilization of nanomaterials. Synthesis of nanoparticles of metals and even semiconductors using irradiation is now well established and the mechanism of production is reasonably understood. Metallic particles embedded in complex matrixes, as well as complex composites of multimetallic particles, core-shell structures of metal-metal, metal-semiconductor and metal-insulator can be generated but their morphology and their thermodynamic stability needs to be investigated. Control of size and in particular size-distribution is a major advantage of radiolytic production of the particles but the size distribution currently achievable (±10%) is still too large. Narrowing the size distribution is a major goal in much of the synthetic effort currently invested in nano-materials studies. Because of the increased free energy of surface in these materials many of their properties are expected to be different from those of the same materials in bulk size. Characterization of the size dependent properties is, therefore, necessary. These cannot be than by radiation methods alone and requires close interaction with a broad range of multidisciplinary expertise. Example is the use of synchrotron-radiation spectroscopies, which utilize similar technologies for the generation of the radiation but at different energy and flux characteristics from those used in radiation processing. Since there is little doubt that one cannot reasonably predict all necessary materials that will be utilized at the nanosize regime, computational methodologies will be of great impact and thus interaction with the materials-theory and computation community is essential**.**

Developing understanding of the fundamental processes that follow the deposition of ionizing radiation in matter is certain to lead to significant technological advances. For example, the understanding of the interactions of holes generated in silver bromide matrixes with various dopants led to a mechanism that describes the scavenging of the holes by formate ions. The use of this scavenger in silver photography eventually led to an increase of the efficiency and sensitivity of the photographic process by an order of magnitude. Similarly, a mechanism that describes the effect of catalytic amounts of metallic nanoparticles is now used to convert all of the radicals that are generated by radiolysis of water can presently quadruple the yield of $H_2$ in this system. This is may offer pathways to the use of nuclear energy in the evolving hydrogen global economy as well as outline strategies for solar energy utilization.

Radiolytic processes in heterogeneous systems are poorly understood in-spite of their common occurrence in many practical applications. When one of the component phases is of nano–dimensions the system is even more complex than a similar bulk heterogeneous system. In such a situation exchange of energy and charge between the two sub-phases is common and may lead to very efferent outcome of the irradiation than that of the two separated systems. Yields of radicals may change and consequently the yields of final products will change as well. This is a relatively new concern to the electronic industry especially but not exclusively in space applications. Therefore, there is a significant incentive to study and understand the consequences of charge exchange across interfaces of nano-scale dimensions. Furthermore, it was shown during the workshop and in many published reports that the factors that limit fuel cell efficiency, solar energy conversion, LED and OLED operation are related to the transport of charge carriers across the nanoparticles to the charge collecting electrodes. Radiation

techniques are best suited to address these questions and offer method to overcome and minimize losses in these process that currently inhibit wide utilization of the corresponding devices.

Nanoparticles might be utilized in environmental remediation efforts. Since ionizing radiation has the energy necessary to penetrate dense soils, it can destroy pollutants adsorbed at naturally occurring particulate materials. In combination with other advanced oxidation techniques the efficiency of the clean-up operation may be significantly increased. Two prerequisites to the wide spread use of irradiation of particulates in environmental remediation still need to be resolved. First the mechanism for the pollutant degradation need to be developed and secondly, charge carriers need to migrate to the surface and be able to perform the degradation process. At present the distance that the charge carrier can migrate is unknown. Similarly, grafting of polymeric materials on top of solid particles, particularly silica, is promising to improve many of their mechanical properties. For this process to be viable interfacial reactions that require charge-carriers migration to the interface are necessary. Whether they do occur and over what distances needs to be determined.

### 3.3. Fabrication of nanostructures using radiation

One of the important approaches is still now vigorously promoted by scientists is 'top-down' methodology. Top-down refers to the approach that begins with appropriate starting materials (or substrate) that is then 'sculpted' to achieve the desired functionality.

This method is used in fabricating devices out of a substrate by the methods of electron beam nanolithography and reactive ion etching. In this process, the energy of radiation is deposited on the materials via an ionization process. The electron generated through ionization loses its energy through interaction with surrounding molecules and eventually thermalized. The initial separation distance between the radical cation and thermalized electron on average is approximately several nanometers, and thus provide a few nanoscale designed imaging system.

Ion track membrane is another example of the formation nano-sized cylindrical structure by ion beam on the plastic film such as PET. The use of radiation such as ion beam and electron beam proved to be a great potential for the fabrication of nano-structured materials to be used in the lithography, membrane for ultrafiltration system, membrane with electrical and magnetic properties as a potential for chemical detectors and biosensors.

Ionizing radiation such as gamma radiation and electron beam has been used widely in industry for crosslinking of polymer, polymer blend and composites. This technology can be well extended to the crosslinking of nanopolymeric materials or nanocomposites.

In recent years, polymer/clay nanocomposites has attracted the interest of industry because of their major improvements in physical and mechanical properties, heat stability, reduce flammability and provide enhanced barrier properties at low clay contents. In many applications, crosslinking of polymer matrix is necessary that can further improved the mechanical and physical properties of the composites.

Study has shown that irradiated nanosized clay enhanced radiation crosslinking of the polymeric matrix and this is one of the potential researches of the applications of radiation crosslinking in nanocomposites. Various type of polymers (natural rubber, polyolefines, polyimide, polystyrene etc) polymer blends (thermoplastic elastomers, etc.), can be used as matrixes and the choices of intercalating agents for the production of nanosize clay play a role in radiation crosslinking of nanocomposites. Similar research can be extended to electron beam crosslinking of electromagnetic nanocomposites which comprised of high volume fraction of inorganic fillers in elastomeric matrix. The effect of radiation on inorganic fillers is believed to has influence on the overall radiation crosslinking of the matrix and hence the properties of the nanocomposites.

The use of nanosized silica as fillers for radiation crosslinked polyacrylates is one of the area that has shown of great sucess. Several acrylates and nanosized silica can be synthesized by the heterogeneous hydrolytic condensation using methacryloxypropyl trimethoxysilane to produce silica modified acrylate (SIMA) and followed by UV/EB crosslinking of the particles in the acrylate based matrix. Such system provides high abrasion and scratch resistant materials that can be used to protect surface of substrate such as automotive parts.

Polymeric *nanogels* and *microgels* are particles of polymers having the dimensions in the order of nano- and micrometers, respectively. Depends on chemical composition they are able to react, usually by a pronounced change in dimensions and swelling ability, to external stimuli such as temperature, pH, ionic strength, concentration of a given substance, electric field, light etc. Such structures may find applications in controlled or self-regulating drug delivery, signal transmission or micromachinery.

A multitude of techniques has been described for the synthesis of polymeric nano-and microgels. Most of them can be classified in two groups. The first group includes techniques based on concomitant polymerization and crosslinking (where the substrates are monomers or their mixtures), called by some authors "crosslinking polymerization". The second group contains methods based on radiation intramolecular crosslinking of macromolecules (where the starting material is not a monomer, but a polymer). Synthesis of nano/microgels by radiation techniques seems to be especially well suited for the synthesis of high-purity nanostructures for biomedical use.

First tests of intramolecular crosslinked individual polymer chains created by ionizing radiation has been initiated. The main advantage of this method is that it can be carried out in a pure polymer/solvent system, free of any monomers, initiators, crosslinkers or any other additives, therefore it seems have been performed on the application of carriers for enzymes, antibodies etc. used in diagnostics (e.g. immunoassays), drug carriers for therapeutic purposes (local, controlled drug delivery), and, potentially, microdevices, artificial biological fluids and synthetic vectors for drug delivery as well as to mimic a functions of living cells. For these products, there are at least two mechanisms allowing for controlled drug delivery. One can load the gel particles with a drug at a pH where the particles are fully swollen (expanded), trap it inside by a pH change leading to the collapse of the microgel, and subsequently allow the drug to diffuse out at a pH-controlled rate. Similar mechanism applies as well to the systems where ionic strength is the stimulus for expansion and collapse, or where both pH and ionic strength effects are operating, e.g. inside of living cells.

Another directions of investigations of the nanostructures is their application as synthetic, non-virial vectors in gene delivery. The latter is regarded as a powerful tool for curing some hereditary diseases and treating genetically based disorders. Certainly, the issue is a very complex one, since such vectors must be capable of performing many processes as binding DNA fragments, attachment to cells, internalization, and intracellular plasmid release. First attempts of using microgel-like structures for gene delivery were based mainly on chitosan, but synthetic structures based on 2-(dimethylamino)ethyl methacrylate, *N*-vinylpyrrolidone and *N*-isoporpylacrylamide have been tested as well, with promising results.

There are trials to design microgel-based intravenous drug carriers that could remain in blood for a suitable period of time, facilitate the cellular uptake and possibly also selectively deliver the drug to a target site. Animal tests have shown that by varying properties of such structures (chemical composition, hydrophilicity) one can change the biodistribution patterns of the nano-and microgels and that drug-loaded structures were more efficient than equivalent concentrations of free drug, e.g. targeted distribution of gold particles in-built into nanospheres or enhanced distribution of photosensitizer among canceric and health cells in order to destroy tumor cells only under of action of radiation.

Radiation technique is essential to fabrication of nanostructures with high resolution and a high aspect ratio because radiation beams can be focused into a few nanometers or less and scanned with quite high speed. The fabrication with resolution lower than 10 nm requires electron beam (EB),

focused ion beam (FIB), and X ray processes. Using these radiation techniques, the fabrication of extremely small structures in nanometer scale such as the world's smallest globe (diameter: 60 μm, smallest pattern: 10 nm), SiC tubes with 5 μm in inner diameter, colour imaging of the polymer films (resolution: 300 nm), and a microwine glass with 2.75 μm external diameter, can be achieved.

Nanostructure formation with aspect ratios higher than 100 requires heavy ion beam processes. Ion track membranes, which possess cylindrical through-holes with diameter ranging from 10 nm to 1 μm, are used as a template for electroplating of nanowires of metal, semiconductor, and magnetic materials. These nanowires can be applied to electric and light emitting devices. Ion beam induced crosslinking of polysilane provides Si based nanowires, which can be used as parts of nanoscopic electronic devices.

In future, X ray, EB, and low energy beams such as EB scanning devices and FIB should be useful for nanolithography and 3D fabrication. On the other hand, heavy ion beam can be useful for fabrication of nanopores and nanowires as well as LIGA processes for mass production of plastic, ceramics or other materials of high aspect ratio with high aspect ratios. The development of dense plasma focus device for X ray lithography was reported.

Furthermore, radiation processing technology using gamma-rays and EB can be used for the production of nanoparticles such as silicon oxide and nano-sized silico-organic particles, and natural rubber/clay nanocomposites, which are used for high performance elastomers. This technique is also employed in preparation of polymeric nanogels, which can be used for filler materials in coating industry, drug delivery carriers, and modern biomaterials such as biocompatible tissue like cartilage and muscles.

### 3.4. Technological applications

A significant impact of nanomaterials is anticipated in biomedical applications and in radiotherapy. As already mentioned, radiation provides the means to synthetically generate drug delivery systems with fine control over the delivery system and over the rate of drug release. By controlling the size and the release rate one may direct to the release to occur at the required location, thus minimizing side effects from the drug and maximizing its efficiency. Furthermore, because of the difference in density of materials nanomaterials offer the opportunity to target irradiation to a certain location and not another, for example into a cancerous cell in a healthy tissue. It is easy to synthesize (using radiation or otherwise) nanoparticles of a-priory engineered surfaces that will recognize some cells and will attach to their surfaces. Because of the higher density of the particles the ionizing radiation will be absorbed primarily by the particle. Thus the damage to the cells will be mostly when they are attached to the nanoparticles (e.g., only cancerous cells) and not the surrounding cells.

*Electron, ion beam and X ray lithography*

- The fabrication with resolution lower than 10 nm requires electron beam (EB), focused ion beam (FIB), and X ray processes.

*Polymeric nanostructures* fabricated by radiation techniques might be used in various ways:

- Nanosizing will make possible the use of low solubility substances as drugs. This will approximately double the number of chemical substances available for pharmaceuticals (where particle size ranges from 100 to 200 nm).
- Nano/microgels polymeric structures have several properties (high solubility in aqueous solvent, defined structure, high monodispersity, low systemic toxicity) that make them attractive components of so-called nanobiological drug carrying devices.
- Targeting of tumors with nanoparticles in the range 50 to 100 nm. Larger particles cannot enter the tumor pores while nanoparticles can move easily into the tumor.

- Active targeting by adding ligands as target receptors on a nanoparticle surface.The receptors will recognize damaged tissue, attach to it and release a therapeutic drug.
- Increase the degree of localized drug retention by increasing the adhesion of finer particles on tissues

Nanosized markers will allow cancer detection in the incipient phase when only a few cancer cells are present.

Polymeric functional nanostructures in form of core- shell protein-friendly spheres were tested for in vivo delivery of biologically active proteins as well as anti-HIV vaccination.

*Nanoparticle Reinforced Polymers*

Requirements for increased fuel economy in motor vehicles demand the use of new, lightweight materials - typically plastics - that can replace metal. The best of these plastics are expensive and have not been adopted widely by U.S. vehicle manufacturers. Nanocomposites, a new class of materials under study internationally, consist of traditional polymers reinforced by nanometer-scale particles dispersed throughout. These reinforced polymers may present an economical solution to metal replacement. In theory, the nanocomposite can be easily extruded or molded to near-final shape, provide stiffness and strength approaching that of metals, and reduce weight. Corrosion resistance, noise dampening, parts consolidation, and recyclability all would be improved. However, producing nanocomposites requires the development of methods for dispersing the particles throughout the plastic, as well as means to efficiently manufacture parts from such composites.

## 4. CONCLUSIONS

- Nanotechnology is becoming one of the most important, strategic fields of R&D. According to the reports, this is one of the discipline, which will be a driving force for the technological developments in the nearest future. Because the field is in its infancy many outstanding scientific issues still need to be resolved.

- The main applications of nanotechnology are nanoelectronics, manufacturing of nanotubes and nanowires, biosensors, nanofilters for environmental applications.

- The radiation is one of the important tools, which is already applied (electron beam and X ray lithography, nuclear track membranes) and its role will grow in the future.

- Important applications of radiation-assisted nanotechnology are foreseen in medicine; controlled drug delivery systems, HIV vaccine, photo- and radio- therapy sensitisers.

- Well established gamma, X ray and electron beam processing will be applied for manufacturing of nanomaterials and nanocomposites e.g. nanoparticles reinforced materials.

Meeting recognazied the important role of the IAEA in coordinating research and development on radiation assisted nanotechnology and in transferring the technology to developing Member States through its research and TC projects.

Since science has interdisciplinary character ((microelectronics, new functional materials, controlled drug delivery systems (HIV vaccinates, sensitizers for photo- and radiation- cancer therapy), new tough materials, sensors)), the interactive programmes between relevant chemistry, physics and biology (including medicine) institutions should be elaborated.

# MOLECULAR NANOTECHNOLOGY. TOWARDS ARTIFICIAL MOLECULAR MACHINES AND MOTORS

V. BALZANI, A. CREDI, F. MARCHIONI, S. SILVI, M. VENTURI
Dipartimento di Chimica "G. Ciamician",
Università di Bologna,
Bologna, Italy

**Abstract**

Miniaturization is an essential ingredient of modern technology. In this context, concepts such as that of (macroscopic) device and machine have been extended to the molecular level. A *molecular machine* can be defined as an assembly of a discrete number of molecular components – that is, a supramolecular system – in which the component parts can display changes in their relative positions as a result of some external stimulus. While nature provides living organisms with a wealth of molecular machines and motors of high structural and functional complexity, chemists are interested in the development of simpler, fully artificial systems. Interlocked chemical compounds like rotaxanes and catenanes are promising candidates for the construction of artificial molecular machines. The design, synthesis and investigation of chemical systems able to function as molecular machines and motors is of interest not only for basic research, but also for the growth of nanoscience and the subsequent development of nanotechnology. A few examples of molecular machines taken from our own research will be illustrated.

## 1. INTRODUCTION

A device is something invented and constructed for a special purpose, and a machine is a particular type of device in which the component parts display changes in their relative positions as a result of some external stimulus. Progress of mankind has always been related to the construction of novel devices. Depending on the purpose of its use, a device can be very big or very small. In the last fifty years, progressive miniaturization of the components employed for the construction of devices and machines has resulted in outstanding technological achievements, particularly in the field of information processing. A common prediction is that further progress in miniaturization will not only decrease the size and increase the power of computers, but could also open the way to new technologies in the fields of medicine, environment, energy, and materials.

Until now miniaturization has been pursued by a large-downward (top-down) approach, which is reaching practical and fundamental limits (presumably ca. 50 nanometers) [1]. Miniaturization, however, can be pushed further on since "there is plenty of room at the bottom", as Richard P. Feynman stated in a famous talk to the American Physical Society in 1959 [2].

The key sentence of Feynman's talk was the following: "The principle of physics do not speak against the possibility of manoeuvring things atom by atom". The idea of the "atom-by-atom" bottom-up approach to the construction of nanoscale devices and machines, however, which was so much appealing to some physicists [3] did not convince chemists who are well aware of the high reactivity of most atomic species and of the subtle aspects of chemical bond. Chemists know [4] that atoms are not simple spheres that can be moved from a place to another place at will. Atoms do not stay isolated; they bond strongly to their neighbours and it is difficult to imagine that the atoms can be taken from a starting material and transferred to another material.

In the late 1970s a new branch of chemistry, called supramolecular chemistry, emerged and expanded very rapidly, consecrated by the award of the Nobel Prize in Chemistry to C.J. Pedersen [5], D.J. Cram [6], and J.-M. Lehn [7] in 1987. In the frame of research on supramolecular chemistry, the idea began to arise in a few laboratories [8-10] that molecules are much more convenient building blocks than atoms to construct nanoscale devices and machines.

The main reasons at the basis of this idea are: (i) molecules are stable species, whereas atoms are difficult to handle; (ii) Nature starts from molecules, not from atoms, to construct the great number

and variety of nanodevices and nanomachines that sustain life; (iii) most of the laboratory chemical processes deal with molecules, not with atoms; (iv) molecules are objects that exhibit distinct shapes and carry device-related properties (e.g., properties 2 that can be manipulated by photochemical and electrochemical inputs); (v) molecules can selfassemble or can be connected to make larger structures. In the same period, research on molecular electronic devices began to flourish [11].

In the following years supramolecular chemistry grew very rapidly [12] and it became clear that the "bottom-up" approach based on molecules opens virtually unlimited possibilities concerning design and construction of artificial molecular-level devices and machines. Recently the concept of molecules as nanoscale objects exhibiting their own shape, size and properties has been confirmed by new, very powerful techniques, such as single-molecule fluorescence spectroscopy and the various types of probe microscopies, capable of "seeing" [13] or "manipulating" [14] single molecules, and even to investigate bimolecular chemical reactions at the single molecule level [15].

Much of the inspiration to construct molecular-level devices and machines comes from the outstanding progress of molecular biology that has begun to reveal the secrets of the natural molecular-level devices and machines, which constitute the material base of life. Bottom-up construction of devices and machines as complex as those present in Nature is, of course, an impossible task [16]. Therefore chemists have tried to construct much simpler systems, without mimicking the complexity of the biological structures. In the last few years, synthetic talent, that has always been the most distinctive feature of chemists, combined with a device-driven ingenuity evolved from chemists' attention to functions and reactivity, have led to outstanding achievements in this field [17-20].

## 2. CHARACTERISTICS OF MOLECULAR MACHINES AND MOTORS

The words *motor* and *machine* are often used interchangeably when referred to molecular systems. It should be recalled, however, that a motor converts energy into mechanical work, while a machine is a device, usually containing a motor component, designed to accomplish a function. Molecular machines and motors operate via electronic and/or nuclear rearrangements and, like the macroscopic ones, are characterized by *(i)* the kind of energy input supplied to make them work, *(ii)* the type of motion (linear, rotatory, oscillatory, ...) performed by their components, *(iii)* the way in which their operation can be monitored, *(iv)* the possibility to repeat the operation at will (cyclic process), and *(v)* the time scale needed to complete a cycle. According to the view described above, an additional and very important distinctive feature of a molecular machine with respect to a molecular motor is *(vi)* the function performed [18].

As far as point *(i)* is concerned, a chemical reaction can be used, at least in principle, as an energy input. In such a case, however, if the machine has to work cyclically [point *(iv)*], it will need addition of reactants at any step of the working cycle, and the accumulation of by–products resulting from the repeated addition of matter can compromise the operation of the device. On the basis of this consideration, the best energy inputs to make a molecular device work are photons [21] and electrons [22]. It is indeed possible to design very interesting molecular devices based on appropriately chosen photochemically and electrochemically driven reactions[20].

In order to control and monitor the device operation [point *(iii)*], the electronic and/or nuclear rearrangements of the component parts should cause readable changes in some chemical or physical property of the system. In this regard, photochemical and electrochemical techniques are very useful since both photons and electrons can play the dual role of "writing" (i. e., causing a change in the system) and "reading" (i.e., reporting the state of the system).

The operation time scale of molecular machines [point *(v)*] can range from microseconds to seconds, depending on the type of rearrangement and the nature of the components involved.

Finally, as far as point *(vi)* is concerned, the functions that can be performed by exploiting the movements of the component parts in molecular machines are various and, to a large extent, still unpredictable. It is worth to note that the mechanical movements taking place in molecular-level machines, and the related changes in the spectroscopic and electrochemical properties, usually obey binary logic and can thus be taken as a basis for information processing at the molecular level. Artificial molecular machines capable of performing logic operations have been reported [23].

## 3. ROTAXANES AND CATENANES AS ARTIFICIAL MOLECULAR MACHINES

Most of the recently designed artificial molecular machines and motors are based [20] on interlocked chemical compounds named rotaxanes and catenanes. The names of these compounds derive from the Latin words *rota* and *axis* for wheel and axle, and *catena* for chain. Rotaxanes [24] are minimally composed (Fig. 1a) of an axle-like molecule surrounded by a macrocyclic compound and terminated by bulky groups (stopper) that prevent disassembly; catenanes [24] are made of (at least) two interlocked macrocycles or "rings" (Fig. 1b). Rotaxanes and catenanes are appealing systems for the construction of molecular machines because motions of their molecular components can be easily imagined (Fig. 2).


*FIG. 1. Schematic representation of a rotaxane (a) and a catenane (b).*

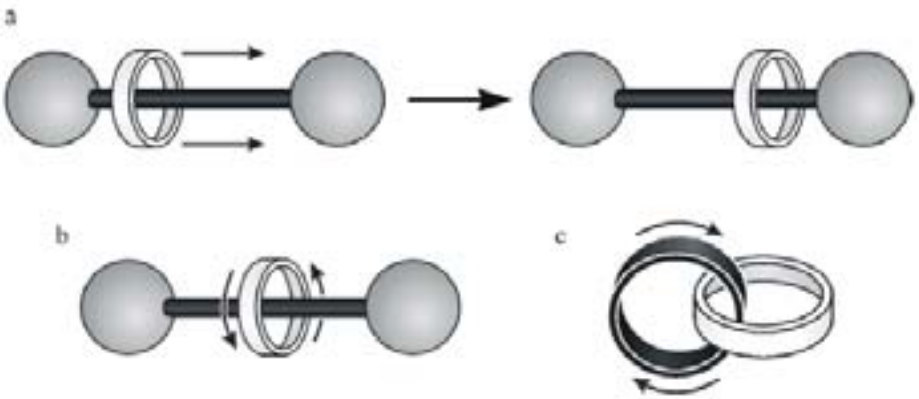


*FIG. 2. Schematic representation of some of the intercomponent motions that can be obtained with rotaxanes and catenanes: shuttling (a) and ring rotation (b, c).*

Important features of these systems derive from noncovalent interactions between components that contain complementary recognition sites. Such interactions, that are also responsible for the efficient template-directed syntheses of rotaxanes and catenanes, involve electron-donor/acceptor cability, hydrogen bonding, hydrophobic/hydrophylic character, π-π stacking, coulombic forces and, on the side of the strong interaction limit, metal-ligand bonding.

In the next sections, a few examples of artificial molecular machines based on rotaxanes and catenanes taken from our research will be illustrated.

## 4. AN ACID-BASE CONTROLLED MOLECULAR SHUTTLE

In rotaxanes containing two different recognition sites in the dumbbell-shaped component, it is possible to switch the position of the ring between the two 'stations' by an external stimulus. A system which behaves as a chemically controllable molecular shuttle is compound $\mathbf{1}^{3+}$ shown in Fig. 3 [25]. It is made of a dibenzo[24]crown-8 (DB24C8) macrocycle and a dumbbell-shaped component containing a dialkylammonium center and a 4,4'-bipyridinium unit. An anthracene moiety is used as a stopper because its absorption, luminescence, and redox properties are useful to monitor the state of the system. Since the $N^+$–H···O hydrogen bonding interactions between the DB24C8 macrocycle and the ammonium center are much stronger than the electron donor-acceptor interactions of the macrocycle with the bipyridinium unit, the rotaxane exists as only one of the two possible translational isomers. Deprotonation of the ammonium center with a base (a tertiary amine) causes 100% displacement of the macrocycle to the bipyridinium unit; reprotonation directs the macrocycle back onto the ammonium center (Fig. 3). Such a switching process has been investigated in solution by $^1$H NMR spectroscopy and by electrochemical and photophysical measurements [25]. The full chemical reversibility of the energy supplying acid/base reactions guarantees the reversibility of the mechanical movement, in spite of the formation of waste products. Notice that this system could be useful for information processing since it exhibits a binary logic behavior. It should also be noted that, in the deprotonated rotaxane, it is possible to displace the crown ring from the bipyridinium station by destroying the donor-acceptor interaction through reduction of the bipyridinium station or oxidation of the dioxybenzene units of the macrocyclic ring. Therefore, in this system, mechanical movements can be induced by two different types of stimuli (acid-base and electron-hole).

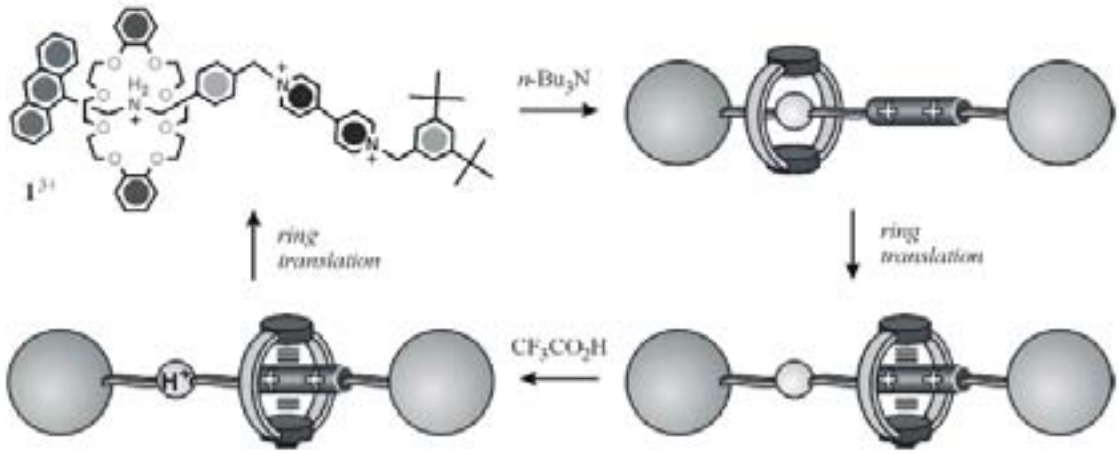


*FIG. 3. A chemically controllable molecular shuttle. The macrocyclic ring can be switched between the two stations of the dumbbell-shaped component by acid-base inputs*

## 5. A LIGHT-DRIVEN MOLECULAR SHUTTLE

For a number of reasons, light is the most convenient form of energy to make artificial molecular machines work [21]. In order to achieve photoinduced ring shuttling in rotaxanes containing two different recognition sites in the dumbbell-shaped component, the thoroughly designed compound $2^{6+}$ (Fig. 4) was synthesized [26].

This compound is made of the electron-donor macrocycle R, and a dumbbell-shaped component which contains (i) $[Ru(bpy)_3]^{2+}$ (P) as one of its stoppers, (ii) a 4,4'- bipyridinium unit ($A_1$) and a 3,3'-dimethyl-4,4'-bipyridinium unit ($A_2$) as electron accepting stations, (iii) a *p*-terphenyl-type ring system as a rigid spacer (S), and (iv) a tetraarylmethane group as the second stopper (T). The structure of

rotaxane $2^{6+}$ was characterized by mass spectrometry and $^1$H NMR spectroscopy, which also established, along with cyclic voltammetry, that the stable translational isomer is the one in which the R component encircles the $A_1$ unit, in keeping with the fact that this station is a better electron acceptor than the other one. The electrochemical, photophysical and photochemical (under continuous and pulsed excitation) properties of the rotaxane, its dumbbell-shaped component, and some model compounds have then been investigated and two strategies have been devised in order to obtain the photoinduced abacus-like movement of the R macrocycle between the two stations $A_1$ and $A_2$: one was based on processes involving only the rotaxane components (intramolecular mechanism), while the other one required the help of external reactants (sacrificial mechanism).

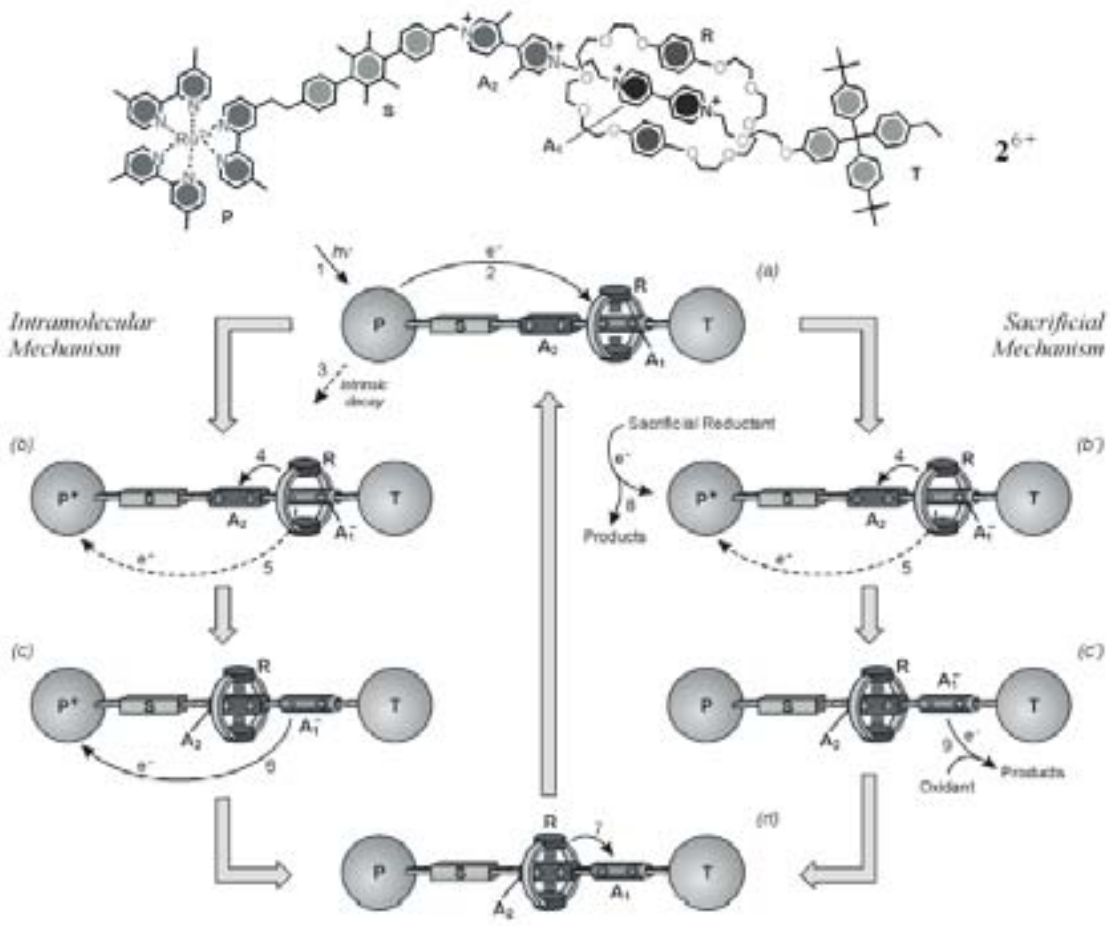


*FIG. 4. Structural formula of the rotaxane $2^{6+}$ and schematic representation of the intramolecular (left) and sacrificial (right) mechanisms for the photoinduced shuttling movement of macrocycle R between the two stations $A_1$ and $A_2$.*

The intramolecular mechanism, illustrated in the left part of Fig. 4, is based on the following four operations [26]:

(a) *Destabilization of the stable translational isomer*: light excitation of the photoactive unit P (Step 1) is followed by the transfer of an electron from the excited state to the $A_1$ station, which is encircled by the ring R (Step 2), with the consequent "deactivation" of this station; such a photoinduced electron-transfer process has to compete with the intrinsic decay of P* (Step 3).

(b) *Ring displacement*: the ring moves from the reduced station $A_1^-$ to $A_2$ (Step 4), a step that has to compete with the back electron-transfer process from $A_1^-$ (still encircled by R) to the oxidized photoactive unit $P^+$ (Step 5). This is the most difficult requirement to meet in the intramolecular mechanism.

(c) *Electronic reset*: a back electron-transfer process from the "free" reduced station $A_1^-$ to $P^+$ (Step 6) restores the electron-acceptor power to the $A_1$ station.

(d) *Nuclear reset*: as a consequence of the electronic reset, back movement of the ring from $A_2$ to $A_1$ takes place (Step 7).

The results obtained [26] do not indicate cleary whether the ring displacement (Step 4) is faster than the electronic reset of the system after light excitation (Step 5; $k$ = 2.4  $10^5$ $s^{-1}$). More detailed laser flash photolysis studies suggest that these two processes could occur on the same time scale [27].

It is worthwhile noticing that in a system which behaves according to the intramolecular mechanism shown in Fig. 4 (left) each light input causes the occurrence of a forward and back ring movement (i.e., a full cycle) without generation of any waste product. In some way, it can be considered as a "four-stroke" cyclic linear motor powered by light.

A less demanding mechanism is based on the use of external sacrificial reactants (a reductant like triethanolamine and an oxidant like dioxygen) that operate as illustrated in the right part of Fig. 4:

(a) *Destabilization of the stable translational isomer*, as in the previous mechanism.

(b') *Ring displacement after scavenging of the oxidized photoactive unit*: since the solution contains a suitable sacrificial reductant, a fast reaction of such species with $P^+$ (Step 8) competes successfully with the back electron-tranfer reaction (Step 5); therefore, the originally occupied station remains in its reduced state $A_1^-$, and the displacement of the ring R to $A_2$ (Step 4), even if it is slow, does take place.

(c') *Electronic reset*: after an appropriate time, restoration of the electron-acceptor power of the $A_1$ station is obtained by oxidizing $A_1^-$ with a suitable oxidant, such as $O_2$ (Step 9).

(d) *Nuclear reset*, as in the previous mechanism (Step 7).

The results obtained [26] show that such a sacrificial mechanism is fully successful. Of course, this mechanism is less appealing than the intramolecular one because it causes the formation of waste products. An alternative strategy is to use a non-sacrificial (reversible) reductant species that is regenerated after the back electron-transfer process [28].

## 6. CONTROLLED RING ROTATION IN CATENANES

In a catenane, structural changes caused by rotation of one ring with respect to the other can be clearly evidenced when one of the two rings contains two non-equivalent units. In the catenane $3^{4+}$ shown in Fig. 5, the electron-acceptor tetracationic cyclophane is "symmetric", whereas the other ring contains two different electron–donor units, namely, a tetrathiafulvalene (TTF) and a 1,5-dioxynaphthalene (DON) unit [29].

In a catenane structure, the electron donor located inside the cavity of the electron-acceptor ring experiences the effect of two electron-acceptor units, whereas the alongside electron donor experiences the effect of only one electron acceptor. Therefore, the better electron donor (i. e., TTF) enters the acceptor ring and the less good one (i.e., DON) remains alongside. On electrochemical oxidation, the first observed process concerns TTF, which thus loses its electron donating properties.

Furthermore, an electrostatic repulsion arises between TTF+ and the tetracationic macrocycle. These effects cause rotation of one ring to yield the translational isomer with the DON moiety positioned inside the acceptor ring. Upon reduction of TTF+, the initial configuration is restored. However, this may happen without the occurrence of a full rotation, because it is equally probable that

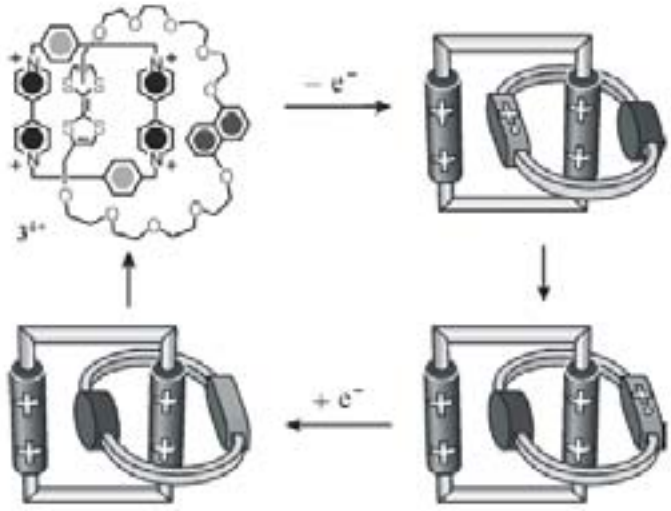


*FIG. 5. Redox controlled ring rotation in a catenane containing a non-symmetric ring*

the reset caused by reduction of TTF+ occurs by a reverse rotation compared to that occurred in the forward switching caused by TTF oxidation. In order to obtain a full rotation, i.e., a molecular-level rotary motor, the direction of each switching movement should be controllable. This goal can likely be reached by introducing appropriate functions in one of the two macrocycles [20,21]. When this goal is reached, it will be possible to convert alternate electrical potential energy into a molecular-level mechanical rotation.

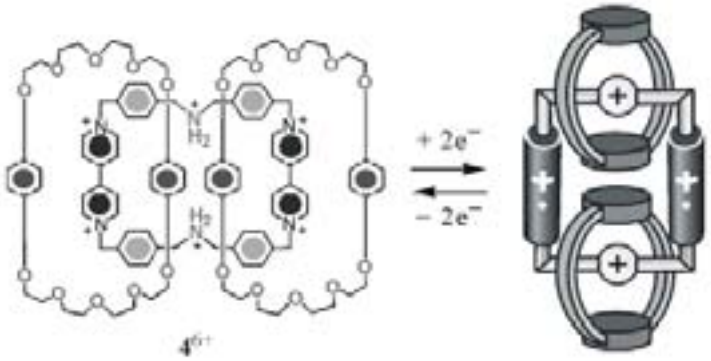


*FIG. 6. Redox controlled movements of the ring components upon reduction-oxidation of the bipyridinium units in a catenane composed of three interlocked macrocycles*

Controlled rotation of the molecular rings has been achieved also in a catenane composed of three interlocked macrocycles ($4^{6+}$, Fig. 6) [30]. Upon addition of one electron in each of the bipyridinium units, the two macrocycles move on the ammonium stations, and move back to the original position when the bipyridinium units are reoxidized. Unidirectional ring rotation has recently been obtained [31] in a peptide-based catenane having the same topology as $4^{6+}$.

## 7. CONCLUSIONS AND PERSPECTIVES

In the last few years, several examples of molecular machines and motors have been designed and constructed [17–20]. It should be noted, however, that the molecular-level machines described in

this chapter operate in solution, that is, in an incoherent fashion. Although the solution studies of chemical systems as complex as molecular machines are of fundamental importance, it seems reasonable that, before functional supramolecular assemblies can find applications as machines at the molecular level, they have to be interfaced with the macroscopic world by ordering them in some way. The next generation of molecular machines and motors will need to be organized at interfaces [32], deposited on surfaces [33], or immobilized into membranes [16a,34] or porous materials [35] so that they can behave coherently. Indeed, the preparation of modified electrodes [22,36] represents one of the most promising ways to achieve this goal. Solid-state electronic devices based on functional rotaxanes and catenanes have already been developed [37]. Furthermore, addressing a single molecular-scale device [38] by instruments working at the nanometer level is no longer a dream [13–15].

Apart from more or less futuristic applications, the extension of the concept of a machine to the molecular level is of interest not only for the development of nanotechnology, but also for the growth of basic research. Looking at supramolecular chemistry from the viewpoint of functions with references to devices of the macroscopic world is indeed a very interesting exercise which introduces novel concepts into Chemistry as a scientific discipline.

## REFERENCES


[1] KEYES, R.W., Proc. IEEE 89 (2001) 227. (b) International Technology Roadmap for Semiconductors (ITRS) (2003) Edition, available at http://public.itrs.net

[2] FEYNMAN, R.P., Eng. Sci. 23 (1960) 22. (b) FEYNMAN, R.P., Saturday Rev. 43 (1960) 45. (See also: http://www.its.caltech.edu/˜feynman)

[3] DREXLER, K.E., Engines of Creation, The Coming Era of Nanotechnology, Anchor Press, New York, (1986). (b) DREXLER, K.E., Nanosystems. Molecular Machinery, Manufacturing, and Computation, Wiley, New York (1992).

[4] SMALLEY, R.E., Sci. Am. 285 (2001) 76.

[5] PEDERSEN, C.J., Angew. Chem. Int. Ed. Engl. 27 (1988) 1021.

[6] CRAM, D.J., Angew. Chem. Int. Ed. Engl. 27 (1988) 1009.

[7] LEHN, J.-M., Angew. Chem. Int. Ed. Engl. 27 (1988) 89.

[8] JOACHIM, C., LAUNAY, J.-P., Nouv. J. Chem. 8 (1984) 723.

[9] BALZANI, V., MOGGI, L., SCANDOLA, F., in Supramolecular Photochemistry, (Ed.: Balzani, V.), Reidel, Dordrecth, (1987), p. 1.

[10] LEHN, J.-M., Angew. Chem. Int. Ed. Engl. 29 (1990) 1304.

[11] AVIRAM, A., RATNER, M.A., Chem. Phys. Lett. 29 (1974) 277.

[12] VÖGTLE, F., Supramolecular Chemistry. An Introduction, Wiley, Chichester (1991).

[13] BALZANI, V., SCANDOLA, F., Supramolecular Photochemistry, Horwood, Chichester (1991).

[14] LEHN, J.-M., Supramolecular Chemistry: Concepts and Perspectives, VCH, Weinheim (1995).

[15] Single Molecule Spectroscopy (Eds.: RIGLER, R., ORRIT, M., TALENCE, I., BASCHÉ,T.), Springer-Verlag, Berlin (2001).

[16] MOERNER, W.E., J. Phys. Chem. B 106 (2002) 910.

[17] Single Molecule Detection in Solution (Eds.: ZANDER, CH., ENDERLEIN, J., KELLER, R.A.), Wiley-VCH, Weinheim (2002).

[18] GIMZEWSKI, J.K., JOACHIM, C., Science 283 (1999) 1683.

[19] HLA, S.-W., MEYER, G., RIEDER, K.-H., ChemPhysChem 2 (2001) 361.

[20] CHRIST, T., KULZER, F., BORDAT, P., BASCHÉ, T., Angew. Chem. Int. Ed. 40 (2001) 4192.

[21] STEINBERG-YFRACH, G., RIGAUD, J.-L., DURANTINI, E.N., MOORE, A.L., GUST, D., MOORE, T.A., Nature 392 (1998) 479.

[22] SOONG, R.K., BACHAND, G.D., NEVES, H.P., OLKHOVETS, A.G., CRAIGHEAD, H.G., MONTEMAGNO, C.D., Science 290 (2002) 1555.

[23] BALZANI, V., CREDI, A., RAYMO, F.M., STODDART, J.F., Angew. Chem. Int. Ed. 39 (2000) 3348.
[24] Acc. Chem. Res. (2001) 34, n. 6 (Special Issue on Molecular Machines, Guest Editor: STODDART, J.F.).
[25] Struct. Bond. (2001) 99 (Special Volume on Molecular Machines and Motors, Guest Editor: SAUVAGE, J.-P.).
[26] BALZANI, V., CREDI, A., VENTURI, M., Molecular Devices and Machines – A Journey into the Nano World, Wiley-VCH, Weinheim (2003).
[27] BALLARDINI, R., BALZANI, V., CREDI, A., GANDOLFI, M.T., VENTURI, M., Acc. Chem. Res. 34 (2001) 445.
[28] BALLARDINI, R., BALZANI, V., CREDI, A., GANDOLFI, M.T., VENTURI, M., Int. J. Photoenergy 3 (2001) 63.
[29] KAIFER, A.E., GÓMEZ-KAIFER, M., Supramolecular Electrochemistry, Wiley-VCH, Weinheim (1999).
[30] BALZANI, V., CREDI, A., VENTURI, M., ChemPhysChem 4 (2003) 49.
[31] Molecular Catenanes, Rotaxanes and Knots (Eds.: SAUVAGE, J.-P., DIETRICHBUCHECKER, C.), Wiley-VCH, Weinheim, Germany (1999).
[32] ASHTON, P.R., BALLARDINI, R., BALZANI, V., BAXTER, I., CREDI, A., FYFE, M.C.T., GANDOLFI, M.T., GOMEZ-LOPEZ, M., MARTINEZ-DIAZ, M.V., PIERSANTI, A., SPENCER, N., STODDART, J.F., VENTURI, M., WHITE, A.J.P., WILLIAMS, D.J., J. Am. Chem. Soc. 120 (1998) 11932.
[33] ASHTON, P.R., BALLARDINI, R., BALZANI, V., CREDI, A., DRESS, K.R., ISHOW, E., KLEVERLAAN, C.J., KOCIAN, O., PREECE, J.A., SPENCER, N., STODDART, J.F., VENTURI, M., WENGER, S., Chem. Eur. J. 6 (2000) 3558.
[34] BROUWER, A.M., FROCHOT, C., GATTI, F.G., LEIGH, D.A., MOTTIER, L., PAOLUCCI, F., ROFFIA, S., WURPEL, G.W.H., Science 291 (2001) 2124.
[35] ASAKAWA, M., ASHTON, P.R., BALZANI, V., CREDI, A., HAMERS, C., MATTERSTEIG, G., MONTALTI, M., SHIPWAY, A.N., SPENCER, N., STODDART, J.F., TOLLEY, M.S., VENTURI, M., WHITE, A.J.P., WILLIAMS, D.J., Angew. Chem. Int. Ed. 37 (1998) 333.
[36] BALZANI, V., CREDI, A., MATTERSTEIG, G., MATTHEWS, O.A., RAYMO, F.M., STODDART, J.F., VENTURI, M., WHITE, A.J.P., WILLIAMS, D.J, J. Org. Chem. 65 (2000) 1924.
[37] ASHTON, P.R., BALDONI, V., BALZANI, V., CREDI, A., HOFFMANN, H.D.A., MARTINEZ-DIAZ, M.V., RAYMO, F.M., STODDART, J.F., VENTURI, M., Chem. Eur. J. 7 (2001) 3482.
[38] LEIGH, D.A., WONG, J.K.Y., DEHEZ, F., ZERBETTO, F., Nature 424 (2003) 174.
[39] STEINBERG-YFRACH, G., LIDDELL, P.A., HUNG, S.-C., MOORE, A.L., GUST, D., MOORE, T.A., Nature 385 (1997) 239.
[40] GUST, D., MOORE, T.A., MOORE, A.L., Acc. Chem. Res. 34 (2001) 40.
[41] BENNETT, I.M., FARFANO, H.M.V., BOGANI, F., PRIMAK, A., LIDDELL, P.A., OTERO, L., SERENO, L., SILBER, J.J., MOORE, A.L., MOORE T.A., GUST, D., Nature 420 (2002) 398.
[42] CHIA, S., CAO, J., STODDART, J.F., ZINK, J.I., Angew. Chem. Int. Ed. 40 (2001) 2447.
[43] ÁLVARO, M., FERRER, B., GARCÍA, H., PALOMARES, E.J., BALZANI, V., CREDI, A., VENTURI, M., STODDART, J. F., WENGER, S., J. Phys. Chem. B 107 (2003) 14319.
[44] COLLIER, C.P., WONG, E.W., BELOHRADSKY, M., RAYMO, F.M., STODDART, J.F., KUEKES, P.J., WILLIAMS, R.S., HEATH, J.R., Science 285 (1999) 391.
[45] COLLIER, C.P., MATTERSTEIG, G., WONG, E.W., LUO, Y., BEVERLY, K., SAMPAIO, J., RAYMO, F.M., STODDART, J.F., HEATH, J.R., Science 289 (2000) 1172.
[46] LUO, Y., COLLIER, C.P., JEPPESEN, J.O., NIELSEN, K.A., DEIONNO, E., HO, G., PERKINS, J., TSENG, H.-R., YAMAMOTO, T., STODDART, J.F., HEATH, J.R., ChemPhysChem 3 (2002) 519.
[47] DIEHL, M.R., STEUERMAN, D.W., TSENG, H.-R., VIGNON, S.A., STAR, A., CELESTRE, P.C., STODDART, J.F., HEATH, J.R., ChemPhysChem 4 (2003) 1335.
[48] METZGER, R.M., Chem. Rev. 103 (2003) 3803.

# AN OVERVIEW OF RECENT DEVELOPMENTS IN NANOTECHNOLOGY: PARTICULAR ASPECTS IN NANOSTRUCTURED GLASSES

S. BACCARO[a], CHEN GUORONG[b]
[a] ENEA, Advanced Technological Physics/ION,
S. Maria di Galeria, Rome, Italy
[b] Institute of Inorganic Materials, School of Materials Science and Engineering,
East China University of Science and Technology, Shanghai, China

**Abstract**

The aim of this article is to provide a brief overview of nanotechnology research related to nanostructure of materials induced by radiation. Some possible examples are presented for variety of materials including polymers, metals and alloys, non-metallic inorganic materials, amorphous films and glasses. Research activities cover nanostructure fabrication, connection and self-organization, nanoscale modification, performance enhancement, and applications of nanotechnology and irradiation to biotechnology. The irradiation source involves γ rays, X rays, energetic particles (ions, electrons, neutron and protons), and ultraviolet, visible and infrared light and laser. Especially, nanostructured glasses are addressed with respect to the formation of nanoscaled photonic structure by irradiation and nanostructure induced enhancement in properties of ZnO excited glasses due to joint roles of irradiation and post thermal treatment. The latter is the current research subject of a collaboration between our laboratory at ENEA Casaccia and East China University of Science and Technology in Shanghai.

## 1. INTRODUCTION

Nanotechnology involves the precise manipulation and control of atoms and molecules to create novel structures with unique properties. This influential technology requires detailed understanding of physical processes, across a range of disciplines, at the scale of one billionth of a metre. The goal is to produce new materials, devices and systems tailored to meet the needs of a growing range of commercial, scientific, and engineering applications – opening new markets and giving dramatic benefits in product performance. Global activity in nanotechnology is growing rapidly, which, driven by strong interest and investment from the commercial and public worlds, is expected to play a strong and critical role in the future.

In the first part of this paper we will give a short review about some possible nanomaterials induced by radiation and in the last part, we reported some examples related to nanostructured glasses, including our specific activity related to ZnO excited glasses.

## 2. RADIATION INDUCED NANOSTRUCTURED MATERIALS

In the following part, we reported some possible examples of nanomaterials induced by radiation; of course, that is only one of many possible choices in this field.

In our opinion, it is impossible to give an overview on nanomaterials without mentioning carbon nanotubes. After the discovery of carbon nanotubes by Iijina in 1991, many efforts have been made to create these tubes and understand the formation mechanism of such materials [1]. Carbon nanotubes are expected to have some interesting properties, and researchers have speculated on their electronic structures and mechanical properties. In the early days of nanotechnology research, carbon nanotubes (CNT) were primarily grown by laser ablation and carbon arc techniques by various research groups across the world. In the last few years, chemical vapour deposition has also emerged as an alternative approach.

From viewpoint of techniques using radiation, new method to grow carbon nanotube was reported in 1996 by Yamamoto et al. where they grown carbon nanotubes by the argon ion beam irradiation on amorphous carbon target under high vacuum condition ($4\times10^{-5}$ Torr) [2]. The incident angle of the ion beam was normal to the target surface [2]; and the acceleration ion energy was 3 keV. Nanotubes are produced outside the sputtering region on the target surface after ion irradiation. The tubes have multilayered walls, the distance between carbon layers is 0.34 nm, and wall thickness of tubes ranges from 10 to 15 sheets. Figure 1a) shows the high resolution transmission electron micrograph of tubes grown on amorphous carbon after argon ion irradiation while 1b) is the secondary electron micrograph of nanotubes grown on the sample surface.

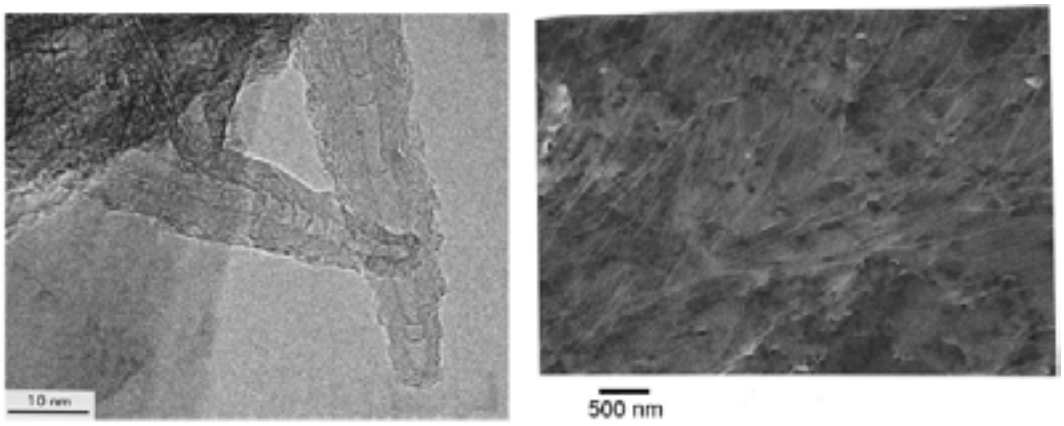


(a) (b)

*FIG. 1. High resolution transmission electron micrograph of tubes grown on amorphous carbon after argon ion irradiation (a); secondary electron micrograph of nanotubes grown on the sample surface after argon ion irradiation (b) [1]*

Single-walled carbon nanotubes (SWNT) have shown to possess most remarkable electronic and mechanical properties and various applications in nanoscale devices have been described. However, little progress has been reported on techniques related to connecting such tubular structures. Although a connection between SWNTs would constitute a novel type of molecular junction, it remained unknown whether such junctions exist at all and if they are stable: this is a key issue because both electronic devices and strong nano-mechanical systems need molecular connections among individual SWNTs.

Recently, Terrones et al. have shown that crossing single-walled carbon nanotubes (SWNT) can be joined by electron beam irradiation to form molecular junctions [3]. Stable junctions of various geometries are created *in situ* in a high voltage transmission electron microscope at specimen temperatures of 800°C. After a few minutes of irradiating two crossing tubes, their merging was observed at the point of contact, resulting in the formation of a junction with an X shape (Fig 2). The ready-formed X junctions can be manipulated in order to create Y- and T-like molecular connections. (Figures 3 and 4 (a-c)). It has been established from Ajayan et al. in 1998 that continuous sputtering of carbon atoms from the nanotube body takes place during irradiation, leading to dimensional changes and surface reconstructions [4]. By using careful conditions of irradiation, they are able to remove one of the “arms” of an X junction in order to create Y or T junction.

Electron beam exposure at high temperatures induces structural defects, which promote the joining of tubes via cross-linking of dangling bonds. The junctions described here are created via vacancies and interstitials, induced by the focused electron beam, that promote the formation of internanotube links. The results suggest that it may now be possible to construct nanotube networks by growing cross-link SWNTs followed by controlled electron irradiation at high temperature. The electrical characterization of SWNT junctions is imperative and remains a challenge for future experiments.

Since the merging of crossing tubes did not occur in the absence of irradiation, we can conclude that electron beam effects are responsible for the formation of the junctions. In the 1999, Banhart showed that the formation of vacancies and interstitials, induce rearrangements within graphitic structures under high energy particle irradiation [3]. At high temperature, carbon interstitials are highly mobile, leading to the annealing of vacancy-interstitial pairs before interstitial agglomerates can form. They assume that the presence of irradiation-induced vacancies within the tubes is also responsible for the formation of junctions.

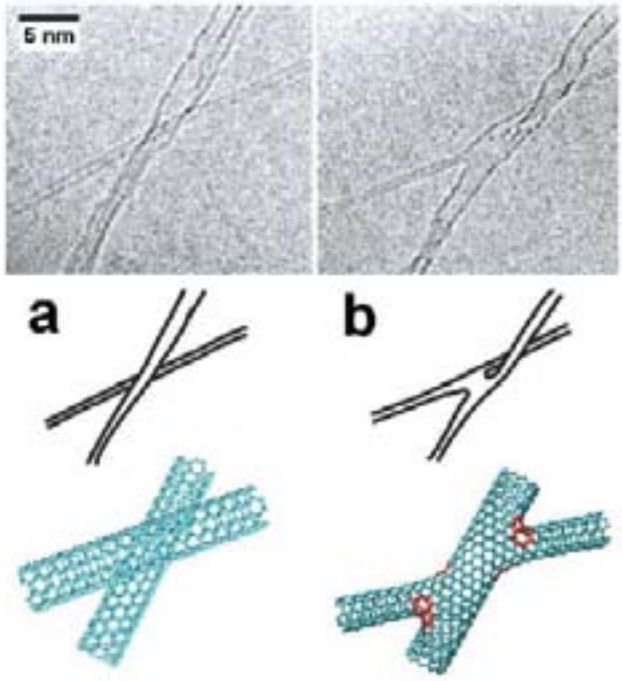


*FIG. 2. (a) A SWNT of ca. 2.0 nm diam. (running from bottom-left diagonally towards top right) crossing with an individual SWNT of ca. 0.9 nm diam. (b) 60 sec of electron irradiation promotes a molecular connection between the thin and the wide tube, forming an ''X'' junction. This junction is twisted out of the plane (heptagonal rings are indicated in red) [3].*

Dangling bonds around vacancies at the point of contact of the two tubes can serve as bridges for the merging process. The observations are supported by molecular dynamics simulations which show that the creation of vacancies and interstitials induces the formation of junctions involving seven- or eight-membered carbon rings at the surface between the tubes.

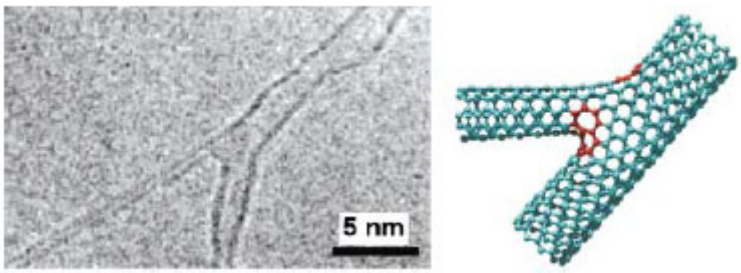


*FIG. 3. High-resolution transmission electron microscopy (HRTEM) image and molecular model of a Y junction created following electron irradiation of an ''X'' structure. One of the arms of the ''X'' junction vanished due to continuous sputtering under the electron beam, and a three-terminal junction remained. The junction exhibits tubes of different diameters which are molecularly joint [3].*

Irradiation of materials by energetic particles (e.g. electrons, ions and neutrons) is associated with very high internal power dissipation, which can drive the underlaying nano- and microstructure far from normal equilibrium conditions. The phenomena of pattern formation and self-organization have been viewed as natural responses of complex systems to strong external stimulation. One of the most unusual responses in this connection is the ability of the material's nano- and microstructure to self-assemble in well-organized, two- and three-dimensional periodic arrangements. The particular situation of energetic particle irradiation is quite interesting and numerous experimental observations on irradiated materials have systematically demonstrated the existence of fully or partially ordered nano- and microstructure in materials under energetic particle irradiation.

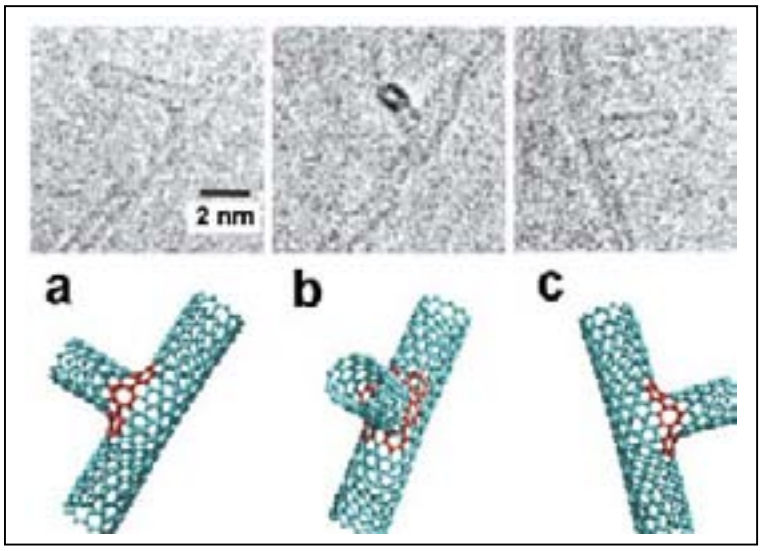


*FIG. 4. HRTEM images of a "T-like" junction formed after irradiating a preformed Y junction (a–c). The sequence shows the motion of this junction and the rotation by 180° under the electron beam irradiation [3].*

The basic physical mechanisms, which control the interaction between defect populations have been identified. When highly energetic particles (electrons, neutrons, ions, alpha particles, etc.) interact with lattice atoms and transfer an energy lager than the displacement threshold, Frenkel pairs (vacancies and interstitials) are generated. A fraction of those Frenkel pairs are clustered as small interstitial aggregates, vacancy loops and so on. Ghoniem et al. review and assess experimental evidence and theoretical models pertaining to the physical understanding of nano- and microstructure self-organization under irradiation conditions [6].

Condensed matter systems show a rich variety of patterns and self-assembled microstructures under irradiation by energetic particles due to the collective interaction between system components under external driving forces, resulting in the self-organization of its constituents. Experimental observations on the formation of self-organized defect clusters, dislocation loops, voids and bubbles are presented.

Experiments indicated that small defect clusters produced in irradiated face-centered-cubic (FCC) metals such as Ni and Cu have a tendency to become aligned along [001] planes under certain conditions. The defect cluster alignement in Cu becomes noticeable at damage levels of 0.1 displacements per atom (dpa) and remains stable up to damage levels in excess of 20 dpa (Fig. 5). Results on the formation of the ordered void and bubble lattices in HCP metals are typically located in two-dimensional layers parallel to the basal plane. In contract, the cavity lattice in FCC and BCC metals adopts the same three-dimensional symmetry as the host lattice.

The experimental observations of void superlattice formation in irradiated BCC and FCC metals showed that voids initially from randomly in irradiated materials, and then gradually transform to an

ordered array under some experimental conditions. The threshold dose for initial development of visible void ordering is a few dpa for BCC metals such as Mo, W and Nb. Fully developed (near-perfect ordering) void superlattices have been observed in irradiated BCC metals after dose levels of 30 dpa.

For example, defect cluster pattern formation has been observed in specimens of copper, as periodic arrays of vacancy loops, and in molybdenum that showed a BCC void superlattice (Figs. 5 and 6), after exposition to 3 MeV protons and 2 MeV $N^+$ ions, respectively. Once at the nanometer scale, the electronic, optical and physical bases of current device designs will be on the use of novel materials to engineer nanoscale devices for applications in electronic and sensing environments. Various techniques have been developed for nanostructure fabrication and the laser-assisted scanning tunneling microscope (STM) is one of the most promising applications. Different mechanisms have been discussed for the formation of these nanostructures, however, they are controversial.

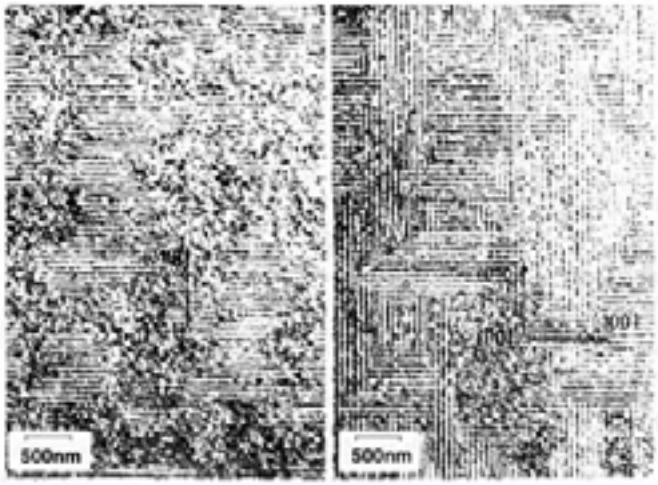


*FIG. 5. Dislocation microstructures (periodic arrays of vacancy loops) in Copper irradiated with protons at an irradiation dose of 2 dpa[6].*

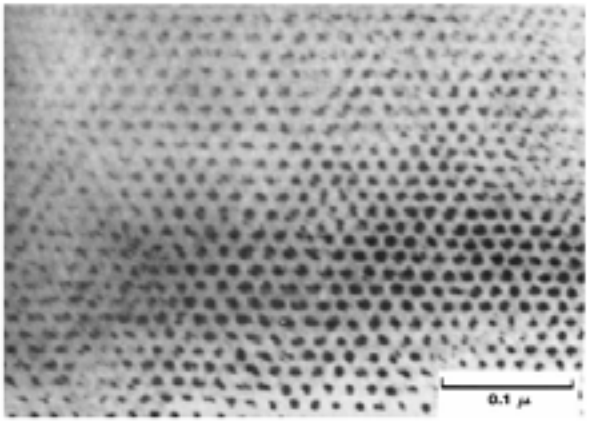


*FIG. 6. Mo void lattice: Electron micrograph showing a BCC void superlattice in Mo irradiated with 2 MeV $N^+$ ions to a dose of 100 dpa at 870°C. The electron beam was parallel to the crystal orientation. The micrograph was taken in an overfocused condition, which causes the voids to appear as dark spots [6].*

For instance, Lu et al., investigated in 2000 nanooxidation on hydrogen (H)-passivated Ge and Si surfaces using a frequency-doubled Nd:Yag laser with a pulse duration of 7 ns, and they explained that the nanooxidation is due to a thermal desorption of hydrogen atoms from the Ge or Si surfaces, stimulated by the tip-enhanced optical field[7]. It is well known that both the thermal expansion and the optical enhancement occur under laser irradiation but it is yet to be understood which mechanism is dominant. Recently, they investigated the mechanism of nanostructure fabricated on gold films and on H-passivated Ge surfaces using a pulsed laser in combination with an STM. A frequency-doubled Nd:YAG laser with pulse duration of 7 ns was focused to the STM junction.

Nanosized pit depth on gold films versus laser intensity is shown as an example in Fig. 7, where (a) is an STM image of created pits with different laser intensities, and curve A in (b) has a linear relationship between pit depth and laser intensity while curve B represents the relation between the calculated thermal expansion of the tip and laser intensity. They proposed also an analytical model to determine the dominant mechanism. During laser irradiation, the thermal expansion is much smaller than the tip-sample distance and no current increase occurs. The tip-enhanced optical field thermally desorbed the hydrogen atoms from the sample surface, resulting in oxidation.

They concluded that mechanism of nanooxidation is based on the optical enhancement under the tip. For instance, nanosized pit fabricated on gold films and on H-passivated Ge surfaces as a function of a pulsed laser intensity in combination with an STM are reported recently [8]. Moreover, nanosized pit depth shows a linear relationship with laser intensity (Fig. 7).

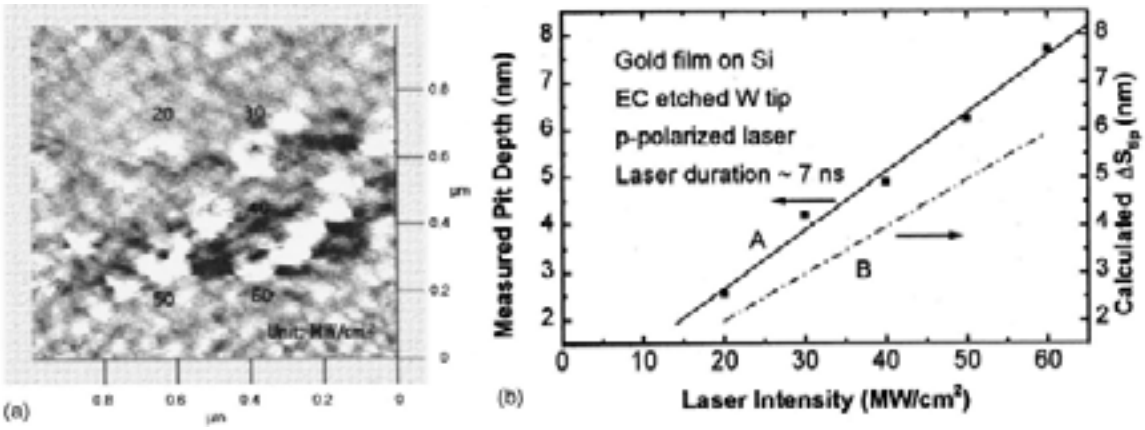


*FIG. 7. (a) Nanopits created on gold film at different laser intensity and (b) dependence of pit depth on laser intensity[8].*

Nanostructure can be also modified efficiently by the way of irradiation. For instance, multi-layered nanostructure of metal-superconductor-semiconductor has been successfully modified by the laser irradiation [8]. Junction between metal, semiconductor and superconductor materials seem to be promising for their application as electronic devices and high power transmission. For most of the power related and microelectronic based applications, superconducting thin films/wires with $J_c$ values of the order of $10^5$ A/cm$^2$ are required and the $J_c$ values can be increased by enhancing the carrier concentration and their mobility. These parameters can be monitored by controlling the preparative conditions of the superconducting thin film/wires.

On the other hand, photosensitive materials irradiated with light significantly increases the electrical conductance. Device with both of these properties can be achieved by forming a junction of photosensitive semiconductor with superconductors. Shirage et al. reported that multi-layered nanostructure of metal-superconductor-semiconductor has been successfully modified by the laser irradiation[8]. For device applications, the Tl-based superconducting oxides present interesting features including high transition temperature at about 127 K.

In this paper, CdSe semiconductor has been selected as it possess good photosensitive and nanocristalline properties. Then photo-induced changes of I-V characteristics of Ag/Tl-Ba-Ca-

CuO/CdSe multilayered nanostructure have been studied at room temperature in dark and in the presence of the red He-Ne laser of 2 mW (632.8 nm) with the photo energy greater than the band gap of CdSe and superconducting system (Fig. 8). The recorded data of measurements show the increased slope of I-V curve with laser irradiation. Further, the increase in the period of irradiation increases the slope of the I-V plot and becomes steady after 3 h. The consequence of such increase in slope (dI/dV) after laser irradiation is the decrease in the normal state resistance of the junction. which might have been caused due to increase in the carrier concentration. The increase in conductivity shows that laser irradiation assist in enhancing the carrier concentrations and their mobility. These carriers drifted according to the applied potential to the junction and hence resulting in increase in conductivity. This will help to increase the superconducting such as $T_c$ and $J_c$ values. Thus, superconductor-semicondutor multi-layered nanostructures could offer superior properties than conventional materials.

Considerable interest has centred on the synthesis of organic inorganic hybrids during the past decade from the viewpoint of both fundamental research and applications. Such materials can show properties that are a combination of those of the original materials, while others possess improved performance not seen in the separate component. In particular, composites consisting of nanosized inorganic particles or fibres dispersed in a continuous polymer matrix have attracted much research attention, and nanosized semiconductor particles such as cadmium sulfide are important dispersed phases within polymer matrices owing to their unique electronic and optical properties, and their potential applications in solar energy conversion, nonlinear optics, photo-electrochemical cells and heterogeneous photo-catalysis. Moreover, polymers not only act as encapsulants for the particles, but are also capable of passivating the materials, preventing particle agglomeration whilst maintaining a good spatial distribution of the particles, and effectively controlling the particle size and size distribution, which has an influence on the electronic and optical properties of the semiconductor materials. In most previous works, however, polymerization and nanoparticle formation were performed separately to obtain nanoparticles well dispersed in the polymer matrices.

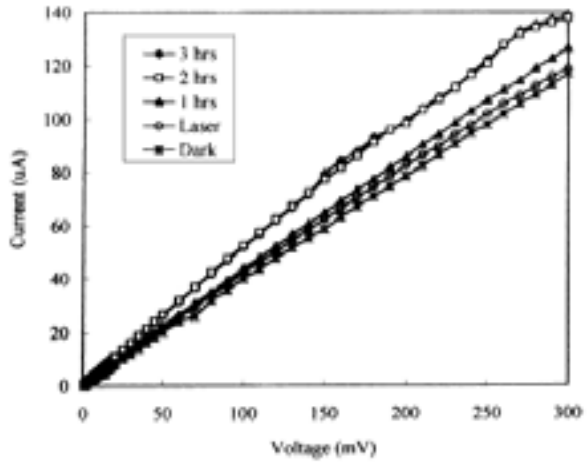


*FIG. 8. Plot of I-V characteristics of Ag/Tl-Ba-Ca-CuO/CdSe multi-layered Nanostructure in dark and with laser irradiation[8].*

Prompted by the importance of nanostructured materials and the limitations of the above processes, many researchers have developed the γ irradiation technique to synthesize nanosized particles. Compared with other methods, γ rays irradiation has advantages such as processing under ambient pressure at room temperature with the starting inorganic compounds and organic monomer mixed homogeneously at the molecular level in solution.

In addition, the quicker formation of polymer chains than the growth leads to an increase of the viscosity of the system, which limits the further growth and aggregation of nanocristallites and so makes them well dispersed in the polymer matrix. Such chain growth leads to an increase of the

viscosity of the system, which limits the further growth and aggregation of nanocristallites and so makes them well dispersed in the polymer matrix. Recently, Meng Chen et al.in 1999 reported for the first time, CdS nanofibers in an alternate copolymer of maleic annydride (MA) and styrene (St) via a one-pot procedure using gamma irradiation under ambient conditions, and have successfully extended the gamma irradiation technique from the synthesis of inorganic partile-homopolymers to CdS-copolymer composites [9].

By Simultaneous in situ Formation (SISF) technique using γ–irradiation several kinds of inorganic nanowires were prepared. A TEM image of an as-prepared composite (46104 Gy) (Fig. 9 left) shows an even dispersion of nanocrystallites on the gray background of the copolymer matrix, where black short fibres with diameters of < 5 nm and lengths from 50 to 100 nm correspond to CdS while the corresponding electron diffraction (ED) pattern (inset of Fig. 9 left) shows a well crystallized diffraction pattern of CdS crystals, as supported by XRD spectra (Fig. 9 right).

$C_{60}$ polymers have attracted much attention as a new form of carbon material due to their both $sp^3$ [3] (diamond) and $sp^2$ (graphite) bond characters, and $C_{60}$ polymer are expected to exhibit physical and chemical properties of both diamond and graphite or to have new functions (Fig. 10). From this point of view, Jun Onoe et al. investigated $C_{60}$ polymer formed with the help of photo or electron-beam irradiation of solid $C_{60}$ [10]. As confirmed by FT-IR spectra and theoretical studies, dumbbell structure of $C_{60}$ dimer is formed by photo-irradiation (Fig. 11a) while the coalesced structure formed by electron-beam irradiation (Fig. 11b). By comparison, a more coalesced $C_{60}$ polymer in the case of EB-irradiation than the $C_{60}$ photopolymer with the [2 + 2] cyclo bond was formed. Structural modification by photo-irradiation changes the electronic properties of the $C_{60}$ film.

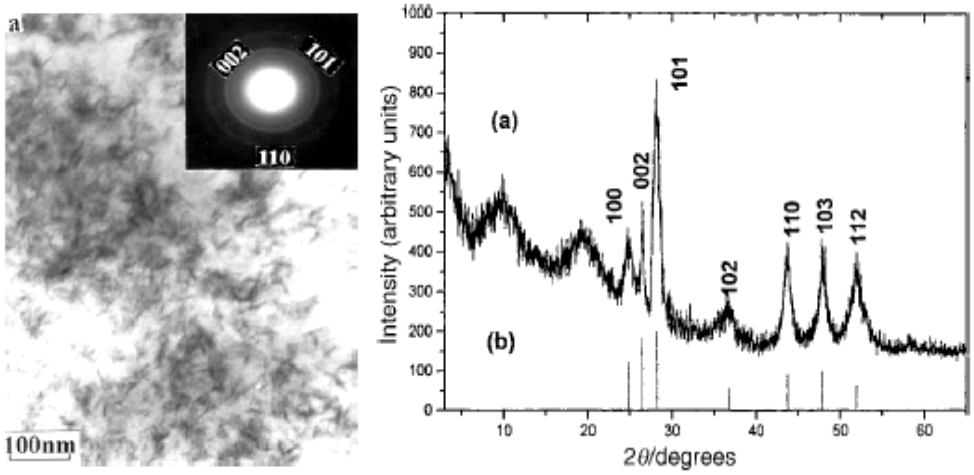


*FIG. 9. TEM image and ED pattern (left) as-prepared CdS/Poly(St-alt-MA) by γ-irradiation (46104 Gy); XRD patterns (right) of the same sample (a) and standard stick pattern for hexagonal CdS nanocrystallines (b) [9].*

It is of great interest to clarify the relationship between the structure and the electronic properties of the photo-transformed $C_{60}$ film. Preliminary results showed that the electron conductivity of the $C_{60}$ film after photo-irradiation was increased by 3 orders of magnitude compared with that of the film. After electron beam irradiation, the specific resistance of the film decreased markedly and its current-voltage curve indicated a metallic character. This is due to the reduction of the band gap and the increase in the density of states at the Fermi level by the enlarged Π electron system of the coalesced product.

The change in the electron character also improved the field emission current. Furthermore, when hydrogen was introduced during EB irradiation, the emission current was enhanced compared to that in the absence of hydrogen. This is because the addition of hydrogen leads to the formation of $sp^3$-carbon, which is a better electron-emission site than $sp^2$-carbon. The ability to create and exploit

devices on the nanoscale is beginning to have a major and practical impact upon biomedicine. Modulated drug delivery may allow the release profiles of therapeutic agents to be manipulated to match the physiologic requirements of the patient; ideally such a system could be coupled to a biosensor system. The goal of this study is photo-thermally modulated drug delivery, where near-infrared (IR) light is converted to heat within a thermally reversible polymer matrix to alter the rate of drug delivery.

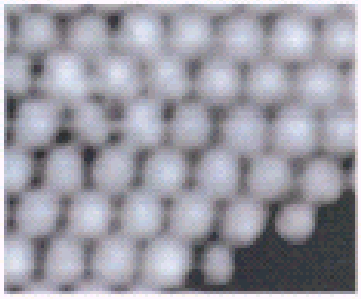

*FIG. 10. STM image of 2D $C_{60}$ hexagonal polymers. Six cross-linkages per unit $C_{60}$ molecule are clearly observed [10].*

Towards this goal, researchers have developed a composite hydrogel material comprised of a temperature-sensitive copolymer and nanoparticles that are designed to strongly absorb near-IR light. Light emitted at wavelengths between 800 and 1200 nm can pass through tissue and then can be absorbed by the nanoparticles that are embedded within hydrogel. Gold nanoshells are a new class of optically active nanoparticles that consist of a thin layer of gold surrounding a dielectric core.

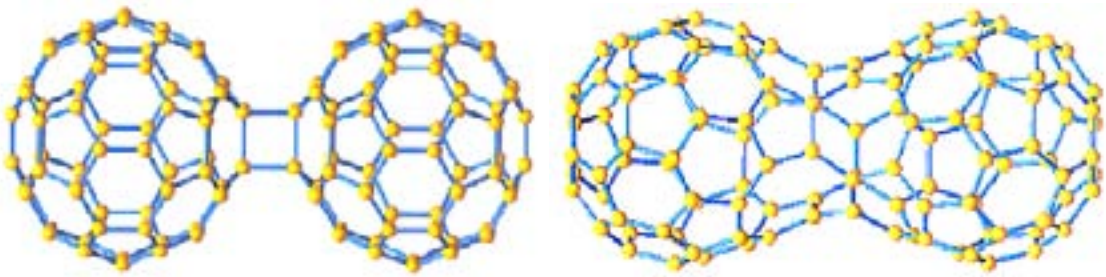

*(a)* *(b)*

*FIG. 11. Dumbbell structure of $C_{60}$ dimer formed by photo-irradiation (a) and coalesced structure formed by electron-beam irradiation (b) were confirmed by FT-IR spectra and theoretical studies [10].*

The diameter of both the core and the shell can be altered in a controlled manner during the nanoparticle fabrication process. Gold is essentially a bioinert material and has been found to be useful in fields ranging from dental surgery to arthritis treatments. It has also been used as a reference material for evaluating the biocompatibility of less inert materials. Interesting purpose is to obtain nanoshells that can be tuned to absorb near-IR light, particularly in a spectral range called the in "water window", a gap in the absorption spectrum of tissue that exists between the absorption spectra of the chromophores (<800 nm) and that of water (>1200 nm).

Varying the shell thickness, core diameter, and the total nanoparticle diameter allows the optical properties of the nanoshells to be tuned over the visible and near-IR spectrum. Since the core and shell sizes can easily be manipulate, the optical excitation profiles of the nanoshells can be modified to optimally absorb light emitted from various lasers. Sershen et al. have developed a composite hydrogel material comprised of a temperature-sensitive copolymer and nanoparticles that are designed to

strongly absorb near-IR light [11]. Light emitted at wavelength between 800 and 1200 nm can pass through tissue and then be absorbed by the nanoparticles that are embedded within the hydrogel. As the near IR light is absorbed by the nanoparticles, heat is generated, resulting in a conformational change in the copolymer that leads to alterations in the release profile of the entrapped drug. Particularly, they investigated the release of methylene blue from the nanoshell-composite gold-gold sulfide nanoshells (Au-$Au_2S$) hydrogels and in a which way it was enhanced in response to irradiation by laser (Nd:YAG laser light at 1064 nm) (Fig. 12).

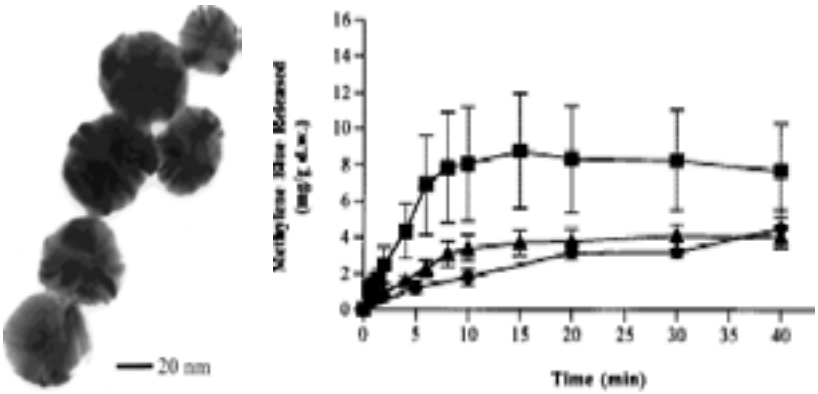


(a) (b)

*FIG. 12. TEM image of a representative sample of Au–$Au_2S$ nanoshells (a); release of methylene blue from nonirradiated (diamond) and irradiated NIPAAm-co-AAm hydrogels (triangle), and irradiated nanoshell-composite hydrogels (square) (b) [11].*

## 3. NANOSTRUCTURED GLASSES

Nanocrystallized (or heterogeneous phases) photonic glasses are new family of materials combining enhanced optical effects with novel nanotechnology. They reserve the advantages of glasses over other materials, for examples, incorporating almost every element in the periodic table, and more easily fabricating into a large size plate or being drawn to a fibre, so as to be more flexible and convenient for difference applications. On the other hand, uniformly dispersed nano-crystals in glass matrix using novel nano-techniques permit refining the microstructure of glasses to a great extent to realize the unique and much improved functional properties.

**Photonic structure of glasses**

Much research has been devoted to understanding the changes of optical properties at the nanometer-scale induced by UV or other irradiations plus post-thermal-treatment. This is important for understanding the mechanism of irradiation-induced phenomena in glasses and also for the fabrication of photonic structures inside such a glass with nanometer precision.

For instance, Lithium niobate ($LiNbO_3$) occupies a central role in optoelectronics as that of silicon in semiconductor technology. However, unlike silicon, this fragile and sensitive material is increasingly being processed through the use of non-traditional methods such as ultrashort laser pulses. Strong correlations exist between laser-induced modifications and resultant optical properties.

Thus, the critical parameters in the creation of both micro- and nanoscale optical devices are the spatial selectivity and chemical and optical uniformity of the structures. In particular, single crystals of lithium niobate ($LiNbO_3$) can be processed using a focused femtosecond laser to induce nanoscale surface and subsurface defects [12]. Electron and ion microscopy techniques have been used to characterize the changes that result during processing. The prevailing observation is that of competing processes—ablation and partial re-deposition, thermal shock, and extreme quenching, as well as effects associated with shock wave propagation, resulting in both amorphization and heavily defective regions at the focal point of the laser pulse (Figure 13).

The ablation region is surrounded by amorphized material (100 nm in the oxygen deficient surface features to about 300 nm oxygen enriched subsurface features) as well as a region containing highly defective crystal. The observed microstructural defects have a direct implication in optical memory or waveguide writing, where the goal is to realize consistent structural features with uniform optical properties.

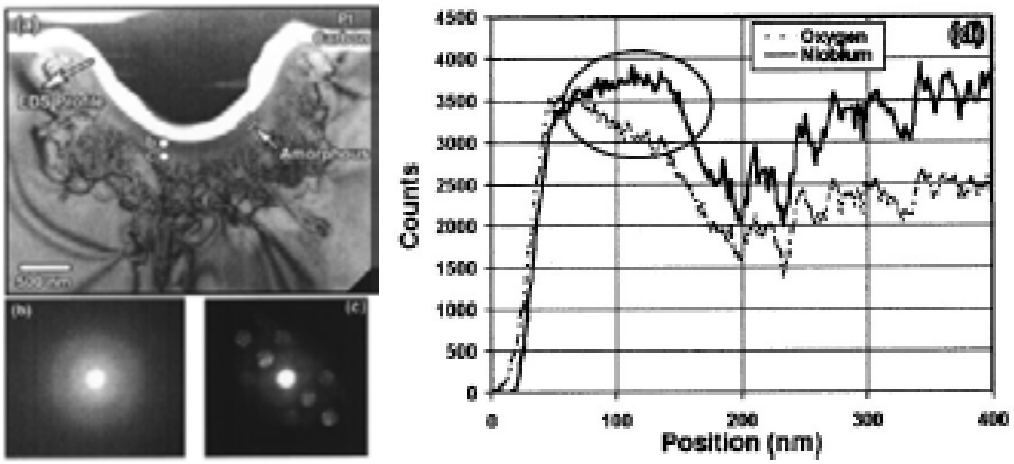


*FIG. 13. A bright-field TEM micrograph of one of the surface processed feature shows that below the extra carbon and platinum layers the semicircular contour of the locally ablated sample is seen (a). Immediately below this contour is an approximately 100-nm-thick layer exhibiting a flat grey contrast. Local electron diffraction in the TEM clearly indicates that this layer is amorphous (b). Adjoining this layer is a second region containing highly defective crystalline material (c) [12].*

As the key material for photonic applications in optical communications, Ge-doped $SiO_2$ glass used as core materials for optical fibres, is very sensitive to irradiation. Much research has been devoted to understanding the changes of optical properties induced by UV irradiation, but little has been addressed to parallel microstructural and compositional changes. Nan Jiang et al. reported that rapid decomposition in Ge-doped $SiO_2$ glass can be realized under high-energy electron (100 keV) irradiation [13]. They report rapid changes in both microstructure and composition in a Ge-doped $SiO_2$ glass due to a high-energy electron beam at the nanometer-scale associated with variations in the spatial distribution of the 5 eV absorption band induced by irradiation. It demonstrates that electron-beam writing is a candidate for creating spatial modifications in Ge-doped glasses on a nanometer scale. These effects can be obtained by the redistribution of Ge in the glasses as a result of patterned electron-beam writing (Figure 14); electron-beam interaction with Ge-doped $SiO_2$ can create an inhomogeneous composition of the glass, with consequent modification of the optical properties on the nanometer scale.

From these observations, they suggested that the Ge (and probably a small amount of Si) is driven out of the irradiation region in the bulk, as well as on the surfaces, due to the interaction between the electron beam and the glass. The driving force to expel the Ge is the positive electric field created by the action of the incident electron beam in removing electrons from the sample.

The white particle-like features shown in the ADF images in Fig. 14 are due to Ge accumulations induced by electron irradiation: since the scanning area is much larger than the probe interaction range, accumulated Ge is trapped inside the area, and these atoms form these randomly distributed features. This is important for understanding the mechanism of irradiation-induced phenomena in Ge-doped $SiO_2$ glasses and also for the fabrication of photonic structures inside such a glass with nanometer precision.

By the recent development of ultrashort pulse lasers with high peak power, it has become possible to induce a change of the refractive index and to change phases from amorphous-to-crystalline in inorganic glass materials. Structures induced by irradiation with femtosecond laser pulses could be used to fabricate new optical devices such as planar transparent electrodes and touch panel sensors for displays. For this applications, thin layers of indium oxide ($In_2O_3$) and tin oxide ($SnO_2$) doped $In_2O_3$ with submicron thickness have been widely used.

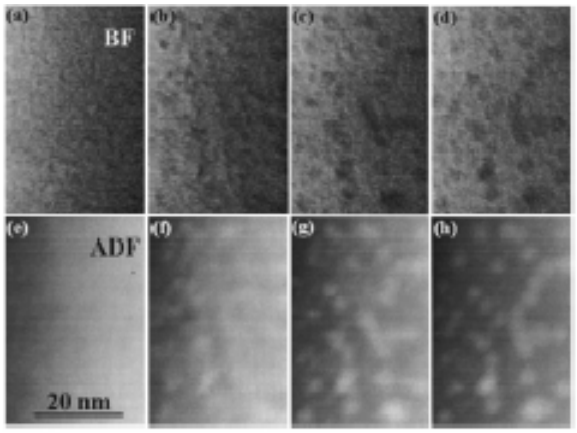


*FIG. 14. Bright field (BF, top row) and corresponding annular dark field (ADF, bottom row) images showing evolution of nanometer-scale features during electron irradiation. The acquisition time of each image is about 6.5 s, and each pair of BF and ADF images was recorded simultaneously. The estimated previous exposure time to the electron irradiation is 0 s in (a), 15 s in (b), 1.5 min in (c), and 5 min in (d) [13].*

Recently, Katayama et al. investigated nanosized crystalline relief grating structures induced by irradiation of near-infrared femtosecond laser pulses on an amorphous inorganic ($In_2O_3$-$TiO_2$) film (100 nm thin layers) (Fig. 15) [14]. Shapes of crystallized relief structures were sensitive to the scanning rate and the focused point height of irradiation, and the optimized irradiation condition gave cone-shaped cross section structures.

An amorphous-to-crystalline phase change in mountain-like structures induced by irradiation was observed, but those mountain-like structures had two peaks with a cave-in at the centre part as shown in Fig. 15. We need to optimize the irradiation condition to induce a more uniform structure such as a cone-shaped or rectangular one.

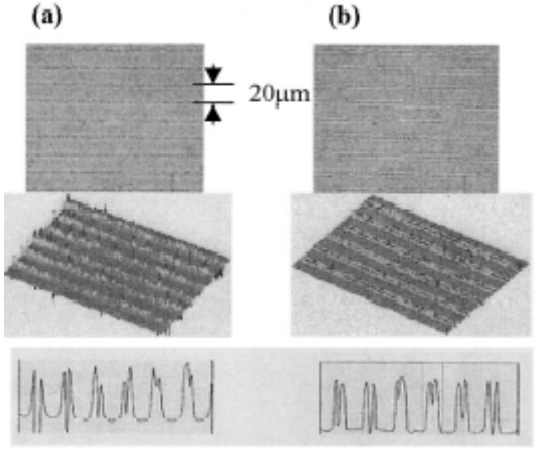


*FIG. 15. Optical interference micrographs of relief grating structures induced by femtosecond laser pulses. (a) Irradiated nonetched sample. (b) Irradiated etched sample [14].*

Certain optical fibre waveguides exhibit the property of photosensitivity which is a practical mean for photo-inducing permanent refractive index changes in the core of those fibres. In this way it is possible to make permanent Bragg grating devices. Photosensitivity is not restricted to fibre structures: it has also been detected in several types of planar glass structures. The general approach for making like permanent Bragg grating devices is to photo-induce a refractive index grating in the photosensitive core of the optical waveguide.

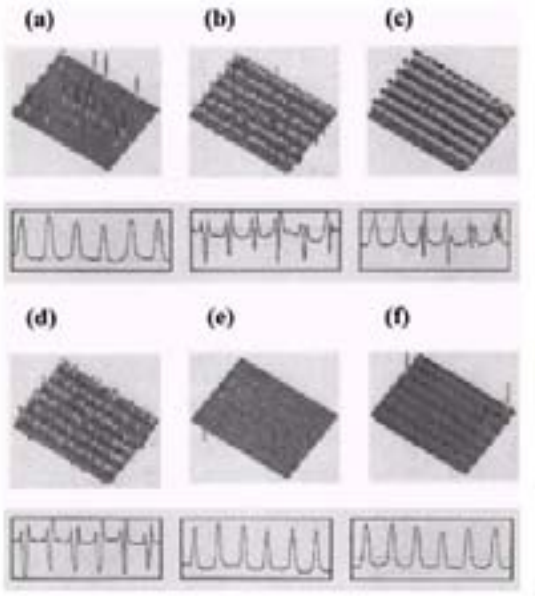


*FIG. 16. Optical interference micrographs of relief grating structures induced by femtosecond laser pulse under various irradiation conditions. Sample scanning rates: a ) 250 mm/s, b) 500 mm/s, and c) 750 mm/s focused position was on the surface). Focused position: d) 50 mm above the surface, e) 100 mm above the surface, and f) 10 mm below the surface (scanning rate was 500 mm/s) [14].*

Reflectivity and refractivity of silicate glasses can be modified by UV light irradiation, thus permanent Bragg gratings can be written in fibres by printing periodic refractive index modulation through use of a special phase mask grating made of silica glass flat transparent to the KrF excimer laser radiation (249 nm), generally used for this application.

As reported by Hill et al [15], a simple method for fabricating high quality Bragg gratings is to use low coherence lasers suitable for industrial environments (Fig.17).

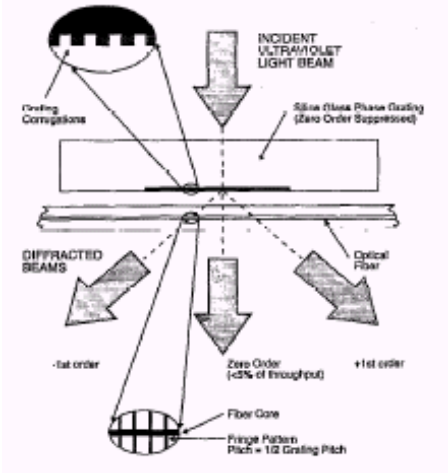


*FIG. 17. Schematic of photolithographic apparatus for photo-imprinting a refractive index Bragg grating in a photo-senstive optical fibre waveguide [15].*

This method of fabricating in-fibre Bragg gratings is flexible, simple to use, results in reduced mechanical sensitivity of the grating writing apparatus and is functional even with low spatial and temporal coherence laser sources.

A direct-write inorganic lithography technique can form nanoscale rings of amorphous metals and semiconductors in glasses. Semiconductor nanorings form quantum dot structures, in which quantum confinement produces levels of discrete energy within the bulk band gap which have been seen in the low-temperature photoluminescence studies. The formation of rings in glasses by electron irradiation is thought to be due to an ionization and field-induced migration process. Rings are normally considered two-dimensional structures in that their thickness is much smaller than their diameter; moreover, the diameter of the ring depends on the exposure time, but not on the specimen thickness.

Adding metal ions to silicates, in general, induces non-bridging oxygen (NBO), which is partially covalently bound to one Si ion and ionically bound to the metal ions (Fig. 18). High-energy electronic excitation induces an Auger cascade, which turns the negatively charged NBO into a positively charged ion, which then breaks the ionic bond between the NBO and the metal ion. Thus the metal ions is released from the glass network.

If the electron-illuminated area is small, the free metal ions are then able to move to an adjacent region in the repulsive electrostatic field that is produced by Auger and secondary electron excitation in the irradiated area, and form ring structure. The size of the ring is dependent on the amount of exposure and current density of the probe, rather than on the size of the probe. The process proposed should be more efficient in glasses than in crystals, because there are more unfilled sites in glasses that can be accommodated by displaced ions. Irradiation usually results in the formation of dangling bonds in crystals, but it is easier to form new bonding configurations in glasses, depending on the chemical dynamics and site availability. Therefore, relaxation associated with excitation processes can yield configuration changes easily in glasses. The mobile ions can occupy interstitial sites in the silica network if the concentration is small, or combine with the free oxygen and form oxides.

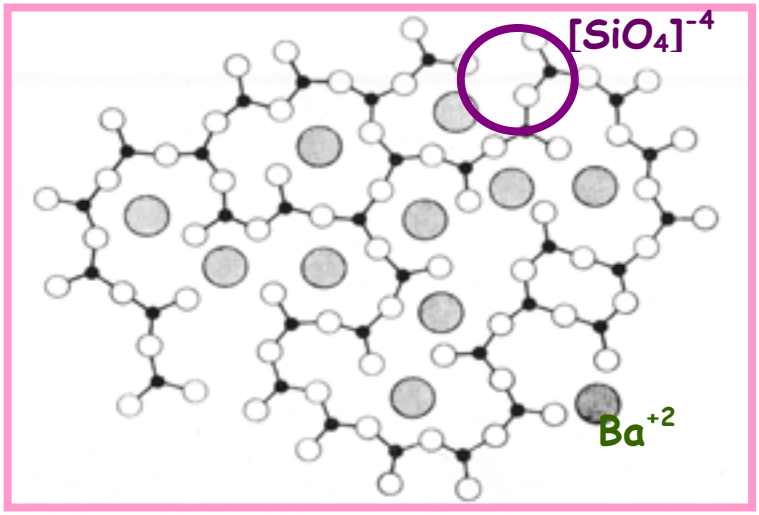


*FIG. 18. Glass structure with metal ion.*

Additionally, amorphous materials can have a variable local structure in the medium range. This variability allows the experiment freedom to choose the constituent atoms and composition (stoichiometric or non-stoichiometric), which, in turn, allows materials design based on the probability of forming rings with the desired properties. Recently N. Jiang et al. described a method of forming patterned nanorings in silicate glasses, based on electron-beam lithography technique that uses a scanning transmission electron microscope (STEM) [16].

Figures 19 a) and b) show rings formed in GeO-$SiO_2$ and $Nb_2O_5$-$LiO_2$-$SiO_2$ glass respectively by an electron probe as a function of the exposure time. Annular dark-field (ADF) images of the rings are shown, and the ADF intensity profiles across the ring diameters are given; the intensities were normalized to the value in the adjacent area of each ring.

Nanometer scale metal particles embedded in glass can substantially modify its optical properties and have attracted much interest as nonlinear optical materials for optical functional devices such as optical switch, shutter, and optical waveguide [17, 18]. Small particles embedded in an insulating matrix are widely studied because of their potential application as non linear optical materials; in fact the optical absorption depends on particle size, surrounding medium as well as particle shape and spatial distribution.

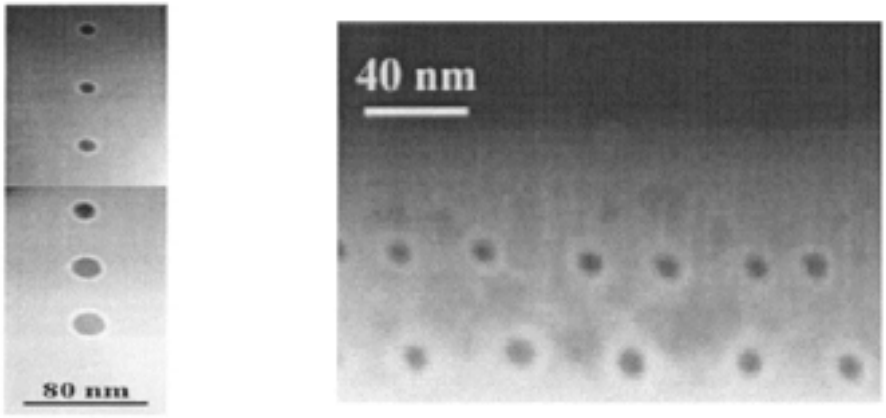


*a.* *b.*

*FIG. 19. a) Experimental ADF STEM image showing the ring structures in $GeO_2$–$SiO_2$ glass b) Nanoring structures in $Nb_2O_5$–$Li_2O$–$SiO_2$ glass [16].*

These materials exhibit a wide size distribution of particles which is often inhomogeneous with respect to the location inside the matrix. In 1997, Hofmeister introduced a new method to generate high concentrations of metal particles inside a glass matrix having a narrow size distribution as well as homogeneous arrangement throughout the glass volume [17]. An example of this material property is given by the Ag particles of 4.2 nm mean diameter formed inside a silver-doped glass submitted to electron irradiation. By this treatment it is possible to achieve a high concentration of particles homogeneously arranged throughout the glass and exhibiting a narrow size distribution. (Fig. 20).

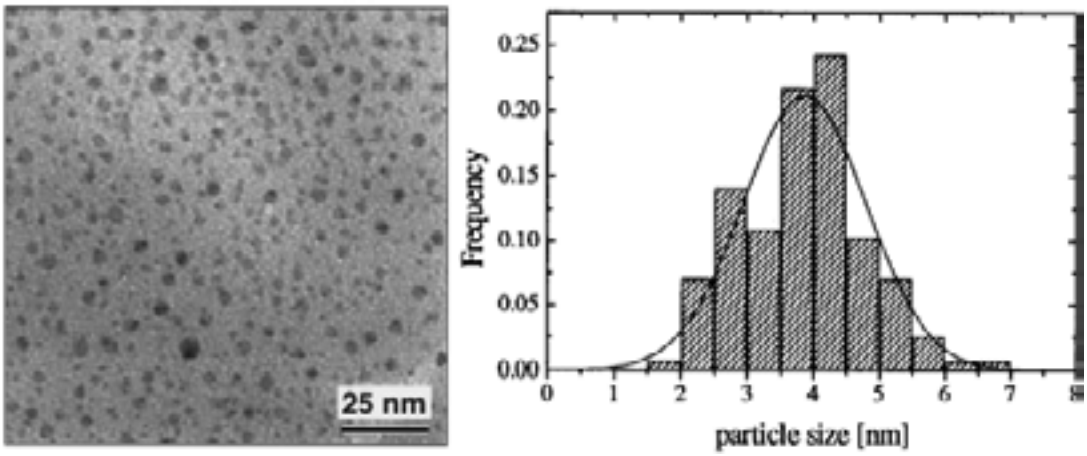


a) (b)

*FIG. 20. Ag particles in a thin slide of ion-exchanged glass subjected to electron beam irradiation (a) and Size distribution of the Ag particles embedded in glass with a Gaussian curve fitted to the data (b) [17].*

The radiation enhanced diffusivity being some orders of magnitude larger than the corresponding thermal one together with band breaking and defect creation inside the glass network favour the precipitation of silver not only at distinctly lower temperatures, but also at considerably higher rates.

Electron induced formation of nanosized silver particles in glass presents:

i) high yield and concentration,
ii) speed and reproducibility,
iii) homogeneous arrangement of particles,
iv) narrow distribution of sizes, and v) absence of additional stresses resulting from thermal treatment.

This route of synthesizing particulate metal-glass composites will allow to produce materials with well defined nonlinear properties if applied on large scale to bulk specimens of ion-exchanged glass.

A procedure of irradiation with UV light, electron beam or X rays and subsequent heat treatment has been used to form nanosized Au, Ag, Cu and Zn particles in photosensitive glasses. For example, a Zn borosilicate glass with large amount ZnO is found very sensitive to electron irradiation. The process of precipitating Zn crystalline particles suggests that high intensity electron irradiation can be used to produce desired *in situ* modifications to the glasses and glass thin films. *In situ* observation of the precipitation of nanometer particles during electron beam irradiation is important to clarify the mechanism of particle formation and to control the size, shape, and distribution of the nanometer particles. The mechanism for the formation of Zn particles by electron irradiation must involve the double ionization process and field-induced micro-migration that has been introduced in interpretation of the phase decomposition induced by electron irradiation in alkaline earth multi-component glasses.

In general, oxide glasses can be considered as mixed ionic-covalent solids: the $SiO_2$ and $B_2O_3$ are more covalent while ZnO is more ionic. It is reasonable to assume that ZnO, $B_2O_3$ and $SiO_2$ in this glass are mixed at the atomic scale. The process occurs via a double ionization mechanism due to irradiation as the major factor in the changes of microstructure and composition in the glass and thermal effects are less important in this process [18]. Nanometer Zn crystalline particles can precipitate rapidly in the glass under high intensity electron irradiation (100 keV) (Fig. 21). Well-recognized particles are seen in Fig. 21c) These particles have relatively bright contrast in the ADF images, which means they consist of relatively heavy atoms.

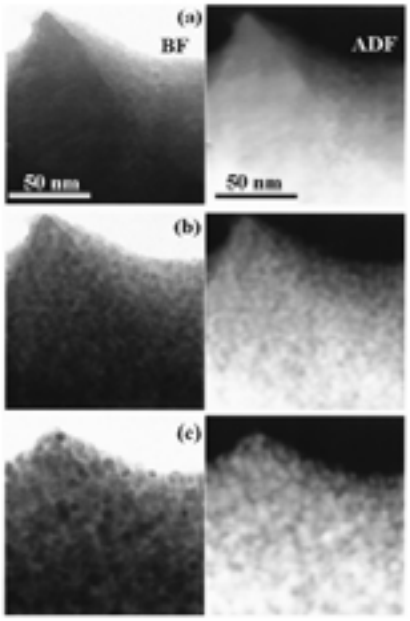


*FIG. 21. Bright-field (left column) and annular dark-field (right column) images showing evolution of nanometer particles during 100 kV electron irradiation. The exposure times are (a) 0.1, (b) 0.2 ms, and (c) 1s, respectively[18].*

**ZnO excited glasses**

Zinc oxide (ZnO) has the high efficiency of spontaneous near band-edge luminescence with subnanosecond lifetime and is of interest for application as the superfast scintillator [19–22]. Many researchers studied the synthesized ZnO films, nanoparticle powders and single crystals, but little attention has been paid on ZnO existing in the form of nanocrystals in a glass matrix. Our activity is essentially devoted to scintillating materials then scintillating glasses for high energy physics scintillation detectors is an attractive solution, since the glasses offer unique advantages over crystals, such as the lower costs, easier fabrication and the higher durability and thermal shock resistance. Comprehensive studies have been performed in this respect jointly by the present authors in ENEA-Casaccia Research Centre and East China University of Science and Technology [23, 24], whereas scintillating glasses based on the emission of ZnO quantum dots in the matrix is a new subject of our recent researches.

Our preliminary work on ZnO excited barium silicate glasses showed that dominant photoluminescence band of glass round 400 nm can be enhanced much which is related to quantum confinement effect in ZnO nanophase induced under the joint roles of focused laser radiation and post-annealing treatment. In other word, the irradiation plus specific annealing at the proper temperatures can be regarded as an efficient way to form ZnO nanophases in the ZnO-rich glass matrix. Glass samples are melted in alumina crucibles at 1300$^{o}$C for 3 hours, quenched in air and annealed at 350$^{o}$C for 1 hour.

Annealed samples are subject to emission spectral measurements and afterward IR femtosecond laser radiation by using a regeneratively amplified 800 nm Ti:sapphire laser to emit 120 fs, 1000 Hz, mode-locked pulses. The laser beam, with an average power of 50 mW, was focused by a 10 x objective lens with a numerical aperture of 0.30 onto the interior of the glass samples with the help of an XYZ stage. Irradiated and nonirradiated samples are annealed at different temperatures as shown in Table I for 5 hours and their emission spectra are measured again. Emission spectra of IR laser irradiated glass annealed under different conditions are shown in Figure 22. From this figure, the obvious and positive effects on the photoluminescence spectra of glasses with respect to both intensity and position of emission band are observed.

TABLE I. POST-TREATMENT CONDITIONS ON GLASS SAMPLE (50ZNO40SIO$_2$10BAO) AFTER IR FEMTOSECOND LASER IRRADIATION

| Sample Code | Temperature ($^{o}$C) | Time (hours) | Appearance | Emission band (nm) |
|---|---|---|---|---|
| Ir-1 | 400 | 5 | Transparent | 398 |
| Ir-2 | 300 | 5 | Transparent | 393 |
| Ir-3 | 200 | 5 | Transparent | 396 |
| No | nonirradiated | | Transparent | 398 |

The broad UV emission band near 400 nm belongs to the ZnO phase and might be related to trapped excitons localized at the ZnO aggregate interface with the glass host. As shown in Figure 22 and Table I, UV emission was enhanced by IR laser irradiation and subsequent annealing accompanying with a slight blue-shift. Since the enhancement and high-energy shift of the excitonic recombination emission in ZnO have been demonstrated to be associated with the reduced size of ZnO particles, i.e. quantum confinement effect, it can be reasonably deduced that IR laser irradiation and post thermal treatment exert obvious impact on aggregation degree of ZnO in glass matrix, resulting in enhanced emission as well as blue-shift when optimal state is achieved. Further research is needed in this respect to obtain more supporting evidences.

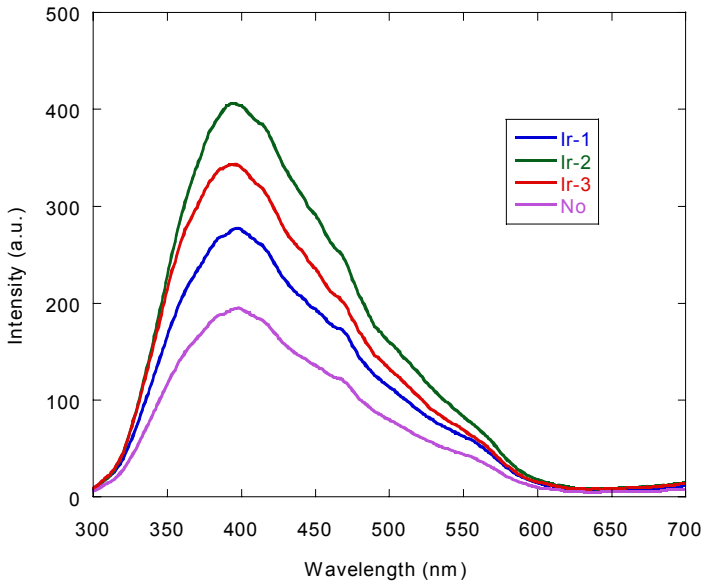


*FIG. 22. Emission spectra of glasses after IR laser irradiation and thermal treatments under different conditions.*

## 4. CONCLUSION

Nanotechnology - in its various forms such as nanoelectronics, nanoelectromechanical systems, ultrasmall and highly sensitive sensors, multifunctional materials, biologically inspired materials, systems and architectures - and nanomaterials induced by radiation are expected to play a strong and critical role in the future. Also, the intersection of nano, bio, and information technologies provides rich possibilities for exploring useful concepts and breakthroughs.

## REFERENCES

[1] IIJMA, S., "Helical microtubules of graphitic carbon" Nature (London), 354, (1991) 56.
[2] YAMAMOTO, K., KOGA, Y., FUJIWARA, S., KUBOTA, M., "New method of carbon nanotube growth by ion beam irradiation", Appl. Phys. Lett., 69 (1996) 4174-4175.
[3] TERRONES, M., BANHART, F., GROBERT, N., CHARLIER, J.C., AJAYAN, P.M., "Molecular junctions by joining single-walled carbon nanotubes", Phys. Rev. Lett., 89 (2002) 1–4.
[4] AJAYAN, P.M., RAVIKUMAR, V., CHARLIER, J.-C., "Surface Reconstructions and Dimensional Changes in Single-Walled Carbon Nanotubes", Phys. Rev. Lett. 81 (1998) 1437.
[5] BANHART, F., "Irradiation effects in carbon nanostructures" Rep. Prog. Phys. 62 (1999) 1181.
[6] GHONIEM, N.M., WALGRAEF, D., ZINKLE, S.J., "Theory and experiment of nanostructure self-organization in irradiated materials", J. Computer-Aided Mater. Design, 8 (2002) 1–38.
[7] LU, Y.F., MAI, Z.H., ZHENG, Y.W., SONG, W.D., "Nanostructure fabrication using pulsed lasers in combination with a scanning tunneling microscope: Mechanism investigation", Appl. Phys. Lett., 76 (2000)1200–1202.
[8] SHIRAGE, P.M., SHIVAGAN, D.D., EKAL, L.A., DESAI, N.V., MANE, S.B., PAWAR, S. H., "Fabrication of Ag/Tl-Ba-Ca-CuO/CdSe nanostructure by electro-deposition technique", Appl. Surf. Sci., 182 (2001) 403–406.
[9] CHEN, M., XIE, Y., QIAO, Z., ZHU, Y., QIAN, Y., "Synthesis of short CdS nanofibre/poly(styrene-alt-maleic anhydride) composites using γ-irradiation", J. Mater. Chem., 10 (2000) 329–332.
[10] ONOE, J., HARA, T., NAKAYAMA, T., AONO, M., TAKEUCHI, K., "A new form of carbon material using C60 fullerene", RIKEN Review: Focused on Nanotechnology in RIKEN II, 38 (August, 2001).

[11] SERSHEN, S.R., WESTCOTT, S.L., HALAS, N.J., WEST J.L., "Temperature-sensitive polymer-nanoshell composites for photothermally modulated drug delivery", Young Investigator Award, World Biomaterials Congress 2000, Kamuela, HI, May 15–20 (2000) 293–298.
[12] STACH, E.A., RADMILOVIC, V., DESHPANDE, D., MALSHE, A., ALEXANDER, D., DAVID DOERR, "Nanoscale surface and subsurface defects induced in lithium niobate by a femtosecond laser", Appl. Phys. Lett., 83 (2003) 4420–4422.
[13] JIANG, N., QIU, J., GAETA, A.L., SILCOX, "Nanoscale modification of optical properties in Ge-doped SiO2 glass by elelctron-beam irradiation ", J., Appl. Phys. Lett., 80 (2002) 2005–2007.
[14] KATAYAMA, S., TSUTSUMI, N., NAKAMURA, T., HORIIKE, M., HIRAO, K., "Femtosecond laser induced crystallization and permanent relief grating structure in amporphous inorganic (In2O3+1 wt % TiO2) film ", Appl. Phys. Lett., 81 (2002) 832–834.
[15] HILL, K.O., MALO, B., BILODEAU, F., JOHNSON, D.C., ALBERT, "Bragg gratings fabricated in monomode photosensitive optical fiber by UV exposure through a phase mask", J., Appl. Phys. Lett., 62 (1993) 1035–1037.
[16] JIANG, N., HEMBREE, G.G., SPENCE, J.C. H., QIU, J., GARCIA DE ABAJO, F.J., SILCOX, J., "Nanoring formation by direct-write inorganic electron-beam lithography", Appl. Phys. Lett., 83 (2003) 551–553.
[17] HOFMEISTER, H., THIEL, S., DUBIEL, M., SCHURIG, E., "Synthesis of nanosized silver particles in ion-exchanged glass by electron beam irradiation", Appl. Phys. Lett., 70 (1997) 1694–1696.
[18] JIANG, N., QIU, J., SILCOX, A. J., "Precipitation of nanometer scale Zn crystalline particles in ZnO-$B_2O_3$-$SiO_2$ glass during electron irradiation", Appl. Phys. Lett., 77 (2000) 3956–3958.
[19] DERENZO, S.E., WEBER, M.J., KLINTENBERG, M.K., "Temperature dependence of the fast, near-band-edge scintillation from cuI, HgI2, PbI2, ZnO:Ga and CdS:In", Nucl. Instr. Meth. Phys. Research A, 486 (2002) 214–219.
[20] BACCARO, S., "Recent progress in the development of Lead Tungstate Crystals", IEEE Transactions on Nuclear Science, 46, (1999) 292–295.
[21] NIKL, M., BOHACEK, P., MIHOKOVA, E., BACCARO, S., VEDDA, A., DIEMOZ, M., LONGO, E., KOBAYASHI, M., AUFFRAY, E., LECOQ, P., "Radiation damage processes in wide-gap scintillating crystals. New scintillation materials", Nuclear Physics (Proc. Supp.), 78 (1999) 471–478.
[22] BACCARO, S., CECILIA, A., MONTECCHI, M., NIKL, M., POLATO, P., ZANELLA, G., ZANNONI, R., "Radiation damage of silicate glasses doped with Tb3+ and Eu3+"J. Non-Crystalline Solids, 315 (2003) 271–275.
[23] BACCARO, S., CECILIA, A., CHEN, G., DU, Y., NENCINI, L., WANG, S., "Optical transmittance and irradiation resistance of rare-earth (Ce3+, Tb3+, Pr3+) doped heavy germinate glasses", Rad. Eff. Defects in Solids, 158 (2003) 451–456.
[24] CHEN, G., BACCARO, S., CECILIA, A., DU, Y., MONTECCHI, M., NIE, J., WANG S., ZHANG, Y., "Ultraviolet and visible transmission spectra of heavy germanate glasses containing Sn2+ and Ce3+", J. Non-Crystalline Solids, 326–327 (2003) 343–347.

# CARBON NANOTUBES: SYNTHESIS AND APPLICATIONS

R. ANGELUCCI[a], R. RIZZOLIA[a], F. CORTICELLIA[a], A. PARISINIA[a],
V. VINCIGUERRA[b], F. BEVILACQUA[c], L. MALFERRARI[d], M. CUFFIANI[e]

[a] CNR - IMM Institute, Bologna, Italy
[b] STMicroelectronics, Catania, Italy
[c] STMicroelectronics, Naples, Italy
[d] INFN Sez. Bologna, Bologna, Italy
[e] Dept. of Physics, University of Bologna, Bologna, Italy

**Abstract**

A highly needed major breakthrough in the nanotubes technology for electronic applications is the development of a fabrication method capable of producing well organized nanotube structures, with uniform nanotubes and reproducible electronic properties. In our Institute we are developing site-selective CVD nanotubes synthesis both on flat substrates with patterned catalyst layers and in nanotemplates. Several types of flat substrates such as silicon, silicon oxide, silicon nitride and porous silicon have been prepared. Transition metal catalysts, such as nickel and iron, have been investigated as seeds to nucleate the growth of nanotubes. Various CVD process parameters (carbon gas precursor type and percentage in the gas mixture, use of etching or carrier gases in the gas mixture and deposition temperature) have been investigated to obtain ordered arrays of reproducible nanotubes. In this paper we report the results of this investigation showing the formation of CNTs on different substrates and different catalysts. The CNTs structural characterization by SEM and TEM observations is reported.

## 1. INTRODUCTION

In recent years Carbon Nanotubes (CNTs) have attracted a huge attention for their unique properties [1,2]. Focusing on the electronic properties of CNTs, worldwide researches and achievements have proved that nowadays CNTs are much more than promising electronic materials. FETs based on semiconducting CNTs [3] and inverters circuits made of complementary CNT-FETs [4] have been reported. Interconnecting wires and nano-vias made of metallic CNTs can support a very large current density, on the order of $1x10^9$ A/cm$^2$ without facing electromigration drawbacks [5]. Recently the monolithic integration of CNTs devices with silicon MOS technology has been reported [6]. In vacuum microelectronics CNTs have been regarded as excellent cold electron sources. They emit electrons at high rate and low voltage and the strong carbon bonds allow CNTs to operate for long period without damage [7]. All these device explorations have motivated and driven synthesis methods for better, more homogeneous and well organized nanotube structures. CNTs with predictable properties at controllable locations and with desired orientation on surfaces will allow for the full exploitation of CNTs impressive electronic, mechanical and thermal properties so moving towards the maturity of CNTs as molecular or nanoelectronics technology.

Within the mainstream of electronic applications we recently started a research activity in the field of carbon nanotubes synthesis and characterization. The fabrication of a position particle detector, cold cathode field emitters for storage devices and the developing of electronic devices, such as FETs have been the driving forces of our research. In the first case an array of CNTs is the charge collector between the active medium and the read-out electronics of the detector. The total charge produced in the active medium (reversed biased thin Si diode) traversed by a particle is driven via the CNTs to the read-out electronics. CNTs, with 10–100 nm diameter (metal or semiconductor type), will allow at least one order of magnitude gain in the spatial resolution of particle detection [8]. In the second case a micro electron gun is the electron source for reading and writing on medium recording cells in a high resolution storage device. The electron beam has to be focused onto the cell with a final diameter of 50 nm and a current density in the range 1–10 A/cm$^2$. CNTs are the electron source that provides the high current density necessary to change the physical status of the medium cell.

In the third case the CNTs are used as channels for the transistors. In every case a highly needed major breakthrough in the CNTs technology is the development of a fabrication method capable of producing well organized nanotube structures, with uniform CNTs and reproducible electronic properties.

Arc discharge, laser ablation, and chemical vapor deposition (CVD) have been the three methods used for CNTs growth. The first two employ solid state carbon precursors to provide carbon sources needed for CNT growth and involve carbon vaporization at high temperatures. Together with impressively narrow diameter distribution the two methods produce only tangled CNT mixed randomly with byproducts. CVD utilizes hydrocarbon gases as sources for carbon atoms and metal catalyst as "seeds" for nanotube growth that takes place at relatively lower temperatures. Recently, it has been proved that site-selective CVD synthesis both on flat substrates with patterned catalyst layers [9] and in nanotemplates [10] grows CNT arrays at controllable locations and with desired orientations on surfaces. Understanding the chemistry involved in the growth and controlling the catalytic nanoparticles could eventually allow for the control of the diameter and chirality of nanotubes and consequently their electronic properties.

In order to meet the requirements of the projects we are involved in we are developing both types of site-selective CVD approaches to the growth. Several types of flat substrates such as silicon, silicon oxide and nitride, and porous silicon (PS) have been prepared. In order to perform the template based CVD growth, a fabrication method to prepare a highly ordered anodic porous alumina matrix has been set up. Transition metal catalysts, such as nickel, iron and cobalt, have been investigated as seeds to nucleate the growth of CNTs. Various CVD process parameters, such as carbon gas precursor type and percentage in the gas mixture, use of etching or carrier gases in the gas mixture and deposition temperature, have been investigated to obtain ordered arrays of reproducible CNTs.

In this paper we present some examples of the CNTs synthesis obtained on different substrates, i.e. silicon dioxide and nanoporous Si, with evaporated Ni and Fe as catalysts, by varying the CVD process parameters. The CNTs structural characterization by Scanning Electron Microscopy (SEM) and Transmission Electron Microscopy (TEM) observations is reported.

## 2. EXPERIMENTAL

### Substrates and catalysts preparation

A 350 nm thick $SiO_2$ layer was grown on silicon wafers ((100), n-type, 1Ω.cm) by using the well established processes of the silicon planar technology, i.e. steam oxidation at 1000°C. Nanoporous silicon was obtained on (100) $n^+$ Si (CZ) wafers, (dopant As, resistance lower than 0.007 ohm), by electrochemical etching in an isopropanol solution of fluoridric acid, for 5 min at a current of 3 A. In these conditions the thickness of the layer is around 4 μm. Ni and Fe films of several thicknesses were deposited on $SiO_2$ and nanoporous Si substrates by e-gun evaporation. Before the CNTs deposition some Fe/nanoporous Si samples were annealed overnight in air at 300°C. The Ni/silicon dioxide samples were heated up and annealed at 700°C in $NH_3$ in order to obtain reduced metal nanoparticles for their use as catalyst.

### CNTs growth process

The CNTs were grown by CVD in a proper designed cylindrical reactor at atmospheric pressure, using $C_2H_2$ and $CH_4$ as carbon precursors. The substrates were placed on top of a boron nitride flat heater and exposed to a parallel gas flow. Before the growth process the system was purged at a final vacuum of $10^{-7}$ Torr. Various $C_2H_2$ and $CH_4$ percentages in the gas mixture and deposition temperatures were investigated.

## 3. RESULTS AND DISCUSSION

In Fig. 1 SEM micrographs of CNTs grown on 4 nm Ni layer evaporated by e-gun on top of $SiO_2$/Si substrate are shown. The Ni catalyst was treated in $NH_3$ gas at 700°C before the CNTs deposition. CNTs were grown in $C_2H_2/NH_3$ gas mixture at 700°C and atmosheric pressure. The central micrograph shows a carpet of carbon tubules with a high degree of vertical alignement. In the insert on the bottom left a higher magnification SEM is displayed. Carbon tubules have diameter of 50-75 nm and present brighter contrast particles on their top. In order to understand the nature of the tubules and their fine structure a series of accurate TEM observations were performed on the same sample. The carpet of tubules was mechanically removed and dispersed in isopropanol alcohol. Then a few drops of the solution were put on a holey carbon films on a Cu grid. The bright field TEM image of Fig. 2 shows that the vertically aligned tubules of Fig. 1 are bundles of tight MW-CNTs with diameters in the range of 50–100 nm. Each single MW-CNT has a bamboo-like inner structure. The High Resolution TEM (HREM) image in the inset clearly shows the multi walled structure of the carbon tubules, with a spacing of 0.34 nm close to that of the (0002) graphite.

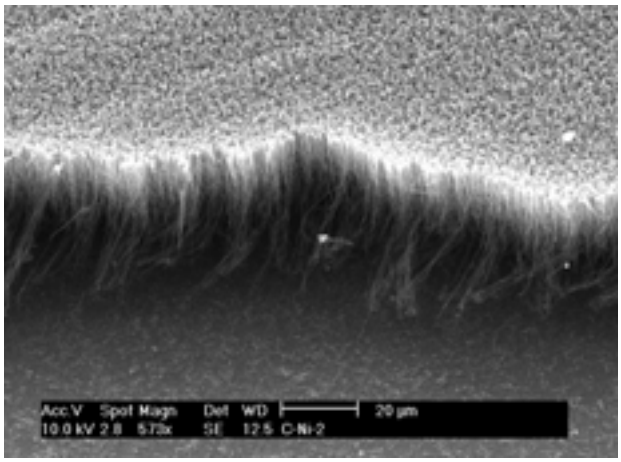


*FIG. 1. SEM micrographs of carbon tubules grown on 4 nm Ni layer evaporated by e- gun on top of $SiO_2$/Si substrate. In the inset a HREM image of a MW-CNT.*

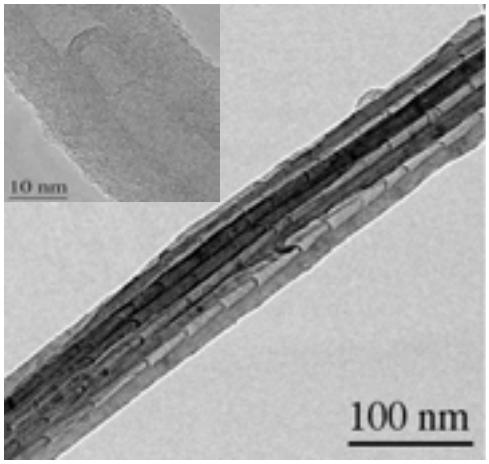


*FIG. 2. Bright field TEM micrograph of a bundle of MW-CNTs. On the top left, the HRTEM image of a MW-CNT.*

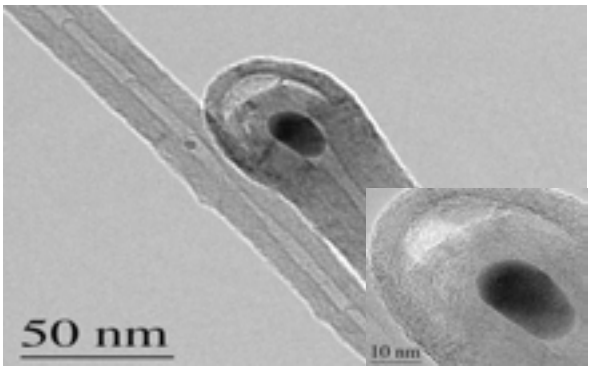


*FIG. 3. Bright field TEM micrograph of two MW-CNTs, always referring to the same sample of Fig.1. In the inset on the bottom right, a HRTEM of the tip of the MW-CNT is displayed.*

A bright field TEM image of two MW-CNTs of the same sample of Fig 1 is shown in figure 3. Electron micro diffraction and Energy Dispersive Spectra show that the two dark particles, i.e. the larger one on the top region of the CNT on the right and the smaller one on the central region of CNT on the left, are Ni particles with a typical FCC crystallographic structure. Sheets of graphene surround the Ni particle till a certain curvature radius, after which the graphene sheets detached from the metal. The elongate shape of the Ni nanoparticles proves that the alignement of the graphene sheets into multi-walled carbon structure couples to a reshaping of the Ni nanoparticles as reported in [11]. The presence of Ni particles on the top of the MW-CNT is in agreement with the tip-growth model even if Ni particles are present both in other areas of CNT and inside nanobeads like structures, not shown here. In the inset, a HREM of the tip of the MW-CNT is reported. As shown in this micrograph, there is a strong correlation between the diameter of the CNTs and the dimensions of the catalyst nanoparticles.

Nanoporous silicon substrates have been widely used in order to investigate the effect of the dispersion of Fe catalyst nanoparticles on the substrate [12]. In this framework, we performed experiments where an Fe layer of few nanometers has been deposited by evaporation through a shadow mask with dots of few millimetres as a diameter. The patterned structure so obtained underwent a deposition process in $C_2H_2$ atmosphere and the deposited structures have been investigated by SEM.

Figure 4 shows a SEM micrograph of CNTs grown on the dot-patterned iron catalyst surface layer, 5 nm thick, on a porous silicon substrate, using acetylene as feeding gas at atmospheric pressure and 700ºC, after an overnight annealing in air at 300ºC. In particular, the micrograph evidences the presence of a 100 μm structure protruding perpendicularly from the surface of the dot. The inset in Fig. 4 shows that this cylindrical structure is formed by fibers that grow upwardly in an entangled form. A deeper structural investigation of these tubules or fibers, achieved by HREM reveals (see Fig. 5) that these fibers grown in an acetylene atmosphere on a Fe layer are MW-CNTs with a mean number of walls of about 10.

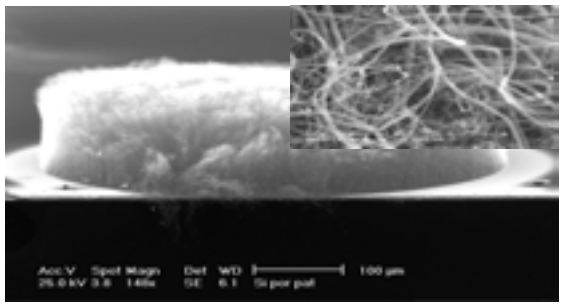

*FIG. 4. SEM micrographs of CNTs grown on 5 nm Fe layer (dot) evaporated by e- gun on a nano-porous Si substrate. Catalyst pre-treatment: overnight annealing in air at ~300°C. CNTs deposition: pure $C_2H_2$, atmospheric pressure and 700ºC.*

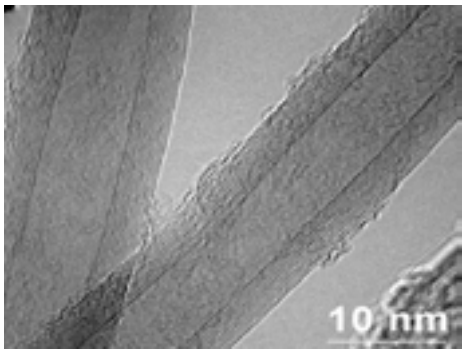


*FIG. 5. HREM micrograph of MW-CNTs grown on 4 nm Fe layer on nanoporous Si substrate. No catalyst pre-treatment. CNT deposition: 5% $C_2H_2$ in Ar, atmospheric pressure and 700ºC.*

We have also investigated how the change on the carbon feedstock gas and its related process temperature affects the deposition by using methane as feeding gas for the growth. In this case, as reported in the SEM micrograph in Fig. 6, the obtained CNTs appear quite shorter than the tubes produced by using acetylene as C feedstock gas, as can be deduced from the comparison with Fig. 4.

The nucleation and growth process is slower in the case of methane gas, the tubes are shorter and the iron nanoparticles used as catalysts move on the top of the CNTs. Three regions can be distinguished in Fig 6: a first region delimited by the iron dot, densily covered by CNTs, as can be deduced by observing the upper-left inset; a circular region surrounding the dot without any nanotube grown and a third region where the nanotubes grow with a low density and jutting out from the porous surface (see the right-bottom inset). All these observations can be explained by considering the emission of Fe nanoparticles from the catalyst patterned dots, owing to the high temperature of the process. In fact, in order to decompose the methane, a temperature of about 900°C is needed.

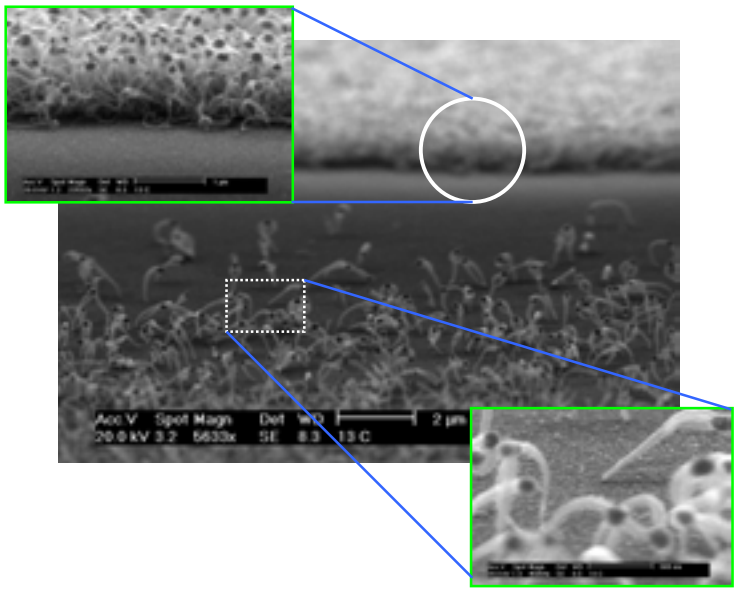

*FIG. 6. SEM micrographs of CNTs grown on 4 nm Fe layer (dot) evaporated by e- gun on a nano-porous Si substrate. No catalyst pre-treatment. CNTs deposition: 50% $CH_4$ in Ar, atmospheric pressure and 900ºC.*

## 4. CONCLUSIONS

In order to meet the requirements of our projects, we are developing site-selective CVD synthesis of CNTs, both on flat substrates with patterned catalyst layers and in nanotemplates. The preliminary results obtained on different substrates, i.e. silicon dioxide and nanoporous Si, with evaporated Ni and Fe as catalysts, by varying the CVD process parameters are encouraging ones and proved that this type of deposition process allows to grow nanotubes arrays at controllable locations and with desired orientations on surfaces. Further efforts are necessary in order to understand the role of the catalyst and its interaction with the substrate, as well as the growth parameters processes, in determining the structural and the electronics properties of the CNTs.

## REFERENCES


[1] COLLINS, P.G., AVOURIS, PH.,"Nanotubes for nanoelectronics", Scientific American 283 (2000) 62–69.

[2] WIND, S., APPENZELLER, J., MARTEL, R., DERICKE, V., AVOURIS, PH.,"Vertical scaling of single-wall carbon nanotubes transistors using top gate electrodes", Appl. Phys. Lett. 80 (2002) 3817.

[3] DERYCKE, V., MARTEL, R., APPENZELLER, J., AVOURIS, PH.," Carbon nanotube inter and intramolecular logic gates", Nano Letters 1 (2001) 453–456.

[4] KREUPL, F., GRAHAN, A.P., DUESBERG, G.S., STEINHOEGL, W., LIEBAU, L., HUNGER, E., HOENLEIN, W., "Carbon Nanotubes as potential building blocks for future nanoelectronics", Microelectron. Eng. 64 (2002) 399–408.

[5] TSENG, Y., XUAN, P., JAVEY, A., MALLOY, R., WANG, Q., BOKOR, J., DAI, H., "Monolithic integration of carbon nanotube devices with silicon MOS technology", Nano Letters 4 (2004) 123–127.

[6] GROENING, P., RUFFIEUX, P., SCHLAPBACH, L., GROENING, O., "Carbon nanotubes for cold electron sources", Adv. Eng. Mater. 5 (2003) 541–550.

[7] ANGELUCCI, R., CORTICELLI, F., CUFFIANI, M., DALLAVALLE, M., MALFERRARI, L., MONTANARI, A., MONTANARI, C., ODORICI, F., RIZZOLI, R., SUMMONTE, C., "Applications of nanotechnologies in high energy physics", Nuclear Physics B (proc. Suppl.) 125 (2003) 164–168.

[8] DAI, H., "Carbon nanotubes: synthesis, integration, and properties", Accounts Chem. Res. 35 (2002) 1035–1044.

[9] LI, J., PAPADOPOULOS, C., MOSKOVITS, M., "Highly ordered nanotube arrays for electronics applications", Appl. Phys. Lett. 75 (1999) 367–369.

[10] HELVEG, S., CARTES, C., SEHESTED, J., HANSEN, P., CLAUSEN, B., ROSTRUP-NIELSEN, J., PEDERSEN, F., NERSKOV, J., "Atomic-scale imaging of carbon nanofibre growth", Nature 427 (2004) 426–429.

[11] FAN, S., CHAPLINE, M., FRANKLIN, N., TOMBLE, T., CASSELL, A., DAI, H., "Self-oriented regular arrays of carbon nanotubes and their field emission properties", Science 283 (1999) 512–514.

# SYNTHESIS AND APPLICATIONS OF NANOSTRUCTURED AND NANOCRYSTALLINE SILICON BASED THIN FILMS

R. RIZZOLI[a], C. SUMMONTE[a], E. CENTURIONI[a], D. IENCINELLA[a], A. MIGLIORI[a], A. DESALVO[b], F. ZIGNANI[b]
[a] CNR - IMM Bologna, Bologna, Italy
[b] Dip. di Chimica Applicata e Scienza dei Materiali, Bologna, Italy

**Abstract**

In the field of nanostructured materials, our research was focussed on the synthesis and applications of silicon based nanostructured films. In particular, we studied nanocrystalline Si and SiC thin films, having film thicknesses in the nanometer range and including nanometric grains, and compositionally modulated nanometric multilayers of a-$Si_3N_4$:H/a-$Si_xN_{1-x}$:H. The Plasma Enhanced Chemical Vapour Deposition (PECVD) technique was used to deposit these materials at low temperature, which is advantageous for device applications. This paper is centred on our main results on *p*-type nanocrystalline Si (*p* nc-Si). The *p* nc-Si films were deposited by Very High Frequency (VHF) PECVD in high hydrogen dilution of the gas mixture at 170 °C. Our results on the application of these films in *nanocrystalline Si / amorphous Si /crystalline Si* heterojunction solar cells are discussed in details. The long range effects of plasma H atoms on the heterojunction nanostructures are studied by the simulation of optical spectra and the High Resolution Transmission Electron Microscopy (HRTEM) observations on the *p* nc-Si/*i* a-Si:H double layers deposited on c-Si substrates. The heterojunction built-in potential of these double layers is larger than in *p* a-Si:H / *i* a-Si:H structures and therefore in the *nanocrystalline Si / amorphous Si /crystalline Si* solar cell a $V_{oc}$ up to 640 mV can be obtained. The simulation of optical spectra and the HRTEM observations are reported and correlated with the corresponding solar cells characteristics.

## 1. INTRODUCTION

The main topics of material science and technology are presently the formation, characterisation, and exploitation of materials at the nanoscale. The research on nanostructured materials and the related technology have been growing very rapidly in the past few years, since it has become clear that creating new materials and devices from nanoscale building blocks could open the way to new and improved properties and functionalities. However, for a rapid advancement in this field many challenges must be faced: increase characterisation capabilities in observation and chemical analysis at finer sizes; be able to manipulate matter at finer size scales and use computational approaches in directing this issue; understand the critical role played by surfaces and interfaces in nanostructures; learn controlling the nanostructure size, size distribution, composition, and assembly; deal with the thermal, chemical, and structural stability of nanostructured materials and the related devices, and achieve reproducibility and scalability of the synthesis processes.

In this field, our research was focussed on the synthesis and applications of silicon based nanostructured films: we studied nanocrystalline Si and SiC thin films (intrinsic and doped), having film thicknesses in the nanometer range and including nanometric grains, and compositionally modulated nanometric multilayers of a-$Si_3N_4$:H / a-$Si_xN_{1-x}$:H. The PECVD technique, at 13.56 MHz (r.f.) and at VHF, was used to deposit these materials at low temperature, which is advantageous for device applications. The growth of Si based thin films by PECVD is well reproducible, the thickness of amorphous films is easily controlled down to about 1 nm, but, in the case of nanocrystalline films, the specific details of the evolution of structure and morphology during growth are still matter of discussion.

The research works on the nanometric a-$Si_{1-x}N_x$:H based multilayers and the nanocrystalline SiC (nc-SiC) are not reported in this paper due to lack of space, however they are briefly summarized in the following to give the related references.

The multilayer structures were deposited by r.f. PECVD at 220°C [1, 2] and consisted of periodic repetitions of stoichiometric a-$Si_3N_4$:H layers, 10 nm thick, and of understoichiometric

a-$Si_{0.6}N_{0.4}$:H layers with thickness ranging from 0.5 to 3 nm. The repetition of the a-$Si_3N_4$:H (5 eV optical gap)/a-$Si_{0.6}N_{0.4}$:H (2.6 eV optical gap) double layers produced barrier/well periodic structures. The interface abruptness in the multilayers was shown by TEM. The photoluminescence efficiency [3] of these structures was up to one order of magnitude larger than that of the film having the composition of the well layers. The peak emission energy increase with decreasing well layer thickness was simulated in terms of spatial, and quantum confinement models. These structures were also inserted in p-i-n light emitting devices, as intrinsic layers, to increase their brightness and shift the wavelength of the emitted light to the blue [4–6].

The crystalline silicon carbide is a semiconductor, which possesses excellent mechanical, chemical, thermal and electrical properties, and is presently subject of large scientific interest, both on fundamental aspects, and in view of a variety of applications [7]. However, it can only be fabricated at high temperature, with consequent limitations, related both to the substrate, and to the device fabrication technology. It is therefore of great interest to attempt to crystallise a-$Si_{1-x}C_x$:H films deposited at low-temperature, as full crystallisation of amorphous layers would open the way to specific applications in electronic devices, with further potentiality coming from the large area attainable with plasma deposition.

Our recent results on nc-SiC obtained by excimer laser irradiation on a set of a-$Si_{(1-x)}C_x$:H samples are reported in ref. [8]. The a-SiC:H films, deposited by VHF-PECVD at 100 MHz and at two different temperatures, 250°C and 350°C [9], showed different stoichiometry, hydrogen concentration, and bonding configuration. The films grown at 350°C in high hydrogen dilution exhibit a large concentration of Si-C bonds, associated to a highly crosslinked structure, no detectable Si-$CH_3$ bending signal in infrared spectra and reduced hydrogen content. After laser treatment of these films, we observed the formation of SiC crystallites, which was accompanied by either Si or graphite crystallites, depending on the composition. The influence of the structural parameters of the as-deposited samples on subsequent crystallisation was studied in detail and evidenced that the mixture of the a-SiC:H alloy with microcrystalline silicon is often referred to in the literature as ‘nano or micro-crystalline silicon carbide’, although such an expression can be misleading in some cases [8].

This review will focus on our recent results on the PECVD synthesis and the characterisation of nanocrystalline Si films, and in particular on the application of *p* nc-Si films in heterojunction solar cells. The *p* nc-Si films were deposited by VHF-PECVD at 100 MHz, in high hydrogen dilution of the gas mixture and at very low temperature, 170°C. We explored the dynamics of amorphous to crystalline transition during growth both on amorphous (glass or intrinsic a-Si:H) and on crystalline substrates, studying a condition close to equilibrium between etching and deposition [10].

These films were applied in the fabrication of amorphous/crystalline heterojunction silicon solar cells. A realistic relatively simple technology can be used to fabricate very high efficiency solar cells using a limited maximum process temperature (< 250°C), with advantages in terms of cost reduction [11, 12]. We demonstrated that the presence of nanocrystals in the emitter produces an increase of solar cell efficiency, as a consequence of increased diffusion voltage and of reduced absorption losses. However, the fabrication of *nanocrystalline/amorphous/crystalline Si* heterojunction structures, including a very thin passivating amorphous *i*-layer on (100) c-Si, is a critical process.

The high hydrogen concentration required to deposit the nanocrystalline emitter using the $SiH_4$-$H_2$ gas mixture promotes hydrogen diffusion into the underlying intrinsic amorphous buffer layer [13], thus causing its partial/total crystallisation. Conversely, a lower hydrogen concentration would result in the formation of an amorphous buffer layer at the initial stage of the *p* nc-Si growth [14]. Either shunts through the interface, or optical absorption losses will occur respectively [15]. Our efforts aiming at obtaining a better control of the thickness and crystallinity of the *p* nc-Si emitter layer in the *nanocrystalline/ amorphous/crystalline Si* structures, and at studying the structural modifications and eventual crystallisation produced by the VHF hydrogen-rich plasma on the underlying amorphous buffer layer are discussed.

The results on the optimization of the heterojunctions, both by the simulation of optical spectra and by HRTEM observations, are reported and correlated to the corresponding solar cells characteristics.

## 2. EXPERIMENTALS

### p-type nanocrystalline Si films and nanocrystalline /amorphous heterojunction solar cells

The *p* nc-Si films were deposited by VHF - PECVD at 100 MHz, 170°C, 0.3 hPa, in conditions close to equilibrium between etching and deposition, with a three step DED process. In the first and second D steps a $B_2H_6$ : $SiH_4$ : $H_2$ gas mixture, with different $B_2H_6\% = [B_2H_6]/[SiH_4]$, a 98.5% $H_2$ dilution and a power density of 156 mW/cm$^2$ were used. In the E step a 20.2 sccm $H_2$ mass flow was fixed. The p-layer deposition conditions applied in the HJ cells are reported in Table I, that includes the standard case of a unique D step (H4 sample, $t_E$ = 0 s). The films deposited with a continuous unique D step present a large nanocrystalline fraction (amorphous fraction ranging from 40% down to undetectable) and variable void fraction, depending on the substrate. A dark conductivity greater than 0.1 S/cm was measured on films as thin as 20 nm deposited on glass, with a 75% nanocrystalline fraction, and optically measured homogeneity within ±4% over 10x10 cm$^2$. An increase in dark conductivity up to 1 S/cm was observed, due to an increase in dopant activation [16], after annealing at 250°C for 1 hour under vacuum. This treatment simulates the maximum temperature undergone by the junction during the indium tin oxide (ITO) deposition. Details on the optimization of these layers are reported in [16] and [17].

The solar cells were deposited on flat n-type c-Si, CZ, 1ohm·cm, 4" wafers. All cells are $p^+$nc-Si/*i* a-Si:H/n c-Si heterojunction (HJ) devices (*nanocrystalline/amorphous*). The *i* a-Si:H layers, ~5 nm thick, inserted in the heterojunction to passivate the c-Si surface, were deposited at 13.56 MHz, 28 mW/cm$^2$, [$SiH_4$] = 20 sccm, 200°C. Using this deposition condition, a completely amorphous layer is obtained on glass.

Before junction formation, the c-Si substrates were etched in 0.5% HF solution in deionized water for 60 s and rapidly inserted in vacuum with no rinse. All cells incorporate a 50 nm microcrystalline $n^+$ back surface layer, deposited at 13.56 MHz, 110 mW/cm$^2$, 170°C, $PH_3$ : $SiH_4$ : $H_2$ = 0.04 : 2 : 94 (sccm) that improves the back contact quality. The solar cell fabrication was then completed with the deposition of indium tin oxide (ITO) by magnetron RF sputtering at 250°C, that acts as an antireflective coating and transparent front contact, and Al contact evaporation on both sides. Further details on solar cells fabrication are reported in [18].

The microstructure of the p/i double layer grown on c-Si and the profile vs. depth of the crystalline-grain fraction ($F_g$) were determined by the simulation of reflectance spectra, using the Bruggemann effective medium approximation and a multilayer model based on Fresnel formulation. The fit parameters were the layer thicknesses, and the nc-Si, a-Si:H and void volume fractions [13]. In some cases the simulation shows that the outermost layer contains a larger percentage of voids. This layer indicates the presence of surface roughness. The structure of the heterojunction cells was also investigated by HRTEM in cross-section geometry. The solar cell J-V characteristics under illumination were measured, at about 25°C, 100 mW/cm$^2$, using an Oriel AM1.5 solar simulator with a Xe arc lamp.

TABLE I. DEPOSITION PARAMETERS OF P-LAYERS INSERTED IN HJ CELL: DIBORANE PERCENTAGE IN THE GAS MIXTURE AND DEPOSITION TIMES, $t_{D1}$ AND $t_{D2}$, OF THE FIRST AND SECOND D STEPS; PLASMA POWER, P, AND EXPOSURE TIME, $t_E$, IN THE E STEP.

| Cell | p-layer | | | | |
|---|---|---|---|---|---|
| | D step | | | E step | |
| | $B_2H_6$% | $t_{D1}$ (s) | $t_{D2}$ (s) | P (W) | $t_E$ (s) |
| H1 | 1.3 x 10$^{-3}$ | 19 | 75 | 10.0 | 5 |
| H2 | 2.7 x 10$^{-3}$ | 19 | 75 | 10.0 | 5 |
| H3 | 2.7 x 10$^{-3}$ | 19 | 75 | 22.5 | 25 |
| H4 | 2.7 x 10$^{-3}$ | 240 | - | - | - |

## 3. RESULTS AND DISCUSSION

The DED process, applied for the *p* nc-Si layer deposition on the ~5nm thick a-Si:H buffer layer of the HJ solar cells, is a layer-by-layer process at the early stage [19, 20]. It is intended to control the nucleation of the *p* nc-Si layers and preserve the *i* buffer layers in the HJ. During the first D step a ~4 nm thick p-layer is formed, which is amorphous despite the large $H_2$ dilution used in the deposition. In fact, under this deposition condition, the p-layer growth on a-Si:H is initially amorphous, becoming crystalline only after approximately 20 nm [10, 21]. This is evidenced by the cross section TEM image of an H4 type solar cell (p-layer deposited with a unique D step) reported in Fig.1.

For this reason, the very thin p-layer deposited in the first D step of the DED process is intended both as a protective layer, to prevent the $H_2$ induced etching of the underlying a-Si:H layer, as well as a seed layer in which the nucleation of nc-Si will be induced by the following E step. The growth of the *p* nc-Si emitters is then completed during the second D step.

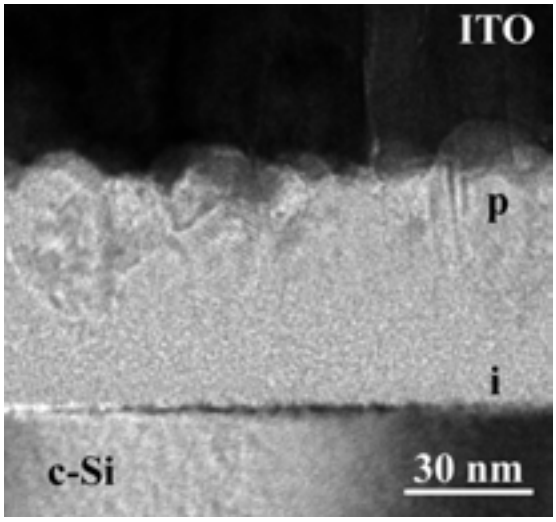


*FIG. 1. Cross section TEM image of a nanocrystalline / amorphous heterojunction H4 type.*

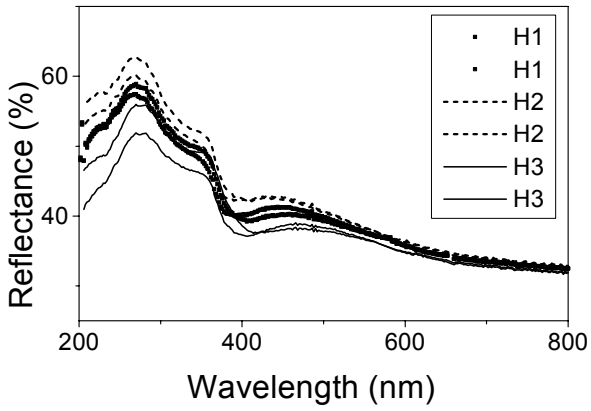


*FIG. 2. Spectral reflectance of DED samples. As a certain spread in the experimental reflectance is observed, for each deposition condition the two extreme curves are reported.*

In Fig. 2, the reflectance spectra of H1, H2, and H3 samples are reported. As a certain spread in the spectra is observed, for each deposition condition the two extreme curves are reported in the figure. For all samples, the two peaks (272 and 366 nm) characteristic of c-Si are evident. In spite of a certain variation among similar samples, the curves do not substantially overlap, indicating that well defined compositions are obtained on DED samples. The reflectance spectra were simulated to determine surface roughness, thickness, composition profile, and crystalline fraction. In Fig. 3 we report the sketches indicating the structural composition profile (depth vs. fraction) as obtained by the simulation of spectral reflectance.

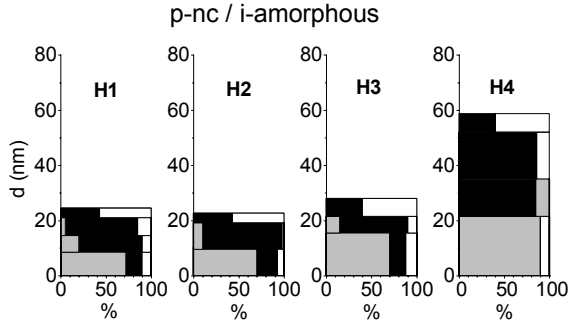


*FIG. 3. Sketches illustrating the results of the simulation of reflectance measurements on p/i double layers. Grey: a-Si:H; black: fine-grain c-Si.; white: voids.*

The sketch H1 in Fig. 3 shows that a certain nanocrystalline fraction exists at the interface with the c-Si substrate. The sample shows an average 10% void fraction and a certain roughness, simulated by a 57% void fraction at the surface. Quite similar results are observed for H2 and H3 samples, deposited using larger $B_2H_6$ fraction in the gas mixture during the D steps. Larger VHF power density and exposure time during the E step (sample H3) result in an interface layer remarkably thicker and with lower crystallinity. In all cases, we do not observe a continuous amorphous buffer layer at the interface with the c-Si substrate; rather we observe crystalline grains reaching this interface.

The results of optical simulation can be compared swith the HRTEM observations. The HRTEM image of sample H1 (Fig. 4) confirms the presence of crystalline grains embebbed in an a-Si:H matrix, down to the interface with the c-Si substrate. The a-Si:H buffer layer is strongly affected by the overall process, resulting no longer continuous. Although a large fraction of a-Si:H is still present at the HJ interface, the highly $H_2$ diluted VHF plasma modifies and partially crystallizes the underlying *i* a-Si:H layer.

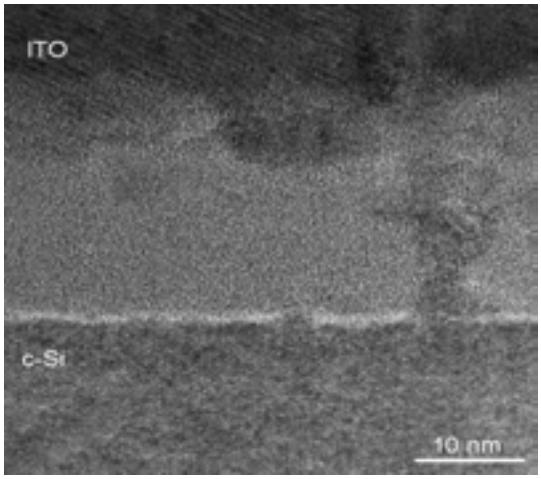


*FIG. 4. HRTEM image of sample HI.*

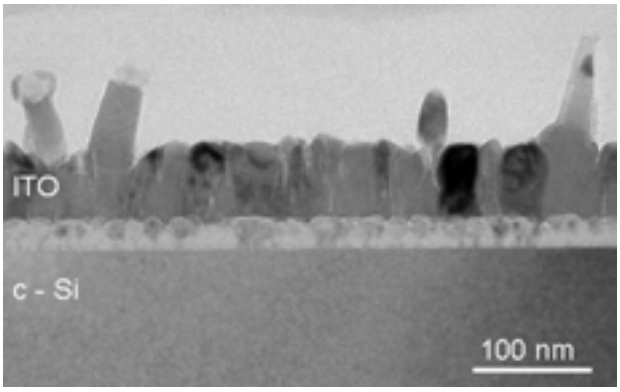


*FIG. 5. Bright field cross section TEM image taken on the H1 heterojunction.*

A bright field image of sample H1 is reported in Fig. 5, which confirms the presence of a rather rough amorphous/nanocrystalline interface and of some surface roughness. The overall agreement of the macroscopic and microscopic techniques confirms the homogeneity of the sample structure.

The increase of surface roughness observed in the case of sample H3 (sketch H3 in Fig. 3) is attributed to larger grains emerging from the sample surface, as confirmed by HRTEM, that shows one of the crystalline grains protruding out of the surface, giving rise to a rms surface roughness of about 10 nm. The increase in grain size can be ascribed to the more efficient seed formation promoted by the higher VHF power density during the E step.

The results of TEM and reflectance spectroscopy are in very good agreement, with respect to both thickness and composition of layers. Table II compares the expected thicknesses of *i* and *p* layers, calculated from the deposition rates, with the TEM and optical total thicknesses and roughnesses.

The p/i emitters of H1 and H2 type cells exhibit a slightly higher $F_g$ fraction with respect to the H3 cells. Moreover, the reflectance spectra show that the two c-Si peaks are attenuated in the H3 sample with respect to H1 and H2, indicating a higher surface roughness. The optical simulation detects such a surface as a 10 nm thick nanocrystalline layer of very low density (40%).

TABLE II. $F_G$ FROM THE SIMULATION OF REFLECTANCE SPECTRA, THICKNESS AND ROUGHNESS OF P/I DOUBLE LAYERS FROM OPTICAL AND TEM MEASUREMENTS. THE TEM TOTAL THICKNESS AND SURFACE ROUGHNESS ARE MEASURED BY BRIGHT FIELD IMAGES.

| Cell | $F_g$ (%) | i + p (nm) | | Roughness (nm) | |
|---|---|---|---|---|---|
| | Opt. | Opt. | TEM | Opt. | TEM |
| H1 | 51 | 23 | 26 | 3 | 5 |
| H2 | 54 | 23 | 26 | 5 | 6 |
| H3 | 35 | 28 | 26 | 7 | 10 |
| H4 | 49 | 60 | 59 | 7 | 8 |

The JV characteristics under illumination (100 mW/cm$^2$, AM1.5 global spectrum) are shown in Fig. 8 and the average values of the cell parameters are reported in Table III. The $J_{sc}$ is calculated on the illuminated area of the cell (subtracting the front grid contact area), in order to compare measurements on cells having a different front contact shadowing. Note the superior $V_{oc}$ homogeneity of sample H4, that includes a continuous *i* a-Si:H layer.

A sequence of PECVD deposition-etching steps was applied in the past to fabricate fairly thick microcrystalline layers [19, 20]. The PECVD is a typical large area deposition technique. The investigation with an optical technique as the reflectance spectroscopy, or other optical large area techniques, leads to a description of the phenomenon in terms of average parameters. In fact, we observe an evolution of the nanocrystalline fraction with $H_2$ exposure time, with diborane fraction in the gas mixture as a limiting parameter.

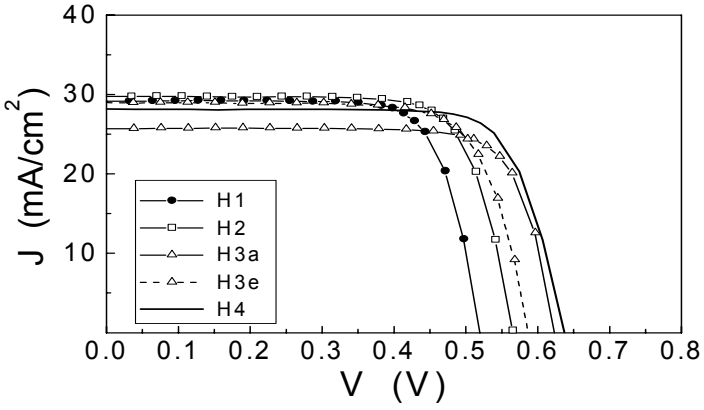


*FIG. 6. Measured JV characteristics under illumination of selected cells.*

However, a close inspection of our samples, by cross section HRTEM observations, evidences the local character of the initial stages of the modification occurring in the thin amorphous silicon buffer layer after the first stage of a layer-by-layer process. We observe an evident modification of the a-Si:H layer upon exposure to $H_2$ plasma. In some cases this result is confirmed by the complete crystallisation down to the c-Si surface, that by the way remains always well visible; while in other cases, Si nanograins form, both within the amorphous layer and at the interface with c-Si, in this last case being preferentially epitaxial.

This observation directly confirms the long range effects of hydrogen inside the amorphous matrix [15, 20] and the conclusion that the crystallisation of the growing p-layer, in the layer-by-layer technique, does not proceed after the almost complete removal of the amorphous component of the just deposited layer, as it was previously suggested [22, 23]. The condition needed to preserve a buried a-Si:H region is a low ion energy, and therefore a shallow H implantation depth [24]. As a confirmation, we observe an increase of the a-Si:H fraction at the interface if a higher power density is used for the E step (sample H3). Both hydrogen flux and ion energy increase with power density, with opposite effects on the crystallinity of the subsurface layer [24]. If the H supply at the surface is not the limiting parameter for crystallisation, the detrimental effect of ion bombardment prevails, thus reducing the crystalline fraction. In the case of a *nanocrystalline/ amorphous* device, this results in limited modification of the *i* a-Si:H buffer layer, with corresponding increase of the $V_{oc}$ (H3 sample).

TABLE III. HJ SOLAR CELL PARAMETERS UNDER 100 MW/CM$^2$, AM1.5 GLOBAL SPECTRUM: AVERAGE AND BEST VALUES. $J_{SC}$ IS CALCULATED ON THE APERTURE AREA.

| Cell | $J_{sc}$ (mA/cm$^2$) | | $V_{oc}$ (V) | | FF (%) | | η (%) |
|---|---|---|---|---|---|---|---|
| | avg | best | avg | best | avg | best | avg |
| H1 | 30.0 | 31.8 | .526 | .541 | 76 | 78 | 12.0 |
| H2 | 29.8 | 31.2 | .569 | .573 | 76 | 77 | 12.9 |
| H3 | 29.0 | 30.4 | .603 | .624 | 75 | 78 | 13.1 |
| H4 | 30.4 | 31.5 | .638 | .638 | 72 | 76 | 14.0 |

The nanoscale inhomogeneities observed in DED samples have a statistical effect on the results of solar cell devices. The measured $V_{oc}$ show a certain spread and an evident correlation with the composition of the p/i emitter is not observed. However, values up to approximately 624 mV are reached in the case of the H3 type samples, having an HJ interface with the microscopic structure shown in Fig. 6.

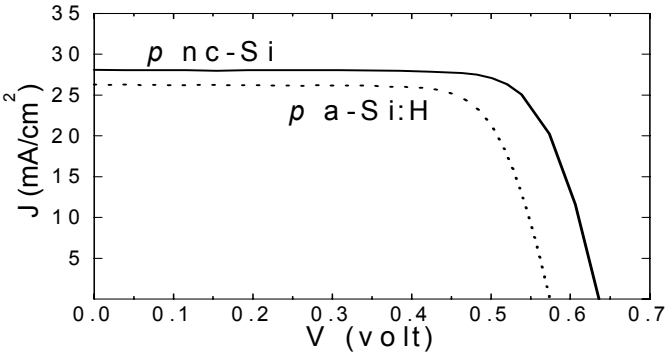


*FIG. 7. Measured JV characteristics under illumination of two HJ cells with the same 5 nm thick i buffer layer and a p-nanocrystalline (H4 type cell) or p-amorphous emitter.*

This indicate that in spite of a large number of crystalline paths crossing the a-Si:H buffer layer in H1, H2 and H3 cells with DED p-layers, the major part of the c-Si surface is still efficiently passivated. We note, in turn, that the best $V_{oc}$ = 638 mV is observed in the case of H4 samples, where a continuous 20 nm thick, (p+i) type, a-Si:H layer exists [21], and a very good c-Si surface passivation is obtained. The one dimensional electrical model D-AMPS can be applied in this case and the measured $V_{oc}$ is in agreement with the theoretical prediction.

When *p* nc-Si emitters are used, the heterojunction built-in potential increases with respect to the *p a-Si:H / i a-Si:H* solar cells, as a consequence of the higher doping level and optical gap of the *p* nc-Si compared to the *p* a-Si:H emitter. In Fig. 7, in fact, the JV characteristic under illumination of the *nanocrystalline/amorphous* HJ solar cell shows a higher $V_{oc}$ than the *amorphous/amorphous* device. Moreover, the $J_{sc}$ of the *nanocrystalline /amorphous* cell is higher thanks to the lower absorption losses in the *p* nc-Si emitter compared to the *p* a-Si:H one of similar thickness.

## 4. CONCLUSIONS

A short review of our research on various nanostructured Si based materials is presented in the introduction. The results on the optimization of the p nc-Si / i a-Si:H double layers for photovoltaic applications are reported in more detail. A set of DED (deposition-exposure to H2-deposition) p nc-Si

films was deposited by VHF PECVD on i a-Si:H / c-Si substrates, with the aim of achieving a good control of the thickness and crystallinity of the p-layer and preserving the good passivation quality of the a-Si:H buffer layer at the c-Si surface. A marked interaction of the hydrogen-rich plasma with the underlying intrinsic amorphous layer is observed even applying the DED deposition sequence. HRTEM cross section images show the formation of nanocrystalline grains not only at the sample surface, but also within the amorphous layer and at the a-Si:H / c-Si interface, thus confirming the long range interaction of hydrogen plasma with the a-Si substrate.

The application of DED layers to HJ solar cells leads to somewhat inhomogeneous results; however, the fairly good Voc values obtained indicate that the passivation of the (100) c-Si surface is preserved.

## REFERENCES


[1] GIORGIS, F., PIRRI, C. F., TRESSO, E., SUMMONTE, C., RIZZOLI, R., GALLONI, R., DESALVO, A., RAVA, P., "Optical, structural and electrical properties of device quality a-$Si_{1-}N_x$:H films deposited by plasma enhanced chemical vapour deposition", Phil. Mag. B 77 (1998) 925.

[2] RAVA, P., GIULIANI, F., GIORGIS, F., PIRRI, C.F., TRESSO, E., MANDRACCI, P., SUMMONTE, C., RIZZOLI, R., DESALVO, A.,"Amorphous silicon nitrogen alloys deposited by PECVD under hydrogen dilution conditions", Proceedings of the 9th International Conference on Physics of Semiconductor Devices edited by V. Kumar and S. K Agarwal (Narosa Publishing House, New Delhi, India, 1997) p. 580.

[3] GIORGIS, F., GIULIANI, F., PIRRI, C.F., TRESSO, E., GALLONI, R., RIZZOLI, R., SUMMONTE, C., DESALVO, A., RAVA, P., "Photoluminescence and Optical Characterization of a-$Si_xN_{1-x}$:H Based Multilayers Grown by PECVD", *Amorphous and Microcrystalline Silicon Technology*, edited by E. Schiff, M. Hack S. Wagner, R. Schropp, I. Shimizu, Mat. Res. Soc. Symp. Proc. Vol. 467 (Pittsburgh, PA, 1997) p.489.

[4] SUMMONTE, C., RIZZOLI, R., GALLONI, R., GIORGIS, F., GIULIANI, F., PIRRI, C.F., TRESSO, E., DESALVO, A., ZIGNANI, F., RAVA, P., "Photoluminescence and electroluminescence properties of a-$Si_{1-x}N_x$:H based superlattice structures", J. of Non-Cryst. Solids 227-230 (1998) 1127.

[5] RIZZOLI, R., SUMMONTE, C., RAVA, P., BARUCCA, G., DESALVO, A., GIORGIS, F., "a-SiN:H multilayer versus bulk structure: a real improvement of radiative efficiency? ", J. of Non-Cryst. Solids 266 - 269 (2000) 1062.

[6] RIZZOLI, R., SUMMONTE, C., GALLONI, R., DESALVO, A., ZIGNANI, F., PINGHINI, R., CENTURIONI, E., GIORGIS, F., PIRRI, C.F., TRESSO, E., RAVA, P., "Carrier confinement in a-$Si_{1-x}N_x$:H multilayer structures for increased light emission", proceedings of symp. X, *Innovative light emitting materials*, 9th CIMTEC International Conference (Florence 1998) edited by P. Vincenzini, G.C. Righini (Techna, Faenza, 1999) p.67.

[7] BERGMAN, P., AND JANZEN, E., (eds), "*Silicon Carbide and Related Materials - 2002*", Trans. Tech. Publ. Mater. Sci. Forum, LTD, USA, 2003, vol.433-436.

[8] SUMMONTE, C., DESALVO, A., RIZZOLI, R., SERVIDORI, M., MILITA, S., NICOLETTI, S., BIANCONI, M., IENCINELLA, D., "Laser induced crystallization of hydrogenated amorphous silicon carbon alloys deposited by very high frequency glow discharge", J. Appl. Phys., submitted for publication.

[9] SUMMONTE, C., RIZZOLI, R., BIANCONI, M., DESALVO, A., IENCINELLA, D., GIORGIS, F., "Wide band-gap silicon-carbon alloys deposited by very high frequency plasma enhanced chemical vapour deposition", J. Appl. Phys., submitted for publication.

[10] SUMMONTE, C., RIZZOLI, R., DESALVO, A., ZIGNANI, F., CENTURIONI, E., PINGHINI, R., BRUNO, G., LOSURDO, M., CAPEZZUTO, P., GEMMI, M., "Plasma enhanced chemical vapour deposition of microcrystalline silicon: on the dynamics of the amorphous-microcrystalline interface by optical methods ", Phil. Mag. B 80 (2000) 459.

[11] JENSEN, N., HAUSNER, R. M., BERGMANN, R.B., WERNER, J.H., RAU, U., "Optimization and characterization of amorphous/crystalline silicon heterojunction solar cells", Prog. Photov.: Res. Appl. 10 (2002) 1.
[12] TANAKA, M., OKAMOTO, S., TSUGE, S., KIYAMA, S., "Development of HIT solar cells with more than 21% conversion efficiency and commercialisation of highest performance HIT modules", Proc. 3rd World Conference on Photovoltaic Energy Conversion, Osaka, May 2003, to be published.
[13] SUMMONTE, C., RIZZOLI, R., DESALVO, A., ZIGNANI, F., CENTURIONI, E., PINGHINI, R., GEMMI, M., "Very high frequency hydrogen plasma treatment of growing surfaces: a study of the p-type amorphous to microcrystalline silicon transition", J. of Non-Cryst. Solids 266-269 (2000) 624.
[14] ROBERTSON, J., "Thermodynamic model of nucleation and growth of plasma deposited microcrystalline silicon", J. Appl. Phys. 93 (2003) 731.
[15] FUJIWARA, H., KONDO, M., MATSUDA, A., " Stress induced nucleation of microcrystalline silicon from amorphous phase", Surface Science 497 (2002) 333.
[16] RIZZOLI, R., SUMMONTE, C., PLÁ, J., CENTURIONI, E., RUANI, G., DESALVO, A., ZIGNANI, F., "Ultrathin μc-Si films deposited by PECVD" , Thin Solid Films 383 (2001) 7.
[17] RIZZOLI, R., SUMMONTE, C., . PLÁ, J., CENTURIONI, E., PINGHINI, R., DESALVO, A., ZIGNANI, F., " Plasma deposition of amorphous free microcrystalline silicon films thinner than 20 nm", Proceedings of the 16th European Photovoltaic Solar Energy Conference, Glasgow, UK, 2000, p. 593.
[18] PLÁ, J., CENTURIONI, E., PINGHINI, R., SUMMONTE, C., RIZZOLI, R., ZIGNANI, F., DESALVO, A., " Low temperature fabrication process for μc-Si / c-Si heterojunction solar cells", Proceedings of the 16th European PVSEC, Glasgow (2000) 597.
[19] HAMMA, S., ROCA I CABARROCAS, P., "In situ correlation between the optical and electrical properties of thin intrinsic and n-type microcrystalline silicon films", J. Appl. Phys. 81 (1997) 7282.
[20] ROCA I CABARROCAS, P., HAMMA, S., "Microcrystalline silicon growth on a-Si:H: effects of hydrogen", Thin Solid Films 337 (1999) 23.
[21] PLÀ, J., CENTURIONI, E., SUMMONTE, C., RIZZOLI, R., MIGLIORI, A., DESALVO, A., ZIGNANI, F., "Homojunction and heterojunction silicon solar cells deposited by low temperature-high frequency plasma enhanced chemical vapour deposition", Thin Solid Films 405 (2002) 248.
[22] VETTERL, O., HAPKE, P., HOUBEN, L., FINGER, F., CARIUS, R., WAGNER, H., "Connection between hydrogen plasma treatment and etching of amorphous phase in the layer-by-layer technique with very high frequency plasma excitation", J. Appl. Phys 85 (1999) 2991.
[23] SAITOH, K., KONDO, M., FUKAWA, M., NISHIMIYA, T., FUTAKO, W., SHIMIZU, I., MATSUDA, A., "Role of hydrogen for microcrystalline silicon formation", MRS Proc. Vol. 507 (1998) p.843.
[24] KALACHE, B., KOSAREV, A.I., VANDERHAGEN, R., ROCA I CABARROCAS, P., "Ion bombardment effects on microcrystalline silicon growth mechanisms and on the film properties", J. Appl. Phys. 93 (2003) 1262.

# FORMATION DURING UHV ANNEALING AND STRUCTURE OF Si/SiC NANOSTRUCTURES ON SILICON WAFERS

D. JONES[a], V. PALERMO[a], A. PARISINI[b]
[a] Istituto per la Sintesi Organica e la Fotoreattivita (ISOF-CNR)
[b] Istituto per la Microelettronica e Microsistemi (IMM-CNR)

Bologna, Italy

**Abstract**

The presence of organic contaminants on silicon oxide/silicon systems nucleates oxide desorption during Ultra-High Vacuum (UHV) annealing leading to localised oxide-free areas, "voids", surrounded by areas where the oxide remains. During radial enlargement of the voids, on further annealing, composite Si/SiC nanostructures form at the void centres, each nanostructure acting as an attractor for silicon surface species which become mobile at the annealing temperatures (>800°C). This phenomenon is studied here using UHV Scanning Tunneling Microscopy (STM) with which one can produce and observe varying quantities of nanostructures of varying size and, by exploiting site-specific chemical reactions on the silicon surface followed by annealing, more regular arrangements of the structures can be obtained. High Resolution Transmission Electron Microscopy (HRTEM) is used to characterise the composite Si/SiC nanostructures. This formation of regular arrangements of nanostructures, much smaller than features currently obtainable using lithographic techniques, has possible practical applications for the economic production of field emission or optical emission arrays over very large areas of silicon wafers.

## 1. INTRODUCTION

During ultra-high vacuum (UHV) annealing of silicon wafers the native oxide (1-2nm thick) desorbs in a non-uniform manner. At certain points on the surface there is the nucleation of oxide-free areas called "voids" which enlarge radially over the surface, meeting and coalescing with other voids eventually leaving the surface completely oxide-free. This process has been followed using series of secondary electron microscopy (SEM) and atomic force microscopy (AFM) images [1,2] but the resolution available was not sufficient to detect the formation of nanostructures within the voids. The oxide removal process through UHV annealing with the formation of Si/SiC nanostructures can, however, be observed using high resolution UHV scanning tunneling microscopy (STM) [3,4]. The number of nanostructures per unit area is related to the levels of contamination [5] on the original native-oxide covered substrate. This paper describes the formation and structural characterisation of the nanostructures and how the self-organisation phenomena leading to nanostructure formation can be exploited to make various arrangements of these structures on silicon surfaces.

## 2. RESULTS AND DISCUSSION

When the phenomenon of oxide desorption from silicon surfaces through the formation of localised oxide-free voids is studied, using UHV STM, the formation of small structures at the centres of the voids during their radial enlargement becomes quite evident [3,4]. Nucleation of these voids and their radial enlargement with concomitant nanostructure formation can be followed through the sequence of STM images shown in Fig. 1.

This process can be schematised through the series of profiles shown in Fig. 2. The lowest profile is raw experimental STM data.

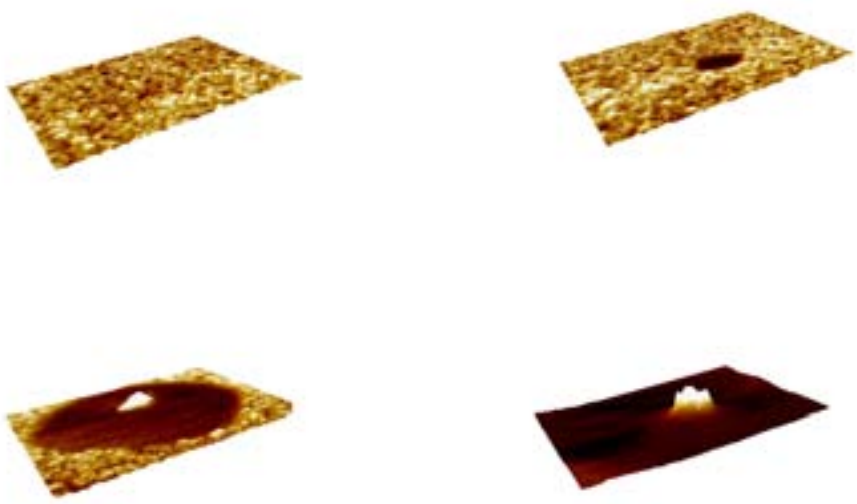

*FIG. 1. Phases in the evolution of native-oxide-covered silicon surfaces during UHV thermal annealing as observed by STM. (a) Oxide covered surface before oxide desorption; (b) Formation of nascent voids; (c) Radial expansion of voids with growth of central columnar structure; (d) Final, completely oxide-free surface showing ~10 nm-high structures.*

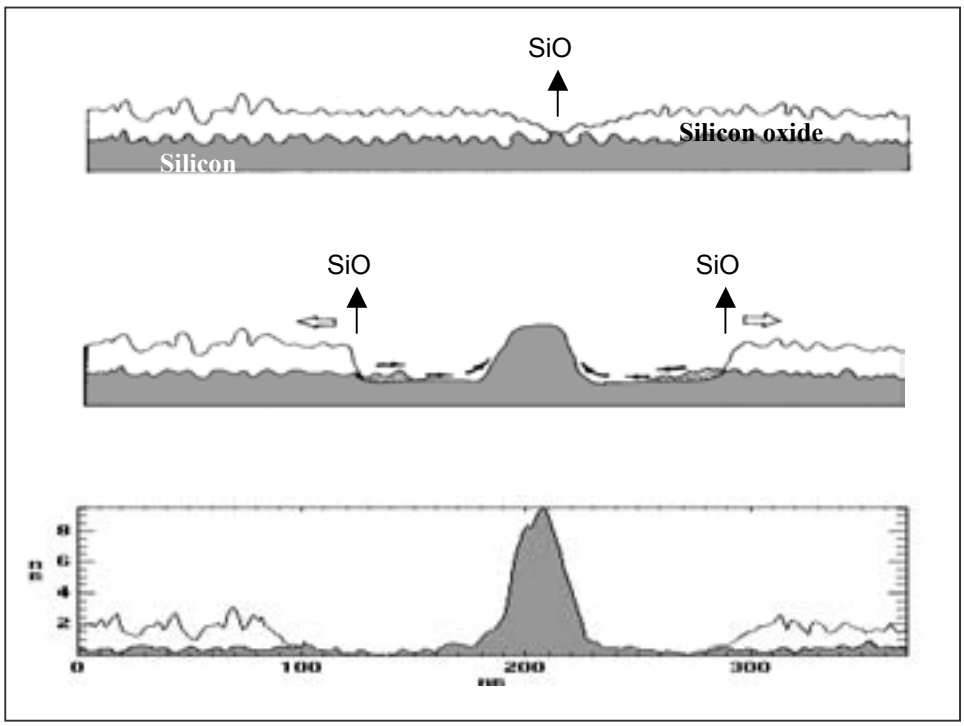


*FIG. 2. Mechanism of nanostructure formation with oxide-void enlargement during UHV annealing of silicon substrate with native oxide. (a) Void nucleation; (b) Radial enlargement of void with nascent central silicon structure; (c) Enlarged void with 9 nm-high primary structure.*

The formation of such nanostructures during UHV annealing of completely oxide-free silicon at the same temperatures is much slower confirming that the oxide desorption process plays an important role in the mobility of surface silicon atoms [6] and thus the construction of these nanostructures.

Gray et al. [7] hypothesized the presence of tiny crystals of silicon carbide on the top of some of these nanostructures deriving from contamination by organic impurities of the original surface concluding that the presence of carbon contamination on the surface was sufficient to create such structures although not essential. This hypothesis was confirmed by results [5] obtained using oxide-covered silicon surfaces with different levels of organic contaminants (see Fig. 3 below).

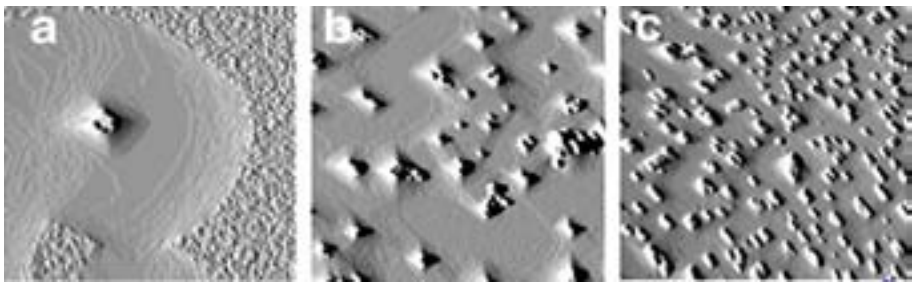


*FIG. 3. STM images showing the effect of organic contamination on nano-island production: (a) Carefully-cleaned sample (400x400nm); (b) Standard clean sample with native oxide (500x500nm); (c) sample "contaminated" with Electronics Grade Methanol before insertion into the UHV system (500x500nm).*

Samples purposely "contaminated" by dipping in Electronics Grade Methanol and drying in nitrogen before introduction into the UHV system (Fig. 3c) show a higher number of islands and easier oxide desorption with respect to standard clean samples with native oxide (Fig. 3b). On the other hand, very clean samples obtained with multi-step cleaning show the development of very few voids, the oxide desorbing from the surface in a more homogeneous manner (Fig. 3a).

To remove any doubt about the presence of silicon carbide nanocrystals "topping" the silicon nanostructures, a sample was prepared and High Resolution Transmission Electron Microscopy (HRTEM) images were obtained from sections through the nanostructures. Figure 4 shows images of a section through the sample (upper image) and through one of the Si/SiC composite nanostructures (lower image).

These images confirm the nature of the SiC nanocrystal forming the apex of the composite nanostructure, through the SiC crystal parameters, and also show that there is a good degree of epitaxy. Another interesting point about these images is the presence of the silicon "shoulders" below the SiC nanocrystal which expose the (311) crystal facet. The predominance of the (311) surface around the nanostructure is in agreement with the theoretical predictions of Oshiyama [8] and may offer the possibility of exploiting site-specific chemical reactions for localised concentrations of molecular species chemically bound to the silicon surface around and immediately adjacent to the nanostructures.

The system of oxide + voids shown above (see Fig. 1c) also provides sites for preferential reactions with chemical species, for example, within the voids or, perhaps, around their perimeters at the $Si/SiO_2$ interface.

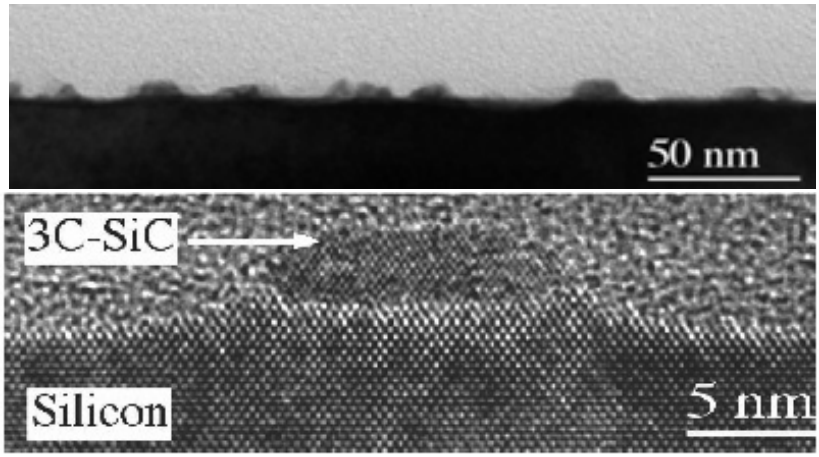


*FIG. 4. HRTEM image (lower image) of Si/SiC composite nanostructure taken from a section (upper image) cut from a silicon sample. Note the epitaxy of the SiC nanocrystal with the underlying silicon lattice.*

In fact, when the naked silicon surface within the void was exposed to certain gases, covalent chemical reactions occurred leading to the creation of nucleation sites for the formation of secondary nanostructures when the UHV annealing is restarted. This second annealing process led to the formation of a series of secondary nanostructures around the original primary one [9] (see Fig. 5).

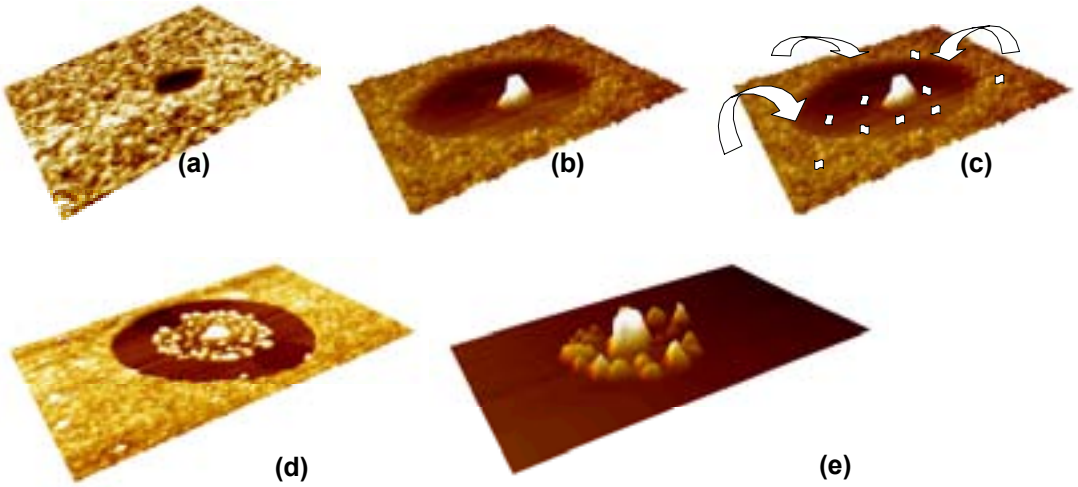


*FIG. 5. Construction of secondary silicon-on-silicon structures following reaction on naked silicon surface within oxide-free void. (a) Oxide loss during UHV thermal annealing begins with void formation; (b) Voids enlarge radially with growth of primary silicon structure which acts as a single attractor for mobile silicon atoms; (c) Process is suspended and gas molecules are adsorbed onto oxide-free area; (d) Heating is resumed. Adsorbed gas molecules become attractors for mobile silicon atoms and secondary structures form around the primary structure; (e) Primary silicon structure surrounded by secondary structures after completion of oxide desorption.*

Site-specific chemical reactions around the perimeter of the voids at the $Si/SiO_2$ interface also occurred by careful choice of the reactant gas. It has been shown that carbon monoxide (CO) does not chemically react with naked silicon surfaces and this was confirmed by our own experiments where even at very high exposures (>100 Langmuirs), carbon monoxide showed no chemical reaction with naked silicon as observed during real-time STM measurements.

It has been observed, however, that although CO does not react with a clean Pt(111) surface at room temperature, when oxygen-containing domains are present on that surface, CO reaction does occur but only along the boundaries between the oxygen-containing (2x2) and the c(4x2) CO domains [10].

In the same way, when our oxide-void-containing surfaces were exposed to CO followed by further UHV annealing, evidence of a site-specific CO reaction (not observed by STM during CO exposure) at the $Si/SiO_2$ interface around the void perimeters was found through the formation of a circular arrangement of nanostructures (see Fig. 6).

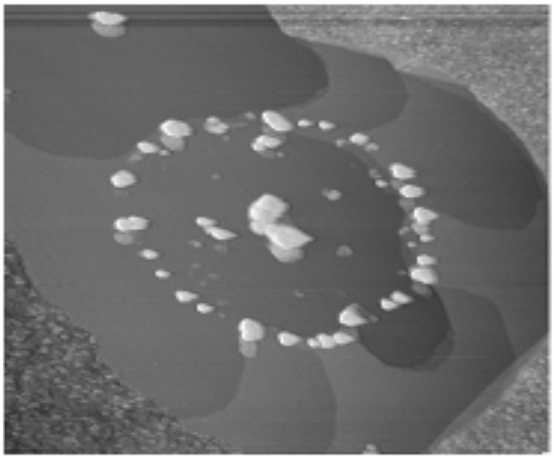

*FIG. 6. Formation of circular arrangement of nanostructures through site-specific chemical reaction of CO along an oxide-free silicon surface void/silicon oxide interface [5].*

Exploitation of this site-specific chemical reaction at the Si/SiO2 interface around the perimeter of the oxide-free void allowed the creation of surface features with dimensions well below those accessible using conventional lithography methods.

This research activity will continue with the exploitation of this site-specific reactivity along the boundaries of oxide patterns produced using conventional lithography and production techniques to obtain much smaller structures along Si/SiO2 edges as schematised in Fig. 7.

The production of similar linear structures which follow the crystal axes of the Si(100) face along atomic steps simply through UHV annealing has been previously demonstrated demonstrated [11]. The addition of small quantities of titanium followed by similar annealing conditions can lead to the formation of nanowires of titanium silicide with similar dimensions and orientations on silicon surfaces [12].

Such structures have also been produced by exploiting surface mobility and step flow on slightly miscut silicon surfaces to concentrate the resulting atomic steps (see, for example, references 13-15). Although this fascinating process of line formation through the concentration of atomic steps leads to nanoscale features in one dimension it produces relatively larger-scale features in the other two.

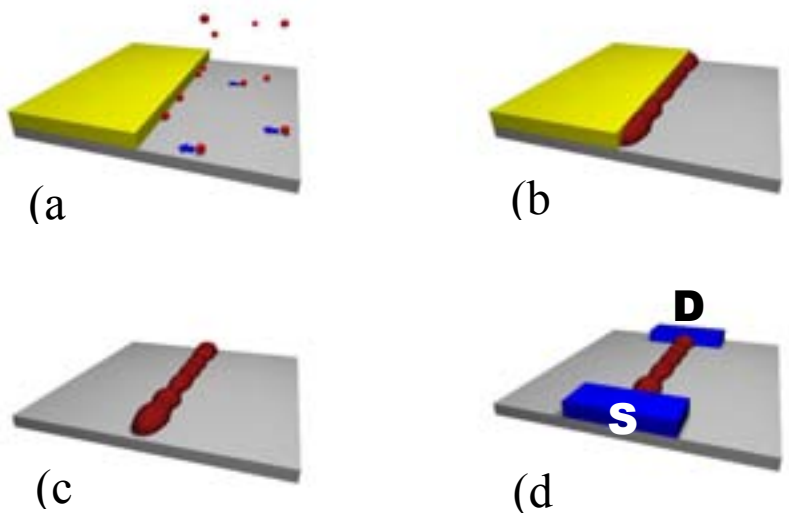


*FIG. 7. Scheme of proposed production of nanostructures by exploiting site-specific chemical reactivity along the edges of oxide patterns. (a) silicon surface (grey) with $SiO_2$ feature (yellow) exposed to reactant molecules; (b) site-specific reaction at interface; (c) remaining nanostructure after oxide removal; (d) electrical connections (blue) to extremities of nanostructure.*

The use of site-specific chemical reactions, on the other hand, offers the possibility of producing nanostructures on silicon surfaces very simply and over large areas even up to the wafer level. Such phenomena also provide a particularly interesting "bridge" between classical "top-down" and more recent "bottom-up" molecular approaches.

## 3. CONCLUSIONS

Composite Si/SiC nanostructures can be directly produced on silicon wafer surfaces in a very simple and economic manner through UHV annealing. A certain degree of control over the numbers of nanostructures per unit area of surface as well as their size is possible through the quantities and type of organic contaminants on the original oxide-covered surface before annealing. Site-specific chemical reactions at Si/SiO2 interfaces allows spatially-designed arrangements of nucleation points for nanostructure formation after subsequent UHV annealing.

Future work exploiting site-specific chemical reactions but using regular oxide patterns, produced an a day-to-day basis in the microelectronics industry, offers the possibility of producing much better-controlled arrangements of nanostructures with dimensions below those accessible with currently used technology.

Such a technique would provide a very economical method of making a large number of devices, such as field emitter or optical emitter arrays, simultaneously over large areas of silicon wafer surfaces.

## REFERENCES


[1] LIEHR, M., LEWIS, J. E., RUBLOFF, G. W., "Kinetics of high-temperature thermal decomposition of $SiO_2$ on Si (100)", J. Vac. Sci. Technol. A 5(4) (1987) 1559-1562.

[2] KOBAYASHI, Y., SUGII, K., "Scanning tunnelling microscope study on mid-desorption stages of native oxide on Si(111)", J. Vac. Sci. Technol. B 9(2) (1991) 748-751.

[3] JONES, D., PALERMO, V., "Production of nanostructures of silicon on silicon by atomic self-organization observed by scanning tunneling microscopy", Appl. Phys. Lett. 80 (2002) 673-675.

[4] PALERMO, V., JONES, D., "Nucleation of nanostructures from surface defects on silicon", Solid State Phenom. 82-84 (2002) 687-692.

[5] PALERMO, V., JONES, D., "Ordered circles of nano-islands on silicon from CO adsorption" Oral presentation at TNT2002, Santiago de Compostela (Spain), September 9-13, 2002.

[6] LICHTENBERGER, H., MUEHLBERGER, M., SCHAEFFLER, F., "Transient-enhanced Si diffusion on native-oxide-covered Si(001) nanostructures during vacuum annealing", Appl. Phys. Lett. 82 (2003) 3650-3652.

[7] GRAY, S. M., JOHANSSON, M. K-J., JOHANSSON, L. S. O., "Nanoscale roughening of Si(001) by oxide desorption in ultrahigh vacuum", J. Vac. Sci. Technol. B 14 (1996).

[8] OSHIYAMA, A., "Structures of steps and appearances of {311} facets on Si(100) surfaces", Phys. Rev. Lett. 74 (1995) 130-133.

[9] PALERMO, V., JONES, D., "Self-organised growth of silicon structures on silicon during oxide desorption", Mat. Sci. Eng. B 88 (2002) 220-224.

[10] WINTTERLIN, J., VÖLKENING, S., JANSSENS, T. V. W., ZAMBELLI, T., ERTL, G., "Atomic and Macroscopic Reaction Rates of a Surface-Catalyzed Reaction", Science 278 (1997) 1931-1934.

[11] PALERMO, V., "Creation of nanometre-scale islands, wires and holes on silicon surfaces for microelectronics", Ph. D Thesis, University of Bologna, 2003.

[12] PALERMO, V., BUCHANAN, M., BEZINGER, A., WOLKOW, R. A., "Lateral diffusion of titanium disilicide as a way to contacting hybrid Si-organic nanostructures", Appl. Phys. Lett. 81 (2002) 3636.

[13] KEEFFE, M. E., UMBACH, C. C., BLAKELY, J. M., J. Phys. Chem. Solids 55 (1994) 965-973.

[14] OGINO, T., HOMMA, Y., KOBAYASHI, Y., HIBINO, H., PRABHAKARAN, K., SUMITOMO, K., OMI, H., SUZUKI, S., YAMASHITA, T., BOTTOMLEY, D. J., LING, F., KANEKO, A., "Design of Si surfaces for self-assembled nano architecture", Surf. Sci. 514 (2002) 1-9.

[15] OMI, H., BOTTOMLEY, D. J., HOMMA, Y., OGINO, T., "Wafer-scale strain engineering on silicon for fabrication of ultimately controlled nanostructures", Phys. Rev. B 67 (2003) 115302.

[16] PALERMO, V., JONES, D., "Formation of nanoclusters on silicon from carbon deposition", Appl. Surf. Sci. 226 (2004) 191–196.

# LIGHT EMITTING DIODES BASED ON ORGANIC MATERIALS

P. DI MARCO, V. FATTORI, M. COCCHI, D. VIRGILI, C. SABATINI
Institute for the Organic Synthesis and Photoreactivity (ISOF-CNR),
Bologna, Italy

**Abstract**

Organic light emitting diodes (OLEDs) have drawn the attention of many researchers for theoretical and for practical reasons. Works on the excited states formation mechanisms in organic thin films and on the chemical and physical factors driving all these processes cover the first aspect. The second is strictly related to the perspective that these devices could revolutionize the market for displays, going to replace liquid crystals in next generation displays for portable devices. They will be thin, brilliant, with wide viewing angle and low power consumption. They will be also assembled into flexible objects like tissues, toys, interior decorations. The drawbacks for an industrial use is still represented by the difficulties to obtain devices operating for more than 10.000 hours, due to the high sensitivity to oxygen and moisture. The recent introduction of monochromatic and colour displays prototypes by some industries (IBM, DuPont, Philips, Kodak, Osram) is the proof of the progress done on this particular aspect in these last years.

## 1. HISTORICAL BACKGROUND

Electroluminescence (EL) from organic light emitting devices (LEDs) is the result of the formation of emitting states via the recombination of charge carriers injected from the electrodes. EL emission was observed for the first time by Bernanose [1] in 1953 on a cellophane film impregnated with a solution of a fluorescent organic compound, then by M. Pope et al. [2] in 1963 on anthracene crystals. Since that time, other organic crystals were considered as good candidates for EL devices [3-5], but the use of thick crystals and the choice of non-suitable contacts required high driving voltages in order to observe light emission. In 1969 J. Dresner [6] realised an electroluminescent device using a polycrystalline film of anthracene with a thickness of some tens of micron, but the voltage applied was as high as 100 V, too high for practical applications. A new interest in organic EL arose in 1987 after the report of Tang and Van Slike [7] concerning a novel multilayer device structure for organic EL, each layer being less than 100 nm thick. The device showed a brightness of more than 1000 cd/m$^2$ at low driving voltages (<10 V). Three years later Burroughes et al. [8] discovered the first electroluminescent polymer, poly(-p-phenylene vinylene) (PPV). Since then a lot of research work has been done and rapid progress has been made. Now the efficiencies of organic EL devices (OLEDs) can be compared with those showed by inorganic LEDs.

## 2. EXCITED STATES FORMATION MECHANISMS

The excited states formation in OLEDs are the result of the following processes [9]: (a) electron and hole injection from the electrodes, (b) their transport through the organic material, (c) their recombination with creation of excited states. In order to obtain EL with high efficiency all these processes must be carefully optimised.

Charge injection can be increased, if the two energy barriers between anode and cathode Fermi levels and HOMO and LUMO levels of the organic material are lowered. High work function materials, as indium tin oxide (ITO), Au, Pt, are generally used as semitransparent hole injecting anodes, Mg or Ca (low work function materials), as electron injecting cathodes. Since each organic material cannot easily fulfil both these requirements, in single layer cells unipolar injection generally occurs. If properly chosen, the use of two different materials in contact with each electrode (double layer cell) can result both in a better alignment of the energetic levels and in better transport properties.

The great majority of the organic materials are unipolar (mostly hole) conductors. Therefore in a single layer cell recombinations take place near one electrode, with high quenching probability of the excited states. This problem is avoided in a double layer cell, where recombination occurs far from the electrodes, near the interface between the two organic layers. Charges recombination passes through coulombically correlated ionic pairs (D+…A-), with the final formation of excited states, when opposite charges are present on neighbouring molecules. The excited state can then undergo a radiationless transition to the ground state, or can deactivate radiatively.

The EL quantum yield φEL is given by the following expression [10]:

$$\varphi EL = Prec \bullet PS \bullet \varphi PL$$

where Prec and PS are respectively the charge carriers recombination and the emitting states formation probabilities and φPL is the luminescence quantum efficiency. Materials with high luminescence efficiency are therefore a requisite for any EL device.

## 3. STRUCTURE AND MATERIALS

OLEDs are generally constituted of one or more organic films having a thickness of the order of some tens of nanometers, placed between two electrodes (at least one should be transparent), as shown in Fig. 1. The colour of the emitted light is typical of the excited molecule. In order to optimise the OLED performances, great effort has been devoted to synthesise new materials. Two parallel ways were taken: one towards polymers, the other towards the synthesis of low molecular weight molecules.

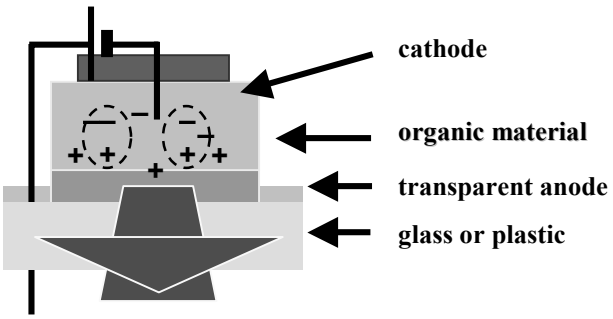


*FIG. 1. Typical configuration of OLED devices.*

### Polymers

The first polymer used was poly(-p-phenylene vinylene) (PPV) [8]. The device was a single layer 70 nm thick PPV film sandwiched between ITO and Al. Yellow green light was detected above a threshold field of $3.10^6$ V/cm. This polymer and his derivatives are at the moment still the best materials for OLEDs. PPV derivatives were synthesised in order to modify its electronic properties (emission spectrum, electron affinity, ionisation potential) and to increase its solubility [11].

Polyfluorenes [12] (PF) (omo and co-polymers) are other classes of conjugated polymers that show good chemical and thermal stability and emit in the blue spectral region. Also polythiophenes [13] derivatives are particularly stable and show good charge transport properties. Finally a huge variety of copolymers made of emitting and transporting units are the object of recent studies [14].

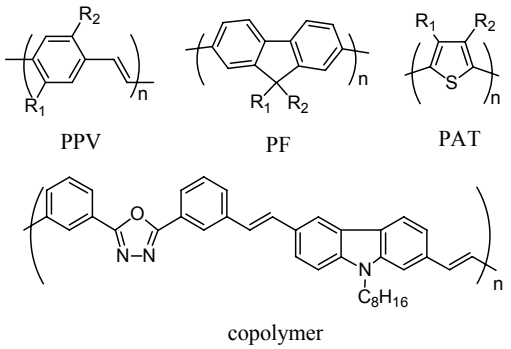


*FIG. 2. Poly(p-phenylene vinylene) (PPV), poly(fluorene) (PF), poly(alkyl-thiophene) (PAT) and copolymer with electrons and holes transporting unities.*

**Low molecular weight molecules**

Also in this area the synthesis of new molecules allowed remarkable advances in devices performances [15]. If polymeric devices (PLED) are generally single layer, those based on small molecules are multilayer devices; each layer devoted to specific functions, as hole or electron injection and transport, and excited states formation with high luminescence efficiency. These devices are therefore constituted of at least two layers, the first one deposited on the anode and with good hole transport properties, the second one in contact with the cathode having good electron transport properties. Charge recombination, followed by emitting states creation, generally occurs in this second layer, which should have also good emitting properties.

**Holes transporting materials (HTM)**

Design and synthesis was focused on good thermal and morphological stability, on thin and uniform film forming capacity, on low ionisation potentials, which favour electron exchange with the anode, on high hole mobility.

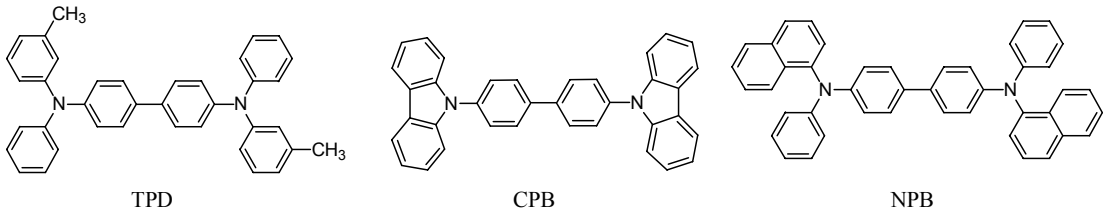


*FIG. 3. Amines with various molecular structures used as holes transporting materials.*

The first molecule used as HTM in OLED was N,N'-diphenyl-N,N'-bis(3-methylphenyl)(1,1'biphenyl)4,4'-diamine (TPD) [7]. A better morphological stability was obtained using the triphenylamine unit in oligomeric molecular structures (MPTAB), or in starburst molecules like MTDATA or TCTA. These structures hinder both film crystallization and morphological instability, slowing down the device degradation.

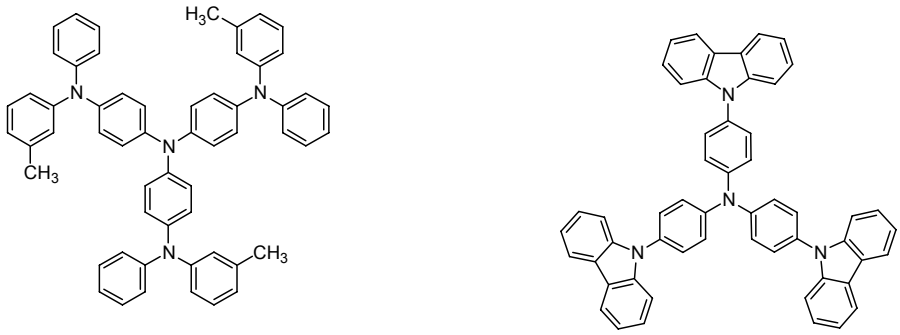


*FIG. 4. Starburst molecules.*

**Electron transporting and emitting materials (ETM and EM)**

$Alq_3$ is still widely used as electron transporting and emitting material, due to synthesis and purification easiness and good thermal stability, allowing deposition by thermal evaporation, with formation of morphologically stable and highly fluorescent films. Numerous derivatives have been synthesized, with the aim of obtaining stronger fluorescence and a blue or red shift of the spectral emission. Other organometallic complexes with interesting electrical and fluorescent properties are Be and Zn chelates (Fig.5).

Besides organometallic complexes, other molecules are good electron transporters and emitters in different spectral regions. Hexathiophene dioxide (T5O2hex) shows a high emission yield in the solid state (37%), being also a good electron transporter. PBD and TAZ are molecules with high electron affinity.

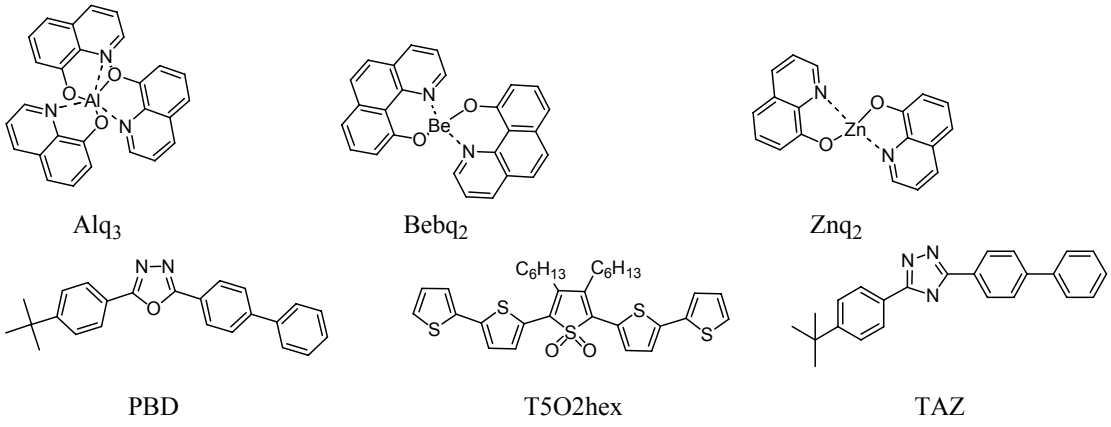


*FIG. 5. Fluorescent molecules and metal complexes used as emitting and electron transporting materials.*

**Emitting dopants**

The need for high stability and good electrical and morphological properties in the solid state limits the use of luminescent compounds. Furthermore, they can be highly luminescent in solution, but poor luminescent in the solid state, due to molecular aggregates formation and luminescence quenching. In order to avoid these problems they can be used as dopants in a matrix. Examples of fluorescent dopants are reported in Fig. 6.

The recent use of phosphorescent dopants [16,17] increased the limit of the EL quantum yield from 25% to 75%. In fact the probability of triplet creation during the recombination process is three times higher than singlet creation. In fluorescent materials, only singlets emit radiatively and therefore any recombination generating triplets is lost for electroluminescence.

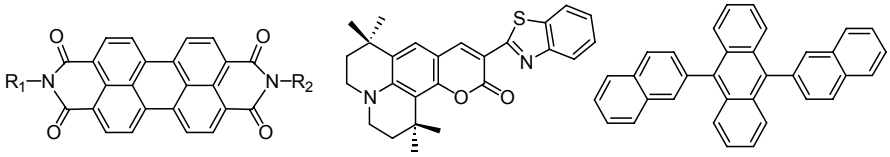


*FIG. 6. Fluorescent dopants with red (perylene derivatives) green (coumarin) and blue (β-DNA) emission.*

The use of phosphorescent materials, in which radiationless transitions to the ground state are avoided, allows the achievement of the highest EL quantum yields. The compounds used (Fig. 7) are heavy atom complexes with strong spin-orbit coupling, or lanthanide complexes that emit from states centred on the metal.

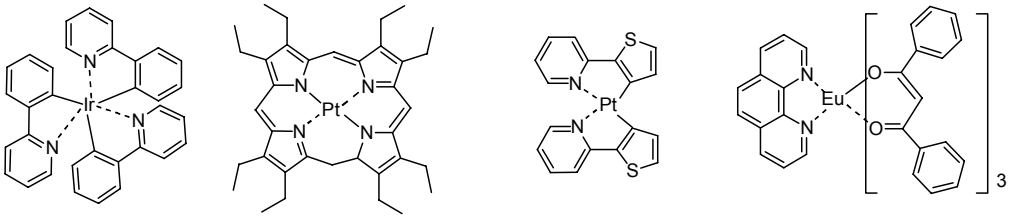


*FIG. 7. Phosphorescent dopants.*

## 4. APPLICATIONS

The materials for OLED applications should combine a high luminescence yield with good electrical and mechanical properties. Colour displays require the coupling of different materials, emitting in the red, blue and green spectral regions. Finally the device lifetime should be acceptable. Many efforts were addressed to the comprehension of the degradation mechanisms operating during the device lifetime. The most important are:

- Poor charge injection from the electrodes: there is a relation between the energetic barrier to charge exchange and instability, in particular at the anode. Barrier decrease can be obtained with treatment of the anode, or by insertion of suitable layers between anode and organic material.
- Poor chemical stability and presence of impurities; oxidation of organics by ITO layer.
- Photo-oxidation of organic materials by self-luminescence.
- Poor morphological stability of the film: crystallisation of the organic material leads to non-uniform films. The use of bigger molecules with three-dimensional geometry can reduce the tendency towards crystallisation.
- Mixing by inter-diffusion between organic layers.
- Poor contact between organic layers.
- Oxidation of organics by oxygen or water**.**

Cathode degradation: cathodes are low work function materials and therefore can be easily damaged in presence of oxygen and water. Device encapsulation using materials impermeable to oxygen and water can reduce this effect. Metal or glass encapsulation can be applied only when using a glass substrate. In case of flexible OLEDs, a thin film type encapsulation is necessary, for instance by means of vacuum sublimation or chemical vapour deposition (CVD).

The advantages of OLEDs, such low voltage operation, light-weight, wide-viewing angle, fast response time, no backlight requirement, low fabrication cost, attract the attention of many industries, with the perspective of a revolution in the display market, going to replace liquid crystals in next generation displays for portable devices. Other OLEDs future applications are foldable displays, lighting, and wearable computers.

As a result of a strong research effort, IBM introduced recently at the SID trade show in Baltimore a prototype colour display with a 50 cm diagonal, and Sony presented a display measuring 60 cm. In 2003 DuPont, Philips, Kodak and OSRAM introduced their own brands for their OLED products. For some time displays made by Pioneer for car stereos and phones have been on the market. Philips now has a shaver with an OLED display and KODAK has a digital camera. OSRAM is targeting the display market for flip phones, car stereos, household appliances and all areas in which self-luminous and extremely flat displays are needed. The solution of some technological problems will probably lead over the next ten years to large-scale production of OLED displays.

## REFERENCES


[1] BERNANOSE A., COMTE, M., VOUAUX, P., "Sur un nouveau mode d'émission lumineuse chez certains composés organiques", J. Chim. Physique 50 (1953) 64-68.

[2] POPE, M., KALLMANN, H.P., MAGNANTE, P., "Electroluminescence in organic crystals", J. Chem. Phys. 38 (1963) 2042-2043.

[3] LOHMANN, F., MEHL, W., "Dark injection and radiative recombination of electrons and holes in naphthalene crystals", J. Chem. Phys. 50 (1969) 500-506.

[4] KALINOWSKI, J., GODLEWSKI, J., "Magnetic field effects on recombination radiation in tetracene crystals", Chem. Phys. Lett. 36 (1975) 345-348.

[5] BASURTO, J.G., BURSHTEIN, Z., "Electroluminescence studies in pyrene single crystals", Mol. Cryst. Liq. Cryst. 31 (1975) 211-219.

[6] DRESNER, J., "Double injection electroluminescence in anthracene", RCA Rev. 30 (1969) 322-334.

[7] TANG, C.W., VAN SLYKE, S.A., "Organic electroluminescent diodes", Appl. Phys. Lett. 51 (1987) 913-915.

[8] BURROUGHES, J.H., BRADLEY, D.D.C., BROWN, A.R., MARKS, R.N., MACKAY, K., FRIEND, R.H., BURNS, P.L., HOLMES, A.B., "Light-emitting-diodes based on conjugated polymers", Nature 347 (1990) 539-541.

[9] KALINOWSKI, J., "Electronic processes in organic electroluminescence" in "Organic electroluminescent devices", Myiata, I., Nalwa, H.S., ed., Gordon and Breach (1997).

[10] KALINOWSKI, J., "Electroluminescence in organics", J. Phys. D: Appl. Phys. 32 (1999) R179-R250.

[11] BRAUN, D., HEEGER, A.J., "Visible light emission from semiconducting polymer diodes", Appl. Phys. Lett. 58 (1991) 1982-1984.

[12] OHMORI, Y., UCHIDA, M., MURO, K., YOSHINO, K., "Blue electroluminescent diodes utilizing poly(alkylfluorene)", Jpn. J. Appl. Phys. 30 (1991) L1941-L1943.

[13] OHMORI, Y., UCHIDA, M., MURO, K., YOSHINO, K., "Visible-light electroluminescent diodes utilizing poly (3-alkylthiophene)", Jpn. J. Appl. Phys. 30 (1991) L1938-1940.

[14] SEGURA, J.L., "The chemistry of electroluminescent organic materials", Acta Polym. 49 (1998) 319-344.

[15] HUNG, L.S., CHEN, C.H., " Recent progress of molecular organic electroluminescent materials and devices", Mat. Sci. Eng. 39 (2002) 143-222.

[16] BALDO, M.A., THOMPSON, M.E., FORREST, S.R., “Phosphorescent materials for application to organic light emitting devices”, Pure Appl. Chem. 71 (1999) 2095-2106.
[17] COCCHI, M., FATTORI, V., VIRGILI, D., SABATINI, C., DI MARCO, P., MAESTRI, M., KALINOWSKI, J., “Highly efficient organic electrophosphorescent light-emitting diodes with a reduced quantum efficiency roll off at large current densities”, Appl. Phys. Lett. 84 (2004) 1-3.

# ORGANIC PHOTOVOLTAICS: TOWARDS A REVOLUTION IN THE SOLAR INDUSTRY

G. RIDOLFI[a], G. CASALBORE-MICELI[a], A. GERI[a], N. CAMAIONI[a], G. POSSAMAI[b], M. MAGGINI[b]

[a] Istituto per la Sintesi Organica e la Fotoreattività (ISOF-CNR), Bologna, Italy
[b] Dipartimento di Chimica Organica, Università di Padova, Padova, Italy

**Abstract**

Organic photovoltaic cells containing blends of regioregular poly (3-alkylthiophenes) and soluble fullerene derivatives are compared. It is shown that the cell performance is substantially affected by the length of the donor side-chain, as it occurs in devices based on pure polythiophenes. We demonstrate that a significant improvement in the power conversion efficiency can be achieved upon a mild thermal treatment of the cells. Furthermore, a molecular structure in which fullerene is covalently linked to a dye, with a strong absorption in the visible region of the spectrum, is proposed as photoactive material.

## 1. INTRODUCTION

Solar energy is potentially one of the most important renewable energy sources. However, the overall cost of the electricity generated from solar power is much higher than that of the electricity from conventional energy sources. The interest in organic solar cells lies in the hope of developing a new photovoltaic technology able to compete commercially with today's expensive silicon photovoltaic cells. The mechanical flexibility and lightness in weight of organic materials, as well as the cheap and well developed technology of thin film plastic deposition are the great benefits of organic photovoltaics. In January 2004, Siemens researchers announced that they have been able to increase the efficiency of organic solar cells to over five per cent[†]. This breakthrough could open the way to the future commercial use of that kind of technology. It is believed that organic solar cells will first be applied in portable solar modules charging mobile telephones, satellite phones or navigation systems.

An encouraging innovation in organic solar cells has been achieved with active layers obtained by mixing an electron donor (D) and an electron acceptor material (A). The interpenetrating D/A network within these so called "bulk heterojunction" solar cells [1] provides both an efficient exciton dissociation at the interface between the donor and acceptor components [2], extended to the entire device volume, and separate pathways to the electrodes for the two types of charge carriers. Conjugated polymers are currently used as electron donor materials, because of both their good hole-transporting properties and light absorption ability, whereas different approaches have been reported for the electron-acceptor material. Polymers [3-4], dyes [5], fullerene [1,6-7] and inorganic nanoparticles [8] have been proposed as acceptor components of blended solar cells.

In this article the performance of D/A solar cells based on blends of regioregular poly (3-alkylthiophenes) (PATs) and soluble fullerene derivatives are compared. While the film forming characteristics and properties of other conjugated polymers, such as poly(p-phenylenevinylene) (PPV) derivatives, with the fullerenes have been thoroughly investigated, devices based on PATs and fullerene have not been studied as extensively. It is therefore interesting to extend the studies to this class of conjugated polymers and to highlight possible structural implications with respect to their photovoltaic behaviour in composite films with functionalised fullerenes. Then we demonstrate how a

[†] The photovoltaics parameters are: power conversion efficiency ($\eta$), percent ratio of maximum electrical power output of the device ($P_{max}$) to incident light power ($P_{in}$), short circuit current density ($J_{sc}$), open circuit voltage ($V_{oc}$) and fill factor (FF) given by the ratio: $FF=P_{max}/V_{oc}\times J_{sc}$.

mild thermal treatment of polythiophene/fullerene solar cells significantly enhances their power conversion efficiency.

Finally we describe the properties and the photovoltaic performances of covalently bonded systems with two moieties with different electron affinity, a fullerene/azothiophene molecule, commonly referred as dyad, and the morphology of the device active layer.

## 2. EXPERIMENTAL

Details regarding the instrumentation used in this work to characterize compounds showed in Fig. 1 have been described elsewhere [9]. The absorption spectra were taken with Perkin-Elmer λ6 and λ9 spectrometers.

### Photovoltaic Devices (PVD)

The device photoactive films were spin coated (2000–3000 rpm) from chloroform solutions (15 g/l) onto Indium Tin Oxide/glass (ITO) substrates previously coated with a layer of polystyrene sulfonic acid doped poly(ethylenedioxythiophene) (PEDOT:PSS). The film thicknesses were routinely determined by using a profilometer Alpha Step 200 (Tencor Instruments). Photovoltaic devices were prepared by subliming an aluminium top electrode in vacuum; the active area of the devices was 3.14 $mm^2$. Except for the cathode deposition, each step of the device fabrication was performed in ambient conditions. The electrical characterization of the devices was executed with a Keithley 2400 source measure unit, under a pressure of $10^{-3}$ torr, in a home made chamber with a heating stage. Junctions were illuminated with a 300 W Xe arc lamp and the light intensity was adjusted by using neutral density filters. The intensity of the incident light was measured with an Oriel thermopile; no correction was made for light reflection. The optical bench was equipped with a water filter to cut off IR radiation. A Pt100 thermoresistor was used for the measurement of the temperature of the cells. The spectral response was obtained dispersing the white light (300 W Xe arc lamp) with an Oriel 77250 monochromator.

### Scanning Force Microscopy (SFM)

Non-contact Scanning Force Microscopy [10] was employed recording both the height signal (output of the feedback signal) and the phase signal (phase lag of the oscillation relative to the driver). While the first type of images provides a topographical map of the surface, the latter is extremely sensitive to structural heterogeneities on the sample surface, being therefore ideal to identify different components in a hybrid film. The SFM Autoprobe CP research (Thermomicroscope) was run in an air environment at room temperature with scan rates of 1–1.5 Hz/line. Images with scan lengths ranging from 60 μm down to 1 μm have been recorded with a resolution of 512 × 512 pixels using the 100 μm scanner and non contact Si ultralevers with a spring constant of $k$ in the range 2.1–17.0 N/m.

## 3. MATERIALS

### Synthesis

While $C_{60}$ was acquired from Bucky USA (98%), all other reagents were employed as purchased from Sigma-Aldrich.

The regioregular PHT and POT were prepared following the procedure reported by McCullough and co-workers [11]. Proton and carbon NMR data were identical to those reported in the literature and the molecular weights were found to be Mn = 18000, Mw = 29500 (PHT) and Mn = 18100, Mw = 33400 (POT). Polydispersity index was 1.44 (PBT) 1.64 (PHT) and 1.85 (POT); in the range of those reported by McCullough and co-workers [12] and Rieke and co-workers [13].

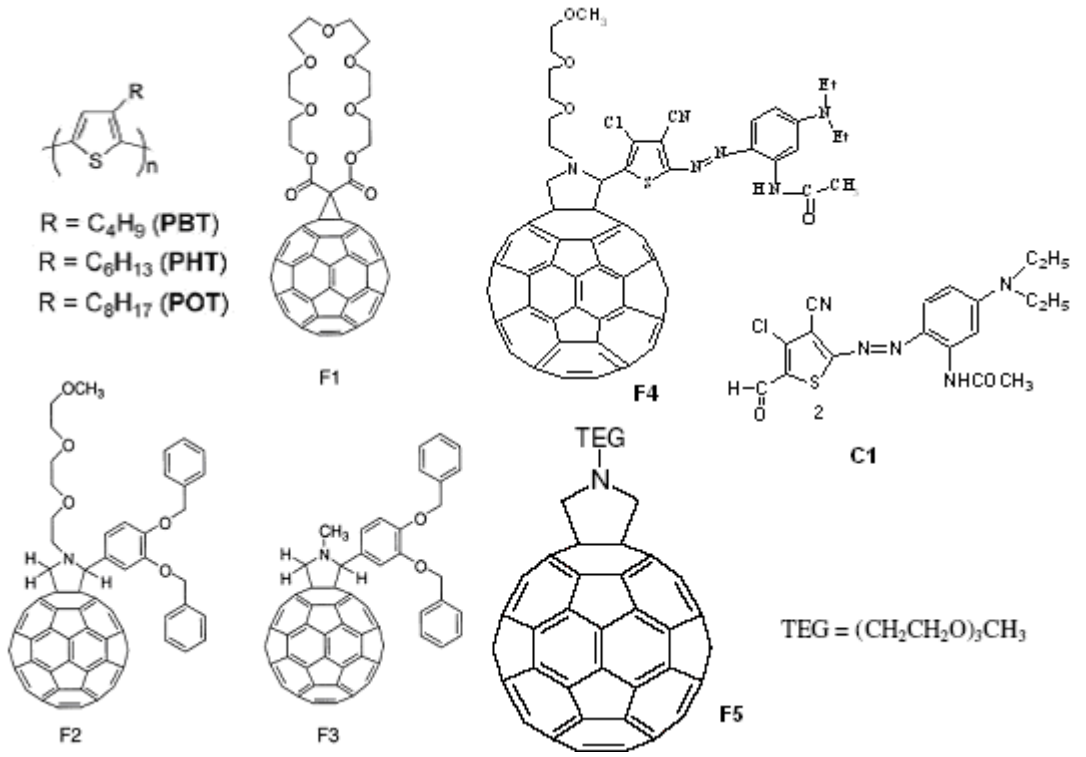


*FIG. 1. Molecular structures.*

Derivative F1 is a methanofullerene that was prepared in 42% isolated yield through a standard cyclopropanation reaction [14] to [60] fullerene using a iodomalonate derivative that formed *in situ* upon treatment of 1,4,7,10,13,16,19-heptaoxacyclodocosane-20,22-dione with iodine and the base azabicyclo[5.4.0]undec-7-ene. Derivatives F2 [15] F3 and F4 are fulleropyrrolidines that were synthesised in 26%, 55% and 42% isolated yields respectively, via the dipolar cycloaddition to [60] fullerene of the azomethine ylide [16] formed when 3,4-dibenzyloxyphenylbenzaldehyde was treated with N-(3,6,9-trioxadecyl)glycine [17] or N-methylglycine, respectively, in refluxing chlorobenzene. All analytical and spectroscopic data were consistent with the structures illustrated in Fig. 1. Azothiophene aldehyde C1 was gifted by BASF-AG (Ludwigshafen, Germany); fulleropyrrolidine F5 was synthesised as described in the literature [17].

## 4. RESULTS AND DISCUSSION

### Fullerene blends

*Fullerene and PATs blends*

The three soluble fullerene derivatives F1–F3 (Fig. 1) were used as acceptors, and regioregular poly(3-butylthiophene) (PBT), poly(3-hexylthiophene) (PHT) and poly(3-octylthiophene) (POT) as donors. Fullerene derivatives F1–F3 have been selected for their good solubility in common organic solvents. This is, among others, a fundamental requisite of the fullerene component for a homogenous mixing with the polymer phase. Regioregular PATs have been used in this investigation because of the their high hole mobility. In the case of regioregular poly(3-hexylthiophene), field effect mobilities of up to 0.1 $cm^2\ V^{-1}\ s^{-1}$ have been reported [18-19]. Very sensitive photosensors based on thin film of D/A composites, in which regioregular PHT has been used as a donor, have been demonstrated, as well as the feasibility of large area image sensing photodiodes [20].

For a comparative study, devices made from a single polymer component were first fabricated. Studies on the comparison of the photoelectrical performance of cells based on regio random PATs,

with different length of the alkyl substituent [21-22] showed that the junction performance increased by shortening the alkyl side chain. It was proposed to be due to a decreased interchain hopping mobility with side chain lengthening, because of the increased interlayer spacing [23]. In the present case one would also expect the polymer with the shortest alkyl chain to display the best photoelectric performance. Contrary to this assumption, the highest values for all photovoltaic parameters were recorded for PHT based cells. The reason for the better performance of PHT relative to PBT could be related to the different optical features shown in their respective absorption spectra. The maximum absorption wavelength of PHT is red shifted by 27 nm if compared to that of PBT. Additionally, no fine structure is visible in the spectrum of PBT. It could be argued that both the mean conjugation length and the extent of the long range order are very different in the two cases, leading to the better performance of PHT based cells. Furthermore, a decreased solubility of PBT could be expected, because of the shorter side chain, leading to a reduction of film forming properties. The overall photovoltaic performance of this type of devices was, as expected, very poor.

The fullerene acceptors F1–F3 were compared by realizing D/A cells with PHT as donor and with a 1:1 PHT/fullerene weight ratio. No substantial differences were observed in the device photovoltaic performances[†] (see Table I).

It is interesting to note that fulleropyrrolidine F3, lacking the oxyethylene solubilizing chain; gives slightly better devices than F1 and F2. Although the difference is not substantial, it indicates that a solubility enhancement of the fullerene partner could not be necessary if a reasonably soluble fullerene derivative is employed. On the other hand, one would expect that a highly functionalized fullerene derivative might disturb the polythiophene main chain conformation, thus altering the conditions for efficient charge transport.

Cells based on F3 were characterised by the highest values of the open circuit voltage ($V_{oc}$), fill factor (FF) and conversion efficiency ($\eta$), although higher short circuit current densities ($J_{sc}$) were observed in the other two cases (Table 1). Upon addition of the fullerene derivatives, a decrease in the $V_{oc}$ was observed. This effect was attributed to the lowering of the quasi Fermi level due to the electron energy loss during electron transfer [24].

TABLE I. PHOTOVOLTAIC PARAMETERS OF PURE PATS AND BLENDS PHT-FN. $J_{SC}$: SHORT CURRENT DENSITY; $V_{OC}$: OPEN CIRCUIT VOLTAGE; FF: FILL FACTOR; $\eta$: POWER CONVERSION EFFICIENCY. WHITE LIGHT IRRADIATION INTENSITY C.A. 20 MWCM$^{-2}$. ROOM TEMPERATURE MEASUREMENTS.

| Active layer | $J_{sc}$ (mA cm$^{-2}$) | $V_{oc}$ (V) | FF | $\eta$ (%) |
|---|---|---|---|---|
| PBT | 0.0140 | 0.76 | 0.22 | 0.010 |
| PHT | 0.0420 | 0.80 | 0.25 | 0.030 |
| POT | 0.0064 | 0.70 | 0.15 | 0.004 |
| PHT/1 (1:1) | 0.98 | 0.50 | 0.20 | 0.37 |
| PHT/2 (1:1) | 0.83 | 0.58 | 0.18 | 0.48 |
| PHT/3 (1:1) | 0.62 | 0.71 | 0.27 | 0.56 |

A substantial amount of the fullerene component is usually present in the active layer of high performance D/A cells. For instance, the weight percentage of the functionalised fullerene PCBM ([6,6]-phenyl-C61-butyric acid methyl ester) in PCBM/MDMO-PPV blends (MDMO-PPV, poly[2-methyl-5-(3',7'- dimethyloctyloxy)-p-phenylenevinylene]) of the 3.3% efficient cells (best published result) was 75%[25].

A study of cell performance as a function of the D/A weight ratio was carried out with the PHT/F3 couple. Blends were prepared with a fullerene content (by weight) ranging from 25% to 75%

[†] The photovoltaics parameters are: power conversion efficiency ($\eta$), percent ratio of maximum electrical power output of the device ($P_{max}$) to incident light power ($P_{in}$), short circuit current density ($J_{sc}$), open circuit voltage ($V_{oc}$) and fill factor (FF) given by the ratio: $FF=P_{max}/V_{oc}\times J_{sc}$.

and the best cell performance was obtained with blends in which the amount of fullerene was in the 33–40% range. The values obtained for the power conversion efficiency are comparable with those already reported [26] for similar cells prepared at ambient conditions and at the same intensity of the irradiation power‡.

Cells made from PHT/F3 and POT/F3 at a 3:2 D/A weight ratio were also compared. The effect of the nature of the donor polymer is not negligible, the power conversion efficiency of a PHT based cell ($\eta = 0.83\%$) being almost twice as much as that made from POT ($\eta = 0.43\%$) (see Table II).

**Improving performances: a mild thermal treatment**

A key factor that influences the power conversion efficiency ($\eta$) of D/A solar cells is the charge carrier mobility, strongly related to the structural order of the donor and the acceptor in the active layer. It is well known that an enhanced degree of crystallinity can be induced in polythiophenes films by a thermal annealing [27] or by treatment with chloroform vapours [28]. Parallel to this, a shift of the maximum absorption towards longer wavelengths is usually observed in the polymer visible spectrum [28]. In this connection, devices made of polythiophene with pendant fullerenes show an increase of the external quantum efficiency (EQE) upon treatment of the active layer with chloroform vapours [29]. An increase of the EQE by a factor of about 1.6 has been also obtained by annealing at 80°C for 1 hour a blend made of regioregular poly(3-hexylthiophene) and a perylene derivative [5].

Regioregular poly(3-hexylthiophene, PHT) and poly(3-octylthiophene, POT) were used as donors and a soluble fulleropyrrolidine (F3, Fig. 1) as acceptor.

Cells with different D/A weight ratios (WR) were prepared and, in all the investigated cases, an impressive and permanent improvement of the device performance was obtained upon heating the devices, under dynamic vacuum, to a temperature as low as 55°C for 30 min in the chamber used for the electrical characterization. The cells were illuminated through the top, semitransparent aluminium electrode (10–11 nm thick), because the frame of the characterization chamber does not allow irradiation through the indium tin oxide (ITO) electrode. A dramatic increase of the short circuit current ($J_{sc}$) was observed by raising the temperature of the cells of just a few degrees above room temperature. As an example, Fig. 2 shows the variation of the principal photovoltaic parameters of a cell based on a PHT/F3 blend (3:2 WR), during the first heating process (at a constant rate of ca. 1°C/min).

The short circuit current, $J_{sc}$, showed a tendency to saturation after a very fast increase between 22 and 40°C and a significant enhancement of both fill factor (FF) and $\eta$ was observed up to about 50–60°C. The open-circuit voltage ($V_{oc}$) began to decrease at about 50°C, after an initial growth. The power conversion efficiency showed a maximum between 50 and 60°C, followed by a decrease at higher temperatures. It was immediately clear that the variations observed during the heating could not be ascribed to a normal temperature dependence of the cell performance. Indeed, upon cooling to room temperature, the photovoltaic parameters were found to be very different with respect to their initial values (see Fig. 2, triangles) and, more interestingly, remained unchanged after an additional thermal cycle from 22°C to 50°C and back again to room temperature (Fig. 2, diamonds).

Apart from $V_{oc}$, all other parameters increased substantially. In particular the thermal treatment produced a three to four fold enhancement of $\eta$ (from 0.65% to about 2.30% for the cell shown in Fig. 2). It is worth mentioning that a similar evolution of the cell parameters was observed for all tested devices, irrespective of the blend components and composition.

The trend of cell parameters shown in Fig. 2 clearly indicates that heating the device at a temperature not higher than 60°C highly enhances the cell performance. Cells, made of POT with different polymer/fullerene WRs, were also tested. Table II summarizes the measured photovoltaic parameters.

‡ Power conversion efficiencies of 0.90% and 0.51% could be calculated for the PCBM–MDMO-PPV cells reported in Ref. [26] under illumination with a 20 $mWcm^{-2}$ monochromatic light.

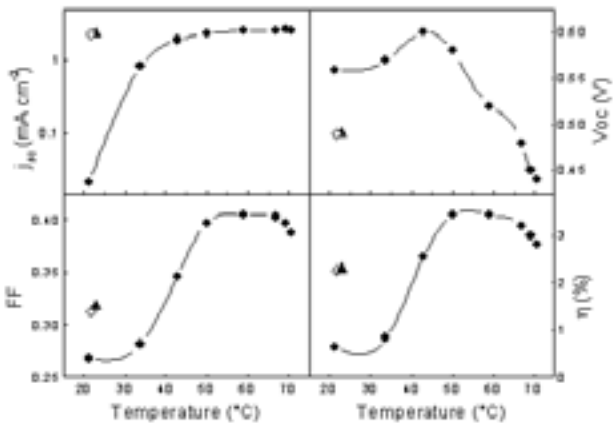


*FIG. 2. Variation of the photovoltaic parameters during the first thermal process of a PHT/**F3** cell (3:2 WR, full circles) and their values after cooling to room temperature (triangles) and after a successive temperature scan between 22 and 50°C (diamond). Linear temperature gradient at ca. 1°C/min. $P_{in}$: 20 mW cm$^{-2}$. Transmittance of the Al layer 14% (at the maximum absorption wavelength of the active layer). The lines are drawn to guide the eye.*

TABLE II. COMPARISON OF THE PHOTOVOLTAIC PARAMETERS OF VARIOUS D/A CELLS MEASURED: (FIRST LINE) AT ROOM TEMPERATURE BEFORE THE DEVICE THERMAL TREATMENT, (SECOND LINE) AT 50°C, (THIRD LINE) AT ROOM TEMPERATURE AFTER THE THERMAL TREATMENT. THE THERMAL TREATMENT WAS DONE AT 55°C FOR 30 MIN. WHITE LIGHT IRRADIATION POWER: CA. 20 MW CM$^{-2}$.

| Active layer | $J_{sc}$ (mA cm$^{-2}$) | $V_{oc}$ (V) | FF | η (%) |
|---|---|---|---|---|
| | 0.54 | 0.67 | 0.25 | 0.43 |
| POT/F3 (3:2) | 2.00 | 0.57 | 0.31 | 1.69 |
| | 1.80 | 0.60 | 0.27 | 1.42 |
| | 0.38 | 0.77 | 0.28 | 0.39 |
| POT/F3 (1:3) | 1.5 | 0.56 | 0.32 | 1.28 |
| | 1.30 | 0.60 | 0.30 | 1.12 |
| | 0.86 | 0.76 | 0.28 | 0.82 |
| PHT/F3 (3:2) | 2.70 | 0.60 | 0.39 | 2.78 |
| | 0.25 | 0.63 | 0.35 | 2.50 |
| | 0.56 | 0.68 | 0.19 | 0.32 |
| PHT/F3 (3:1) | 1.00 | 0.56 | 0.32 | 0.84 |
| | 0.82 | 0.59 | 0.31 | 0.68 |
| | 1.00 | 0.70 | 0.25 | 1.22 |
| PHT/F3 (2:1) | 1.40 | 0.59 | 0.26 | 1.49 |
| | 1.40 | 0.59 | 0.26 | 1.49 |

The maximum η value at room temperature (2.50% after the thermal treatment) was achieved for a PHT/F3 based cell (3:2 WR). A steady decrease of $V_{oc}$ of about 100 mV was observed in all tested cells upon the thermal treatment. The $V_{oc}$ drop off could be accounted by a variation of the oxidation potential of the polymer [30] during the thermal processing, indeed a reduction of about 100 mV in the oxidation potential has been observed in the cyclic voltammogram of a PHT/F3 (3:2) film after heating at 55°C for 30 min.

Parallel to the enhancement of cell performance, a remarkable red shift of the absorption spectrum of the device active layer was observed after the thermal treatment. For example, the

absorption spectra of PHT and of the blend PHT/**F3** (3:2 WR), registered before and after the same thermal treatment (55°C for 30 min), are compared in Fig. 3 (top panel solid and dotted line respectively). The shift of the maximum absorption wavelength is from 495 to 516 nm. Before the thermal treatment, the peak wavelength of the interband transition of PHT was blue shifted, in the blend spectrum, with respect to its position in the spectrum of the pure polymer (not shown). This blue shift, towards shorter and shorter wavelengths by increasing the fullerene concentration, has been already reported in the case of blends between regio random poly(3-alkylthiophenes) and fullerene [31-32].

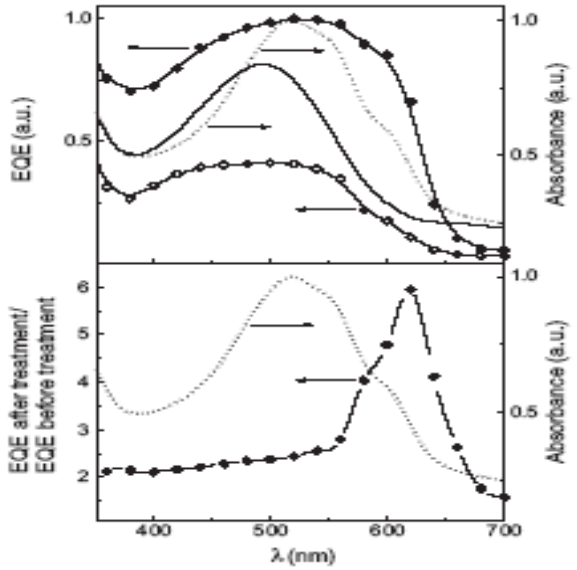


*FIG. 3. Top: Absorption spectra of spin-coated PHT/**F3** (3:2WR) films from a chloroform solution before (solid line) after (dotted line) thermal treatment; external quantum efficiency of a PHT/**F3** (3:2WR) based cell before (open circles) and after (solid circles) the thermal treatment. Bottom: ratio of the external quantum efficiency after treatment to that before the treatment (solid circles); the absorption spectrum of the active layer after the thermal treatment (dotted line) is also shown for a better comparison.*

Similar spectral evolutions were also observed at different polymer/fullerene weight ratios. The shift of the absorption characteristics to longer wavelengths, promoted by the heating process, is likely related to an increase in the crystallinity of the material, with a concomitant appearance of the typical vibronic structure of pure PHT. Although the EQE is enhanced for all wavelengths as results of the thermal treatment (Fig. 3 top panel, circle), its most dramatic change was observed in the spectral region related to the vibronic structure arising as a consequence of the heating process (Fig. 3 bottom panel). Similar results and conclusions have been reported for blends of regio regular poly (3-hexylthiophene) and a perylene derivative [5].

In order to investigate more thoroughly the origin of cell performance enhancement, films made of PHT/F3 (3:2 WR) were thermally treated (55°C for 30 min) before the Al metallization. Indeed a moderate improvement in the power conversion efficiency (of about 20%) with respect to that of the untreated cells was observed with these devices. However, a further thermal treatment to 55°C after the Al deposition was necessary to reach $\eta$ values comparable to those reported in Table II for the annealed devices. An explanation of this behaviour based only on a change in the material organization or geometry turned out inadequate. Parallel to the enhancement of the cell parameters, a dramatic improvement in the dark current/voltage curves was observed in all treated cells. A typical example is shown in Fig. 4.

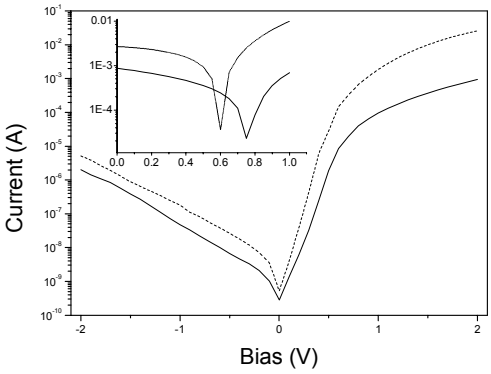


*FIG. 4. Semi-log scale of current/voltage curve in the dark of a PHT/**F3** cell (3:2 WR) before (full line) and after (dotted line) thermal treatment at (55°C, 30 min.). Inset: curves under 20 mWcm$^{-2}$ illumination.*

Higher forward currents (e.g. more than an order of magnitude at +2V) and higher rectification ratios (usually improving by more than one order of magnitude at 2 V) were obtained upon thermal processing. The same behaviour, both of the diode properties in the dark and the photovoltaic performance, was observed when cells with a magnesium cathode were subject to the same thermal treatment. These findings could be explained by a change in the charge transfer properties at the interface close to the contact. This likely translates into better ohmic contact and a reduced device series resistance.

The photovoltaic parameters of a number of cells, after the above described thermal treatment, taken at 50°C are also shown in Table II (third line). The performance at 50–60°C is of utmost importance for solar cells designed for near earth operation. These temperatures are those expected upon exposing the device to solar radiation, without any artificial heating. We obtained the best efficiency at 50°C (2.8% at 20 mW cm$^{-2}$) in the case of a PHT/F3 (3:2 WR) device. An increment of $J_{sc}$, FF and $\eta$ (typically of 15% for the power conversion efficiency) and a decrease of $V_{oc}$ at 50°C with respect to room temperature were found (Table 2). The decrease of $V_{oc}$ was extremely reproducible (about 30 mV in all cases).

A positive temperature dependence of the power conversion efficiency of plastic solar cells has been already demonstrated in the temperature range 18–55°C [33] and it has been attributed to a thermal activation of charge carrier mobility. It has already been demonstrated that the short circuit current is controlled to a considerable extent by the mobility of the majority carriers in the active layer [34]. Furthermore, a decrease of the cell series resistance, mainly due to the high resistivity of the active film, could be expected by increasing the temperature, owing once again to a carrier mobility enhancement. Accordingly, the positive temperature dependence of FF is justified.

**Dyad**

Parallel to the blend approach other promising approach include the use of molecular dyads and triads made of a functionalized fullerene covalently linked to oligomeric conjugated architectures. This would avoid the occurrence of detrimental phenomena, such as phase separation of D and A into discrete domains, being a bottleneck of the charge carrier generation, mobility and collection at the external electrodes [25, 35-36]. The dyad F4 is designed so that its absorption expands in the visible spectral region for a better matching of the solar emission spectrum. The solid-state optical absorption spectra of the different molecular systems are shown in Fig. 5. The spectrum of the F5:C1 film, in a 1:1 molar ratio, results as the precise superimposition of the spectra of the two isolated components.

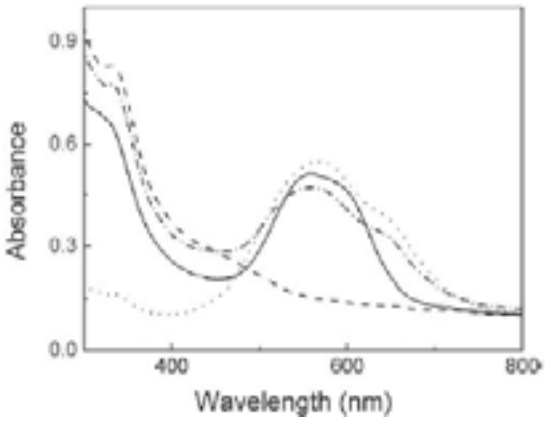


*FIG. 5. Absorption spectra of dyad F4 (solid line), Azothipohene aldehyde (dotted line), fulleropyrrolidine F5 (dashed line), F4:C1 (1:1 molar ratio) dashed-dotted line.*

**Device characterization**

Cells based on dyad F4 were prepared with different thicknesses of the active layer and characterised under white light illumination in the irradiation power ($P_{in}$) of 80 mW $cm^{-2}$ through the ITO contact. The electrical characterization was performed under a pressure of about $5\times10^{-3}$ mbar.

The device performance was found to be dependent on the photoactive layer thickness. The photovoltaic parameters of F4 based cells, extracted from the current voltage curves recorded under 80 mW $cm^{-2}$ white light irradiation (sketched in Fig. 8), are listed in Table III.

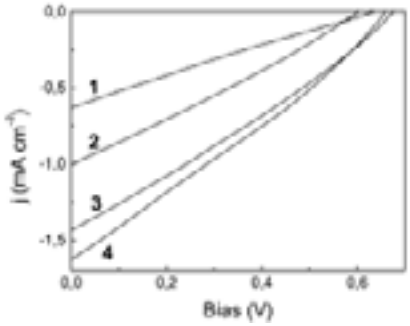


*FIG. 6. Current/voltage curves (fourth quadrant only) of cells made from dyad **F4**. Active layer thickness: 105 nm (1); 85 nm (2); 60 nm (3); 45 nm (4). White light irradiation power: 80 mW $cm^{-2}$*

A progressive increasing of the values of both $\eta$ and $J_{sc}$ was observed by reducing the film thickness from 100 to about 60 nm, but no meaningful improvement of the device performance was obtained with a further reduction of the active layer thickness (to 40–50 nm). In organic solar cells the optimum thickness is determined by the best compromise between a high amount of absorbed photons and a low rate of charge recombination processes. A maximum for the short circuit current, therefore for the cell performance, versus the active layer thickness should be observed, as the active layer thickness leading to the highest device performance depends on both the film optical density and charge carrier mobility of the chosen materials [34].

As the carrier mobility decreases, the optimum active layer thickness shifts towards thinner and thinner values, but less and less photons are absorbed because of the progressive reduction of the film optical density. The data reported in Fig. 8 indicate that for F4 based cells the thinnest layer (40–50 nm) could be a good compromise between the two factors.

TABLE III. CELL PHOTOVOLTAIC PARAMETERS UNDER WHITE-LIGHT IRRADIATION OF 80 MW CM$^{-2}$ INTENSITY. ROOM TEMPERATURE.

| Active layer | Thickness (nm) | $J_{sc}$ (mA cm$^{-2}$) | $V_{oc}$ (V) | FF | η (%) |
|---|---|---|---|---|---|
| F4 | 105 | 0.63 | 0.64 | 0.23 | 0.12 |
| F4 | 85 | 1.00 | 0.60 | 0.28 | 0.21 |
| F4 | 60 | 1.40 | 0.67 | 0.28 | 0.33 |
| F4 | 45 | 1.60 | 0.66 | 0.28 | 0.37 |
| F5:C1 [a] | 90 | 0.05 | 0.50 | 0.28 | 0.008 |

[a] 1:1 molar ratio

Using the thinnest film, a power conversion efficiency of 0.37% was obtained. This represents to our knowledge the highest for cells based on dyads, which convey a fullerene, tethered to an electron rich component. The differences in the open circuit voltage ($V_{oc}$) could be due to shunt effects. A value of 0.28 for the fill factor (FF) was found in all the investigated case, with the exception of the thinnest layer. The reduction of FF at 100 nm can be attributed to the higher series resistance. The values of fill factor obtained with this kind of molecular structures are rather poor. Values not higher than 0.3 have been reported so far, even when a LiF/Al cathode has been used [37].

Cells based on the blend between compounds F5 and C1 were realised in 1:1 molar ratio, in order to compare their performance with those obtained with the dyad F4. The photovoltaic parameters, for an incident irradiation power of about 80 mW cm$^{-2}$, are listed in Table III. The power conversion efficiency is significantly lower than that obtained with the dyad F4. In the blend case a phase segregation could be expected, leading to a loss of device efficiency and accounting for the lack of photoinduced electron transfer reactions pointed out by the photophysical characterisation.

**Morphology characterization**

The morphology of the surface of the device active layers, namely the one of the dyad as well as the one of the blend between **F5** and **C1**, was investigated by means of Scanning Force Microscopy in non-contact mode. Fig. 9A displays the morphology of a dyad film in the 30 μm scale. It reveals a pretty smooth surface, which exhibits some taller grains with a diameter up to some hundreds of nanometers and a height of 15–60 nm (see white arrows).

The surface flatness was characterized by its root mean square roughness

$$R_{rms} = \sqrt{\left[1/\left(N^2 - 1\right)\right]\sum_{mn=1}^{N\times N}\left(h_{mn} - \bar{h}\right)^2}$$

where $N\times N$ is the number of pixels (512×512), $h_{mn}$ is the height value of the pixel $mn$ and is $\bar{h}$ the mean height of the pixel calculated from the $N\times N$ values. The value of $R_{rms}$ of (0.40±0.05) nm was determined in a 1×1 μm image. This provides evidence for a remarkable flatness of the film.

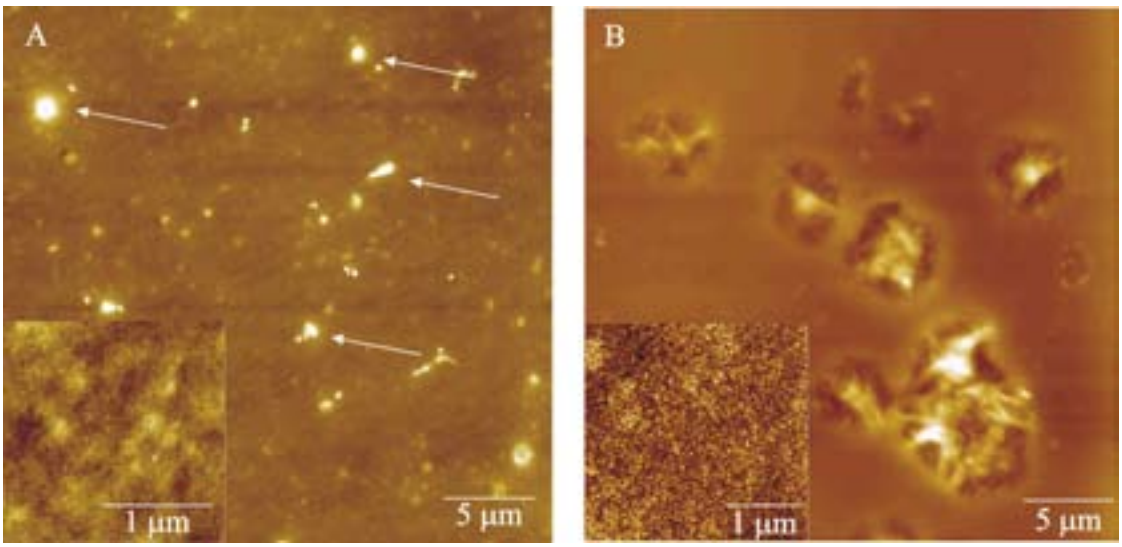


*FIG. 7. Topographical SFM images recorded in non-contact mode. Film: A) dyad **F4**; B) blend **F5:C1**, 1:1 in molar ratio. The films, ca. 100 nm thick, were deposited onto an ITO substrate previously coated with a 80 nm thick of PEDOT:PSS. The insets show zooming in the flat areas of the respective images. Z scale (h): A) h=40 nm; inset A) h=5 nm; B) h=303 nm; inset B) h= 15 nm.*

Differently the blend film conveys different phases, which are segregated in the micrometers scale. The image in Fig. 9B shows aggregates with a lateral size in the 1 to 10 μm scale and thicknesses up to 150 nm which are located randomly on a flat surface. By changing the ratio between the two components in the blend we could give more emphasis to one or the other constituent, permitting an unambiguous assignment of the flat area to the donor molecules and the big aggregates to the fullerenes. This is in good agreement with the well known tendency of fullerenes to form clusters via π-π interactions [38-39] which leads to remarkable variations in the photophysical and photochemical properties [40]. The $R_{rms}$ of the flat areas was also quantified; it amounts to (2.2±0.3) nm as determined in a 1×1 μm image. Comparing the two different roughnesses it appears evident that a better control of the morphology can be gained by a proper covalent functionalization of the fullerenes with a dye moiety.

A role in the different fatnesses of the films could also be played by the different solubility of the components in chloroform. In fact the dyad is much more soluble than the two mixed components, in particular of the dye unit. Since the flat part of the structure in the blend conveys the dye, a bad solubility in chloroform obtained during the film processing could lead to the formation of aggregates at surfaces. This would increase the roughness of the dry films.

## 5. CONCLUSIONS

We have shown how a mild thermal treatment of blended solar cells, made of regioregular poly(3-alkyl)thiophenes and a soluble fulleropyrrolidine, substantially enhances the cell performance: a three four fold increase of the power conversion efficiency has been obtained by just heating the devices to 55°C for 30 min. We speculate that this behaviour is likely due to an increase of the order degree of the photoactive material, leading to better transport properties and to higher charge carrier mobilities. The highest η value, for an incident irradiation power of 20 mW $cm^{-2}$, was 2.5% at room temperature, which grows to 2.8% at 50°C.

A maximum power conversion efficiency of 0.37 % was obtained with a dyad cell. This value is the highest reported for solar cells based on D/A dyads in which the fullerene is directly bonded to a donor component, although it is a still low efficiency, if compared with the one of blended active layers. We believe that the design of new donor-linked fullerenes with a wider absorption spectrum for a better harvesting of the solar light and a more favourable supramolecular organization in the solid state, could lead to notable improvement of the photovoltaic performance.

## REFERENCES


[1] YU, G., GAO, J., HUMMELEN, J.C., WUDL, F., HEEGER, A.J., Science 270 (1995) 1789.
[2] SARICIFTCI N.S., SMILOWITZ, L., HEEGER, A.J., WUDL, F., Science 258 (1992) 1474.
[3] HALLS, J.J.M., WALSH, C.A., GREENHAM, N.C., MARSEGLIA, E.A., FRIEND, R.H., MORATTI, S.C., HOLMES, A.B., Nature 376 (1995) 498.
[4] YU, G., HEEGER, A.J., J. Appl. Phys. 78 (1995) 4510.
[5] DITTMER, J.J., MARSEGLIA, E.A., FRIEND, R.H., Adv. Mater. 12 (2000) 1270.
[6] SHAHEEN, S.E., BRABEC, C.J., SARICIFTCI, N.S., PADINGER, F., FROMHERZ, T., HUMMELEN, J.C., Appl. Phys. Lett. 78 (2001) 9841.
[7] CHEN, L., ROMAN, L.S., JOHANSSON, D.M., SVENSSON, M., ANDERSSON, M.R., JANSSEN, R.A.J., INGANAS, O., "Excitation transfer in polymer photodiodes for enhanced quantum efficiency", Adv. Mater. 12 (2000) 1110.
[8] HUYNH, W.U., DITTMER, J.J., ALIVISATOS, A.P., Science 295 (2002) 2424.
[9] BIANCO A., GASPARRINI, F., MAGGINI, M., MISITI, D., POLESE, A., PRATO, M., SCORRANO, G., TONIOLO, C., VILLANI, C., J. Am. Chem. Soc. 119 (1997) 7550.
[10] SAMORI', P., RABE, J.P., J. Phys. Condens. Matter 14 (2002) 9955.
[11] LOEWE, R. S., KHERSONSKY, S.M., MC CULLOGH, R.D., Adv. Mater. 11, (1999) 250.
[12] MC CULLOGH, R.D., Adv. Mater. 10 (1998) 93.
[13] CHEN, T.-A., WU, X., RIEKE, R. D., J. Am. Chem. Soc. 117 (1995) 233.
[14] NIERENGARTEN, J.-F., HABICKER, T., KESSINGER, R., CADULLO, F., DIEDERICH, F., GRAMLICH, V., GISSELBRECHT, J.-P., BOUDON, C., GROSS, M., Helv. Chim. Acta 80 (1997) 2238.
[15] RUSECKAS, A., THEANDER, M., ANDERSSON, A.M., SVENSSON, M., PRATO, M., INGANAS, O. SUBDSTORM, V., Chem. Phys. Lett. 322 (2000) 136.
[16] PRATO, M., MAGGINI, M., Acc. Chem. Res. 31 (1998) 519.
[17] DA ROS, T., PRATO, M., NOVELLO, F., MAGGINI, M., BANFI, E., J. Org. Chem. 61 (1996) 9070.
[18] BAO, Z., DODABALAPUR A., LOVINGER, A. J., Appl. Phys. Lett. 69 (1996) 4108.
[19] SIRRINGHAUS, H.,TESSLER, N., FRIEND, R.H., Science 280 (1998) 1741.
[20] YU, G., SRDANOV, G., WANG, J., WANG, H., CAO, Y., HEEGER, A.J., Synth. Met. 111-112 (2000) 133.
[21] FANG, Y., CHEN, S.-A., CHU, M. L., Synth. Met. 52 (1992) 261.
[22] CAMAIONI, N., CASALBORE-MICELI, G., CATELLANI, M., LUZZATI, S., PORZIO, W., Mater. Sci. Eng. C 15 (2001) 261.
[23] WINOKUR, M. J., Handbook of Conducting Polymers, ed. T. A. Skotheim, R. L. Elsenbaumer and J. R. Reynolds, Marcel Dekker, New York, 1998, pp. 707–726.
[24] BRABEC, C.J., CRAVINO, A., ZERZA, G., SARICIFTCI, N.S., KIEBOOMS, R., VANDERZANDE, D., HUMMELEN, J.C., J. Phys. Chem. B 105 (2001) 1528.
[25] BRABEC, C.J., SHAHEEN, S.E., WINDER, C., SARICIFTCI, N.S., DENK, P., Appl. Phys. Lett. 80 (2002) 1288.
[26] GEBEYEHU, D., BRABEC, C.J., PADINGER, F., FROMHERZ, T., HUMMELEN J.C., BADT, D., SCHINDLER, H., SARICIFTCI, N.S., Synth. Met. 118 (2001) 1.
[27] Zhao, y., yuan, g.x., roche, p., leclerc, m., Polymer 36 (1995) 2211.
[28] BERGGREN, M., GUSTAFSSON, G., INGANAS, O., ANDERSSON, M.R., WENNERSTROM, O., HJERTBERG, T., Appl. Phys. Lett. 65 (1994) 1489.
[29] ZHANG, F., SVENSSON, M., ANDERSSON, M.R., MAGGINI, M., BUCELLA, S., MENNA, E., INGANAS, O., Adv. Mater. 13 (2001) 1871.
[30] BRABEC, C.J., CRAVINO, A., MEISSNER, D., SARICIFTCI, N.S., FROMHERZ, T., RISPENS, M. T., SANCHES, L., HUMMELEN, J. C., Adv. Funct. Mater., 11 (2001) 374.
[31] MORITA, S., KIYOMATSU, S., ZAKHIDOV, A. A., YOSHINO, K., J. Phys.: Condens. Matter 4 (1992) L103.
[32] SMILOWITZ, L., SARICIFTCI, N.S., WU, R., GETTINGER, C., HEEGER, A. J., WUDL, F., Phys. Rev. B 47 (1993) 13835.
[33] KATZ, E.A., FAIMAN, D., TULADHAR, S.M., KROON, J.M., WIENK, M.M., FROMHERZ, T., PADINGER, F., BRABEC, C.J., SARICIFTCI, N.S.," Temperature dependence for the

photovoltaic device parameters of polymer-fullerene solar cells under operating conditions", J. Appl. Phys. 90 (2001) 5343.
[34] BRABEC, C.J., SHAHEEN, S.E., FROMHERZ, T., PADINGER, F., HUMMELEN J.C., DHANABALAN, A., JANSSEN, R.A.J., SARICIFTCI, N. S., Synth. Met. 121 (2001) 1517.
[35] SHAHEEN, S.E., BRABEC, C.J., SARICIFTCI, N.S., PADINGER, F., FROMHERZ, T., HUMMELEN J. C., Appl. Phys. Lett. 78 (2001) 9841.
[36] ROMAN, L.S., ANDERSSON, M.R., YOHANNES, T., INGANAS, O., Adv. Mater. 9, (1997) 1164.
[37] GULDI, D. M., LUO, C., SWARTZ, A., GOMEZ, R., SEGURA, J.L., MARTIN, N., BRABEC, C.J., SARICIFTCI, N.S., J. Org. Chem. 67 (2002) 1141.
[38] SUN, Y.P., BUNKER, C., Nature 365 (1993) 398.
[39] ALARGOVA, R., DEGUCHI, S., TSUJII, K., J. Am. Chem. Soc., 123 (2001) 10460.
[40] GULDI, D.M., PRATO, M., Acc. Chem. Res. 33 (2000) 695.

# POLYMERIC FUNCTIONAL NANOSTRUCTURES FOR IN VIVO DELIVERY OF BIOLOGICALLY ACTIVE PROTEINS

L. TONDELLI[a], M. BALLESTRI[a], L. MAGNANI[a], K. SPARNACCI[b], M. LAUS[b]
[a] Istituto per la Sintesi Organica e la Fotoreattivita (ISOF-CNR),
Bologna
[b] Departimento di Scienze e Tecnologie Avanzate,
Università degli Studi del Piemonte Orientale,
Alessandria

Italy

**Abstract**

Poly(methyl methacrylate) core-shell particles in the submicron scale range were prepared by dispersion polymerization through an appropriate selection of the experimental parameters. Due to the versatility of this reaction, the macromolecular design can be directed towards the preparation of nano/microspheres with extensively hydrophilic and protein-friendly surfaces with low non-specific interactions. If the steric stabilizer is soluble in physiologic medium, the formation of a core shell structure, constituted by a soft outer shell, made up of long soluble arms able to fix the protein, anchored to an inner hard insoluble core can be envisaged. In the presence of commercial polymeric stabilizers Eudragit L100-55 and Eudragit E100, acid and basic microspheres can be obtained, able to interact with biologically active proteins.

## 1. OBJECTIVE OF THE RESEARCH

Due to the importance of bioactive peptides and proteins for pharmaceutical purpose, there is a growing interest for suitable delivery systems, able to increase their bioavailability and to target them to the desired location. Some of the most studied delivery systems involve encapsulation or entrapment of drugs into biocompatible polymeric devices, but some concerns arise in the case of easily degradable proteins.

Therefore our objective focuses on the design, preparation and physico-chemical properties of polymeric core-shell nano/microspheres able to reversibly adsorb proteins on the surface, without affecting their biological activity.

Colloidal carrier systems are of special importance in drug targeting because they demonstrated to be able to direct the drug to the target tissue and improve the drug propensity to cross the biological barriers, including membranes [1,2]. In addition, an active protection of the drug against enzyme degradation was demonstrated [3-5] and this effect is very important for bioactive molecules and vaccines based on peptides, proteins, oligonucleotides and DNA, which are easily degraded in vivo.

Nanoparticles are colloidal systems ranging from 10 up to 1000 nm in size. The nanoparticle size is a key parameter for many reasons. In fact, the blood capillaries can be as small as 3–4 μm, and consequently only smaller particles should be able to transverse the capillaries reaching all tissues6. In addition, it was demonstrated that the incidence of irritant reactions at the injection site decreases as the particle size decrease [7]. Consequently, it is essential to control the particle size and the particle size distribution.

In drug delivery systems consisting of core-shell nanospheres, the drug can be encapsulated or adsorbed onto the nanosphere surface. Specially in the latter case, the structural design and the requirements of the shell are of outmost importance according to the distinct roles played by the shell with respect to various aspects of the delivery. The shell should be able to interact with the drug via non specific interactions or through specific functional groups. In addition, it must assure chemical and colloidal stability of the particles against adverse external conditions through electrostatic or steric

stabilization mechanisms or by a combination of both. Finally, as the shell, including the drug eventually adsorbed, is in immediate contact with the biological medium, its structure directs the nanoparticle-drug complex biodistribution [8,9]. Consequently, it is important to control the chemical nature of the particle surface.

Core-shell nanoparticles can be obtained by dispersion polymerization. This technique [10,11] is based on a very peculiar particle forming process which involves the polymerization of a monomer dissolved in an organic diluent which is a poor solvent for the resulting polymer. Once initiated the polymerization reaction, the growth of the macromolecular chains (initially oligomers) happens in presence of a polymeric stabilizer which can be a graft copolymer or its precursor. When sufficiently long oligomer chains has been formed, nucleation takes place and the resulting particles continue to grow being sterically stabilized by the graft copolymer. By appropriately choosing of the stabilizer it is possible to prepare a great variety of core-shell particles. In addition, monodisperse particle systems are often obtained, depending on the parameters of reaction and the concentration of employed reagents.

The aim of this study is to describe the properties of poly(methyl methacrylate) core-shell particles12,13 in the submicron scale range. The steric stabilizer employed in the present study are two commercial statistical copolymer (Eudragit L100-55 and Eudragit E 100) with the following structures (Fig. 1&2):

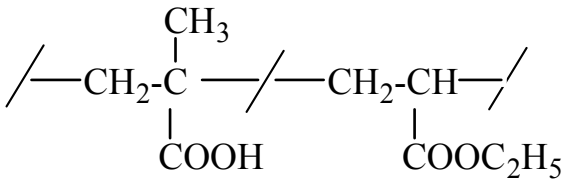


*FIG. 1. Eudragit L110-55*

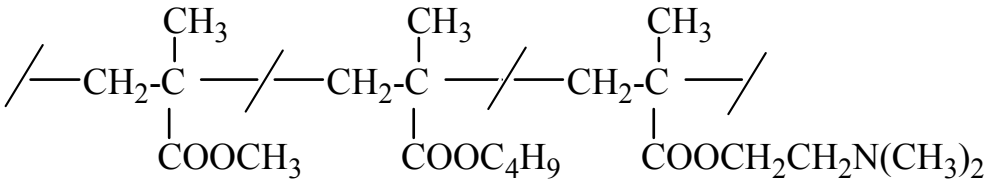


*FIG. 2. Eudragit E100*

As these Eudragit copolymers are water soluble, depending on the pH medium, the formation of nanoparticles with a tentacle structure can be envisaged. The hydrophilic arms constitute the outer layer and the presence of carboxylic or amino groups permits its specific interaction with the proteins.

## 2. MATERIALS AND METHODS

Core-shell nanospheres were prepared as described elsewhere [14–15]. Particle size and size distribution were measured using a JEOL JEM 100CX scanning electron microscope (SEM) operating at an accelerating voltage of 20–30 kV. The samples were sputter coated under vacuum with a thin layer (10–30 Å) of gold. The magnification was given by the scale on each micrograph. The SEM photographs were digitalized and elaborated by the Scion Image processing program. From 150 to 200 individual microsphere diameters were measured for each sample. Photon Correlation Spectroscopy

(PCS) measurements were run in water (hplc grade) on a Malvern Zetasizer 3000 HS instrument, at a scattering angle of 90°C and at 25°C. Each nanosphere preparation was analyzed in triplicate with 10 readings per sample.

The amount of Eudragit L 100-55 linked to the microsphere surface was determined by back titration of the excess NaOH after complete reaction of the acid groups and microsphere removal by centrifugation. Similarly, the amount of Eudragit E100 was determined by back titration of exceeding HCl. ζ–potential measurements were carried out at 25°C on a Malvern Zetasizer 3000 HS instrument, after dilution of nanospheres in water. All measurements were run in triplicate.

The adsorption behaviour of Bovine Serum Albumine and Trypsin as model proteins on the microsphere samples was investigated. For this purpose, 5.0 mg of microspheres were incubated in 1.0 ml of a 20 mM sodium phosphate buffer at pH 7.4 in the presence of different protein concentrations (from 10 to 300 μg/ml) for 2 h at room temperature. Then, the microspheres were collected by centrifugation at 15000 g/min for 10 min and the amount of the residual protein in the supernatant was estimated using the BCA assay. The amount of adsorbed protein was then calculated as the difference between the feed and the residual protein.

## 3. RESULTS AND DISCUSSION

Under the appropriate reaction conditions, the dispersion polymerization of methylmethacrylate in the presence of commercial copolymers, namely Eudragit L100-55 and Eudragit E100, gives rise to core-shell nanospheres which are sterically stabilized by the presence of the graft copolymer at the surface.

All the prepared samples were physico-chemical characterized by means Scanning Electron Microscopy analysis (SEM), Photon Correlation Spectroscopy (PCS), Electrophoretic Mobility (ζ-potential) and acid-base titration of surface charged groups [14,15]. Due to their monodisperse diameter size, two sample of each type of microspheres were chosen for protein immobilization experiments: sample H1D, bearing carboxylic groups on the surface, and sample HE1D, bearing amino groups on the surface. The representative SEM micrographs of sample H1D is shown in Figure 3.

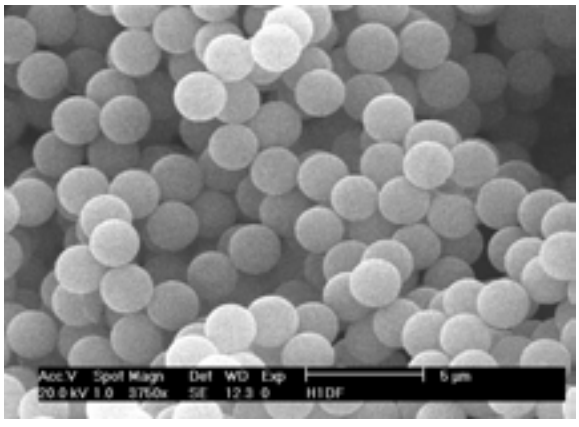


*FIG. 3. SEM micrograph of acid core-shell microsphere (sample H1D)*

In principle, according to their isoelectric points, acid and basic proteins can be preferentially adsorbed on basic and acid microspheres respectively, by means of reversible electrostatic interaction with the functional groups present in the outer shell. Therefore, the microsphere ability to bind model proteins, BSA (pI≅5) and Trypsin (pI≅9), was measured in the presence of 20 mM sodium phosphate buffer at physiological pH (7.4) by means of the BCA colorimetric method.

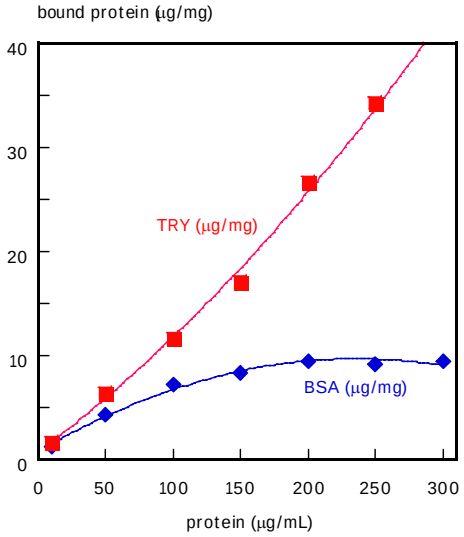


*FIG. 4. Amount of bound protein onto carboxylic H1D microsphere sample.*

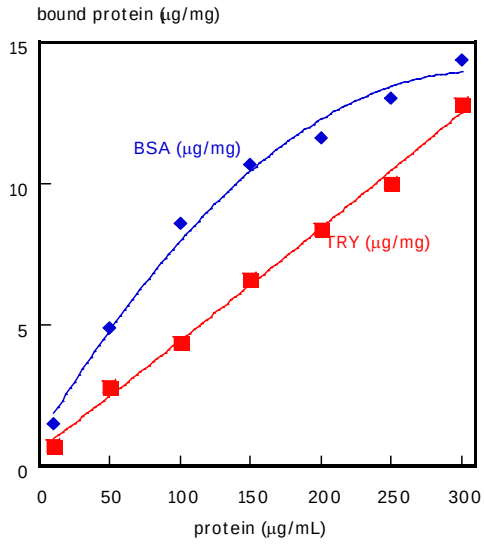


*FIG. 5. Amount of bound protein onto amino HE1D microsphere sample.*

Figure 4 and 5 report the adsorption trend of BSA and Trypsin on carboxylic and amino microsphere samples respectively, at physiological pH. The amount of adsorbed protein increases linearly as the protein solution concentration increases, in agreement with their high compatibility towards the microsphere surface. In particular, BSA (acid protein) is preferentially adsorbed onto basic microsphere surface, whereas Trypsin (basic protein) onto acid microsphere surface.

With respect to the initial amount of protein present in the suspension, the adsorption efficiency reaches the maximum values (60–80%) in the case of trypsin adsorption onto acid microsphere sample H1D. These microspheres are also able to immobilize the highest amounts of protein (up to 42 µg/mg) at physiological pH, without reaching surface saturation conditions, at least under the described experimental conditions.

As the size and nature of sample H1D are reasonably compliant with in vivo applications as drug delivery system, carboxylic core-shell microspheres represent promising basic protein carriers

[16]. To this purpose, entrapment of peptides and proteins in biodegradable microspheres has been widely investigated, but this method doesn't seem suitable for fragile proteins, which can be easily degraded and/or denaturated following release from the polymeric matrix [17]. On the contrary, there is evidence to suggest that lifling the molecule off the surface by "attaching" it through a tether might protect its structure in the folded state, which is usually required for biological activity [18].

## REFERENCES


[1] KREUTER, J., "Nanoparticles" in: Colloidal Drug Delivery Systems, J. Kreuter, Ed., Marcel Dekker, New York 1994, p. 219.
[2] KAWAGUCHI, H., Prog. Polym. Sci. 2000, 25, 1170.
[3] FRITZ, H., MAIER, M., BAYER, E.J., Colloid Interf. Sci. 1997, 195, 272.
[4] TONDELLI, L., RICCA, A., CITRO, G., LELLI, M., LAUS, M., Nucleic Acid Research, 1998, 29, 5425.
[5] FATTAL, E., VAUTHIER, C., AYNIE, I., NAKADA, Y., LAMBERT, G., MALVY, C., COUVREUR, P., J. Control. Release 1998, 53, 137.
[6] Pouton, C.W., Seymour, L.W., Adv. Drug Deliv. Rev. 2001, 46, 187.
[7] Little, K., J. Parkhouse, Lancet 1962, 2, 857.
[8] PERACCHIA, M.T., VAUTHIER, V., PUISIEUX, F., COUVREUR, P., J. Biomed. Mat. Res. 1997, 34, 317.
[9] TROSTER, D., WALLIS, K.H., MULLER, R.H., KREUTER, J., J. Control. Release 1992, 20, 247.
[10] BARRET, K.E., "Dispersion Polymerization in Organic Media", Wiley & Sons, London 1975.
[11] CAWSE, J.L., "Dispersion Polymerization" in: Emulsion Polymerization and Emulsion Polymers, P.A. LOVELL, M.S. EL-AASSER, Eds., J. Wiley & Sons, New York 1997, p.743.
[12] KOBAYASHI, S., UYAMA, H., MATSUMOTO, Y., YAMAMOTO, I., MAKROMOL. Chem. 1992, 193, 2355.
[13] SHEN, S., SUDOL, E.D., EL-AASSER, M.S., J. Polym. Sci., Polym. Chem. 1993, 31, 1393.
[14] SPARNACCI, K., LAUS, M., TONDELLI, L., MAGNANI, L., BERNARDI, C., Macromol.Chem Phys. 2002, 203, 1364.
[15] SPARNACCI, K., LAUS, M., TONDELLI, L., BERNARDI, C., MAGNANI, L., CORTICELLI, F., MARCHISIO, M., ENSOLI, B., CASTALDELLO, A., CAPUTO, A., Biomacromolecules, 2004, under revision
[16] CAPUTO, A., BROCCA-COFANO, E., CASTALDELLO, A., DE MICHELE, R., ALTAVILLA, G., MARCHISIO, M., GAVIOLI, R., ROLEN, U., CHIARANTINI, L., CERASI, A., DOMINICI, S., MAGNANI, M., SPARNACCI, K., LAUS, M., TONDELLI, L., ENSOLI, B., Vaccine, 2004, in press
[17] O'HAGAN, D.T., Adv. Drug Delivery Rev. 1998, 34, 305.
[18] KAZZAZ, J., NEIDLEMAN, J., SINGH, M., OTT, G., O'HAGAN, D.T., J. Control. Release 2000, 67, 347.

# EXPLORING THE NANOSCALE WORLD WITH SCANNING PROBE MICROSCOPIES

P. SAMORÌ
Istituto per la Sintesi Organica e la Fotoreattività - Consiglio Nazionale delle Ricerche, Bologna, Italy

**Abstract**

Unravelling physico-chemical properties of molecule-based architectures on the nanoscale is one of the most intriguing goals of materials science. Making use of Scanning Probe Microscopies (SPMs) it is possible not only to produce beautiful pictures of surfaces, but, most interestingly, also to gain insight into a variety of physical and chemical properties of molecule-based structures occurring in scales ranging from the hundreds of micrometers down to the sub-nanometer regime. Moreover SPM allow to manipulate objects with a nanoscale precision, thereby making it possible to nanopattern a surface or to cast light onto the nanomechanics of complex assemblies. Hence, they can provide crucial information for the optimisation of functional nanomaterials. The presentation will highlight Scanning Probe Microscopies nanoscale investigations and manipulations of rod-like and disk-like supramolecular and macromolecular structures on flat solid surfaces. These obtained results will be of help for the fabrication of nanodevices operating at surfaces.

## 1. OBJECTIVE OF THE RESEARCH

The research activity in our laboratory aims at the exploitation of SPM bestow information onto the physico-chemical properties of nanoscale complex supramolecular architectures and at their use to fabricate prototypes of nanoscale organic electronics devices operating at surfaces.

In the last two decades there has been an increasing genuine curiosity in the 'nanoworld'. The science and technology on such a small realm, namely nanoscale science and nanotechnology, are multi-disciplinary burgeoning fields involving functional systems whose structures and components, due to their small size, hold extraordinary properties. The processing and the manipulation of complex architectures on the nanoscale as well as the fabrication of devices with new sustainable methodologies are crucial issues towards a technology based on intelligent materials. The scientific community has been trying to approach the nanoscale by exploring at surfaces the structures of organic materials, probing their chemical and physical properties on the molecular scale, and comparing the properties of a single molecule with those of an ensemble or Avogadro number of molecules. This offered tools to achieve a better control over the properties of molecule based nanomaterials, thus paving the route towards the implementation and optimization of nanoscale devices operating at a surface.

Organic molecules are excellent candidates for the realization of electronic and photonic devices. In fact the level of sophistication reached by modern chemical synthesis, in particular after the advent of supramolecular chemistry, offers easy access to a large variety of molecular building blocks bearing well defined sizes, shapes and chemical properties which can be used to tailor and produce a new generation of functional nanomaterials. Understanding and controlling the nanoscale physico-chemical properties of supramolecular architectures self-assembled at surfaces is a fundamental step for tuning the properties of the material, with a great potential in molecular information storage, catalysis and electronics.

## 2. EXPERIMENTAL RESULTS

In this frame, Scanning Probe Microscopies (SPMs) have played a paramount role. In particular Scanning Force Microscopy and Scanning Tunnelling Microscopies being very versatile tools, they have been exploited at various interfaces, in order to visualize structures as well as dynamic processes, such as chemical reaction, in real time [1, 2].

Making use of these techniques it has been possible to approach the nanoworld in various ways, going far beyond the pure imaging of a surface: manipulating single molecules at room temperature [3] opening new avenues towards the study of the conformational and nanomechanical properties of individual molecules, [2] visualizing Ostwald ripening in polycrystalline structures at the solid–liquid interface [4] stimulating photochemical reactions with light and following the reaction in real-time at interfaces, [5, 6] probing the electronic properties of single molecules by means of scanning tunneling spectroscopy (STS) [7, 8, 9] and inducing with the scanning tunneling microscope (STM) tip the electroluminescence of a conjugated thin film [10] are just a few examples.

Here some of the recent results obtained by using Scanning Force Microscopy and Scanning Tunnelling Microscopy to investigate self-assembled π-conjugated (macro) molecular architectures at surfaces and interfaces are presented. Particular attention is paid to the analysis of structures, dynamic processes and reactions occurring at surfaces as well as to the nanomanipulation of ordered interfaces with a molecular scale precision.

In the frame of organic electronics, the self-assembly of π-conjugated polymers on insulating solid substrates represents a strategy for building up well defined and stable nanostructures with tailored made chemical functionalities and physical properties, which might be used as active components in the fabrication of nanoelectronic devices. Since transport phenomenon in molecular materials depends on the interplay between electronic structure and order in the molecular assembly, it is important to achieve a full control over the structural order in 2D and 3D polymolecular architectures by making use of intramolecular, intermolecular and interfacial forces.

Scanning Tunnelling Microscopy (STM) investigations at the interface between an almost saturated solution of an alkylated *para*-phenyleneethynylene trimer and a solid substrate of highly oriented pyrolitic graphite (HOPG) enabled us to characterize both the structure and the dynamics of these molecules at surfaces. These oligomers pack in an epitaxial 2D polycrystalline structure (Figure 1a). To a crude approximation the contrast in STM current imaging is determined by the chemical nature of the adsorbate. More precisely, it is ruled by a resonant tunnelling occurring between the Fermi level of the substrate and the frontier orbitals of the moieties composing the adsorbed layer [11]. According to this, in the present case the brighter rods in the images in Figure 1a can be ascribed to the conjugated rod-like backbones of the molecules while the darker part of the images can be assigned to the aliphatic side groups. The molecular dynamics at the interface in a 22 minutes time scale exhibits Ostwald ripening, which is driven by a minimization of the line energies [12]. A high resolution imaging enabled us to bestow information onto the kinetics of this process and to draw some conclusions on thermodynamic and kinetic contributions to this grain coarsening.

The corresponding polydisperse system was visualized with a sub-molecular resolution. These macromolecules exhibit a nematic-like molecular order at the interface with HOPG (Fig 1b). Single rods are oriented along preferential directions according to the three-fold symmetry of the substrate. The true molecular lengths for several hundreds of molecules were determined from STM images. The key result is a macromolecular fractionation occurring at the interface between the organic solution and the solid substrate. The average length of the physisorbed rods is shifted to higher rod lengths with respect to the peak of the distribution of the molecular weights according to the Schulz-Zimm distribution. Comparing this result with the one obtained with Monte Carlo simulations of the macromolecular physisorption of rigid rods on HOPG, it was possible to gain deeper insight into this phenomenon and to discern the enthalpic and entropic contribution leading to this filtering process [14].

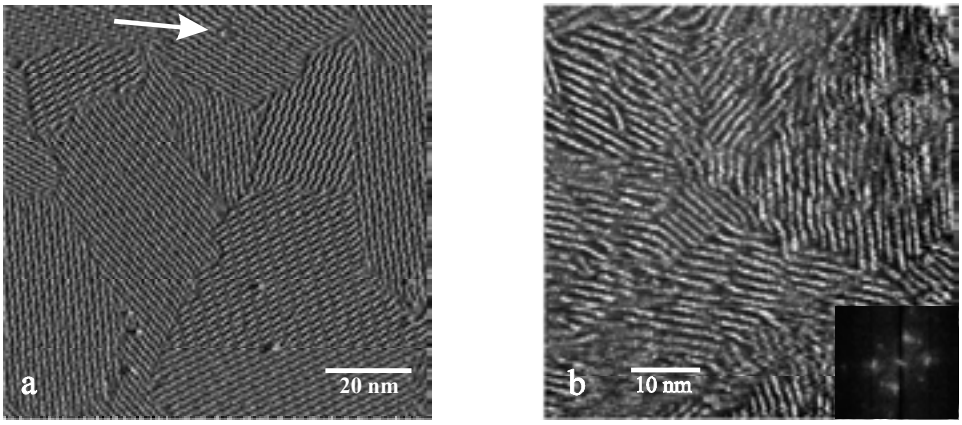


*FIG. 1. STM constant current image of a para-phenyleneethynylene (a) trimer, and (b) polymer at the interface between an organic solution and the basal plane of HOPG. The trimer in (a) shows an epitaxial polycrystalline structure. The arrow indicates a defect within a single crystal as two missing molecules. The 7.9 nm long polymer in (b) self-assembles into a nematic texture. 2D-Fast Fourier Transform indicates that the order at the molecular level is induced by the symmetry of the (0001) surface of HOPG [14].*

Dried macromolecular adsorbates of alkylated polymeric *para*-phenyleneethynylene derivatives (PPE) prepared by solution casting were studied with Scanning Force Microscopy (SFM) in Tapping Mode [15, 16, 17]. Varying systematically several parameters during the self-assembly, like the substrate [18], the solvent [19], the concentration of the solution [20] and the average length of the macromolecule [21] along the conjugated backbone, it was possible to drive the growth of these architectures towards epitaxially oriented micrometer long nanoribbons [21] (Figure 2). These nanostructures are typically two monolayers thick with their alkyl chains oriented perpendicular to the substrate. The distribution of ribbon widths is in good agreement with the molecular weights distribution according to the Schulz-Zimm distribution. This result indicates that SFM offers an alternative valuable route to determine molecular weight distributions for a rigid rod polymer [21]. These nanoribbons are supramolecular architectures which upon thiol functionalisations at their edges are nanostructures ready to bridge Au nanoelectrodes in a prototype of molecular nanowire device.

As previously described, the contrast in STM current imaging is strongly determined by the chemical nature of the substrate and of the admolecule; in addition to this contribution, the position acquired by the molecules in the plane X-Y with respect to the lattice of the crystalline substrate [22] and the position of the molecule along the Z axis, i.e. molecule-substrate distance, [23] causing different overlaps of the frontier orbitals of the molecule with the Fermi level of the substrate, also play key roles in the contrast in STM. Accurate studies revealed that the interaction with the conductive substrate induces a strong perturbation of the electronic structure of a synthetic polycyclic aromatic hydrocarbon adsorbed on a HOPG substrate in the first epitaxial monolayer.

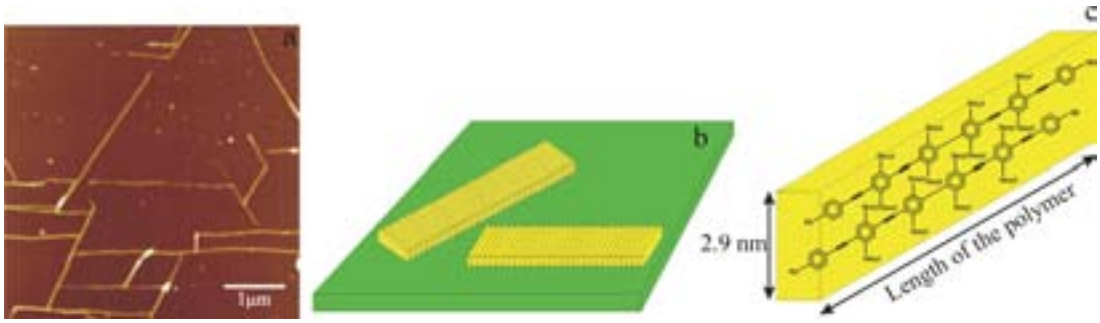


*FIG. 2. (a) Tapping Mode SFM topographical image of poly(para-phenyleneethynylene) nanoribbons self-assembled by drop-casting a solution in a mixture of phenyloctane and THF on a mica surface. The average contour length of the macromolecule employed, as determined by* $^1$*HNMR analysis, amounts to 7.9 nm. The vertical scale is 20 nm. These anisotropic architectures, which possess a molecular cross-section and a length of several micrometers, can be oriented along the crystallographic axis of the mica crystalline surface. (b,c) Cartoon of the supramolecular arrangement forming the ribbon: b) the ribbon consists of several rods assembled parallel one to each other. c) Each rod typically conveys two PPE molecules packed with the hexyl lateral chains perpendicular to the basal plane of the substrate [21].*

In a second epitaxial layer, where the same ad-molecule is 0.335 nm distant from the surface, the molecules are electronically unperturbed (Figure 3) [24]. The possibility to single out and control the properties of single molecules interacting with metallic electrodes is of great importance for tailoring contacts [25, 26, 27] in view of the future fabrication of nanoelectronic devices.

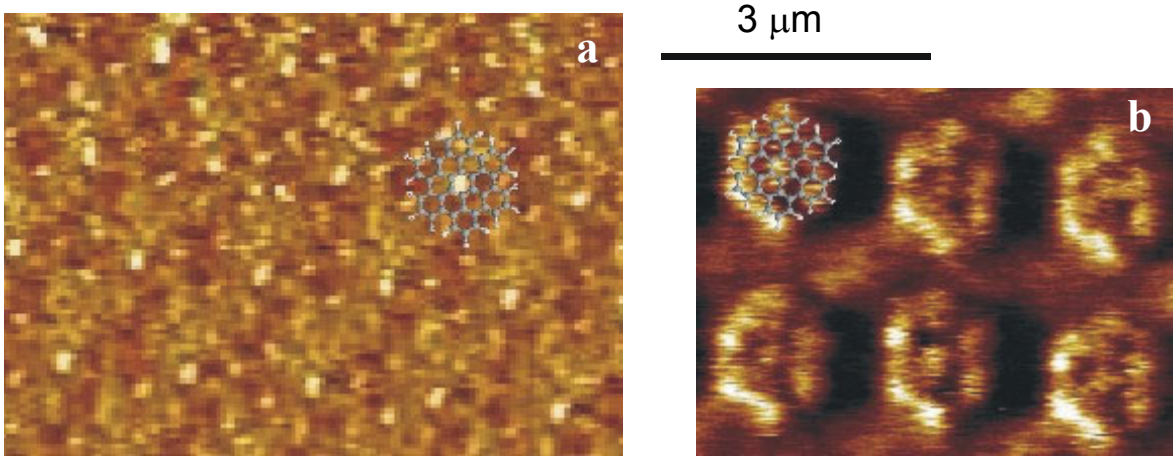


*FIG. 3. STM constant height images of self-assembled architectures of hexa-peri-hexabenzocoronene (HBC) at the solution – HOPG interface. (a) hexagonally packed first layer adjacent to the substrate. The structure possesses a unit cell* a*=(1.37±0.04) nm and* $\alpha$*=(60±1)°, leading to an area* A*=(1.63±0.05)* $nm^2$*. The observed features do not reflect the frontier orbital of the neat HBC. (b) Second layer adjacent to the substrate. The unit cell dimensions are a=(3.7±0.3) nm, b=(3.6±0.3) nm,* $\alpha$*=(86±5)°, and A=(3.3±0.3)* $nm^2$*. The contrast reflects accurately the nodal planes of the frontier orbitals of the neat HBC. Tunnelling condition of the STM image: (a)* $U_t$*=351 mV, average* $I_t$*=436 pA. (b)* $U_t$*= 1250 mV, average* $I_t$*=125 pA [24].*

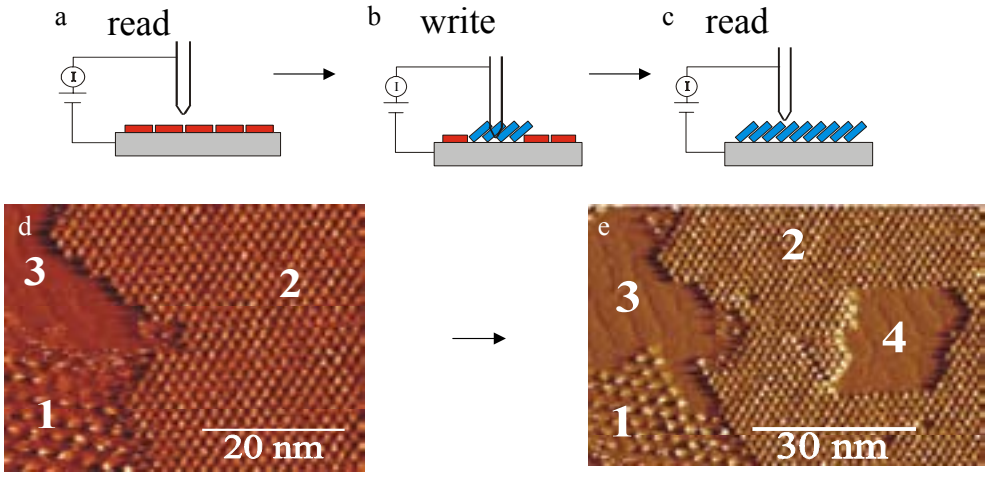


*FIG. 4. Cartoon showing the STM tip being employed to (a) 'read the surface', (b) 'write on the surface', and (c) 'read the surface' again. The STM images were recorded at the gel–HOPG interface: (d) reading the surface before the manipulation; (e) reading the surface after the manipulation. The area indicated by 4 in (e) has been manipulated by inducing a mechano-chemical switch from the 'face-on' hexagonally packed structure to the 'edge-on' lamellae architecture [28, 29].*

STM permits also to manipulate surfaces and interfaces with a resolution down to the single molecule scale. STM studies and manipulation where done at the gel-substrate interface on a crown ether-functionalised phthalocyanines. Sub-molecularly resolved STM imaging exhibited the co-existence of three different arrangements on a some hundreds of square nanometres area (Fig. 4). Two (1 and 2) highly ordered 'face-on' hexagonal phases, and another one (3) arranged 'edge-on', forming lamellae consisting of $\pi$–$\pi$ stacked phthalocyanines. Being this gel–graphite interface very durable, it became possible to carry out STM measurements continuously for many days with the tip immersed in the gel. In addition, the slow dynamics of the single molecules at this interface made it possible not only to follow the coarsening of a single molecule on the several hours timescale, but also to readily manipulate the molecular adsorbate with a precision on the molecular scale. In this set of experiments, after having 'read' the surface (figures 4(a), (d)), the tip of the STM was employed in an invasive mode to 'write' information on the molecular scale (figure 4(b)). This could be accomplished by reducing the tunnelling gap impedance, thus inducing a mechanochemical switch from the 'face-on' to the 'edge-on' packing. Going back to the non-invasive measurement conditions, the surface was 'read' again and the switching which took place in area 4 was monitored (figures 4(c), (e)) [28, 29].

## 3. CONCLUDING REMARKS

Scanning Probe Microscopies are indisputably established stars in the firmament of nanoscale science. They make it possible to probe different physico-chemical properties of single molecules and of their supramolecular arrangements as well as to nanoengineer complex hybrid architectures at surfaces. Their versatility and simplicity in the different modes as well as their applicability to different types of samples offer direct access to new realms at the interface between different disciplines including chemistry, physics and biology, and open up a huge range of applications that foster materials science into the nanoscale world.

## REFERENCES


[1] YAZDANI, A., LIEBER, C. M., "Up close and personal to atoms", Nature 401 (1999) 227-230.

[2] GIMZEWSKI, J. K., JOACHIM, C., "Nanoscale science of single molecules using local probes", Science 283 (1999) 1683–1688.

[3] JUNG, T. A., SCHLITTLER, R. R., GIMZEWSKI, J. K., TANG, H., JOACHIM, C., "Controlled room-temperature positioning of individual molecules: Molecular flexure and motion", Science 271 (1996) 181–184.

[4] STABEL, A., HEINZ, R., DESCHRYVER, F. C., RABE, J. P., "Ostwald Ripening of 2-Dimensional Crystals at the Solid-Liquid Interface", Journal of Physical Chemistry 99 (1995) 505–507.

[5] HEINZ, R., STABEL, A., RABE, J. P., WEGNER, G., DE SCHRYVER, F. C., CORENS, D., DAHAEN, W., SUELING, C., "Scanning tunneling microscopic study of the photochemical reaction of 10-diazo-2-hexadecylanthrone on graphite", Angewandte Chemie-International Edition in English 33 (1994) 2080–2083.

[6] ABDEL-MOTTALEB, M. M. S., DE FEYTER, S., GESQUIÈRE, A., SIEFFERT, M., KLAPPER, M., MÜLLEN, K., DE SCHRYVER, F. C., "Photodimerization of cinnamate derivatives studied by STM", Nano Letters 1 (2001) 353–359.

[7] GIMZEWSKI, J. K., STOLL, E., SCHLITTLER, R. R., "Scanning tunneling microscopy of individual molecules of copper phthalocyanine adsorbed on polycrystalline silver surfaces", Surface Science 181 (1987) 267–277.

[8] STABEL, A., HERWIG, P., MÜLLEN, K., RABE, J. P., "Diode-Like Current-Voltage Curves for a Single Molecule- Tunneling Spectroscopy with Submolecular Resolution of an Alkylated, Pericondensed Hexabenzocoronene", Angewandte Chemie-International Edition in English 34 (1995) 1609–1611.

[9] ABDEL-MOTTALEB, M. M. S., GOMAR-NADAL, E., DE FEYTER, S., ZDANOWSKA, M., VECIANA, J., ROVIRA, C., AMABILINO, D. B., DE SCHRYVER, F. C., "Adlayers and low-dimensional assemblies of a TTF derivative at a liquid-solid interface", Nano Letters 3 (2003) 1375–1378.

[10] LIDZEY, D.G., BRADLEY, D.D.C., ALVARADO, S.F., SEIDLER, P.F., "Electro-luminescence in polymer films", Nature 386 (1997) 135–135.

[11] LAZZARONI, R., CALDERONE, A., BRÉDAS, J. L., RABE, J. P., "Electronic structure of molecular van der Waals complexes with benzene: Implications for the contrast in scanning tunneling microscopy of molecular adsorbates on graphite", Journal of Chemical Physics 107 (1997) 99–105.

[12] SAMORÌ, P., MÜLLEN, K., RABE, J. P., "Molecular scale tracking of the self-healing of polycrystalline monolayers at the solid-liquid interface", submitted (2004.

[13] SAMORÌ, P., FRANCKE, V., ENKELMANN, V., MÜLLEN, K., RABE, J. P., "Synthesis and solid state structures of functionalized phenyleneethynylene trimers in 2D and 3D", Chemistry of Materials 15 (2003) 1032–1039.

[14] SAMORÌ, P., SEVERIN, N., MÜLLEN, K., RABE, J. P., "Macromolecular fractionation of rod-like polymers at atomically flat solid-liquid interfaces", Advanced Materials 12 (2000) 579–582.

[15] BUSTAMANTE, C., KELLER, D., "Scanning Force Microscopy in Biology", Physics Today 48 (1995) 32–38.

[16] TAKANO, H., KENSETH, J. R., WONG, S. S., O'BRIEN, J. C., PORTER, M. D., "Chemical and biochemical analysis using scanning force microscopy", Chemical Reviews 99 (1999) 2845–2890.

[17] TAMAYO, J., GARCIA, R., "Deformation, Contact Time, and Phase Contrast in Tapping Mode Scanning Force Microscopy", Langmuir 12 (1996) 4430–4435.

[18] SAMORÌ, P., SIKHARULIDZE, I., FRANCKE, V., MÜLLEN, K., RABE, J. P., "Nanoribbons from conjugated macromolecules on amorphous substrates observed by SFM and TEM", Nanotechnology 10 (1999) 77–80.

[19] SAMORÌ, P., FRANCKE, V., MÜLLEN, K., RABE, J. P., "Growth of solution cast macromolecular pi-conjugated nanoribbons on mica", Thin Solid Films 336 (1998) 13–15.

[20] SAMORÌ, P., FRANCKE, V., MANGEL, T., MÜLLEN, K., RABE, J.P., "Poly-para-phenylene-ethynylene assemblies for a potential molecular-nanowire: an SFM study", Optical Materials 9 (1998) 390-393.
[21] SAMORÌ, P., FRANCKE, V., MÜLLEN, K., RABE, J.P., "Self-assembly of a conjugated polymer: from molecular rods to a nanoribbon architecture with molecular dimensions", Chemistry-a European Journal 5 (1999) 2312–2317.
[22] RABE, J.P., BUCHHOLZ, S., "Commensurability and mobility in two-dimensional molecular patterns on graphite", Science 253 (1991) 424–427.
[23] SAMORÌ, P., FECHTENKÖTTER, A., JÄCKEL, F., BÖHME, T., MÜLLEN, K., RABE, J.P., "Supramolecular staircase via self-assembly of disklike molecules at the solid-liquid interface", Journal of the American Chemical Society 123 (2001) 11462–11467.
[24] SAMORÌ, P., SEVERIN, N., SIMPSON, C.D., MÜLLEN, K., RABE, J.P., "Epitaxial composite layers of electron donors and acceptors from very large polycyclic aromatic hydrocarbons", Journal of the American Chemical Society 124 (2002) 9454–9457.
[25] KUMMEL, A.C., "How to assemble a molecular junction", Science 302 (2003) 69–70.
[26] CAHEN, D., HODES, G., "Molecules and electronic materials", Advanced Materials 14 (2002) 789–798.
[27] NAZIN, G.V., QIU, X. H., HO, W., "Visualization and spectroscopy of a metal-molecule-metal bridge", Science 302 (2003) 77–81.
[28] SAMORÌ, P., ENGELKAMP, H., DE WITTE, P., ROWAN, A.E., NOLTE, R.J.M., RABE, J. P., "Self-assembly and manipulation of crown ether phthalocyanines at the gel-graphite interface", Angew. Chem.-Int. Edit. 40 (2001) 2348-2350.
[29] SAMORÌ, P., RABE, J.P., "Scanning probe microscopy explorations on conjugated (macro)molecular architectures for molecular electronics", Journal of Physics-Condensed Matter 14 (2002) 9955–9973.

# CONVENTIONAL AND RADIATION SYTHESIS OF POLYMERIC NANO- AND MICROGELS AND THEIR POSSIBLE APPLICATIONS

J.M. ROSIAK, P. ULANSKI, S. KADŁUBOWSKI
Institute of Applied Radiation Chemistry,
Technical University of Lodz,
Lodz, Poland

**Abstract**

A multitude of techniques has been described for the synthesis of polymeric nano-and microgels. Most of them can be classified in two groups. The first one are techniques based on concomitant polymerization and crosslinking (where the substrates are monomers or their mixtures), called by some authors "crosslinking polymerization". The second group are methods based on intramolecular crosslinking of macromolecules (where the starting material is not a monomer, but a polymer).

## 1. INTRODUCTION

Soft nanomaterials - polymeric nanogels and microgels - have made a fast and brilliant career, from an unwanted by-product of polymerization processes to an important and fashionable topic of interdisciplinary research in the fields of polymer chemistry and physics, materials science, pharmacy and medicine. Together with their larger analogues – macroscopic gels, most known in the form of water-swellable hydrogels – they have a broad field of actual and potential applications ranging from filler materials in coating industry to modern biomaterials.

There are at least two ways of defining polymeric *nanogels* and *microgels*. One of them originates from the definition of polymer gels. A *polymer gel* is a two-component system consisting of a permanent three-dimensional network of linked polymer chains, and molecules of a solvent filing the pores of this network. *Nanogels* and *microgels* are particles of polymer gels having the dimensions in the order of nano- and micrometers, respectively. The other definition says that a *nanogel* or a *microgel* is an internally crosslinked macromolecule. This approach is based on the fact that, in principle, all the chain segments of a nanogel or microgel are linked together, thus being a part of one macromolecule. It also reflects the fact that such entities can be synthesized by either by intramolecular crosslinking of single linear macromolecules or in a single polymerization event (*e.g.* initiated by one radical) that in the absence of crosslinking would lead to the formation of a single linear polymer chain.

The latter definition allows us to consider nano- and microgels as a specific form of macromolecules, along with linear, branched, comb-like, circular, star-shaped, dendrimer, and others. Since usually the shape of a nano- or microgel resembles a linear macromolecule in a coiled conformation, these structures are often seen as permanently "frozen" polymer coils.

In fact, molecular weights and dimensions of swollen nanogels are often similar to these of typical single macromolecules in solution, but the presence of internal bonds results in different physicochemical properties, including fixed shape, different rheological behavior, higher resistance to degradation and the ability to trap other molecules within their structure.

Microgels belong to the large family of crosslinked polymeric *microparticles*. Their distinct property is the ability to swell in a suitable solvent. Certainly, the choice of such a solvent is a function of the chemical structure of the polymer network. Therefore a crosslinked microparticle that remains impermeable and does not swell in contact with a group of solvents, may become a microgel in another group of solvents.

Very important and perhaps most studied so far are microgels composed of hydrophilic polymers, thus being capable of swelling in water. Such gels, irrespective of their dimensions, form a

large group of compounds named *hydrogels*. Typical hydrogel-forming polymers are those containing hydrophilic groups as -OH, -COOH, $-NH_2$, $-CONH_2$, -CONH-, $-SO_3H$ or ether linkages. In principle, nearly all water-soluble polymers, including those of natural origin, can be transformed into hydrogels. Macroscopic hydrogels have been extensively studied since 1960's [1] and till now a number of large-scale applications emerged from this field (contact lenses, drug-delivery systems, wound dressings etc.) [2-6]. Hydrogels, due their good biocompatibility and ability to mimic the properties of some tissues like cartilage and muscles, are especially suitable for use as biomaterials.

All polymer gels, macro- and microscopic, can be divided in two classes with respect to the character of the bonds linking the chains. In a *physical gel* or *pseudogel*, the links may be relatively weak van der Waals forces, hydrophobic or electrostatic interactions or hydrogen bonds. These phenomena will not be discussed here. *Chemical gels* or *permanent gels* are polymer networks where the links between the chains are covalent bonds. Therefore, such gels cannot be easily destroyed or dissolved, since their destruction would require the covalent bonds to be broken.

A distinct class of nano-and microgels are stimuli-sensitive ("smart", "intelligent") structures. They are able to react, usually by a pronounced change in dimensions and swelling ability, to external stimuli such as temperature, pH, ionic strength, concentration of a given substance, electric field, light etc. Such structures may find applications in controlled or self-regulating drug delivery, signal transmission or micromachinery.

First reports regarding microgels date from 1930's, when Staudinger described the formation of a styrene-divinylbenzene microgel [7, 8]. Since then, hundreds of reports have been published on this topic. For a full insight, the reader is directed to the excellent review papers by Funke *et al* [9]and Saunders and Vincent [10], covering most of the relevant aspects, as well as to a number of reviews dedicated to more specific issues [11-13].

In this report we will first discuss the methods used to synthesize microgels, than briefly review their actual and potential applications.

## 2. SYNTHESIS

A multitude of techniques has been described for the synthesis of polymeric nano-and microgels. Most of them can be classified in two groups. The first group includes techniques based on concomitant polymerization and crosslinking (where the substrates are monomers or their mixtures), called by some authors "crosslinking polymerization". The second group consists of methods based on intramolecular crosslinking of macromolecules (where the starting material is not a monomer, but a polymer).

### 2.1. Formation of microgels by crosslinking polymerization

Crosslinking polymerization is the most common process used to synthesize polymeric network. The substrate is usually a mixture of monomers, where at least one of the components contains two or more polymerizable functions. For example, in the case of free-radical crosslinking polymerization of vinyl compounds this would require that at least one of the monomers contains two or more vinyl groups. When radicals are generated in such system, in the process of propagation monomer molecules add one after another to the free radical at the end of the growing chain. Since some monomer molecules bear two or more active groups, upon incorporation in the (initially) linear chain, some of their functionalities are not yet used and form pendant active groups along the macromolecule.

Therefore, the propagating chain may react not only with monomer molecules, but also with these pendant groups. If the pendant group belongs to another chain, the two chains become linked together (intermolecular crosslinking). If the propagating radical reacts with a pendant group localized on its own chain, a closed loop is formed (intramolecular crosslinking).

Intermolecular crosslinking leads to the formation of branched structures and finally to macroscopic gel filling the whole volume of the reaction vessel ("wall-to-wall" gel). In an ideal case, after all the functionalities reacted, the final product would be a single molecule occupying the whole reaction vessel, with all chain segments linked together. On the other hand, pure intramolecular crosslinking leads to separate, highly internally crosslinked single macromolecules, *i.e.* nanometer-size microgels. In practice we can speak about prevailing inter- or intramolecular crosslinking. Most microgels synthesized by crosslinking polymerization are formed by combination of these two processes.

## 2.2. Crosslinking polymerization in solution

Most of the work on the microgel synthesis by crosslinking polymerization is solution has been done on the systems reacting according to the free-radical mechanism. An alternative is the synthesis by anionic crosslinking polymerization in solution.

*a) Free-radical polymerization*

Free-radical crosslinking polymerization in solution, although less commonly used than emulsion-based techniques, is a subject of considerable interest, both in the area of gelation theories and experimental studies. This seems to result from the fact it is probably the simplest available method for the preparation of microgels, it has a broad range of applications, is highly versatile and does not require the use of surfactants. The latter, employed in most versions of emulsion polymerization techniques, may be present in the final product and may need to be removed in a separate purification step, thus making the synthetic procedure more complex. On the other hand, microgel formation by crosslinking polymerization in solution requires a very careful choice of reaction parameters. In general, it provides less precise control of the size of the products and yields microgels of broader size distribution than emulsion polymerization.

In order to obtain microgels by crosslinking copolymerization in solution, it is necessary to control the competition between propagation of linear chains, intermolecular crosslinking and intramolecular crosslinking in such a way that microgels of desired average molecular weight and/or dimensions are formed, but no macrogelation occurs. One of the decisive factors is the concentration of the monomer mixture. In a dilute solution where the growing chains are separated, the local concentration of the pendant reactive groups within the macromolecule is much higher than their average concentration in the whole reaction volume. Therefore, reaction of the growing chain end with a pendant group belonging to its own chain is much more probable than a reaction with a pendant group of another chain. Thus, intramolecular crosslinking is promoted and, at a certain stage, the system contains mainly microgels. On the contrary, in a concentrated solution where the coils of both growing and dead chains overlap, the probability of the chain end reacting with a "foreign" pendant group may be higher that with its own one. This promotes intermolecular crosslinking and, in consequence, macrogelation, often not being preceded by a distinct microgelation stage. For a detailed description of the phenomena related to microgel formation in free-radical crosslinking polymerization, consult the review paper of Funke et al. [9] and a recent theoretical study of Okay [14].

In the course of a crosslinking polymerization reaction proceeding through a microgelation stage, two factors tend to shift the competition between intra- and intermolecular crosslinking towards the latter process. The first factor is that the number (and concentration) of microgels increases, making the interparticle contact and reaction more probable. The second is that within a microgel particle the number of pendant groups available for further intramolecular crosslinking events decreases (probably not only due to their actual decay in the crosslinking reaction, but also due to the increasing sterical constraints within the internally crosslinked structure). Therefore, even in the relatively dilute systems where intramolecular crosslinking initially prevails, one can finally expect macrogel formation.

An interesting example illustrating how versatile this method may be is the first report on the synthesis of fullerene-containing microgel structures [43]. Fullerenes, acting as multi-functional monomers, were co-polymerized, in a free-radical process in *o*-dichlorobenzene solutions, with 4-vinylbenzoic acid, as well as with 2- and 4-vinylpyridine to form submicron- and micron size microgels of interesting rheological and electroactive properties.

Another new and elegant way to control the kinetics and yields of free-radical crosslinking polymerization reactions is the idea of radical living polymerization [16-22]. In this technique, a spin-trapping agent (iniferter) is present in the polymerizing system that can reversibly combine with the propagating radical at the end of a growing polymer chain.

The free chains, spin trap and their product – blocked, inactive ("dormant") radical – are in equilibrium. As a result of that, at given polymerization conditions the momentary concentration of active propagating (or crosslinking) radicals can be kept at a much lower level than in the absence of the iniferter. This concentration may be controlled by varying the concentration of the spin trap. The use of living polymerization is rapidly expanding in polymer synthesis due to its many advantages (*e.g.* precisely controlled average molecular weight and molecular weight distribution), and has also found its way to the field of synthesis of microgels.

A specific case of crosslinking polymerization in solution is precipitation polymerization, when the microgels being formed in solution have the tendency of de-swelling and precipitation. Since the further growth and cyclization reactions are limited mostly to the surface and the inner sphere of such a phase-separated particle (that can be considered as a de-swollen, collapsed microgel), the resulting products are often nearly monodisperse.

It seems that precipitation polymerization is especially suitable for preparing thermo-sensitive microgels, since one can control the precipitation/deswelling tendency by changing temperature. For example, for a polymer that undergoes a phase transition leading to precipitation above a given temperature (lower critical solution temperature, LCST), it is possible to carry out precipitation polymerization above LCST, and subsequently re-solubilize the product by lowering the temperature.

Recent studies indicate that precipitation polymerization can be also used to fabricate a sort of imprinted microgel structures [23], per analogy to the molecularly imprinted non-swellable microspheres of broad biomedical use, synthesized by a similar technique [24].

*b. Anionic polymerization*

In ionic polymerization [25-28], the active centers participating in chain growth are not radicals, but ions. In principle, three groups of monomers can be used: hydrocarbon (including vinyl), polar (acrylates, methacrylates) and cyclic (oxiranes, lactones etc.). Although the ring-opening polymerization of the latter group of compounds is a promising technique used to obtain microspheres [83], so far only the first two groups have gained some attention in the field of microgel synthesis. The carbanions being the active centers in anionic polymerization usually do not undergo any spontaneous deactivation, thus such a process may be considered as a living polymerization. However, since carbanions react rapidly with any substances bearing reactive H-atoms (water, carboxylic acids, alcohols), a pre-requisite of performing a living polymerization is high purity of the reactant mixture. Since even traces of water from air can prevent the polymerization and in general the concentration of impurities should be kept at a submicromolar level, this requirement is one of the main difficulties encountered when using this technique. In the case of polar monomers, polymerization is often carried out at a low temperature (e.g. below -75°C) in order to eliminate side reactions.

The technique of anionic polymerization, due to the formation of (theoretically) infinitely long-lasting active centers, is particularly useful in the synthesis of structured microgels, mostly based on block copolymers. A typical approach is a two-step procedure. In the first step, only one monomer (A) is polymerized until the monomer is used up but the active centers at the chain ends still present. Upon addition of a second monomer (B), the polymerization continues.

In a simplest case, a block copolymer of the structure $(A)_n$-$(B)_m$ is formed. If A is a bifunctional monomer and B is a monofunctional one, this approach leads to the formation of core-shell star-shaped structures, with a microgel as a core and linear chains bound as branches. This technique (called by some authors "core-first") has been applied to the systems where the microgel core is built of 1,4-divinylbenzene [29-33]. A reverse technique ("arm-first"), where the bifunctional monomer is added to the living linear chains, was used e.g. to synthesize products having EGDMA microgel core and poly(*t*-butyl acrylate) arms [34]. Much work has been done on the microgel formation in another block copolymer system, *t*-butylstyrene-divinylbenzene (TBS-DVB) [35-39]

## 2.3. Emulsion polymerization

*a) Macroemulsion*

In the synthesis of microgels by polymerization is solution, the most important difficulty is how to avoid macrogelation, i.e. how to confine the crosslinking reactions into small, separated spaces. This problem can be overcome by using emulsion polymerization, where each micelle may serve as a separate microreactor, protected from the contact with other micelles by the stabilizing action of a surfactant. Thus, in such a confined space the polymerization and crosslinking reactions can be carried out to a high degree of monomer conversion, resulting in a single microgel particle, with no or very limited macrogel formation. Because of this advantage, emulsion polymerization is a very popular way of microgel fabrication.

In a classical free-radical emulsion polymerization [40, 41], the system initially consists of monomer molecules that are dispersed in the liquid phase (usually water) in the form of micelles (of a size in the order of a few nm) and monomer droplets, typically of the size of 0.1 ÷ 1 mm. Such microheterogeneous system is stabilized by the presence of surfactants. The radicals are generated in the liquid phase. In some systems, initiation and first propagation steps also take place in the solution. As the growing chain has the tendency to become phase-separated, surfactant-protected polymer-monomer particles are being formed, where the further polymerization and crosslinking steps take place. In other systems (especially when monomers are poorly soluble in water), initiation may occur within a monomer-filled micelle by an initiator radical that diffuses into the micelle from solution. During the chain growth, monomer molecules diffuse from the droplets and any inactive micelles to the active particles containing growing chains. After these outer monomer sources are used up and only the rests of monomer inside the active particles react, these particles do not grow any longer (or may even contract due to internal crosslinking when multifunctional monomers are present) and, upon nearly complete consumption of the monomer, the process is finally terminated.

Emulsion polymerization of monofunctional monomers leads to the formation of coagulated polymer particles (latexes), while in the presence of multifunctional monomers internally crosslinked particles – microgels – are formed, having the ability to swell in a good solvent.

*b) Microemulsion*

Some of the disadvantages of the classical emulsion polymerization can be avoided by using miniemulsion of microemulsion polymerization [9, 13, 42, 43]. In a monomer-containing emulsion, with increasing surfactant concentration the amount of monomer stored in the droplets decreases while more monomer molecules form micelles. When a critical value of emulsifier concentration is reached, no monomer droplets are left, with all the monomer being present in micelles (and to some extent in the solution). Such a transparent micellar solution is a starting point for the polymerization in microemulsion. In such a system the polymerization in monomer droplets is avoided.

In the absence of this side effect known from the macroemulsion technique, nearly monodisperse microgels can be easily synthesized.

*c) Inverse emulsion*

Most of the emulsion polymerization syntheses are performed in systems where the continuous liquid phase is water or aqueous solution, and the monomers and polymers are of relatively hydrophobic character. Certainly, it is possible to reverse this situation and polymerize hydrophilic monomers in organic, hydrophobic liquid phase.

The mechanism and kinetics of microgel formation in inverse emulsion polymerization have been extensively studied in the case of acrylamide [44]. The influence of the kind of solvent, kind and concentration of emulsifier, monomer content, agitation speed etc. on the rate of process and product properties were described.

Beside of synthesizing neutral hydrophilic microgels [44, 45], this technique is especially well suited for producing polyelectrolyte microgels of uniform size. For example, spherical gel microparticles of acrylic acid co-polymerized with diethylene glycol diacrylate have been fabricated by inverse miniemulsion polymerization [13]. The products were having various diameters, depending on the surfactant concentration, and a polydispersity lower than 10%.

*d) Surfactant-free emulsion polymerization*

Emulsion polymerization, besides its numerous advantages, has also some shortcomings, the most important being the presence of surfactants that usually have to be removed from the products in a separate step after the synthesis. A complete removal of a surfactant is not always possible, since its molecules may be in some cases incorporated (bound or trapped) into the products. This problem is especially pronounced in the case of microemulsion polymerization, where, relatively large quantities of emulsifiers must be used in order to force all monomer to be present in micelles.

A way out of this problem, although limited to some particular systems, is the use of a technique called by some authors "surfactant-free emulsion polymerization" (SFEP), where the stabilization of emulsions is provided by the monomer and/or polymer itself. This can be realized in at least two ways: either the initiator of free-radical polymerization is an ion, that, when incorporated into a growing oligomeric chain, causes this molecule to be surface active, or the substrates for polymerization are unsaturated (*i.e.* polymerizable) oligomers bearing ionized groups at one or two ends.

## 2.4. Crosslinking polymerization in the bulk

Bulk polymerization is a possible but, in general, not particularly suitable way of synthesizing microgels, primarily since the polymerizing and crosslinking system tends to form a macroscopic "wall-to-wall" gel in the whole reaction volume. According to classical gelation theory[46] involving homogeneous growth of linear chain and their subsequent linking together, formation of distinct microgels as intermediate stages should not take place.

However, in reality most polymerizing and crosslinking systems are not strictly homogeneous. If, before macrogelation is reached, the polymerization and crosslinking processes proceed trough stages characterized by inhomogeneous density of crosslinks, i.e. when microgels are formed that are not (yet) linked together, there is some chance that they could be potentially separated.

## 2.5. Polymerization with non-classical initiation

Most of the work on the synthesis of microgels by combined polymerization and crosslinking has been done using classical initiation methods, i.e. with chemical initiators, which, when activated (mostly thermally decomposed) give rise to reactive intermediates capable of initiating the chain reactions of polymerization and crosslinking.

This approach, although most commonly used, has some disadvantages. First of all, the initiator or its fragments usually remain in the products, either chemically bound or entrapped within the

polymer structure. This may pose serious problems in these applications where purity of the material is of high importance (biomaterials, optics, electronics). Secondly, in some cases the heating of the reaction mixture in order to activate the initiator may be undesirable.

Therefore there is a need for alternative techniques where initiation is provided by other means. One may envisage that the techniques already used in polymerization processes, like photopolymerization, radiation polymerization, initiation by the action of ultrasound or microwaves will find an application in the microgel synthesis as well. Photopolymerization and photocuring are very intensely studied synthetic techniques, widely used in industry [47, 48].

Radiation-induced polymerization is a well-established, versatile synthetic technique used in the polymer science and, to a limited extent, also in technology. Polymerization initiated by ionizing radiation (typically gamma rays from isotope sources or fast electrons generated by accelerators) is quite similar to the classical one and can be performed in the bulk, in solution, in emulsion etc., the main difference being only the initiation step. Ionizing radiation can interact with monomers and polymers by direct or indirect effect. In the former, the energy is absorbed by a monomer molecule, which may result in a radical formation, in the latter the energy is absorbed by the solvent, and reactive products (mostly radicals) resulting from this event may in turn attack monomer to initiate polymerization. In the case of aqueous systems, the species initiating the polymerization is most often the hydroxyl radical.

Ionizing radiation can be used in the synthesis of polymer gels (both macro- and microscopic) in two general ways: either by inducing crosslinking polymerization of monomers, or by inducing crosslinking of polymer chains in the absence of monomers. The latter technique has some important advantages and will be discussed separately. It is important to know that at late stages of radiation-induced polymerization, when only low quantities of free monomer molecules are left in the system and the radicals are still generated randomly along the chains, intermolecular recombination (crosslinking) reactions may occur with a considerable yield even in the total absence of any bifunctional monomer. Therefore, by using ionizing radiation it is possible to obtain a polymer gel starting from monofunctional monomers. More often than not, multifunctional monomers are used anyway, usually in order to increase the yield of crosslinking and thus reduce the radiation dose necessary to produce a gel of a given crosslink density. Applications of this technique range from the formation of gels based on relatively simple compounds (e.g. acrylamide [57] or *N*-vinylpyrrolidone [4]) to complex stimuli-sensitive “smart” gels targeted for advanced biomedical purposes [58–62]).

Examples of radiation-induced polymerization employed to synthesize internally crosslinked polymer microparticles are the works of Yoshida et al. [63–67] and Naka et al. [68–70]. Various monomer mixtures, mainly containing diethylene glycol dimethacrylate, were irradiated without any auxiliary substances in organic solution to yield products that were suitable for derivatization or immobilization of biomolecules, and intended for biomedical applications. Microgels can be also synthesized by radiation-induced crosslinking polymerization in emulsion, as shown on the example of styrene-based gels co-polymerized with cationic polymerizable surfactants [71].

Ultrasound is often used in microgel or microparticle synthesis, albeit not for initiating chemical reactions, but rather as a tool for solubilization, agitation, homogenization, formation of mini-emulsions etc. It seems that the well known fact that the same ultrasound can induce polymerization [72–74] has so far largely escaped the attention of the researchers working on microgel synthesis.

It seems that the well known fact that the same ultrasound can induce polymerization [72–74] has so far largely escaped the attention of the researchers working on microgel synthesis. Although no extensive studies on the possibility of microgel synthesis by ultrasound have been made so far, there are first reports on the possibility of ultrasound-induced polymerization of bifunctional monomers [75] and fabrication of microspheres [76].

It has been shown that concomitant action of ionizing radiation and ultrasound may lead to interesting results in the synthesis of internally crosslinked microspheres (that would become

microgels in a suitable solvent). In a radiation-induced crosslinking polymerization of diethyleneglycol dimethacrylate in ethyl acetate, the action of ultrasound affects the size and shape of formed particles, probably by promoting interparticle interactions [77].

## 2.6. Intramolecular crosslinking of polymer chains: monomer-free techniques

In most research work and applications, microgels are synthesized using procedures based on polymerization processes starting from monomers as the basic substrates. This is, however, not the only possible way. An alternative approach to the synthesis of microgels, in particular the *nanogels* of small size (typically <0.1 μm), is intramolecular crosslinking of individual macromolecules. An obvious and important advantage of this method is the absence of monomer. This is of great value when the product is intended for biomedical use, where even small quantities of residual monomer may be potentially harmful and thus unacceptable. Furthermore, intramolecular crosslinking may provide means to obtain crosslinked structures of various molecular weight and size, including very small structures, depending on the molecular weight of the parent polymer. Such nanogels obtained from single macromolecules are interesting physical forms of polymers as they are a sort of "frozen" polymer coils of limited segmental mobility. One can also expect that a combination of intra- and intermolecular crosslinking [78–80] will provide a tool for synthesizing nanogels and microgels of independently chosen molecular weight and dimensions (various internal densities). Last but not least, intramolecular crosslinking of individual macromolecules is an interesting reaction. A number of questions regarding this process, particularly its kinetics, have not been answered yet [81–83].

## 2.7. Chemical intramolecular crosslinking

Intramolecular crosslinking, similarly as polymerization, can be performed either as a thermally initiated chemical reaction or as a photo- or radiation-induced process. Chemical intramolecular crosslinking of individual polymer chains can be achieved in at least two ways. One is to prepare linear or branched polymer with pendant reactive (e.g. vinyl) groups and initialize the crosslinking by a suitable initiator. Another way does not require any special substrate preparation (no polymerizable pendant groups needed). It has been shown that intramolecular crosslinking of single chains of water-soluble polymers can be carried out by reacting them with a suitable crosslinking agent in dilute solutions. The crosslinker must be capable of reacting with the functional groups (-OH, -COOH etc.) of the polymer, and should be at least bi-functional. Synthesis is carried out in solution. Polymer concentration must be chosen sufficiently low to avoid intermolecular crosslinking, i.e. it must be significantly lower than the coil overlap concentration. By varying the concentration of the crosslinker one can influence the internal crosslink density. Burchard *et al.* used this approach to synthesize internally crosslinked single macromolecules (nanogels) of poly(vinyl alcohol) with glutaraldehyde as the crosslinker [84] and of poly (allylamine) crosslinked with 1,4-dimethoxybutane-1,4-diimine dihydrochloride [85, 86, 87]. Similar approach is used to obtain microgels of polysaccharides.

## 2.8. Radiation-induced crosslinking

Synthesis of nano/microgels by intramolecular crosslinking of individual polymer chains can be also initiated by ionizing radiation. The main advantage of this method is that it can be carried out in a pure polymer/solvent system, free of any monomers, initiators, crosslinkers or any other additives, therefore it seems to be especially well suited for the synthesis of high-purity products for biomedical use. In this approach, discussed in more detail below, pure aqueous solution of a polymer is subjected to a short (a few microseconds), intense pulse of ionizing radiation. In this way, many radicals are generated simultaneously along each polymer chain, and their intramolecular recombination leads to the formation of nanogels. This approach has been first tested on neutral water-soluble polymers: poly(vinyl alcohol) [82], polyvinylpyrrolidone [88] and poly(vinyl methyl ether) [89, 90], and later expanded to poly (acrylic acid) as an exemplary polyelectrolyte [83, 91].

The main parameter influencing the competition between inter- and intramolecular recombination of polymer radicals in dilute solutions is the average number of radicals present at each macromolecule at the same time [81]. If this number, under the given synthesis conditions, is much

lower than 1, there is only a meager chance that a radical will find a reaction partner within the same chain. In such cases, recombination is only possible between radicals localized on two separate macromolecules. On the other hand, when there are tens of radicals present along each chain, the probability of intramolecular encounters and reactions is higher than that of intermolecular ones.

The latter processes are relatively slow, since they require that two large entities – polymer coils – diffuse towards each other.

In the case of the radiation-induced radical formation, these two opposite conditions, i.e. a very low or very high number of radicals per chain, can be fulfilled by means of a proper choice of irradiation conditions. Continuous irradiation at a relatively low dose rate, such as typical irradiation with gamma rays from isotope sources, leads to a steady-state concentration of polymer radicals in the order of $10^{-7}$ M. When the concentration of polymer coils is significantly higher than this value (this condition is usually easily fulfilled), the average number of radicals per chain is much lower than unity and intermolecular crosslinking is observed. In order to promote intramolecular crosslinking, short, intense pulses of radiation can be employed, such as pulses of fast electrons from an accelerator, generating radical concentrations in the order of $10^{-4} \div 10^{-3}$ M. If the concentration of polymer coils is low (that is to say, $10^{-6} \div 10^{-4}$ M), many radicals are generated on each macromolecule (typically many tens or even over a hundred), and the conditions for intramolecular recombination are fulfilled. Certainly, this does not mean that intermolecular reactions are totally eliminated in such a case. Some coils may come into contact before all the radicals decay, and if there is an uneven number of radicals on a chain, at least one of them must finally find a reaction partner at a neighboring macromolecule.

The data on changes in molecular weight, viscosity and radius of gyration following the pulse-irradiation of dilute polymer solutions clearly indicate that strongly internally crosslinked nanogels are formed, which, in comparison with the starting macromolecules, have somewhat higher molecular weight but at the same time significantly lower dimensions [82, 83, 88, 91]. While the main reason for the increase in molecular weight is the intermolecular crosslinking occurring in the system with very low yields in parallel to intramolecular recombination, the latter process is the dominant reason for the reduction in coil dimensions.

A balance between inter- and intramolecular recombination of polymer radicals may be also maintained when continuous irradiation is used. Therefore it is possible to synthesize microgels by crosslinking in a solution using isotope sources, as has been experimentally demonstrated and supported by simulations for poly (vinyl alcohol) by Wang et al. [78–80, 92].

### 2.9. Disruption of macroscopic networks

The idea of obtaining microscopic gel particles by disrupting continuous "wall-to-wall" gels seems to be conceptually the simplest of all synthetic approaches, since the procedures used to obtain macroscopic networks are usually simple, with less parameters to be controlled than in the above described typical microgel synthesis methods – there is no need to control the micelle size or to observe the precautions necessary to avoid macrogelation.

Disadvantages of this "non-elegant" method are that the size distribution is very broad (however for microgels in the scale of many micrometers it can be reduced *e.g.* by using mechanical sieves), one cannot usually expect producing extremely small gel particles in this way nor obtaining products of a regular, spherical shape. On the other hand, the disruption method may be of some advantage for synthesizing microgel fractions of various diameters, but precisely the same crosslink density (since they are derived from one specimen of a macroscopic gel) [93]. In the authors' laboratory this method is used routinely to fabricate large amounts of coarse polyvinylpyrrolidone microgel of dimensions below 50 μm, following radiation-induced synthesis of macroscopic gel in the bulk [94]. A gel disruption process has been reported to yield crosslinked polysaccharide microgels (of dimensions in the 100 nm range), as one of the steps to construct polysaccharide/phospholipide biovectors for drug delivery [95].

It should be noted that important final steps of almost all synthetic procedures used to obtain microgels are purification and drying. It has been clearly demonstrated that drying methods and conditions may have significant influence on the final structure and properties of microgels [45, 96].

## 3. APPLICATIONS

### 3.1. Biomaterials

The possibilities of employing macroscopic polymer gels as biomaterials, mostly in the form of hydrogels based on synthetic polymers, have been explored since 1960's, when these materials were first synthesized [1]. Since then, a number of products reached the stage of commercial application, soft contact lenses, drug delivery systems and wound dressings being the most widely known examples. Given the number of research groups involved and progress being made in this field, one may anticipate that in the future the number of hydrogel-based biomedical products on the market will be constantly increasing.

Broad, although not very recent publications on the medical use of hydrogels are the collective works edited by Peppas [2] and DeRossi et al. [92]. Park et al. reviewed the narrower field of biodegradable hydrogels [98]. Out of more recent books and book chapters on this subject [99] provides more general outlook, while the scope of ref. [100] is limited to silicone-based hydrogels. For exemplary review papers on the medical applications of hydrogels [3, 101-108].

Although certainly the characteristics of hydrogels differ from one to other formulation, a few common properties can be listed that make these materials suitable for biomedical applications. In their high water content and hydrophilicity hydrogels are similar to tissues. They also mimic some properties of soft tissues as reversible swelling and elasticity. Due to their network structure they may be loaded with a drug, which can be subsequently released at a controlled rate. This rate can be adjusted, one of the main factors being the mesh size. The latter parameter allows also constructing semi-permeable membranes or containers, for example an outer shell of a hybrid artificial organ (an implant containing living cells) allowing the transport of water, oxygen, nutrients and enzymes, but being impermeable to larger entities as immunoglobulins and other components of the immune system [109-111]. Due to their fair to excellent biocompatibility, hydrogels are usually well tolerated as implants.

An example of a mature biomaterial technology based on classical, homogeneous hydrogels is the large-scale production of wound dressings, by a technique combining radiation-induced crosslinking of polyvinylpyrrolidone and concomitant sterilization of the final product [4, 112]. A number of other products based on similar technology, e.g. systems for local delivery of anticancer drugs and for induction of childbirth, have successfully passed clinical tests.

While "regular" hydrogels are already common components of biomaterials, current efforts of the researchers are now concentrated on the stimuli-sensitive ("intelligent", "smart") gels. These materials are able to respond to external stimuli, such as temperature, pH, ionic strength, light, electric field or even to (selective) changes in the concentration of a given chemical species. The latter property can be used e.g. in glucose-responsive insulin-releasing devices [120] or antigen-responsive systems [121]. The response to the stimulus, being induced by conformational changes of the polymer chain segments, usually manifests itself as a pronounced change in the gel volume (strong contraction or expansion) and in the amount of bound liquid (decrease or increase in the degree of swelling). Due to these properties, stimuli-sensitive gels are tested for applications as sensors, actuators, chemical valves, controllable or self-regulating drug-delivery systems or even artificial muscles. Certainly, there is still some gap between the artificial hydrogel fish that moves by swinging its tail in a laboratory bath [122] or electrically driven gel finger working in the air [123] and a future implementation of a hydrogel-based muscle, but fast developments in the field of stimuli-sensitive hydrogels allow to expect that biomaterials based on these materials will be implemented very soon.

Microgels are also intensely studied with respect to their biomedical applications. Of course, the product range is different than that of macroscopic gels, although there is a significant overlap in the field of controlled drug delivery. The most important microgel applications in the biomedical field are: carriers for enzymes, antibodies etc. used in diagnostics (e.g. immunoassays), drug carriers for therapeutic purposes (local, controlled drug delivery), and, potentially, microdevices, artificial biological fluids and synthetic vectors for drug delivery.

Coupling microgels with selective biochemicals leads to materials applicable in biological testing. This technique is used since some time with solid nanospheres. In some cases, in comparative tests microgels performed better than polystyrene-based microsphere supports, providing testing material of higher sensitivity [135]. A typical way of action of the microgel-based immunoassay is based on an aggregation of antibody-bearing microgels with the specific antigens. The large particles formed in this way can be detected by microscopic techniques. In a modified immunoassay, magnetic microgels can be applied, containing encapsulated polymer core with adsorbed magnetic nanoparticles [128, 130]. Magnetically labeled cells can be separated from a cell mixture by applying magnetic field, for example in a section of tubing in which the cell mixture is flowing.

Albeit there is a broad field of potential biomedical applications of conventional microgels, a strong tendency is observed to focus the research on complex microgels and on stimuli-sensitive systems. The preference for using stimuli-sensitive gels is even more pronounced for microgels than for the "wall-to-wall" gels. One of the important reasons is much shorter response time. While the reaction of macroscopic responsive gels to a stimulus is sometimes unacceptably slow (for example, when the molecules of a chemical stimulus have to diffuse into the whole volume of a gel slab), microgels, due to their small dimensions and high surface-to-volume ratio respond much faster.

Temperature-sensitive microgels are tested for controlled binding of biomolecules. It has been shown that poly(*N*-isopropylacrylamide) – pNIPAM – microgels can bind various proteins by physical sorption above the phase transition temperature (i.e. at ca. 40°C), and release them upon lowering the temperature to 25°C [137, 138]. Proteins can be also covalently bound to such gels, and their activity can be controlled by temperature changes [139]. In complex systems such as described by Yasui et al.[140], one can achieve high enzyme activity within a defined, relatively narrow (a few degrees) temperature range. Pichot and co-workers demonstrated the possibility of using thermo- and pH-responsive microgels for binding nucleic acids [118, 141]. It has been shown that the interaction of temperature-sensitive microgels with elements of the immune system like granulocytes (foreign-body attacking cells) can be moderated by changes in temperature [142]. It is worth noting that the interaction of pNIPAM gel particles was much weaker than that of polystyrene microspheres, which may indicate that, in the context of attack by immune system cells, these microgels have higher biocompatibility than solid microspheres.

Thermosensitive microgels have been also tested as drug carriers. The structure and hydrophilic/hydrophobic properties of the drug have been identified as important factors influencing the phase transitions and uptake/release characteristics of poly (N-vinyl caprolactam) gel particles [143]. In order to achieve the desired release profile, composite microgels may be used, for example combined nonporous silica/pNIPAM gels [144]. The rate of the thermally triggered drug release may be then controlled by changing the composition of this hybrid product. Another interesting example of a composite structure based on drug-loaded thermosensitive microgels is a wound dressing, where drug-bearing pNIPAM gel particles are incorporated into a self-adhesive film [145]. The product combines adhesive and temperature-controlled absorptive functions, and is easy to peel off after use.

Compositions containing poly (*N*-vinylcaprolactam-*co*-sodium acrylate) microgels and gelatin undergo a reversible macrogelation upon temperature increase above ca. 32°C [146]. Such materials, liquid (injectable) at R.T., but forming a gel at the temperature of human body, are considered for applications in surgery and drug delivery.

Another group of responsive materials tested for use as biomaterials are pH-sensitive and/or ionic-strength-sensitive microgels. For these products, there are at least two mechanisms allowing for

controlled drug delivery. One can load the gel particles with a drug at a pH where the particles are fully swollen (expanded), trap it inside by a pH change leading to the collapse of the microgel, and subsequently allow the drug to diffuse out at a pH-controlled rate. Similar mechanism applies as well to the systems where ionic strength is the stimulus for expansion and collapse, or where both pH and ionic strength effects are operating. Another mechanism is pH-dependent reversible ionic binding of drugs. Drug- and protein binding and release from anionic microgels have been studied e.g. by Eichenbaum et al.[141, 148] and Soppimath et al.[149], while Vinogradov et al.[132, 150, 151] described the synthesis and properties of some cationic systems.

Sophisticated drug-delivery system, mimicking the action of secretory granules, has been constructed by Kiser et al.[152, 154]. The core is an anionic microgel particle based on methacrylic acid, loaded with a drug. Subsequently, by lowering pH, a collapse of the microgel is induced. In this form, the particle is coated with a lipid bilayer, to simulate the natural secretory granule and to protect the particle from premature swelling. Poration of the lipid bilayer (e.g. by applying electric field) causes the gel to swell, allowing release of the drug. A different synthetic procedure leading to similar systems is based on encapsulation of hydrogel-forming components into liposomes and subsequent polymerization [155]. Further example of this kind is a group of products intended for drug delivery of vaccine formulations, consisting of crosslinked polysaccharide microgel core surrounded by a lipid bilayer [95].

A pH-sensitive microgel preparation based on poly(methacrylic acid-*co*-ethyl acrylate) has been devised for oral delivery of a novel drug being a HIV-1 protease inhibitor [156]. It has been demonstrated that the absorption of this poorly water soluble drug from the tested system was much better than from the suspension of a free drug.

Solid sustained release devices for oral delivery of drugs can be obtained by compressing microgels. Such a system based on polyurethane microgels has been shown to retain its integral structure but become microporous on swelling with water [131].

Microgels can be functionalized not only by coupling them with biomolecules, but also by molecular imprinting. This process leads to microgels bearing structural binding sites specific to target molecules. A general procedure of molecular imprinting of a polymer is as follows. Monomers being in contact with a template molecule are polymerized and crosslinked, the template is removed and the polymer network contains a complementary binding site able to rebind the same template or analogous molecules. Ye et al. and Biffis *et al.* demonstrated the applicability of this procedure for synthesizing molecularly imprinted microgels and proved their binding performance [23, 24, 157].

Stability of shape and dimensions of microgels when compared with linear polymer chains may be helpful in their potential use for blocking dental microchannels in cases when there is a need to use a synthetic substitute for the natural gel-like substance performing this function [158].

An interesting and potentially valuable property of microgels is their enhanced resistance against degradation when compared to linear macromolecules [107, 159]. As a result of any intense or long-lasting stimulus inducing chain breakage (a mechanochemical action, ultrasound, the formation of peroxyl radicals along the chain etc.), a linear macromolecule is easily degraded to short fragments. The same number of chain breaks formed in a microgel may cause no or very little fragmentation, since the chain segments are linked together in many points and will not fall apart as a result of a single chain break.

The above described effect has been demonstrated on microgels of poly(acrylic acid) – PAA [91, 160]. Aqueous solutions of linear chains and microgels of PAA were subjected to the action of ionizing radiation in the presence of oxygen. Under such conditions, no crosslinking takes place in the system. Initially formed carbon-centered radicals are rapidly converted into the corresponding peroxyl radicals, which in turn initiate processes leading to chain scission. As the concentrations of linear and crosslinked chains of similar average molecular weight were identical, the yield of scission events should be equal for both samples. However, the changes in molecular weight and in the radius of

gyration in the case of linear and microgel PAA revealed striking differences. While linear PAA is easily degraded even at relatively low doses, which is evidenced by parallel decrease in weight-average molecular weight and radius of gyration, microgels, within the same dose range, seem to remain intact, their molecular weight and radius of gyration being constant.

This degradation-resistance combined with suitable rheological properties may be used in fabricating materials for medical applications. A commercialized example of such a product is a polymer drug based on microgels of a natural polysaccharide used to enhance the viscoelasctic performance of malignant synovial fluid [161]. These macromolecules are subjected to mechanochemical stress and to the attack of reactive oxygen species, mainly free radicals. It has been shown that under such conditions internally crosslinked macromolecules perform better than the corresponding linear ones [162]. Preliminary tests on a substitute synovial fluid containing microgels made of a synthetic polymer proved the high degradation resistance and proper viscoelastic properties of this product [163].

First tests have been performed on the application of microgels as synthetic, non-virial vectors in gene delivery. The latter is regarded as a powerful tool for curing some hereditary diseases and treating genetically based disorders. Certainly, the issue is a very complex one, since such vectors must be capable of performing many processes as binding DNA fragments, attachment to cells, internalization, and intracellular plasmid release. First attempts of using microgel-like structures for gene delivery were based mainly on chitosan, but synthetic structures based on 2-(dimethylamino)ethyl methacrylate, *N*-vinylpyrrolidone and *N*-isoporpylacrylamide have been tested as well, with promising results [126].

There are also projects to design microgel-based intravenous drug carriers that could remain in blood for a suitable period of time, facilitate the cellular uptake and possibly also selectively deliver the drug to a target site. Animal tests have shown that by varying properties of such structures (chemical composition, hydrophilicity) one can change the biodistribution patterns of the microgels and that drug-loaded microgels were more efficient than equivalent concentrations of free drug in curing melanoma in mice [120].

Some further perspectives in the application of nano- and micro-sized particles and devices in drug delivery are discussed in ref. 127].

## 4. COATINGS

When actual, large-scale applications of microgels are concerned, the surface coatings industry seems to be the most prominent field. Hundreds of research papers published and patents issued [164–180] dealing with microgel-containing coatings emphasize the significance of this application. The interest in the use of microgels as components of coatings originated mainly from environment protection needs and regulations. In order to reduce the amount of volatile organic compounds in the coating formulations, the manufacturers tend to increase the total solid content. This is, however, problematic if polymer components of a given molecular weight range are used in binders, since the viscosity of formulations becomes too high. When microgels are used, viscosity can be maintained at a desired level. Another approach besides the high-solid products is to use water-borne coating systems. Microgels can be used both in solvent-borne and water-borne coating products. Besides their advantageous rheological properties, they often exert reinforcing effect on the cured coating. The use of microgels in coating technologies has been the subject of concise but informative reviews [9, 181, 182, 183].

Microgel-containing solutions and dispersions are usually characterized by pseudoplastic, strongly non-Newtonian rheological properties. They are highly viscous at low shear rate (they don't flow at a zero shear rate), but their viscosity decreases remarkably with increasing shear rate. This is in a perfect accordance with the needs for a typical paint application process. In the storage tank (no or low shear rate) the viscosity should be high to prevent pigment settling, during the gun-spraying (high

shear rate) low viscosity is desired, and at the object surface (no or low shear rate again) viscosity should increase rapidly so that no sagging effect occurs, even for films of high thickness. Another useful property of microgels is their positive influence on the orientation of flake pigments in metal effect coatings.

Microgels have also positive influence on the mechanical properties of cured paint films as stone chip resistance, impact flexibility and elasticity. This is attributed to the crosslinked polymer structure, high molecular weight of gel particles and the microheterogeneous structure of the microgel-containing polymer film that probably allow the impact energy to be more efficiently dissipated [181].

In the automotive industry, the primer coating layer is often applied by electrodeposition. It has been shown that compositions containing amine-based cationic microgels, mostly in the form of aqueous dispersions, can be used for electrocoating [184, 85].

Problems that have been recently investigated with respect to the use of microgels in coatings include deeper understanding of the relationship between microgel structure and rheological properties (and ways to adjust the latter) [186], the influence of substrate composition and synthetic procedures on the shelf stability of the product and affinity between microgels and pigments [187], influence of microgels on the drying time [44] and ability to form films suitable for drying at ambient temperatures [188].

Microgels can be used not only as constituents of regular coatings, but also as self-adsorbing and self-organizing film-forming layers for protecting metal surfaces against corrosion. It has been shown that core-shell microgels based on styrene, butyl acrylate and phosphate-substituted acrylates form a layer of a structured molecular order on a surface of technical aluminum and provide efficient protection against corrosion in standard tests [189, 190].

Albeit the use of synthetic microgels in coatings started in the late 1960's [191] or, depending on what we consider as true microgel, perhaps rather in the 1970's [192, 193], one should mention that physical and chemical studies on a highly durable ancient oriental lacquer used in Asia since millennia revealed a structure containing self-formed, natural core-shell-like microgel particles [194].

### 4.1. Miscellaneous

Besides their applications in coatings (biggest market) and in biomaterials (perhaps the most promising direction for the future), microgels are used or tested for use in a number of other fields.

Besides large-scale use of microgels in coating industry, similar properties make them interesting for the manufacturers of *cosmetics*, namely nail varnishes [195, 196]. In varnishes based on organic solvents, organophilic clays are used to prevent pigment sedimentation. These compounds, however, exert some unwanted side effects and usually require toluene as a component of the formulation. The presence of microgels allows reducing or eliminating the use of clays, while maintaining the proper rheological properties of the varnish and preventing the precipitation of the pigments.

Historically one of the first applications of microgels was in the *papermaking* [197–199]. In manufacturing quality products starch and other polysaccharides used as paper and paperboard sizes may be replaced with poly(vinyl alcohol) (PVAL) for better performance. It has been demonstrated that microgels of PVAL show clear advantages over the same polymer in a linear form, e.g. they have lower tendency to penetrate into paper, which is an undesirable effect.

Microgels can be a valuable component of *fibers*. An exemplary application is the admixture of vinylidene chloride gels to an acrylic fiber, significantly improving the flame retardancy [200]. Similar gels have been shown to improve load-bearing properties and flame retardancy of polyurethane *foams* [201].

Microgels can be also applied as supports in *catalysis*. Organo-aluminum compounds coupled to organopolysiloxane microgel particles serve as co-catalysts in the polymerization of olefins [2002, 2003]. By using microgel-supported catalyst, a homogeneous catalysis in a flow reactor may be carried out. If the inlet and outlet of the reactor are equipped with membranes that the gel particles cannot pass, the reactants are in a constant flow but the catalyst remains in the reactor, despite it is present in a nearly molecular dispersion.

Particular rheological properties as well as higher mechanochemical resistance of microgel solutions when compared to the solutions of linear chains are the basis of their applications in the fields of liquid thickening, *oil recovery* and *hydraulics*. Solutions of relatively inexpensive polyacrylamide-based microgels are used as thickening agents and agents for restricting the flow of liquids through subterranean formations [204]. Microgel solutions can be applied as a non-Newtonian, shear-resistant, non-leaking hydraulic fluid for hydraulic energy transmission systems and devices absorbing mechanical energy (liquid springs, shock absorbers) [205].

Due to their swelling and water-retaining properties, hydrophilic microgels have been postulated and tested, with good results, for use as *soil conditioner* [206–208].

An extensively tested and potentially broad field of microgel application is in *printing* and *photographic technology*. Since the rheological properties of microgel can be tailored to meet specific needs (a sophisticated method of viscosity adjustment may be varying the hair length of a core-hair type microgels), they may be useful in liquid photopolymer formulations used to cover the screen in the screen printing technique [209]. Incorporation of microgels in the photosensitive layer of a kind of modern lithographic plates leads to a product that can be developed directly on a printing press, without a post-exposure wet development step [210]. This technology allows saving time and labor as well as reduced the use of volatile organic compounds. Another technology has been elaborated to obtain printing plates for flexographic printing [211, 212]. Microgel-based photosensitive resin allows the plates to be water-developable, thus eliminating the use of harmful halogen-containing solvents used to develop the plates in a conventional technique. A variety of photosensitive compositions for use in printing and manufacture of printed circuit boards employ microgels to enhance physical properties, eliminate cold flow, improve storage stability, enhance photospeed and to render these materials the suitability for water-processing [213–216].

Some inks and electrographic liquid developers contain finely dispersed microparticles of magnetic substances. Several problem have to be overcome in producing these “magnetic fluids”, one the most important being the poor dispersion stability. This can be significantly improved when incorporating these solid microparticles, during synthesis, into polymeric microgels [217].

Macroscopic polymer gels can be made photosensitive, not only by introducing chromophores that undergo permanent changes (e.g. crosslinking) upon irradiation, but also by incorporating structures that enable reversible photochemical switching of properties (reversible crosslinking) [218]. This indicates that also microgels themselves can be turned into photosensitive materials, either by using suitable monomers or by post-synthesis modification. In fact, coumarin-containing organosilicon microgels have been demonstrated to undergo photoinduced cluster formation [219]. So far, most often microgels are used in photography and imaging as auxiliary substances, either as binding agents improving the physical properties of the film layers, or as additives that help to incorporate the photographically active or other (e.g. antistatic) substances into the photographic layers [220, 221].

Debord et al. have demonstrated that relatively simple microgels made of poly (N isopropylacrylamide) can be manipulated to form colloidal crystals of specific colors depending on the fabrication parameters [222]. In another approach, polymeric nanospheres are incorporated into a stimuli-sensitive hydrogel [223]. Under the action of a chemical stimulus, the distances between the nanospheres can be varied, thus causing shifts the wavelength of the Bragg peak of the diffracted light. This leads to the changes in color of the specimen. It is expected that such colloidal crystals can find a wide range of applications in *photonics* and *chemical sensing*.

One may expect that in the near future interesting applications will be found for the recently described *electrically conducting microgels* based on pyrrole and aniline polymers bound to a gel core [224] products have promising properties in the aspects of electrical conduction, electromagnetic frequency interference shielding and electrostatic prevention.

*Sorption* and *binding* of a variety of compounds is an intensely studied application field of polymer gels. Most of research in this area concerns the use of hydrogels. Exemplary applications of macroscopic hydrogels being investigated, besides drug-delivery systems described in section 4.1, include e.g. binding of metal ions [225] selective removing of pollutants (arsenate and selenite [226], textile dyes [227], organic substances [228] or collecting uranyl ions from seawater [229]. Reversible sorption of water by hydrogels is tested for an application in sludge dewatering [230].

A number of studies revealed the potential application of microgels in *metal ion binding* and *ion exchange*. An advantage of using micro- instead of macrogels is primarily the binding kinetics – in microgels the binding groups are easily accessible, in contrast to most macroscopic gel structures, where considerable time is needed for the substrates to diffuse into the gel volume. Gel particles bearing carboxylate groups bind divalent alkali earth cations ($Mg^{2+}$, $Ca^{2+}$, $Sr^{2+}$, $Ba^{2+}$) more effectively than monovalent cations (as $Na^{+}$) [231]. Binding of calcium ions has been studied in more detail [146, 232]. Other studies have shown that there may be a pronounced selectivity in binding divalent metal ions. For example, binding of $Hg^{2+}$ cations by poly (*N*-vinylcaprolactam-*co*-sodium acrylate) microgels is much stronger than binging of $Cu^{2+}$ and divalent alkali metal ions [233]. Strong, albeit reversible, binding of $Pb^{2+}$ by microgels of poly (*N*-isopropylacrylamide-*co*-sodium acrylate) has been reported as well [234, 235]. These observations indicate that microgel-based systems may be used for selective ion binding.

One of the most fascinating prospective uses of stimuli-microgels is in *microdevices* and *micromachinery*. Due to their fast response time, they may be for example used as self-regulated, pH- or temperature-controlled microvalves. Contrary to conventional microactuators (electromagnetic, electrostatic, thermopneumatic etc.), microgel-based valves are simple and do not require external power for operation. Fully operational exemplary devices of this kind, having short response times, have been recently presented by Beebe et al. [236].

Microgels can be used as building bricks for constructing complex polymer structures and materials. A simple example may be a fabrication of a polymer material (foil, coating, etc.) of well-developed, rough (in the microscale) surface. This may be carried out just by casting a foil from a microgel solution. Such a surface, even after drying and collapse of microgels due to a loss of solvent remains structured, when compared to analogous sample obtained from solution of linear chains of the same polymer [91].

## REFERENCES


[1] O. WITCHERLE and D. LIM, Nature 185, 117 (1960).
[2] N.A. PEPPAS, *Hydrogels in Medicine and Pharmacy*, CRC Press, Boca Raton (1986).
[3] N.A. PEPPAS and J.J. SAHLIN, Biomaterials 17, 1553 (1996).
[4] J.M. ROSIAK, in *Radiation Effects on Polymers*, Edited by R. C. Clough and S. W. Shalaby, ACS Book Series Vol. 475, Am.Chem.Soc., Washington,D.C. (1991), p. 271.
[5] O. HIRASA, Journal of Intelligent Material Systems and Structures 4, 538 (1993).
[6] P. MOLYNEUX, *Water-Soluble Synthetic Polymers. Properties and Applications*, CRC Press, Boca Raton (1987).
[7] H. STAUDINGER and W. HEUER, Chem. Ber. 67, 1164 (1934).
[8] H. STAUDINGER and E. HUSEMANN, Chem. Ber. 68, 1618 (1935).
[9] W. FUNKE, O. OKAY, and B. JOOS-MÜLLER, Adv. Polym. Sci. 136, 139 (1998).
[10] B.R. SAUNDERS and B. VINCENT, Adv. Colloid Polym. Sci. 80, 1 (1999).
[11] R.PELTON, Adv. Colloid Interface Sci. 85, 1 (2000).
[12] M. ANTONIETTI, Angew. Chem. 100, 1813 (1988).
[13] M. ANTONIETTI and K. LANDFESTER, Prog. Polym. Sci. 27, 689 (2002).

[14] O. OKAY, Polymer 40, 4117 (1999).
[15] P.L. NAYAK, S. ALVA, K. YANG, K. DHAL PRADEEP, J. KUMAR, and S.K. TRIPATHY, Macromolecules 30, 7351 (1997).
[16] D. GRESZTA, D. MARDARE, and K. MATYJASZEWSKI, Macromolecules 27, 638 (1994).
[17] D. MARDARE and K. MATYJASZEWSKI, in *Polymeric Materials Encyclopedia*, Edited by J. C. Salomone, Vol. 5, CRC Press, Boca Raton (1996), p. 3840.
[18] T.E. PATTEN, J. XIA, T. ABERNATHY, and K. MATYJASZEWSKI, Science 272, 866 (1996).
[19] K. MATYJASZEWSKI, ACS Symp. Ser. 85, 2 (1998).
[20] S.G. GAYNOR, K. BEERS, S. COCA, A. MUHLENBACH, J. QIU, J. XIA, X. ZHANG, and K. MATYJASZEWSKI, ACS Symp. Ser. 765, 52 (2000).
[21] *Controlled/Living Radical Polymerization*, Edited by K. Matyjaszewski,ACS Symp. Ser. Vol. 768, Am.Chem.Soc., Washington, D.C. (2000).
[22] K. MATYJASZEWSKI, J. QIU, D. SHIPP, and S. G. GAYNOR, Macromol. Symp. 155, 15 (2000).
[23] L. YE, P.A.G. CORMACK, and K. MOSBACH, Anal. Chim. Acta 435, 187 (2001).
[24] L. YE and K. MOSBACH, React. Funct. Polym. 48, 149 (2001).
[25] M. SZWARC, *Carboanions, Living Polymers and Electron Transfer Processes*, Interscience, New York (1968).
[26] M. SZWARC, *Ions and Ions Pairs in Organic Reactions*, Wiley Interscience, New York (1974).
[27] M. SZWARC and M. VAN BEYLEN, *Ionic Polymerization and Living Polymers*, Kluwer Academic Publishers, (1993).
[28] H. L. HSIEH and R. P. QUIRK, *Anionic Polymerization: Principles and Practical Applications*, Marcel Dekker, New York (1996).
[29] D.J. WORSFOLD, J.G. ZILLIOX, and P. REMPP, Can. J. Chem. 42, 3379 (1969).
[30] A. KOHLER, J.G. ZILLIOX, P. REMPP, J. POLLACEK, and I. KOESSLER, Eur. Polym. J. 8, 627 (1972).
[31] L.K. BI and L. J. FETTERS, Macromolecules 9, 732 (1976).
[32] R.N. YOUNG and L.J. FETTERS, Macromolecules 11, 899 (1978).
[33] F.A. TAROMI and P. REMPP, Makromol. Chem. 190, 1791 (1989).
[34] D. HELD and A.H.E. MULLER, Macromol. Symp. 157, 225 (2000).
[35] O. OKAY and W. FUNKE, Makromol. Chem. Rapid Commun. 11, 583 (1990).
[36] O. OKAY and W. FUNKE, Macromolecules 23, 2623 (1990).
[37] L. PILLE and D.H. SOLOMON, Macromol. Chem. Phys. 195, 2477 (1994).
[38] S. ABROL and D.H. SOLOMON, Polymer 40, 6583 (1999).
[39] M. NGUYEN, R. BECKETT, L. PILLE, and D.H. SOLOMON, Macromolecules 31, 7003 (1998).
[40] I. PIIRMA, *Emulsion polymerization*, Academic Press, New York (1982).
[41] *Emulsion Polymerisation and Emulsion Polymers*, Edited by P.A. Lovell and M. S. El Aasser, Wiley, Chichester (1997).
[42] M. ANTONIETTI, R. BASTEN, and S. LOHMANN, Macromol. Chem. Phys. 196, 441 (1995).
[43] F. CANDAU, in *Polymerization in Organic Media*, Edited by E. C. Paleos, Gordon & Breach, Philadelphia (1992), p. 215.
[44] L.-W. CHEN, B.-Z. YANG, and M.-L. WU, Progr. Org. Coatings 31, 393 (1997).
[45] S.-Y. LIN, K.-S. CHEN, and L. RUN-CHU, Polymer 40, 6307 (1999).
[46] P.J. FLORY, J. Am. Chem. Soc. 63, 3083 (1941).
[47] J.-P. FOUASSIER, *Photoinitiation, Photopolymerization, and Photocuring: Fundamentals and Applications*, Hanser Gardner Pubns, Munich (1995).
[48] *Photopolymerization: Fundamentals and Applications*, Edited by A.B. Scranton, C. Bowman, and R.W. Peiffer,ACS Symposium Series Vol. 673, Am.Chem.Soc., Washington,D.C. (1997).
[49] A. CHARLESBY, *Atomic Radiation and Polymers*, Pergamon Press, Oxford (1960).
[50] M. DOLE, *The Radiation Chemistry of Macromolecules*, Academic Press, New York (1972).
[51] J. E. WILSON, *Radiation Chemistry of Monomers, Polymers and Plastics*, Marcel Dekker, New York (1974).
[52] *CRC Handbook of Radiation Chemistry*, Edited by Y. Tabata, Y. Ito, and S. Tagawa, CRC Press, Boca Raton (1991).

[53] *Radiation Processing of Polymers*, Edited by A. Singh and J. Silverman, Carl Hanser, München (1992).
[54] V.S. IVANOV, *Radiation Chemistry of Polymers*, VSP, Utrecht, The Netherlands (1992).
[55] R.J. WOODS and A. K. PIKAEV, *Applied Radiation Chemistry: Radiation Processing*, Wiley-Interscience, New York (1993).
[56] *Recent Trends in Radiation Polymer Chemistry* , Edited by S. Okamura,Advances in Polymer Science Vol. 105, Springer, (1993).
[57] J. ROSIAK, K. BURCZAK, W. PEKALA, N. PISLEWSKI, S. IDZIAK, and A. CHARLESBY, Radiat. Phys. Chem. 32, 793 (1988).
[58] I. KAETSU, K. UCHIDA, Y. MORITA, and M. OKUBO, Radiat. Phys. Chem. 40, 157 (1992).
[59] N. NAGAOKA, A. SAFRANJ, M. YOSHIDA, H. OMICHI, H. KUBOTA, and R. KATAKAI, Macromolecules 26, 7386 (1993).
[60] Z.-L. DING, M. YOSHIDA, M. ASANO, Z.-T. MA, H. OMICHI, and R. KATAKAI, Radiat. Phys. Chem. 44, 263 (1994).
[61] M. CARENZA and F. M. VERONESE, J. Controlled Release 29, 187 (1994).
[62] G.A.MUN, Z.S. NURKEEVA, V.V. KHUTORIANSKIY, A.D. SERGAZIYEV, and J.M. ROSIAK, Radiat. Phys. Chem. 65, 67 (2002).
[63] Y. MORITA, M. YOSHIDA, M. ASANO, and I. KAETSU, Colloid Polym. Sci. 265, 916 (1987).
[64] M. YOSHIDA, T. YOKOTA, M. ASANO, and M. KUMAKURA, Colloid Polym. Sci. 267, 986 (1989).
[65] M. YOSHIDA, T. YOKOTA, M. ASANO, and M. KUMAKURA, Eur. Polym. J. 26, 121 (1990).
[66] A. SAFRANJ, S. KANO, M. YOSHIDA, H. OMICHI, R. KATAKAI, and M. SUZUKI, Radiat. Phys. Chem. 46, 203 (1995).
[67] M. YOSHIDA, M. ASANO, I. KAETSU, and Y. MORITA, Yakuzaigaku 42, 137 (1982).
[68] Y. NAKA, Y. YAMAMOTO, and K. HAYASHI, Radiat. Phys. Chem. 40, 83 (1992).
[69] Y. NAKA and Y. YAMAMOTO, J. Polym. Sci. ,Part A: Polym. Chem. 30, 1287 (1992).
[70] Y. NAKA and Y. YAMAMOTO, J. Polym. Sci. ,Part A: Polym. Chem. 30, 2149 (1992).
[71] M. DREJA, W. PYCKHOUT-HINTZEN, and B. TIEKE, Macromolecules 31, 272 (1998).
[72] G.J. PRICE, in *Chemistry under Extreme or Non-classical Conditions*, Edited by R. van Eldik and C. D. Hubbard, Wiley/Spektrum Akademischer Verlag, New York/Heidelberg (1997), p. 381.
[73] T.J. MASON and J.P. LORIMER, *Sonochemistry: Theory and uses of ultrasound in chemistry*, Ellis Horwood, Chichester (1988).
[74] *Current Trends in Sonochemistry*, Edited by G. J. Price, Royal Society of Chemistry, Cambridge (1992).
[75] H. FUJIWARA and K. GOTO, Polymer Bulletin 25, 571 (1991).
[76] K.S. SUSLICK, M.W. GRINSTAFF, K.J. KOLBECK, and M. WONG, Ultrasonics Sonochem. 1, 65 (1994).
[77] Y. NAKA and Y. YAMAMOTO, Kobunshi. Ronbunshu. 50, 287 (1993).
[78] B. WANG, S. MUKATAKA, M. KODAMA, and E. KOKUFUTA, Langmuir 13, 6108 (1997).
[79] B. WANG, S. MUKATAKA, E. KOKUFUTA, M. OGISO, and M. KODAMA, J. Polym. Sci. Part B: Polym. Phys. 38, 214 (2000).
[80] B. WANG, S. MUKATAKA, E. KOKUFUTA, and M. KODAMA, Radiat. Phys. Chem. 59, 91 (2000).
[81] P. ULANSKI, ZAINUDDIN, and J. M. ROSIAK, Radiat. Phys. Chem. 46, 917 (1995).
[82] P. ULANSKI, I. JANIK, and J. M. ROSIAK, Radiat. Phys. Chem. 52, 289 (1998).
[83] P. ULANSKI, S. KADLUBOWSKI, and J. M. ROSIAK, Radiat. Phys. Chem. 63, 533 (2002).
[84] U. BRASCH and W. BURCHARD, Macromol. Chem. Phys. 197, 223 (1996).
[85] M. FRANK and W. BURCHARD, Makromol. Chem. , Rapid Commun. 12, 645 (1991).
[86] W. ARBOGAST, A. HORVATH, and B. VOLLMERT, Makromol. Chem. 181, 1513 (1980).
[87] B. GEBBEN, H. W.A. VAN DER BERG, D. BARGEMAN, and C.A. SMOLDERS, Polymer 26, 1737 (1985).
[88] P. ULANSKI and J. M. ROSIAK, Nucl. Instr. Meth. Phys. Res. B 151, 356 (1999).

[89] S. SABHARVAL, H. MOHAN, Y.K. BHARDWAJ, and A.B. MAJALI, Radiat. Phys. Chem. 54, 643 (1999).
[90] K.-F. ARNDT, T. SCHMIDT, and R. REICHELT, Polymer 42, 6785 (2001).
[91] S. KADLUBOWSKI, J. GROBELNY, W. OLEJNICZAK, M. CICHOMSKI, and P. ULANSKI, Macromolecules In press (2003).
[92] K.S. SCHMITZ, B. WANG, and E. KOKUFUTA, Macromolecules 34, 8370 (2001).
[93] R. CZECHOWSKA-BISKUP, M.Sc. Thesis, Technical University of Lodz, Poland, 2002.
[94] N.C. SANTOS, A.M.A. SOUSA, D. BETBEDER, M. PRIETO, and M.A.R.B. CASTANHO, Carbohydr. Res. 300, 31 (1997).
[95] C.B. AGBUGBA, B.A. HENDRIKSEN, B.Z. CHOWDHRY, and M.J. SNOWDEN, Colloid Surface A 137, 155 (1998).
[96] *Polymer Gels. Fundamentals and Biomedical Applications*, Edited by D. DeRossi, K. Kajiwara, Y. Osada, and A. Yamauchi, Plenum Press, New York (1991).
[97] K. PARK, W.S. W. SHALABY, and H. PARK, *Biodegradable Hydrogels for Drug Delivery*, Technomic, Lancaster (1993).
[98] *Hydrogels and Biodegradable Polymers for Bioapplications*, Edited by R. M. Ottenbrite, S.J. Huang, and K. Park,ACS Symposium Series 627 American Chemical Society, Washington, D.C. (1996).
[99] *Silicone Hydrogels: the Rebirth of Continuous Wear Contact Lenses*, Edited by D. Sweeney, Butterworth-Heinemann Medical, Oxford (2000).
[100] A.S. HOFFMAN, in *Macromolecules*, Edited by H. Benoit and P. Rempp, (1982), p. 321.
[101] K.R. KAMATH and K. PARK, Adv. Drug Delivery Rev. 11, 59 (1993).
[102] J.M. ROSIAK, J. Controlled Release 31, 9 (1994).
[103] J.M. ROSIAK, P. ULANSKI, L.A. PAJEWSKI, F. YOSHII, and K. MAKUUCHI, Radiat. Phys. Chem. 46, 161 (1995).
[104] N.A. PEPPAS, P. BURES, W. LEOBANDUNG, and H. ICHIKAWA, Eur. J. Pharm. Biopharm. 50, 27 (2000).
[105] M.E. BYRNE, K. PARK, and N.A. PEPPAS, Adv. Drug Delivery Rev. 54, 149 (2002).
[106] A.S. HOFFMAN, Adv. Drug Delivery Rev. 54, 3 (2002).
[107] N.B. GRAHAM, Chemistry & Industry 15/1990, 482 (1990).
[108] K. BURCZAK, T. FUJISATO, M. HATADA, and Y. IKADA, Proc. Japan Acad. Ser. B. Phys. Biol. Sci. 67, 83 (1991).
[109] M. KOZICKI, P. KUJAWA, L.A. PAJEWSKI, M. KOLODZIEJCZYK, J. NAREBSKI, and J. M. ROSIAK, Eng. Biomater. 2, 11 (1999).
[110] P. ULANSKI, I. JANIK, S. KADLUBOWSKI, M. KOZICKI, P. KUJAWA, M. PIETRZAK, P. STASICA, and J. M. ROSIAK, Polym. Adv. Technol. 13, 951 (2002).
[111] J. M. ROSIAK, A. RUCINSKA-RYBUS, and W. PEKALA, US Patent 4,871,490 (1989).
[112] J. M. ROSIAK, W. DEC, and A. J. KOWALSKI, Med. Sci. Monit. 2, 78 (1996).
[113] J. M. ROSIAK, A. J. KOWALSKI, and W. DEC, Radiat. Phys. Chem. 52, 307 (1998).
[114] A.S. HOFFMAN, MRS Bulletin Sept. 1991, 42 (1991).
[115] J. ED. DUSEK, *Responsive Gels: Volume Transitions*,Adv. Polym. Sci. Vol. 109, Springer, Berlin (1993).
[116] R. LANGER, Nature 392 (Supplement), 5 (1998).
[117] C. PICHOT, A. ELAISSARI, D. DURACHER, F. MEUNIER, and F. SAUZEDDE, Macromol. Symp. 175, 285 (2001).
[118] R. YOSHIDA, K. SAKAI, T. OKANO, and Y. SAKURAI, Adv. Drug Delivery Rev. 11, 85 (1993).
[119] D. SHIINO, Y. MURATA, K. KATAOKA, Y. KOYAMA, M. YOKOYAMA, T. OKANO, and Y. SAKURAI, Biomaterials 15, 121 (1994).
[120] T. MIYATA, N. ASAMI, and T. URAGAMI, Nature 399, 766 (1999).
[121] T. SHIGA, Y. HIROSE, A. OKADA, T. KURAUCHI, and O. KAMIGAITO, Proc. 1st Japan International SAMPE Symposium 659 (1989).
[122] T. SHIGA, Y. HIROSE, A. OKADA, and T. KURAUCHI, J. Intel. Mater. Syst. Struct. 4, 553 (1993).
[123] A. REMBAUM, S. P. S. YEN, and W. VOLKSEN, Chemtech March 1978, 182 (1978).

[124] A. REMBAUM and Z.A. TOKES, *Microspheres: Medical and Biological Applications*, CRC Press, Boca Raton (1988).
[125] S. MITRA, T. K. DE, and A. MAITRA, in *Encyclopedia of Surface and Colloid Science*, Edited by P. Somasundaran, Marcel Dekker, (2002), p. 2397.
[126] D. LAVAN, D. LYNN, and R. LANGER, Nature Drug Discovery 1, 77 (2002).
[127] S.P.S. YEN, A. REMBAUM, and R.S. MOLDAY, US Patent 4,157,323 (1979).
[128] A. REMBAUM, S. P. S. YEN, and W. J. DREYER, US Patent 4,138,383 (1979).
[129] M. NAIR and J.S. TAN, US Patent 5,078,994 (1992).
[130] N.B. GRAHAM and J. MAO, US Patent 5,994,492 (1999).
[131] A.V. KABANOV and S.V. VINOGRADOV, US Patent 6,333,051 (2001).
[132] A. REMBAUM, S. P.S. YEN, E. CHEONG, S. WALLACE, R.S. MOLDAY, I.L. GORDON, and W.J. DREYER, Macromolecules 9, 328 (1976).
[133] P. GUIOT and P. COUVREUR, *Polymeric Nanoparticles and Microspheres*, CRC Press, Boca Raton (1986).
[134] T. DELAIR, F. MEUNIER, A. ELAISSARI, M.H. CHARLES, and C. PICHOT, Colloid Surface A 153, 341 (1999).
[135] F. SAUZEDDE, A. ELAISSARI, and C. PICHOT, Colloid Polym. Sci. 277, 1041 (1999).
[136] H. KAWAGUCHI, K. FUJIMOTO, and Y. MIZUHARA, Colloid Polym. Sci. 270, 53 (1992).
[137] K. FUJIMOTO, Y. MIZUHARA, N. TAMURA, and H. KAWAGUCHI, J. Intelligent Mater. Syst. Struct. 4, 184 (1993).
[138] T. SHIROYA, N. TAMURA, M. YASUI, K. FUJIMOTO, and H. KAWAGUCHI, Colloid Surface B 4, 267 (1995).
[139] M. YASUI, T. SHIROYA, K. FUJIMOTO, and H. KAWAGUCHI, Colloid Surface B 8, 311 (1997).
[140] A. ELAISSARI, L. HOLT, C. VOISSET, C. PICHOT, B. MANDRAND, and C. MABILAT, J. Biomat. Sci. , Polym. Ed. 10, 403 (1999).
[141] K. ACHIHA, R. OJIMA, Y. KASUYA, K. FUJIMOTO, and H. KAWAGUCHI, Polym. Adv. Technol. 6, 534 (1995).
[142] H. VIHOLA, A. LAUKKANEN, J. HIRVONEN, and H. TENHU, Eur. J. Pharm. Sci. 16, 69 (2002).
[143] Y. SHIN, J.H. CHANG, J. LIU, R. WILLIFORD, Y.-K. SHIN, and G.J. EXARHOS, J. Controlled Release 73, 1 (2001).
[144] S.-Y. LIN, K.-S. CHEN, and L. RUN-CHU, Biomaterials 22, 2999 (2001).
[145] S. PENG and CH. WU, J. Phys. Chem. B 105, 2331 (2001).
[146] G.M. EICHENBAUM, P.F. KISER, D. SHAH, S.A. SIMON, and D. NEEDHAM, Macromolecules 32, 8996 (1999).
[147] G.M. EICHENBAUM, P.F. KISER, A. V. DOBRYNIN, S.A. SIMON, and D. NEEDHAM, Macromolecules 32, 4867 (1999).
[148] K.S. SOPPIMATH, A.R. KULKARNI, and T.M. AMINABHAVI, J. Controlled Release 75, 331 (2001).
[149] S. VINOGRADOV, E. BATRAKOVA, and A. KABANOV, Colloid Surface B 16, 291 (1999).
[150] S. V. VINOGRADOV, T.K. BRONICH, and A.V. KABANOV, Adv. Drug Delivery Rev. 54, 135 (2002).
[151] P.F. KISER, G. WILSON, and D. NEEDHAM, Nature 394, 459 (1998).
[152] P.F. KISER, G. WILSON, and D. NEEDHAM, J. Controlled Release 68, 9 (2000).
[153] R.A. SIEGEL, Nature 394, 427 (1998).
[154] S. KAZAKOV, M. KAHOLEK, I. TERAOKA, and K. LEVON, Macromolecules 35, 1911 (2002).
[155] F. DE JAEGHERE, E. ALLEMANN, F. KUBEL, C. GALLI, R. COZENS, E. DOELKER, and R. GURNY, J. Controlled Release 68, 291 (2000).
[156] A. BIFFIS, N.B. GRAHAM, G. SIEDLACZEK, S. STALBERG, and G. WULFF, Macromol. Chem. Phys. 202, 163 (2001).
[157] L.-A. LINDEN, in *Proc. 5th Int.Symp. "Chemistry Forum'99"*, Edited by M. Jarosz, Warsaw University of Technology, Warsaw (1999), p. 65.
[158] S. KADLUBOWSKI, A. HENKE, and P. ULANSKI. Unpublished data.
[159] S. KADLUBOWSKI and P. ULANSKI. Unpublished data.

[160] E.A.L. BALAZS, in *Cellulosics Utilisation*, Edited by H. P. Inagaki, Elsevier Applied Science, London (1989), p. 233.
[161] S. AL-ASSAF, G.O. PHILLIPS, D.J. DEEBLE, B. PARSONS, H. STARNES, and C. VON SONNTAG, Radiat. Phys. Chem. 46, 207 (1995).
[162] A. HENKE, M.Sc. Thesis, Technical University of Lodz, Poland, 2002.
[163] D.S. GIBBS, J.F. SINACOLA, and D.E. RANCK, US Patent 4,324,714 (1982).
[164] H.J. WRIGHT, D.P. LEONARD, and R.A. ETZELL, US Patent 4,377,661 (1983).
[165] H.J. WRIGHT, D.P. LEONARD, and R.A. ETZELL, US Patent 4,414,357 (1983).
[166] W.T. SHORT, R. A. OTTAVIANI, and D. J. HART, US Patent 4,570,734 (1985).
[167] K.G. OLSON, S.K. DAS, and R. DOWBENKO, US Patent 4,540,740 (1985).
[168] T. KURAUCHI, K. ISHII, A. YAMADA, and J. NOZUE, US Patent 4,563,372 (1986).
[169] C. GAJRIA and Y. OZARI, US Patent 4,567,246 (1986).
[170] K.G. OLSON, S.K. DAS, and R. DOWBENKO, US Patent 4,611,026 (1986).
[171] Y. TSUCHIYA and K. TOBINAGA, US Patent 5,200,461 (1993).
[172] G.P. CRAUN, D.J. TELFORD, and H.J. DEGRAAF, US Patent 5,508,325 (1996).
[173] G.P. CRAUN and V.V. KAMINSKI, US Patent 5,554,671 (1996).
[174] W. DANNHORN, L. HOPPE, E. LUHMANN, and H.-J. JUHL, US Patent 5,565,504 (1996).
[175] G.P. CRAUN, US Patent 5,576,361 (1996).
[176] G.P. CRAUN, US Patent 5,733,970 (1998).
[177] G.P. CRAUN, B.A. SMITH, and N.S. WILLIAMS, US Patent 5,877,239 (1999).
[178] H.-D. HILLE, S. NEIS, and H. MULLER, US Patent 5,977,258 (1999).
[179] M. ROTH, Q. TANG, and S.H. ELDIN, US Patent 5,994,475 (1999).
[180] D. SAATWEBER and B. VOGT-BIRNBRICH, Progr. Org. Coatings 28, 33 (1996).
[181] *Automotive Paints and Coatings*, Edited by G. Fettis, VCH Verlagsgesellschaft, Weinheim (1995).
[182] *Polymer Dispersions and Their Industrial Applications*, Edited by D. Urban and K. Takamura, Wiley-VCH, Weinheim (2002).
[183] V.G. CORRIGAN and S. R. ZAWACKY, US Patent 5,096,556 (1992).
[184] P.W. UHLIANUK, US Patent 5,407,976 (1995).
[185] C. RAQUOIS, J. F. TASSIN, S. REZAIGUIA, and A. V. GINDRE, Progr. Org. Coatings 26, 239 (1995).
[186] K. ISHII, Colloid Surface A 153, 591 (1999).
[187] Y.-J. PARK, M. J. MONTEIRO, S. VAN ES, and A. L. GERMAN, Eur. Polym. J. 37, 965 (2001).
[188] A. HENKE, E. JAEHNE, and H.-J. P. ADLER, Macromol. Symp. 164, 1 (2001).
[189] A. HENKE, Farbe und Lack 106, (2000).
[190] N. D. P. SMITH, UK Patent 1,242,054 (1967).
[191] W. FUNKE, J. Oil Col. Chem. Assoc. 60, 438 (1977).
[192] S. PORTER JR and B. N. MCBANE, US Patent 4,075,141 (1978).
[193] J. KUMANOTANI, Progr. Org. Coatings 34, 135 (1998).
[194] J.-F. TRANCHANT, H.-G. RIESS, and A. MEYBECK, US Patent 6,280,713 (2001).
[195] A. KUENTZ, H.-G. RIESS, A. MEYBECK, and J.-F. TRANCHANT, US Patent 5,711,940 (1998).
[196] J. C. SOLENBERGER, US Patent 3,941,728 (1976).
[197] J. C. SOLENBERGER, US Patent 3,941,730 (1976).
[198] A. J. DEYRUP, US Patent 4,012,352 (1977).
[199] D. S. GIBBS, US Patent 4,164,522 (1979).
[200] D. S. GIBBS, J. H. BENSON, and R. T. FERNANDEZ, US Patent 4,232,129 (1980).
[201] H. ALT, F. BAUMANN, J. WEIS, and A. KOPPL, US Patent 6,358,876 (2002).
[202] A. KÖPPL, H. G. ALT, and R. SCHMIDT, J. Organometal. Chem. 577, 351 (1999).
[203] M. L. ZWEIGLE and J. C. LAMPHERE, US Patent 4,172,066 (1979).
[204] B.-L. LEE and L. C. HRUSCH, US Patent 6,237,333 (2001).
[205] R.A. HERRETT and P. A. KING, US Patent 3,336,129 (1967).
[206] S.N. YEN and F.D. OSTERHOLTZ, US Patent 3,900,378 (1975).
[207] K. TANAKA, US Patent 5,013,349 (1991).

[208] T. TAKAHASHI, H. WATANABE, N. MIYAGAWA, S. TAKAHARA, and T. YAMAOKA, Polym. Adv. Technol. 13, 33 (2002).
[209] S.-M. CHENG, R.-C. LIANG, and Y.-H. TSAO, US Patent 5,811,220 (1998).
[210] S. SATAKE, Y. YATSUYANAGI, M. FUJI, and I. IMAGAWA, US Patent 5,545,694 (1996).
[211] S. SATAKE, Y. YATSUYANAGI, M. FUJI, and I. IMAGAWA, US Patent 5,547,999 (1996).
[212] M. FRYD and T. R. SUESS, US Patent 4,726,877 (1988).
[213] M. FRYD and T. R. SUESS, US Patent 4,753,865 (1988).
[214] M. FRYD, E. LEBERZAMMER, and S.A.R. SEBASTIAN, US Patent 5,075,192 (1991).
[215] K. KANDA, Y. ICHINOSE, S. ARIMATSU, K. KONISHI, and T. HASE, US Patent 5,393,637 (1995).
[216] A. KITAHARA and K. KONNO, US Patent 4,749,506 (1988).
[217] D. KUCKLING, I. G. IVANOVA, H.-J.P. ADLER, and T. WOLFF, Polymer 43, 1813 (2002).
[218] C. GRAF, W. SCHAERTL, and N. HUGENBERG, Adv. Mater. 12, 1353 (2000).
[219] G. HELLING, US Patent 4,513,080 (1985).
[220] M. NAIR, L.A. LOBO, and T.K. OSBURN, US Patent 6,001,549 (1999).
[221] J.D. DEBORD, S. EUSTIS, S.B. DEBORD, M.T. LOFYE, and L.A. LYON, Adv. Mater. 14, 658 (2002).
[222] J.H. HOLTZ and S.A. ASHER, Nature 389, 829 (1997).
[223] Y.-B. KIM, C.-H. PARK, and J.-W. HONG, US Patent 6,399,675 (2002).
[224] G.C. REX and S. SCHLICK, J. Phys. Chem. 89, 3598 (1985).
[225] J.H. MIN and J. G. HERING, US Patent 6,203,709 (2001).
[226] S. DURAN, D. SOLPAN, and O. GUVEN, Nucl. Instr. Meth. Phys. Res. B 151, 196 (1999).
[227] H. ICHIJO, R. KISHI, O. HIRASA, and Y. TAKIGUCHI, Polym. Gels and Networks 2, 315 (1994).
[228] T. CAYKARA, R. INAM, and C. OZYUREK, J. Polym. Sci. ,Part A: Polym. Chem. 39, 277 (2001).
[229] H. UNNO, X. HUANG, T. AKEHATA, and O. HIRASA, in *Polymer Gels. Fundamentals and Biomedical Applications*, Edited by D. DeRossi, Plenum Press, New York (1991), p. 183.
[230] G.M. EICHENBAUM, P.F. KISER, D. SHAH, W.P. MEUER, D. NEEDHAM, and S.A. SIMON, Macromolecules 33, 4087 (2000).
[231] S. PENG and C. WU, Macromolecules 34, 6795 (2001).
[232] S. PENG and C. WU, Polymer 42, 6871 (2001).
[233] B.R. SAUNDERS, H.M. CROWTHER, G.E. MORRIS, S.J. MEARS, T. COSGROVE, and B. VINCENT, Colloid Surface A 149, 57 (1999).
[234] G.E. MORRIS, B. VINCENT, and M.J. SNOWDEN, Progr. Colloid Polym. Sci. 105, 16 (1997).
[235] D.J. BEEBE, J. S. MOORE, J. M. BAUER, Q. YU, R.-H. LIU, C. DEVADOSS, and B.-H. JO, Nature 404, 588 (2000).

# IONIZING RADIATION INDUCED SYNTHESIS OF POLYMERS AND BLENDS WITH DIFFERENT STRUCTURES

G. SPADARO[a], C. DISPENSA[a], G. FILARDO[a], A. GALIA[b], G. GIAMMONA[b]
[a] Department of Chemical Engineering Processing and Materials,
Università degli Studi di Palermo
[b] Department of Chemistry and Pharmaceutical Technologies,
Università degli Studi di Palermo, Palermo,

Italy

**Abstract**

A review of radiation induced synthesis of polymer systems having ordered microstructures is reported. The aim of this reaserach is to propose the use of ionizing radiation as polymerization initiator in alternative to the more conventional chemical ways. In this paper the most significant results about: the radiation curing of epoxy resin based systems in order to obtain polymer matrices for advanced composites; the radiation induced dispersion polymerization of methylmethacrylate in carbon dioxide in near critical conditions; the synthesis of microgels through gamma radiation of aqueous solutions of α,β-poly(N-2-hydroxyethyl)-DL-aspartamide (PHG) in the presence of polyethylene glycol (PEG) derivatives, for controlled actives delivery, are reported.

## 1. INTRODUCTION

The applications of "Radiation Processing" in the Science and Technology of Materials have received, in the last period, more and more attentiont due to their possible advantages, with respect to the more traditional chemical processes, in term of energy saving, final properties of the obtained materials and environmental impact. In particular, several results are reported in the scientific literature about the use of ionizing radiation in order to induce polymerization processes, to modify the chemical structure and the properties of yet polymerized materials.

It is well known that ionizing radiation can promote both radical and/or ionic polymerization. Radical polymerization can be successfully performed by high energy radiation and can be carried out at room temperature, while chemical initiators are effective in well established temperature range. Furthermore radical polymerization does not need the use of initiators with a significant improvement of the purity of the materials thus obtained.

More strict operative conditions, instead, are requested for the ionic polymerization. For instance, cationic polymerization requires the presence of apt photo initiators which can overcome the inhibition action of the basic impurities present in the irradiated system, even in very small traces.

The irradiation of polymers can cause several molecular effects, such as chain scission, with molecular degradation, chain branching, with molecular weight increase, and crosslinking. All these phenomena usually coexist, and the prevalence of one depends on several parameters, such as the molecular structure of the irradiated polymer and the irradiation conditions, i.e. the total absorbed dose, the dose rate, the irradiation temperature, and the presence or not of gases in the irradiation environment. These molecular modifications significantly affect the most important applicative properties of the irradiated polymers, like mechanical and electrical. It is worth to note that polymer modifications also occur during radiation polymerization processes, due to the interactions of ionizing radiation with the polymerizing material.

All these behaviours allow to consider "radiation processing" an emerging technology; in particular its versatility makes this process very apt to induce controlled structure and morphology of the materials, both in the micro and nano scales.

In this paper a review of the main results obtained in the last years in some polymerization processes induced by ionizing radiation are presented; and in particular the curing of epoxy resins in presence of thermoplastic for synthesis of polymer matrices for high performance composites, the polymerization of vinyl monomers in "dense" $CO_2$ and the synthesis of hydrogels for controlled drug delivery are discussed

## 2. DISCUSSION

Curing of epoxy resins in the presence of thermoplastic for synthesis of polymer matrices for high performance composites [1–3].

In the last years manufacturing technologies which use high energy radiation for curing of epoxy resins have been paid of rising attention for the competitive advantages offered in term of product quality, environmental impact and low energy. Underpinning a wider commercial exploitation of these technologies is the availability of variety of resins formulations that can ensure the thermal, mechanical, adhesive properties and environmental resistance which would make them suitable for use as composite matrices. The first successful attempts to cure polymer matrices by ionizing radiation reported in literature are via radical polymerisation of acrylate-epoxy systems. The obtained materials did not match the required behaviour in term of glass transition temperature and mechanical properties for advanced aerospace and automotive applications.

Cationic polymerization in the presence of iodonium salts as initiators allowed to produce materials with better properties. Similarly to the well established thermal techniques, which use thermoplastic-epoxy resin formulations, in order to improve both the processing behaviour and the toughness, also cationic radiation curing of epoxy resins, in the presence of high molecular weight high performance thermoplastics, have been performed.

Here some results obtained in the radiation curing of epoxy resin based systems are discussed. The material formulations consist in mixtures of bifunctional and polyfunctional epoxy resins, with an iodonium salt as initiator in the presence or in absence of high modulus, high Tg, thermoplastic toughening agents.

Epoxy monomers curing has been done irradiating the monomer/thermoplastic mixtures at 150 kGy and the cured materials were analysed just after irradiation or after a thermal post-curing at 175°C for 2 hours. All the materials were characterized by dynamic mechanical thermal (DMTA) and morphological analysis. As general behaviour, DMTA tests, for samples only irradiated, always show two relaxations, thus indicating an heterogeneous structure. The first one (at temperatures in the range of about 60–70°C) can be related to the glass transition of a weekly cross-linked structure formed during irradiation, while the second one (at temperatures in the range 170–200°C) can be related to the glass transition of more cross-linked parts, which can be formed both during irradiation and during the evolution of those parts having low glass transition temperatures caused by the thermal treatment inherent to the heating during DMTA tests. A confirmation of this hypothesis is the fact that samples tested after post-irradiation thermal curing present only the relaxation at high temperature.

For what concerns the effect of the system composition, we can observe that the presence of a three-functional monomer significantly increases the high temperature glass transition up to about 200°C, while no plasticization effects are seen for systems containing the thermoplastic component.

The morphology of the formulations with thermoplastic additives has been also investigated by scanning electron microscopy. In order to achieve high mechanical performances, in fact, a uniform distribution of well anchored thermoplastic particles in the matrix has to be obtained. SEM analyses indicate that in some irradiation conditions a co-continuous structure can be obtained with particles dimensions of tenth of nanometres.

**Polymerization of vinyl monomers in "dense" $CO_2$ [4,5]**

Aim of this research is to study the use of ionizing radiation to induce a dispersion polymerization of vinyl monomers in carbon dioxide at temperatures and pressures near the critical conditions.

During recent years, the use of supercritical carbon dioxide as reaction medium has seen a rapid growth, primarily due to the need to develop environmentally acceptable alternative to conventional organic solvents in a wide range of processes, including polymerization. In fact $CO_2$ offers many advantages over conventional solvents because is a non-toxic, non flammable, inexpensive and readily available and its critical values, 32.1°C and 7.4 MPa, are relatively low with respect to other possible critical reaction media. Furthermore the use of ionizing radiation as initiator for polymerization reactions allows carrying out the process at lower temperature compared with processes with chemical initiators and it is possible to operate in $CO_2$ near-critical conditions with a significant reduction in the operating pressure.

The results here discussed are obtained using methylmethacrylate (MMA) as vinyl monomer, which is soluble in dense $CO_2$. If the polymerization is conducetd in the presence of only MMA, the solubility of the polymerizing material decreases up to precipitation. In these operative conditions, precipitation polymerization, it is not possible to control the molecular weight and the structure of the obtained polymer. A possibility to control the polymerizations is the use of siloxane-based macromonomers, which allow to carry out the polymerization in micelles dispersed in the reaction medium.

The reactions conditions were: P = 60 bar when the temperature was 30°C and P=77 bar when the temperature was 39°C. The process was conducted with different siloxane based macromonomers, with different chain terminations (winyl, acetoxy and epoxy) and with different molecular weights (in the range 1000–20000 g/mol).

MMA undergoes to radical polymerization with a conversion which is linearly dependent on the abosorbed dose up to very high conversion values (about 80%) both at low and high temperature The presence of stabilisers allows to obtain spherical particles with a very uniform distribution in the range of diameters of 2–6 μm. For what concerns the molecular behaviour, the polymethyl methacrylate obtained in these conditions has a high molecular weight, $M_n$ up to 830 Kg/mol, and dynamic mechanical analysis in the melt state indicates that the material has a complex structure, with high density of entanglements.

## 3. SYNTHESIS OF MICROGELS FOR ACTIVE RELEASE [6,7]

Hydrogels are three-dimensional water swollen structures composed of mainly hydrophilic homopolymers or copolymers. These have been proposed for use as wound dressing, biosensors, contact lenses, artificial organs, and as drug delivery systems. Hydrogels are called reversible or physical gels when the networks are held together by molecular entanglements and/or by secondary forces including ionic. On the contrary they are called permanent or chemical gels when the network is formed by covalent bond among the molecular chains. There are a number of different chemical and physical methods used for the formation of permanent hydrogels; but the use of ionising radiation appears to be very useful for all the applications when very pure products are required, such as for medical purposes.

Here we report the synthesis and characterization. of microgels through irradiation of aqueous solutions of acryloated α,β-poly(N-2-hydroxyethyl)-DL-aspartamide (PHG) in the presence of polyethylene glycol (PEG) derivatives, i.e. poly(ethylene glycol) dimethacrylate (PEGDMA) or poly(ethylene glycol) dyacrylate (PEGDA). The irradiation at low doses (2.5-3.5 kGy) gives rise to the formation of microgels whose rheological behaviour depends on the presence of PEG derivatives. It is

interesting to note that the lyophilized microgels, when kept in contact with water, retain their initial properties, an homogeneous structure with transparency and rehological behaviour comparable to that of the starting materials.

## REFERENCES


[1] DISPENZA, C., SCRÒ, F., VALENZA, A., SPADARO, G., "High energy radiation cure of resin systems for structural adhesives and composite applications", Radiat. Phys. Chem. 63 (2002) 69–73.

[2] DISPENZA, C., DI CRISTOFALO, A., CALDERARO, E., SPADARO, G., "Novel radiation curable epoxy systems for composite applications", 23rd International SAMPE Europe Conference, Paris, 9–11 April 2002, 359–368.

[3] SPADARO, G., CALDERARO, E,. TOMARCHIO, E., DISPENZA, C., "Novel epoxy formulations for high energy radiation curable composites", Radiat. Phys. Chem. in press.

[4] FILARDO, G., CAPUTO, G., GALIA, A., CALDERARO, E., SPADARO, G., "Polymerization of methyl methacrylate through ionizing radiation in $CO_2$ based dense systems", Macromolecules 33 (2000) 278–283.

[5] CAPUTO, G., SPADARO, G., GALIA, A., SCRÒ, F, FILARDO, G., "Gamma-radiation induced polynerization of vinyl monomers in dense $CO_2$" Radiat. Phys. Chem. 63 (2002) 45–51.

[6] PITARRESI, G., LICCIARDI, M., CAVALLARO, G., SPADARO, G., GIAMMONA, G., "Hydrogels containing 5-Fluorouracil obtained by γ–irradiation. Synthesis, characterization and in vitro release studies" Colloid and Polymer Science 279 (2001) 579–588.

[7] PITARRESI, G., LICCIARDI, M., CRAPARO, E.F., CALDERARO, E., SPADARO, G., GIAMMONA, G., "Hydrogels of polyaspartamide and 65 (2002) 159–167.

# RADIATION EFFECTS ON NANOPARTICLES

D. MEISEL
The Radiation Laboratory and Department of Chemistry & Biochemistry,
University of Notre Dame, Notre Dame, IN,
United States of America

**Abstract**

Radiation techniques can aid in the synthesis of nanoparticles. Whereas other approaches are commonly used as well, the control provided by the broad range of dose and dose-rate might offer advantages in fine-tuning the size and the size distribution of the particles. Using these techniques, complex structures such as bimetallic or metal-insulator core-shell structures can be produced using radiolytic methods, alone or in combination with chemical approaches. Because particles in the nanosize regime allow use of spectrophotometric techniques the utilization of radiation tools, such as pulse radiolysis in combination with its various detection methods, allow detailed studies of the mechanisms that govern the processes initiated by the radiation. These in turn provide information on improving and broadening the synthetic methods. Most significantly they also provide information on how to better utilize the nanostructure. Radiation in combination with nanomaterials may be used to improve the function of the material. Examples from three areas: Redox catalysis, environmental remediation and radiotherapy are provided. In aqueous solutions, nanoparticles of noble metals can convert all of the reducing and oxidizing equivalents to produce $H_2$ from water (and alcohol). This is because the particles catalyze the conversion of radical to two-electron reductants. Radiation, which can penetrate opaque materials, is used in the clean up of contaminated soils. In combination with other techniques its efficiency can be enhanced significantly. Using the extreme flexibility and enormous specificity provided by surface modification of nanoparticles with biomolecules one could suggest future direction to utilize them in targeted radiotherapy.

## 1. INTRODUCTION

In recognition that the scientific community is turning to focus on the interactions between molecules, rather than atoms within a molecule, we were studying the effects of radiation on assemblies of molecules. This led us to study radiation effects at the nanoscale regime. We identify areas of interesting scientific questions, we show how they can be addressed using radiation chemistry tools and we propose directions to follow, which will also lead to technological advances. We discuss only bottom-up approaches, from the molecular level to the nano-size ensemble. Others in this workshop discuss top-down approaches, such as radiation-based lithographic techniques.

The potential of combining radiation effects with nanomaterials has been recognized from the very early stages of nano-science research. As was extensively shown in this workshop in the many uses of nanostructures, and nanoparticles in particular, from catalysis, bio sensing, nano-electronics, magnetic applications including separations, mechano-chemical conversion, and to molecular computing, radiation can play a significant role. Two complementary approaches to nanomaterials were discussed in this workshop:

- The Top-Down approach - where one starts with the bulk material and machines his way down to the nano-scale, and
- The Bottom-Up approach, starting at the molecular level and building up the material through the small cluster level to the nanoparticle and the assembly of nanoparticles.

The use of radiation, UV beam, electron-beam, or focused ion-beam has been discussed and is clearly central to the fabrication of the nanostructured systems. The relative advantages and deficiencies of each of them are still to be clarified as the technology advances. Whether UV or electron beam will lead to the highest resolution is still debated but it is clear that these techniques offer unmatched reproducibility and very narrow size distribution.

For these advantages, though, one pays with relatively slow generation rate and rather high production cost. The bottom-up approach, however, offers fast and simple production methods, lower

size regime, down to the molecular level, and lower costs. Combination of both approaches may perhaps offer the ultimate approach [1].

In the following we summarize our own perception of the use of radiation in the bottom-up strategy of generating nanoparticles and in the combined utilization of radiation and nanoparticle systems. This combination, if properly employed, may offer advantages beyond the algebraic sum of the two. Rather, we expect significant synergistic effects to result from the use of radiation on nano-sized systems, far beyond the effects one observes in bulk materials. We show that radiation can be extremely useful in the three stages of science and technology research:

1. In the synthesis and the production of the nanoparticles, both metallic and semiconductor particles. In this application radiolysis is but one more method, out of the large arsenal of synthetic strategies available to the scientist. Nonetheless, because of the extreme range of reactivity of species produced by the radiation, it creates redox levels that are hard to achieve by other methods. Furthermore, because of the ability to fine-tune the dose and the dose-rate it may offer better control over the sizes and size distribution that one may obtain.
2. In understanding the processes and the mechanisms that operate and lead to the observable phenomena. Here the combination of radiation sources and detection techniques provides a powerful tool to study how things happen and what leads to the ultimate result. This in turn is used to improve either the method of production of the particles or the application of the nanomaterial.
3. The application of nanoparticles in combination with radiation may offer advantages over using either one alone. Here we provide examples from redox catalysis, specifically hydrogen production from water, and from environmental remediation. We also suggest future applications in radiotherapy, where targeted preferential destruction of specific cells may be possible using the higher density of solid particles and the unmatched surface modification methodologies that nanoparticles offer.

It should be emphasized that nano-science is a relatively young science and technology enterprise. Therefore, the scientific effort presently dominates while the technology is beginning to emerge. Furthermore, the three directions listed above are not as hierarchical as it may seem; rather, it is an integrative effort. The information collected from one approach contributes to the other. Synthetic difficulties are overcome as the mechanisms for the radiolytic production become clear and improved utilization of the nanoparticle may be developed once the synthesis is improved and the mechanism of operation is understood. Finally, it is clear that nano-science will break disciplinary barriers. The structures involved are beyond the size of simple molecules and thus will require material science expertise; on the other hand, these dimensions are well within the regime of common biomolecules. Significantly, many of the functions expected from the nanoparticles resemble functionalities routinely performed by biochemical entities, e.g., specific molecular recognition in sensing devices. A combination of chemical, physical, and biological disciplines will be needed in the application of nano-structures. This multidisciplinary approach should apply here, in the use of radiation in nano-science, as well. Tight contact of various disciplines and areas of expertise is required in order to bring about the beneficial uses of radiation in science and technology.

**Radiation in Production and Synthesis**

The use of radiation to synthesize nanoparticles in aqueous dispersions started in the late seventies. An early report of Henglein suggested not merely the synthesis of metallic particles in water but also their utilization as redox catalyst in the conversion of reducing organic radicals to H2.2. Since then numerous reports describe the use of radiolysis in the synthesis of metallic nanoparticles and a few extend this approach to the synthesis of semiconductor particles.

Henglein and coworkers [3–5] and Belloni and coworkers [6–8] describe the radiolytic reduction of many metal ions either single metal or in combination with another metal to generate

metallic or bimetallic mixtures as well as core-shell structures. To obtain metallic particles from their parent ions one only needs to ensure reductive conditions during the irradiation. The oxidizing equivalents, OH radicals, can conveniently be converted to reducing radicals by the addition of organic scavengers (e.g., alcohols, formate ions). The latter will produce reducing radicals following hydrogen abstraction by the OH radical.

$H_2O$ /\/\/—> e-aq, H, OH, $H_2$, $H_2O_2$ (1)
OH + $RCH_2OH$ —> RC•HOH + $H_2O$ (2)
nC•HOH + M(I)—> (M)n + $RCH_2OH$ (where M is a metal) (3)
ne-aq + M(I) —> (M)n (4)

The radiolytic approach may offer some advantages because of the fine control over the rate of generation of the growing species afforded by the control over the dose rate delivered to the sample [9–11]. Furthermore, the mechanism of nucleation and growth can be delineated and properties, such as absorption spectra or redox potentials, of the growing clusters can be determined [12, 13].

**Core**

¨ $H_2O$ /\/\/\Ń > $e^-_{aq}$, ?H, ?OH
?OH (?H)+$CH_3OH$ Ń > ?$CH_2OH$ + $H_2O$ ($H_2$)
$e^-_{aq}$ + $N_2O$ (+$H^+$) Ń > ?OH + $N_2$

n$AuCl_4^-$ + n(?$CH_2OH$) Ń > ($Au_n^0$)

**Shell**

‡ $Ag(CN)_2^-$ + ?$CH_2OH$ -- > $Ag^0$ + $CH_2O$ + $H^+$ + $2CN^-$

Î $(Au)_n$+$Ag(CN)_2^-$ + ?$CH_2OH$ Ń > $(Au)_nAg^0$ + $CH_2O$ + $H^+$ + $2CN^-$

*FIG. 1. Scheme I: Generation of Au-Ag core-shell nanoparticles using radiolytic reduction. Note that the silver cyanide complex cannot be reduced directly by the methanol radicals, as illustrated in Scheme II.*

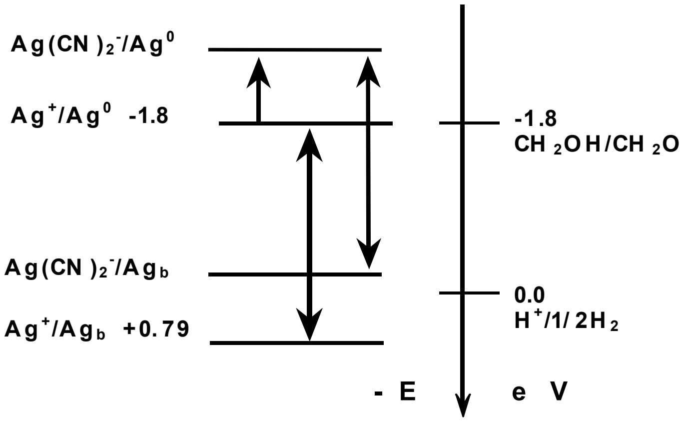

*FIG. 2. Scheme II: Redox potentials of Ag+/Ag and $Ag(CN)_2^-$ to the single atom and to an atom on the bulk metal. The redox potential of $CH_2OH/CH_2O$ is also shown for comparison. The double-arrow lines represent the lattice stabilization by the seed metal. The small arrow represents the complexation energy.*

Scheme I describes the production of core-shell nanoparticles of silver on gold. To generate bimetallic core-shell structures one would rely on the large difference in redox potentials between the reduction of the parent ion to a single atom and its reduction to the bulk metal. This is illustrated in

Scheme II for the case of silver and gold. Reduction of silver cyanide by $CH_2OH$ radicals to the single-atom level is essentially impossible but its reduction on top of existing seed metallic particles of silver or gold is nearly 2 V more positive and therefore, easily achievable. The core seed particles of the first metal will then serve as the nuclei for the shell metal. Using this strategy only few new seeds are generated and most of the reduction occurs on top of the existing seeds.

When the same metal is deposited on existing seeds, e.g., using a different parent complex so the redox potential allows only reduction at the surface of "seeds", the synthesis leads merely to increase in the particles size [14]. The rate of particle growth is inversely proportional to the square of the size of the particle because the generation of a new monolayer is proportional to the square of the radius. On the other hand, the rate of reduction of the precursor ion is directly proportional to the size (the rate constant is proportional to the diffusion coefficient of the reducing radical or accepting ion and to the radius of the particle). The net rate of size increase is, therefore, inversely proportional to the size. This results in narrowing of the size distribution as the particles grow. The smaller particles grow faster than the larger ones focusing the distribution of sizes. An example of the particles produced is shown in Figure 3. As can be seen in that figure, high quality, narrow size distribution is obtained in these preparations. The four micrographs of Figure 3 show particles obtained by using the previous preparation as seed cores for the next one and increasing the total concentration of silver by a factor of eight each time (clockwise from top-left). The size then increases by a factor of two, as expected if no new seeds are generated upon the reduction of the Ag (CN)2- complex on top of the existing Ag seeds.

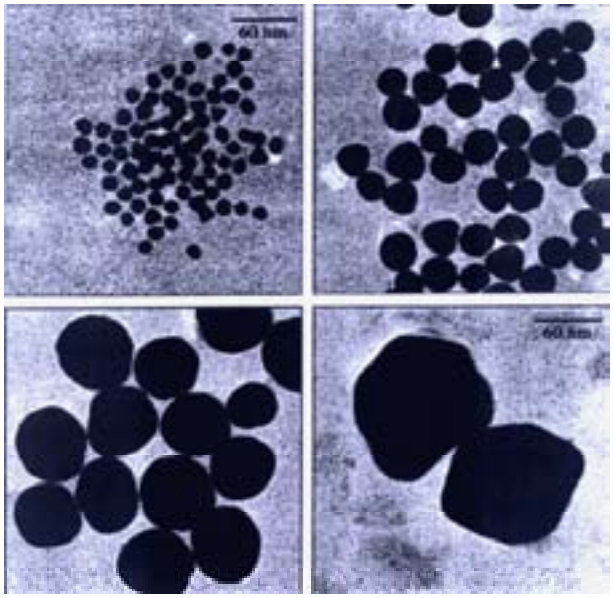

*FIG. 3. Example of particle production.*

Well-defined, shells with clear boundaries of Ag on Au cores were obtained by several groups. No stress is introduced at the bimetallic interface because the lattice parameters of silver and gold are essentially identical.

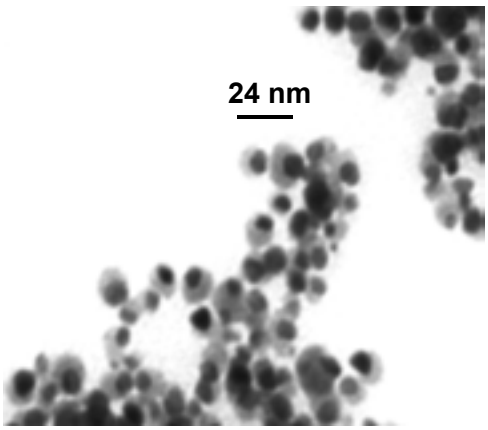


*FIG. 4. Ag "shells" radiolytically deposited on 8 nm Pt core nanoparticles. Note that the shell is eccentric.*

Figure 4 demonstrates the consequences of mismatch of only a few percent in the lattice parameters of the core and the shell, specifically for silver shell on platinum core. Instead of generating a concentric shell, the growing Ag layers prefer to deposit on partially formed islands of Ag rather than on the Pt core. This leads to an eccentric growth of the shell [15]. It was also discovered that the core shell structures, even of the gold-silver pair, rapidly alloy as the particle size decreases.16 This was attributed partially to the excess free energy of the particles that leads to a pronounced reduction of the melting temperature of the small particles [17].

Furthermore, the abundance of defects available at the bimetallic interface of the small nanoparticles contributes significantly to enhanced diffusion of the metals into one another.

To initiate radiolytic growth of semiconductors one component of the material, e.g., Ag+ or Cd2+ is added to the solution. An organic precursor that contains the counter ion, RX, where X is a halide or chalcogenide, is also added. The reaction of RX with $e^-_{aq}$ releases the counter ion, $X^-$ (Reaction 5; R often contains an hydrophilic group, e.g., -OH or -CO2H to increase solubility). This initiates the growth process that can be then followed using spectrophotometric or conductivity detection techniques [18–20].

$$e^-_{aq} + RCH_2X \longrightarrow RCH_2 + X^- \quad (X^- = SH^- \text{ for CdS or halide for AgX}) \quad (5)$$

A major motivation to use radiolytic techniques to initiate the production of the particles is to study the mechanism of their growth and the properties of the various intermediates. Indeed, using this approach the absorption spectrum of the single molecule (e.g., AgX, CdS) could be measured and the equilibrium constant between the molecule and its component ions were determined. As might be expected, these studies reveal that the single molecule dissociates into its component ions to a much larger extent than the bulk material. Further, using this approach the effect of dose and dose rate on the size and size distribution of the resulting bimetallic Au-Pd and CdS could be delineated [9, 10]. Many chemical analogous techniques were devised to prepare similar nanoparticle combinations using a wide variety of reducing agents. Because of the generation of similar reactive radical in radiation and sonochemical initiation of reductive processes, generation of metallic and semiconductor particles using sonolysis is quite similar to the radiolytic approach [21, 23].

**Mechanistic Understanding from Radiolytic Studies**

The examples described above, which focused on synthetic capabilities of nanoparticles using radiation, already demonstrate the great potential in using radiation-based techniques to provide understanding of physical and chemical processes. Developing the mechanism for utilizing

nanoparticles can be just as useful. Here we provide two more examples where mechanistic understanding can improve the utilization of the nanoparticles in other areas. In the first example, understanding of redox catalysis of the hydrogen evolution reaction on metallic nanoparticles provides the rationale for their use in diverse catalytic applications including photoelectrochemical solar cells and the generation of hydrogen for the anticipated hydrogen economy [24]. The second example is an example of the general "current doubling" effect that led to a significant enhancement of the sensitivity of silver photography [25, 26].

Reactions that occur at the surface of nanoparticles are relatively easy to detect using conventional optical spectroscopy because the size of the particles is often much smaller than the wavelength of the incident light thus minimizing light scattering interference. Using pulse and steady-state radiolysis techniques Henglein and coworkers.24 have shown that many reducing organic radicals may be used to reduce water to molecular hydrogen in the presence of metallic nanoparticle, rather than react via their usual recombination or disproportionation pathways. Several other reduction processes, such as the reduction of alkyl halides or the reduction of metal ions as described in the previous section, could be induced as well by the same reducing radicals. The now widely accepted mechanism assumes two essentially independent steps for the catalytic reduction process:

**Electron transfer from the reducing radical to the nanoparticle**

Accumulation of electrons on the particles and their transfer to an acceptor in the solution (e.g. metal ion in the last reaction of Scheme I, or water in the hydrogen evolution reaction) once enough overpotential for the relevant reaction has been achieved. The "nanoelectrode" mechanism for redox catalysis is shown in Scheme III (Fig. 5).

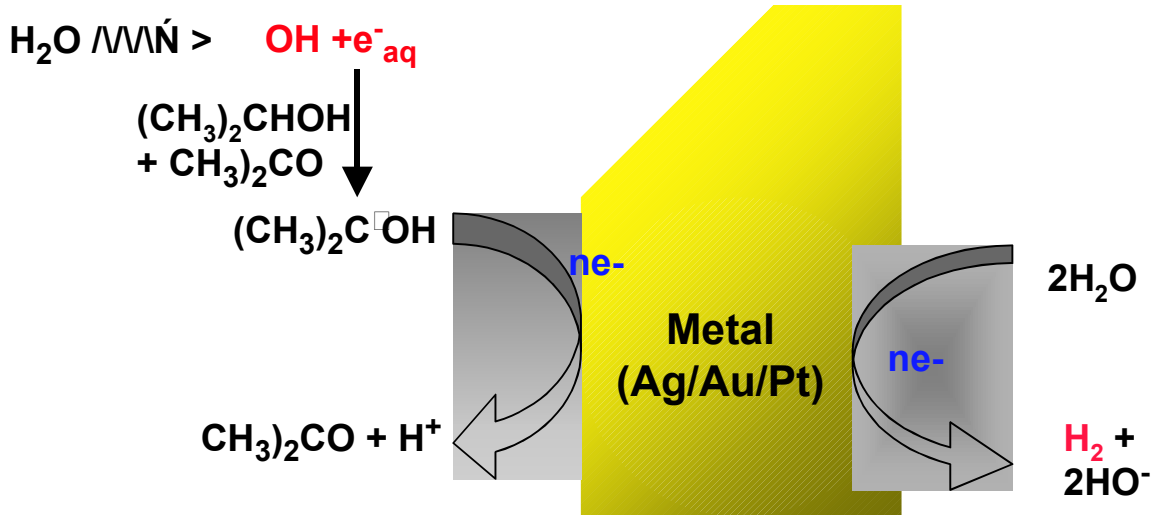


*FIG. 5. Scheme III: The nanoelectrode mechanism for the conversion of reducing organic radicals to molecular hydrogen (following the cover page of J. Phys. Chem. B 107 (issue 30) 2003, Arnim Henglein Festschrift).*

For the hydrogen evolution reaction this catalytic process increases the yield of H2 from G(H2) = G(H) + G0(H2) = 1.1 molecules per 100 eV to G(H2) = G(H) + G0(H2) + [G(OH) + G(e-aq)]/2 = 3.9 molecules per 100 eV upon the addition of metallic nanoparticles. Of course, this increase in hydrogen yield comes at the expense of the destruction of isopropanol and acetone.

The conversion of OH radicals, strongly oxidizing species, to strongly reducing radicals by a reaction with an alcohol is commonly labeled "current doubling reaction" in electrochemistry. In

Scheme III it doubles the number of electrons that are passed to the nanoelectrode relative to G (e-aq) since G(OH) = G (e-aq). In fact its effect on the ability of the system to generate hydrogen is much larger than merely doubling the amount of $H_2$. In the presence of the oxidizing OH radicals a large fraction of the reducing radicals (e.g., e-aq) will recombine with the former radical. A well-documented current-doubling reaction is the abstraction of H atom from formate.

$$OH + HCO_2^- \longrightarrow CO_2^- + H_2O \qquad (2a)$$

This reaction, Reaction 2a, generates the strongly reducing $CO_2^-$ ($E^0(CO_2/CO_2^-)$ = 1.9 V vs. NHE). This basic mechanism has been recently utilized to significantly enhance the sensitivity of silver-based photography [25].

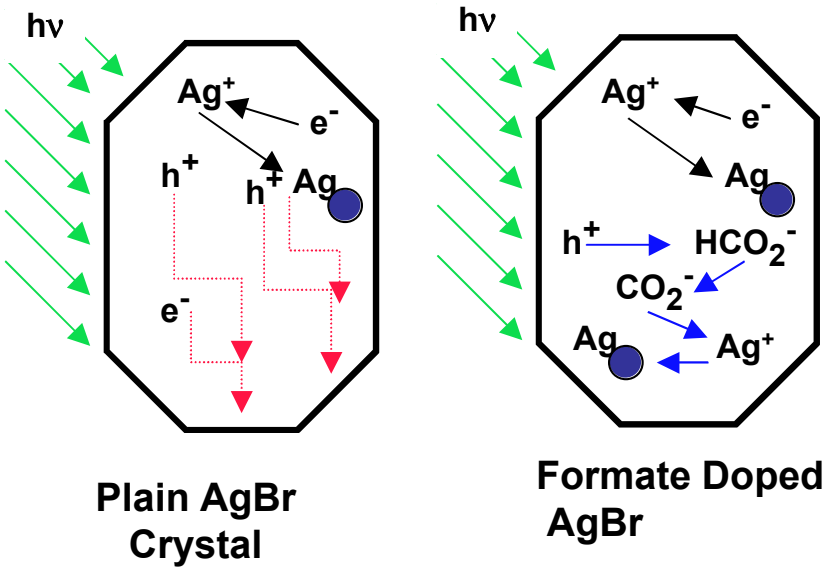


*FIG. 6. Enhanced sensitivity of silver photography by doping with formate. Left: Plain crystal. Red dotted arrows indicate annihilation processes. Right: Formate doped crystal. Following Ref. 26.*

Formate ions doped in silver bromide emulsions scavenge the light-generated holes in the silver bromide crystallites and generate CO2- radicals. Elimination of the holes prevents their recombination with electrons and allows reduction of Ag+. The generation of CO2- radicals doubles the reduction equivalents (Figure 6) [26]. The combined effect enhances the sensitivity of the photographic emulsion by an order of magnitude.

**Radiation and Nanoparticles Symbiotic & Synergistic Applications**

The dimensions of nanoparticles are similar to the dimensions of the common spurs in low LET irradiation of polar solvents. Therefore, it is conceivable that ionization events within the solid particle will find their way to the particle surface. In such a case then, ionization events within the particle can be passed on to the other phase, e.g., an aqueous solution or a polymeric matrix. This "communication" between the two phases may be utilized to enhance the effect of the radiation on the continuous phase. The first question, therefore, is do the ionization products migrate to the surface of the particle? It should be recognized, of course, that these are highly reactive intermediates, and therefore, the migration to the surface and reaction with the solution phase competes with other processes such as recombination and annihilation or trapping of the holes and electrons within lattice

or surface defects. There is no doubt that if the particle is large enough none of the charge carriers will escape the solid. Thus, the distance of migration within a particle is a question of kinetic competition and its dependence on size.

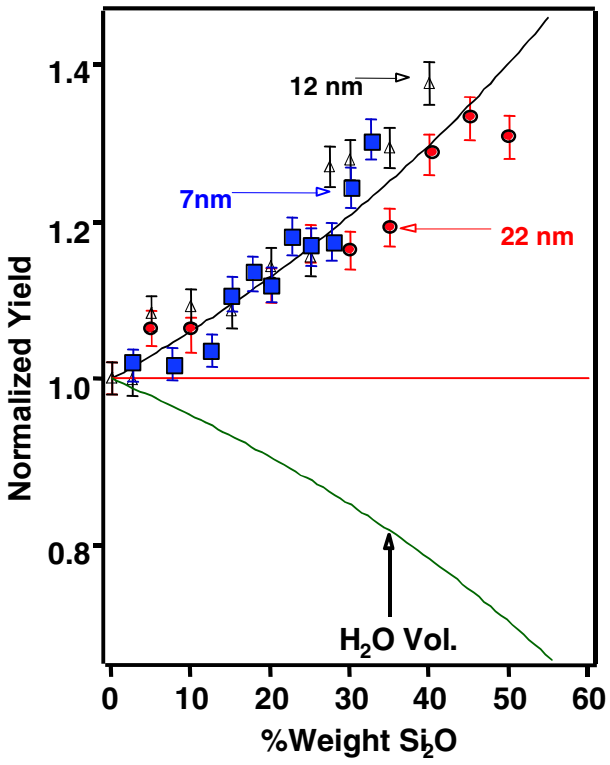


*FIG. 7. Normalized yield of hydrated electrons from irradiated suspensions of silica particles of various sizes. The upper and lower curves are the increase in density and decrease of water volume with increasing $SiO_2$ loading, respectively.*

Recent results from our group show that hot electron from silica nanoparticles do migrate the aqueous phase even from the largest available particles (22 nm in diameter) [28]. In stark contrast, holes remain trapped even at the smallest particles studied (7 nm) [29]. Counter intuitive, as can be seen in Figure 7, decreasing the fraction of water in suspensions of silica particles increases the concentration of e-aq. This increase in concentration of e-aq is attributed to the increase in absorbed dose by the sample. From this result one may conclude that the yield of molecular hydrogen from aqueous suspensions will be larger than it is from the solution in the absence of the silica particles. If, in addition to the silica particles the suspension also includes small amounts of metallic nanoparticles (mM on atom basis), all these hydrated electrons can be transformed to H2, further increasing the yield of hydrogen beyond that shown in Scheme III.

The question of how far can these additional electrons migrate before the competing reactions prevent their appearance at the interface has only recently been addressed. The amount of electrons that appear at the aqueous-particle interface can be estimated by adsorbing electron acceptors to the surface of the particles [30].

Figure 8 shows the time-profile of absorption at 395 nm (the maximum absorption from MV+ radicals) following 14 ns radiation pulse on silica (5 w%) suspension coated with sub-monolayer methyl viologen (MV2+; 3 mM) N2O saturated solution.

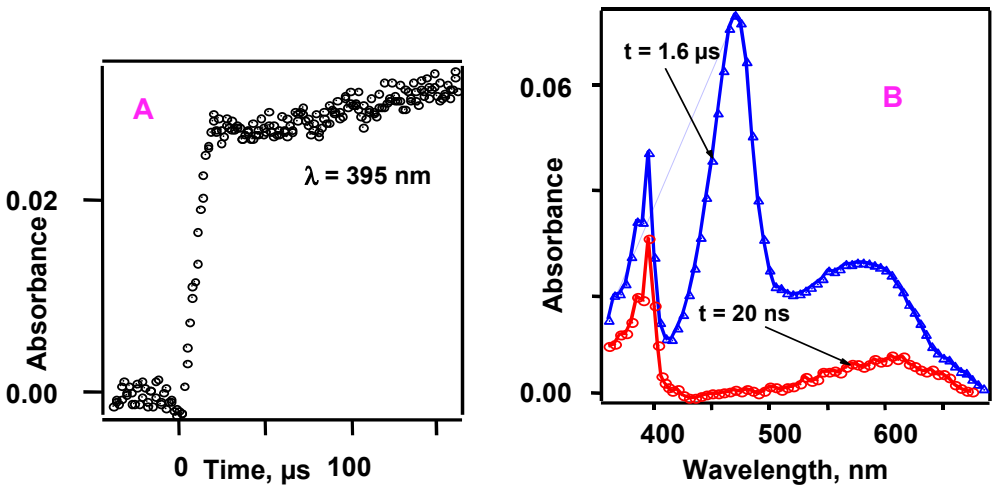


*FIG. 8. A) Time profile for the formation of $MV^{+}$ radicals in silica suspension (5 w%) containing sub-monolayer adsorbed $MV^{2+}$ (3 mM). B) Absorption spectra of the product immediately after the pulse and 1.6 μs later showing the difference between $MV^{+}$ from electrons in the particle and $MVOH^{2+}$ adduct from OH reaction from the bulk water. Taken from Ref. 31.*

The spectrum of this species is indeed identical to that of MV+ (Figure 8B) and easily distinguishable from the slowly produced product of the OH reaction with MV2+. From these observations it is clear that the adsorbed molecules capture electrons that are generated inside the particle [31]. The amount of electrons captured at the interface depends on the surface coverage and the size of the particle. For a given surface coverage, less electrons are captured at the surface of the larger particles because the probability that the competing reactions of recombination or trapping will occur increases with the particle size. As can be seen in Figure 9, at any coverage the dependence on particle size extrapolates to a vanishing small yield when the radius of the particle is 15 nm. Stated differently, when the particle size is larger than 30 nm no electrons will appear at the surface. To our knowledge this is the only material for which we have such information.

Knowledge of the distance that the charge carriers may migrate is very useful in estimating the outcome of irradiation of a multi-component system where at least one component is of nanoscale dimensions. As already mentioned this may determine the yield of hydrogen generation from aqueous suspensions, a question of major interest in the management of nuclear waste [32]. Its relevance to radiation induced polymerization and the possibilities that it offers in initiating cross-linking at the surface of solid particles were discussed at the IAEA Experts Meeting in Notre Dame in September 2003. Similarly, the utilization of solid particles in improving the mechanical properties of rubber products depends on binding the particles to the polymeric material, as discussed in the present Experts Meeting.

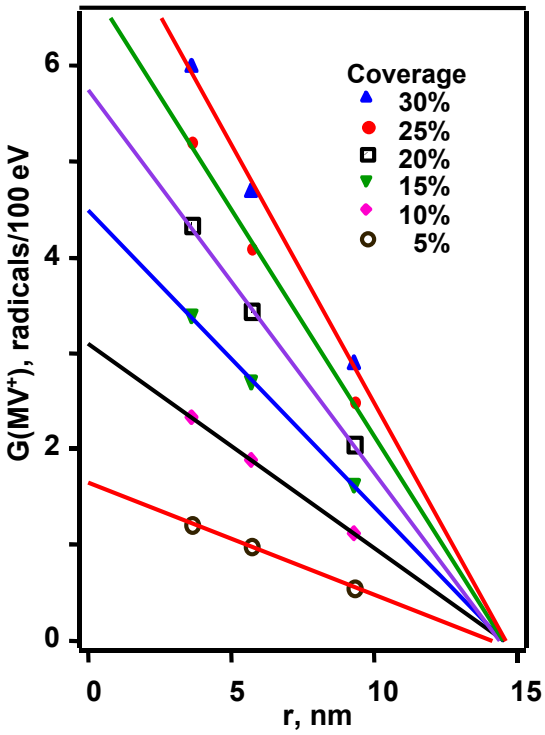


*FIG. 9. The dependence of the yield of instantaneous $MV^+$ on particles radii at various surface coverage. Experimental conditions as in Figure 8.*

The availability of charge carriers at the surface of particles has been extensively utilized in environmental clean-up studies [33, 36]. Oxidative routes via both direct hole oxidation and indirect oxidation by OH radicals, formed in the presence of water, were reported. Reductive pathways for the destruction of the pollutants are also well documented. In particular, halogenated hydrocarbons, such as hexachlorobenzene and similar derivative, are susceptible to dissociative electron attachment upon reaction with electrons from the solid or solvated electrons in the presence of a liquid polar medium. The advantages of radiation methods relative to other advanced oxidation techniques that are often used to degrade the same contaminants include the ability to penetrate opaque media, such as soils and the ability to achieve high redox levels, which are unattainable using light in photocatalytic degradation. For example excitation of transparent wide-band gap metal oxides, such a $SiO_2$ or $ZrO_2$, is impossible with visible or UV light, but as shown above, it is easily achieved using ionizing radiation. Once an electron is placed in the conduction band (or hole in the valence band) its redox potential is much higher than that of an electron in the conduction band of narrow band semiconductor. This approach has been field-tested at several locations in the US with good results.

Finally we explore future applications of nanomaterials in conjunction with radiation effects, particularly the potential use of nanoparticles in radiotherapy. The density of the nanoparticles is the same as the density of the bulk material, usually much higher than that of water or living tissues. Since the electron density of the material, which is close to the mass density, is the major factor that determines the amount of energy absorbed by the material one may be able to direct the absorption of radiation primarily to the particles. If the energy that is deposited in the nanoparticle migrates to the surface and is able to initiate damage in the outer phase, perhaps one could target the absorption of radiation into specific areas of an organ, e.g. malignant cells.

A strategy is proposed for the use of gold nanoparticles in phototherapy. With slight modifications a similar approach might be used in radiotherapy. With density of 19.3 g $cm^{-3}$ (electron density of 15 per $cm^3$) the amount of energy deposited in the particle will be more than an order of magnitude larger than in the same volume of water. The specificity that one may obtain in surface

modification of gold particles allows tailoring the gold particles to bind specifically to some cells rather than randomly to others. Furthermore, gold particles are essentially nontoxic; in fact they were used in various therapeutic procedures. Thus, the main question that remains unanswered is can the charge carriers be funneled out of the metallic particles before they recombine. Because of the high density of electrons in the conduction band of the metal, recombination is believed to be extremely fast, yet localization in water is also a sub-picosecond process and might, therefore, be able to compete with recombination. Should this be proven a viable process, nanoparticles, metallic or even of metal-oxides materials, in conjunction with ionizing radiation may become useful therapeutic vehicles.

## REFERENCES


[1] TSUKUDA, S., SEKI, S., TAGAWA, S.; SUGIMOTO, M., IDESAKI, A., TANAKA, S., OSHIMA, A., "Fabrication of Nanowires Using High-Energy Ion Beams", *J. Phys. Chem. B* 2004, *108*, 3407–9.

[2] HENGLEIN, A., "Catalysis of Hydrogen Formation from an Organic Radical in Aqueous Solution by Colloidal Silver"; *Angew. Chem., Int. Ed. Engl.* 1979, *18*, 418.

[3] HENGLEIN, A., "Mechanism of Reactions on Colloidal Micrelectrodes and Size Quantization Effects," *Top. Curr. Chem.* 1988, *143*, 113–80.

[4] HENGLEIN, A., "Electronics of Colloidal Nanometer Particles", *Ber. Bunsenges. Phys. Chem.* 1995, *99*, 903–13.

[5] HENGLEIN, A.; MEISEL, D., "Radiolytic Control of the Size of Colloidal Gold Nanoparticles", *Langmuir* 1998, *14*, 7392–6.

[6] BELLONI, J., MOSTAFAVI, M., REMITA, H., MARIGNIER, J.-L., DELCOURT, M.-O., "Radiation-induced Synthesis of Mono- and Multi-metallic Clusters and Nanocolloids", *New J. Chem.* 1998, *22*, 1239–55.

[7] MARIGNIER, J.L., BELLONI, J., DELCOURT, M.O., CHEVALIER, J.P., "Microaggregates of Non-Noble Metals and Bimetallic Alloys Prepared by Radiation-Induced Reduction", *Nature* 1985, *317*, 344–5.

[8] DELCOURT, M.-O., BELLONI, J., MARIGNIER, J.-L., MORY, C., COLLIEX, C., "Metal Microaggregates Prepared by Radiolytic Reduction in Liquids." *Radiat. Phys. Chem.* 1984, *23*, 485–7

[9] REMITA, H., ETCHEBERRY, A., BELLONI, J., "Dose Rate Effect on Bimetallic Gold-Palladium Cluster Structure", *J. Phys. Chem. B* 2003, *107*, 31–6.

[10] MOSTAFAVI, M., LIU, Y., PERNOT, P., BELLONI, J., "Dose Rate Effect on Size of CdS Clusters Induced by Irradiation", *Rad. Phys. Chem.* 2000, *59*, 49–59.

[11] TREGUER, M., COINTET, C., REMITA, H., KHATOURI, J., MOSTAFAVI, M., AMBLARD, J., BELLONI, J., KEYZER, R., "Dose Rate Effects on Radiolytic Synthesis of Gold-Silver Bimetallic Clusters in Solution", *J. Phys. Chem.* 1998, *102*, 4310–21.

[12] HENGLEIN, A., "Remarks on the Electrochemical Potential of Small Silver Clusters in Aqueous Solution." *Ber. Bunsenges. Phys. Chem.* 1990, *94*, 600–3

[13] BELLONI, J., PERNOT, P., "Role of Nuclearity-Dependent Properties of Small Clusters in the Nucleation Process and Thermal Hysteresis at the Phase Transition", *J. Phys. Chem. B* 2003, *107*, 7299–302.

[14] MULVANEY, P., LINNERT, T., HENGLEIN, A., "Surface Chemistry of Colloidal Ag in Aqueous Solutions: Observation on Chemisorption and Reactivity." *J. Phys. Chem.* 1991, *95*, 7843–6.

[15] LAHIRI, D., ZHANG, Z., CHATTOPADHYAY, S., SHIBATA, T., MISHRA, B., TERRY, J., MEISEL, D., BUNKER, B., "Core-Shell and Alloyed Pt-Ag and Pd-Ag Nanoparticles", *J. Appl. Phys.* 2004, *Submitted for publication*.

[16] SHIBATA, T., BUNKER, B., ZHANG, Z., MEISEL, D., VARDEMAN, C., GEZELTER, D., "Size Dependent Alloying of Au-Ag Nanoparticles in Aqueous Solutions at Ambient Temperature", *J. Am. Chem. Soc.* 2002, *124*, 11989–96.

[17] DICK, K., DHANASEKARAN, T., ZHANG, Z., MEISEL, D., "Size Dependent Melting of Silica - Encapsulated Gold Nano-Particles", *J. Am. Chem. Soc.* 2002, *124*, 2312–7.

[18] HAYES, D., SCHMIDT, K. H., MEISEL, D., "Growth Mechanisms of Silver Halide Clusters from the Molecule to the Colloidal Particle." *J. Phys. Chem.* 1989, *93*, 6100–9.

[19] HAYES, D., MICIC, O.I., NENADOVIC, M.T., SWAYAMBUNATHAN, V., MEISEL, D., "Radiolytic Production and Properties of Ultrasmall CdS Particles." *J. Phys. Chem.* 1989, *93*, 4603–8.
[20] SCHMIDT, K.H., PATEL, R., MEISEL, D., "Growth of Silver Halides from the Molecule to the Crystal. A Pulse Radiolysis Study." *J. Am. Chem. Soc.* 1988, *110*, 4882–4.
[21] CARUSO, R.A., ASHOKKUMAR, M., GRIESER, F., "Sonochemical Formation of Colloidal Platinum", *Colloids and Surfaces A*. 2000, *169*, 219–25.
[22] CARUSO, R.A., ASHOKKUMAR, M., GRIESER, F., "Sonochemical Formation of Gold Sols", *Langmuir* 2002, *18*, 7831–6.
[23] SOSTARIC, J.Z., CARUSO, H.R.A., MULVANEY, P., GRIESER, F., "Ultrasound-Induced Formation and Dissolution of Colloidal CdS", *J. Chem. Soc., Faraday Trans.* 1997, *93*, 1791–5.
[24] HENGLEIN, A., LILIE, J., "Storage of Electrons in Aqueous Solution: The Rates of Chemical Charging and Discharging of the Colloidal Ag Microelectrode." *J. Am. Chem. Soc.* 1981, *103*, 1059–66.
[25] BELLONI, J., TREGUER, M., REMITA, H., KEYZER, R.D., "Enhanced Yield of Photoinduced Electrons in Doped Silver Halide Crystals", *Nature* 1999, *402*, 865–7.
[26] BELLONI, J., "Photography: Enhancing Sensitivity by Silver-halide Crystal Doping", *Rad. Phys. Chem.* 2003, *67*, 291–6.
[27] WARDMAN, P., "Reduction Potentials of One-Electron Couples Involving Free Radicals in Aqueous Solution", *J. Phys. Chem. Ref. Data* 1989, *18*, 1637–55.
[28] SCHATZ, T., COOK, A.R., MEISEL, D., "Charge Carrier Transfer Across the Silica Nanoparticle / Water Interface." *, J. Phys. Chem.* 1998, *102*, 7225–30.
[29] DIMITRIJEVIC, N. M., HENGLEIN, A., MEISEL, D., "Charge Separation Across the Silica Nanoparticle/Water Interface", *J. Phys. Chem. B,* 1999, *103*, 7073–6.
[30] SCHATZ, T., COOK, A., MEISEL, D., "Capture of Charge Carriers at the Silica Nanoparticle - Water Interface", *J. Phys. Chem. B* 1999, *103*, 10209–13.
[31] MILOSAVLJEVIC, B.H., PIMBLOTT, S.M., MEISEL, D., "Yields and Migration Distances of Reducing Equivalents In The Radiolysis Of Silica Nanoparticles", *J. Phys. Chem. B* 2004, *In Press*.
[32] ORLANDO, T., MEISEL, D., In "Radiation-Induced Processes in Aqueous Suspensions of Nanoparticles And Nanoscale Water Films: Relevance to $H_2$ Production in Mixed Waste and Spent Nuclear Fuel", Eller, G., Heineman, W., Eds., ACS Symposium Series, 2001, Vol. 778, pp 284–96.
[33] PELLER, J., WIEST, O., KAMAT, P.V., "Mechanism of Hydroxyl Radical-Induced Breakdown of the Herbicide 2,4-Dichlorophenoxyacetic Acid", *J. Phys. Chem. A* 2001, *105,* 3176–81.
[34] ZACHEIS, G.A., GRAY, K.A., KAMAT, P. V., "Radiation induced catalytic dechlorination of hexachlorobenzene on various oxide surfaces", *J. Phys. Chem. B* 2001, *105*, 4715–20.
[35] ZACHEIS, G.A., GRAY, K. A., KAMAT, P.V., "Radiation-Induced Catalysis on Oxide Surfaces: Degradation of Hexachlorobenzene on Gamma-Irradiated Alumina Nanoparticles." *J. Phys. Chem. B* 1999, *103*, 2142–50.
[36] ZACHEIS, G.A., GRAY, K.A., KAMAT, P.V., "Radiolytic Reduction of Hexachlorobenzene in Surfactant Solutions: A Pulse Radiolysis Study", *Environ. Sci. Technol.* 2000, *34*, 3401–7.

**SOLID STATE RADIOLYSIS OF DRUGS-POLYESTER MICROSPHERES**

A. FAUCITANO, A. BUTTAFAVA
University of Pavia, Department of General Chemistry,
Pavia, Italy

**Abstract**

A concise description is given of the free radical chemistry lying behind the radiolytic degradation of a microsphere drug release polyester matrix based on the polylactide-co-glycolide 50/50 copolymer (PLGA) and its composites with the active principles bupivacaine and clonazepam. For the sake of comparison also the radiolytic behaviour of the corresponding homopolymers polylactic (PLA) and polyglycolic acids( PGA) were investigated and presented in this report.

## 1. INTRODUCTION

Drug delivery systems are based on polymer matrices, often in form of microspheres, containing a dispersion of the active principle in molecular or nanoparticle forms. The sterilization methodologies based on ionising radiations (both electron beam and gamma) can modify the morphology and the drug release properties of these molecular and nano-composites as a consequence of the radiolytic process where free radicals intermediates play a major role. The understanding of such reaction mechanisms is a prerequisite for preventing undue effects or for promoting the changes which lead to an improvement of the performance of the pharmaceutical formulation. A research line on this argument was started years ago at the Radiation Chemistry Laboratory of the General Chemistry Department of the University of Pavia in collaboration with Pharmaceutical Chemistry Departments of the Universities of Pavia and Milan [1, 2, 3, 4]. In this abstract a concise description will be given of the free radical chemistry lying behind the radiolytic degradation of a microsphere drug release polyester matrix based on the polylactide-co-glycolide 50/50 copolymer (PLGA) and its composites with the active principles bupivacaine and clonazepam. For the sake of comparison also the radiolytic behaviour of the corresponding homopolymers polylactic (PLA) and polyglycolic acids( PGA) were investigated and are described in this report.

## 2. EXPERIMENTAL SECTION

Commercial Bupivacaine, Clonazepam, PLGL, PLA and PGA were used as received. PLGA and PLGA+Clonazepam, PLGA+Bupivacaine microspheres were obtained by spray evaporation of the solutions in $CH_2Cl_2$. Irradiations were performed in a 60-Co source (0.75 kGy/hr) with total doses of 25 kGy. The qualitative and quantitative characterization of the free radical intermediates was performed by low temperature matrix EPR spectrometry.

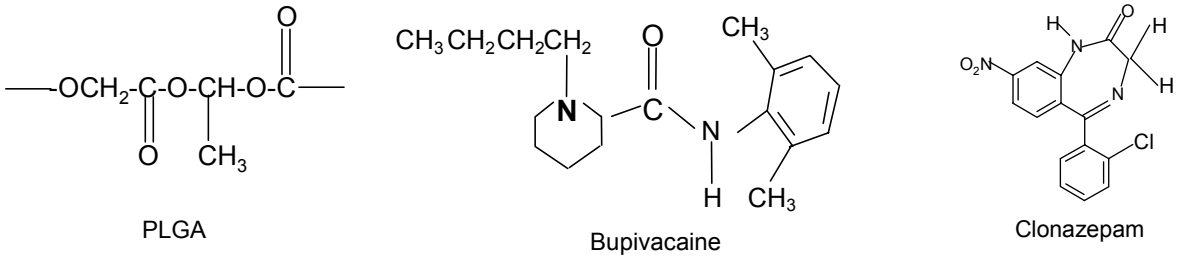


*FIG. 1. Microscopic drug release polymers used for experiments.*

3. RESULTS

**PLGA matrices**

The table I summarizes the results pertaining the nature and radiolytic yield of the free radical intermediates in the solid state low temperature radiolysis of PLGA. The major radiolytic processes at 77 K are the C—O ( chain scission) and C—H bond scissions, the former being favoured at the tertiary sites leading to the radical $-C^{\bullet}(CH_3)$. On warming above 77 K the chain scission radicals undergo H abstraction reactions with the polymer backbone. In this process the secondary –(CH)—H bond shows almost the same reactivity of the tertiary >C— H bond presumably because of the superimposition of stereoelectronic effects to the bond energy factor.

TABLE I. RADIOLYTIC YIELDS OF FREE RADICALS INTERMEDIATES IN THE 77 K RADIOLYSIS OF PLGA

| Radical | Radical | Radical | Radical |
|---|---|---|---|
| $-CH_2^{\bullet}$ | $-CH^{\bullet}(CH_3)$ | $-C^{\bullet}(CH_3)O-$ | $-CH^{\bullet}O-$ |
| $G(-CH_2)$ 0.071μmole/J | $G(-CH^{\bullet}(CH_3))$ 0.087μmole/J | $G(-C^{\bullet}(CH_3)O-)$ 0.060μmole/J | $G(-CH^{\bullet}O-)$ 0.042μmole/J |

**PLGA/Bupivacaine matrices**

The radiolytic behaviour of this polymer/drug composite follows the additivity law. No appreciable spin transfer phenomena or effects causing a change of the radiostability of the pure compound was detected (Table II).

TABLE II. RADIOLYTIC YIELDS OF FREE RADICALS INTERMEDIATES IN THE 77 K RADIOLYSIS OF PLGA + BUPIVACAINE COMPOSITES ( 40% BUPIVACAINE)

| *Sample* | *Radical radiolytic yield (μ moli/J)* |
|---|---|
| Bupivacaine | 0.066 ± 0.01 |
| Placebo microspheres | 0.26 ± 0.05 |
| Bupivacaine loaded microspheres | 0.20 ± 0.04 |
| Calculated | 0.20 ± 0.04 |

**PLGA/Clonazepam matrices**

Important spin transfer phenomena are detected in this system causing the increase of the free radical yield of the drug above its value in the pure state at expenses of a decrease of the radical yield of the polymer (Table III). The mechanism of the spin transfer was elucidated by EPR being based on spin trapping reactions by the nitro group – $NO_2$ and its nitroso radiolytic product –N=O.

TABLE III. RADIOLYTIC YIELDS OF FREE RADICALS INTERMEDIATES IN THE 77 K RADIOLYSIS OF PLGA+ CLONAZEPAM

| Sample | *Radical radiolytic yield (μ moli/J)* |
|---|---|
| Pure Clonazepam | 0.0030 ± 0.0006 (experimental) |
| Placebo microspheres | 0.26 ± 0.04 (experimental) |
| Clonazepam loaded microspheres | G(total rad)=0.22 ± 0.04(additiviy law) |
| “ | G(total rad)=0.12 ± 0.02(experimental) |
| “ | G(PLGA)=0.055 ± 0.001(experimental) |
| “ | G(Clonazepam)=0.065 ± 0.001(experimental) |

## 4. CONCLUSIONS

The results have shown that important reactions can take place between the polymer matrix and the active principle in drug release systems. These interactions are bound to be deeply affected by the characteristics of the dispersion, their efficiency being expected to decrease on going from the molecular type solutions to nano-particles, micro or greater size particle dispersions. The control of these morphologies by adopting suitable preparation methods and their characterization through the proper methodologies will greatly improve the prediction/control of the radiation induced decomposition as well as the pharmaceutical properties. Depending on the composite morphology, the radiation chemical processes can produce useful effects which are worth being exploited.

## REFERENCES


[1] MONTANARI, L., COSTANTINI, M., SIGNORETTI, E.C., VALVO, L., SANTUCCI, M., BARTOLOMEI, M., FATTIBENE, P., ONORI, S., FAUCITANO, A., CONTI, B., GENTA, I.,"Gamma irradiation effects on poly(DL-lactide-co-glycolide) microspheres", Journal of Controlled Release 56 (1998) 219–229.

[2] MONTANARI, L., CILURZO, F., CONTI, B., GENTA, I., GROPPO, A., VALVO, L., FAUCITANO, A., BUTTAFAVA, A., "Gamma irradiation effects and EPR investigation on poly (lactide-co-glycolide) microspheres containing bupivacaine ", Il Farmaco 57, (2002) 427–433.

[3] MONTANARI, L., CILURZO, F., VALVO, L., FAUCITANO, A., BUTTAFAVA, A., GROPPO, A., GENTA, I.,CONTI, B., "Gamma irradiation effects on stability of poly(lactide-co-glycolide) microspheres containing clonazepam", Journal of Controlled Release 75 (2001) 317–330.

[4] FAUCITANO, A., BUTTAFAVA, A., MONTANARI, L., CILURZO, F., CONTI, B., GENTA, I., VALVO, L., "Radiation-induced free radical reactions in polymer/drug systems for controlled release: an EPR investigation", Radiation Physics and Chemistry 67 (2003) 61–72.

# NANO- AND MICROGELS OF POLY(VINYL METHYL ETHER) OBTAINED BY RADIATION TECHNIQUES

J.M. ROSIAK
Institute of Applied Radiation Chemistry,
Technical University of Lodz,
Lodz, Poland

**Abstract**

Hydroxyl radicals were generated radiolytically in $N_2O$-saturated aqueous solutions in the presence of poly(vinyl methyl ether) (PVME, $6 \times 10^4$ Da, $10^{-3} – 10^{-2}$ mol dm$^{-3}$ in monomer units). As measured by pulse radiolysis, they react ($k = 2.2 \times 10^8$ dm$^3$ mol$^{-1}$ s$^{-1}$) with PVME by giving mainly rise to alkoxyalkyl radicals (~72%) that reduce ($k \approx 2 \times 10^9$ dm$^3$ mol$^{-1}$ s$^{-1}$) $Fe(CN)_6^{3-}$, $IrCl_6^{2-}$ or tetranitromethane. Based on the formaldehyde yield in the presence of the latter two oxidants (~40 % of $^{\bullet}OH$), it is concluded that OH radicals undergo H-abstraction at $ROCH_2$-H, $R_3C$-H and $R_2HC$-H with probabilities of ~40%, ~32% and ~28%, respectively. The momentary rate constant of the decay of the PVME radicals depends on the number of radicals per polymer chain and drops as they decay. The yield of intermolecular crosslinks, as measured by an increase of the molecular weight, strongly increases with decreasing dose rate, and it is concluded that the majority of crosslinks occur intramolecularly, even at the lowest dose rate used [0.0015 Gy s$^{-1}$, $G$(intermolecular crosslinks) = $0.62 \times 10^{-7}$ mol J$^{-1}$]. At low temperatures and low polymer concentrations the intramolecular crosslinking reaction is favored. A large number of radicals are formed in a short period of time during each pulse of accelerated electrons. The combination of the formed polymeric radicals is in the intramolecular way and nanogels formation occurs. Without changes in the molecular weight the dimension (radius of gyration and hydrodynamic radius), as well as the intrinsic viscosity of the nanogels decreases with increasing radiation dose. At temperatures above the LCST PVME molecules collapse to globular particles. Electron beam irradiation of these stable phase-separated structures leads to the formation of temperature-sensitive microgel particles. The additive-free method of crosslinking of polymers in aqueous solutions by high-energy radiation offers the application of these microgels in the field of medicine because of no remaining toxic substances (monomers, initiators, crosslinkers, etc.). The variation of the crosslinking density and the particle diameter can be performed by varying the polymer concentration and the radiation dose. Applying the closed-loop system reduces the amount of un-crosslinked molecules (sol content).

## 1. INTRODUCTION

Poly (vinyl methyl ether), PVME, is one of the simplest water-soluble polymers [1]. Its aqueous solutions have the unusual property of reverse temperature solubility, i.e. the polymer precipitates at around 34–37°C. Its interactions with water and the mechanism of the phase transitions are presently the subject of considerable interest.[2–4].

Hydrogels, i.e. water-swollen, covalently crosslinked polymer networks, made of poly (vinyl methyl ether) are also heat-sensitive [5-8] property, as well as the fact that the gel collapses at a temperature close to body temperature, has elicited a number of studies on its possible use as a stimulus-sensitive biomaterial, e.g. as a thermosensitive (and/or bioadhesive) drug-delivery system [7, 9–11] and even as an artificial muscle [7, 12]. Other interesting applications of poly (vinyl methyl ether) hydrogels are recyclable separation systems [5, 13, 14] and chemomechanical valves [15].

In general, ionizing radiation is a very efficient tool for the formation of hydrogels. The reaction can be carried out at room temperature, is easy to control and environment-friendly (no additional chemicals, no waste). Using γ-irradiation, homogeneous products of any desired shape and size can be produced. For biomedical applications, the radiation technique allows one to carry out in one step the formation of the hydrogel as well as its sterilization [17, 18].

In particular, hydrogels of poly(vinyl methyl ether) have already been obtained by this method [6, 8, 19–21]. For a further development of this promising technique, it seems worthwhile to investigate in some detail the underlying radiation chemistry of poly(vinyl methyl ether) in aqueous solution. First attempts in elucidating these processes have already been undertaken, [20–22] but there are marked discrepancies among the published data.

The aim of the present work is to present a more complete picture by combining kinetic and product studies. To aid our interpretations, the radiation-induced reactions of 2,4-dimethoxypentane, a low-molecular-weight model compound of poly (vinyl methyl ether), were also investigated and are described in the preceding paper [23].

## 2. EXPERIMENTAL

Poly (vinyl methyl ether) (Lutonal M40, BASF) has been purified by dissolving it in water (~50 g $dm^{-3}$) at room temperature. The temperature of solution was then raised above 37ºC until the polymer precipitated. The liquid fraction was discarded, and after this procedure had been repeated five times the polymer solution was subjected to continuous ultrafiltration (Amicon TCF 10 with a Diaflo YM10 membrane of a nominal 10 kDa cut-off) until the UV absorption $\lambda > 200$ nm of the permeate fell below 0.01. After such a treatment the weight-average molecular weight of PVME was $6 \times 10^4$ Da as determined by low-angle laser light-scattering.

Tetranitromethane was washed several times with water to reduce the background level of nitroform anion. All other chemicals were of analytical grade. Solutions were made-up in Milli-Q-filtered (Millipore) water.

γ-Irradiations were carried out with a panorama $^{60}$Co-γ-source (Nuclear Engineering) at dose rates ranging from 0.0015 to 0.15 Gy $s^{-1}$. Pulse radiolysis experiments were performed with a 2.8 MeV van de Graaff accelerator generating electron pulses of 0.4 μs duration, equipped with optical and conductometric detection systems [24]. Optical measurements were based on thiocyanate dosimetry [25] and conductometric measurements on dimethyl sulfoxide dosimetry [26].

Formaldehyde was determined by HPLC after derivatization with 2,4-dinitrophenyl-hydrazine (Nucleosil C18 column, eluent: acetonitrile-water 1/1 v/v, optical detection at $\lambda = 360$ nm) [27]. The yield of $H_2O_2$ and organic hydroperoxides was determined spectrophotometrically with molybdate-activated iodide [28]. The absorbance of $I_3^-$ resulting from the reaction with $H_2O_2$ appears immediately after mixing, while the subsequent slower increase is attributed to the reduction of organic hydroperoxides [29].

The weight-average molecular weight was determined by low-angle laser light-scattering at $\lambda = 633$ nm (Chromatix KMX-6) after having filtered the samples (0.45 μm, Minisart NML, Millipore). The specific refractive index increment ($dn/dc$) of PVME in aqueous solutions was determined with a laser differential refractometer (Chromatix KMX-16, $\lambda = 633$ nm, 25ºC). Extrapolation to zero PVME concentration yielded $dn/dc = 0.127$ $cm^3$ $g^{-1}$. Molar concentrations of PVME solutions are given in terms of its repeating unit (molecular weight = 58 g $mol^{-1}$).

### 2.1. Generation and UV-optical properties of PVME radicals

Upon irradiation of dilute, $N_2O$-saturated PVME solutions, OH radicals and H atoms are formed in reactions (1) and (2). Under such conditions the radiation-chemical yield of OH radical is $G = 5.8 \times 10^{-7}$ mol $J^{-1}$, while the H atoms are formed with $G = 0.6 \times 10^{-7}$ mol $J^{-1}$.

$$H_2O \xrightarrow[\text{radiation}]{\text{ionizing}} e_{aq}^-, {}^{\bullet}OH, H^{\bullet}, H^+, H_2O_2, H_2 \qquad (1)$$

$$e_{aq}^- + N_2O \rightarrow {}^{\bullet}OH + N_2 + OH^- \qquad (2)$$

The OH radicals and H atoms react with PVME by H-abstraction [e.g. reactions (3)-(5)]. For the sample used in present study, the rate constant for the OH radical is $2.2 \times 10^8$ $dm^3$ $mol^{-1}$ $s^{-1}$, while the H atoms react more slowly ($k < 1 \times 10^7$ $dm^3$ $mol^{-1}$ $s^{-1}$) [21, 22].

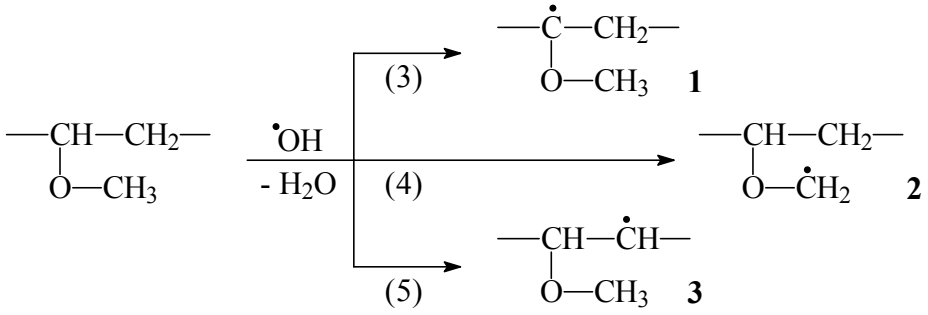

Initial absorption spectra of PVME-radicals **1** - **3** are featureless and only show an increasing absorbance towards shorter wavelength.[22] Thus, they resemble the spectra of the radicals derived from the model compound 2,4-dimethoxypentane [23] as well as spectra for other ether-derived radicals, e.g. diisopropyl ether [30] and 2,4-dioxane [31]. It has been reported that the absorption spectra of PVME-derived radicals maximize at 310 nm.[20]. We reproduced this result with a non-purified commercial sample, and conclude that low-molecular-weight impurities contained in the commercial material must give rise to the absorption maximum at 310 nm.

### 2.2. Oxidation of radicals 1 and 2 by $Fe(CN)_6^{3-}$, $IrCl_6^{2-}$ and tetranitromethane

Among the three radicals which are formed upon $^{\bullet}OH$ attack [reactions (3)–(5)] radicals 1 and 2 carry an alkoxyl group in α–position and thus are strongly reducing, i.e. they react rapidly with oxidants. Their one-electron oxidation leads to carbocations [e.g. 4, reaction (6)] which react rapidly with water giving rise to hemiacetals [*e.g.* 5, reaction (7)]. These are unstable and, for example, 5 releases formaldehyde [reaction (8)].

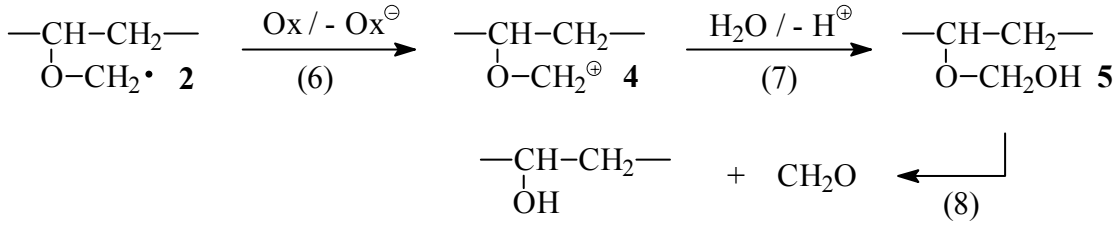

In a pulse radiolysis experiment, the oxidation by $Fe(CN)_6^{3-}$ has been studied by following the bleaching of $Fe(CN)_6^{3-}$ at $\lambda = 420$ nm as a function of the $Fe(CN)_6^{3-}$ concentration. There was only one kinetic component in the bleaching process ($k = 1.9 \times 10^9$ dm$^3$ mol$^{-1}$ s$^{-1}$), and the total bleaching of $Fe(CN)_6^{3-}$ corresponds to 75% of the initial yield of $^{\bullet}OH + H^{\bullet}$. Thus, radicals 1 and 2 react at a very similar rate. At the low rate of the reaction of $H^{\bullet}$ with the polymer and its high rate with $Fe(CN)_6^{3-}$ ($k = 6.3 \times 10^9$ dm$^3$ mol$^{-1}$ s$^{-1}$) [32] practically all $H^{\bullet}$ (>90%) is scavenged by $Fe(CN)_6^{3-}$. Based on this correction, we calculate that $^{\bullet}OH$ radicals produce ~72% reducing radicals 1 and 2 and thus ~28% radicals 3.

The same result was obtained upon γ-radiolysis. This indicates that an H-transfer reaction, that would convert radicals 3 into radicals 1 and/or 2 does not occur under these conditions. Such an H-transfer was, in fact, observed in the free radical chemistry of low molecular alcohols [33] as well as in poly (vinyl alcohol) [34], where the rate constants for this reaction is in the order of 500 s$^{-1}$.

A similar phenomenon, as in PVME, i.e. the absence of a reasonably fast H-transfer, has also been observed with its low-molecular-weight model, 2,4-dimethoxypentane [23]. In H-transfer

reactions, six-membered transition states are favourable, but five-membered transition states are not, i.e. in the latter case such reactions may be substantially retarded by steric effects. These seem to play a substantial role in PVME (an apparently also in the model system). In PVME, the polymer segments within the coil are packed much more tightly as in other polymers as evidenced by comparatively smaller coil dimensions at a similar molecular weight (Janik, unpublished results). This may suggest that there are structure-building hydrophobic interactions, which could also result in a high activation barrier for a configuration change necessary for the H-transfer.

In experiments carried out with other oxidants, namely tetranitromethane and $IrCl_6^{2-}$, the total yield of α-alkoxyalkyl radicals was confirmed, by optical measurements of nitroform anion formation and $IrCl_6^{2-}$ bleaching, to be ~75% of the initial yield of $^{\bullet}OH + H^{\bullet}$, again, with no difference whether these experiments were carried out using pulse radiolysis or γ-radiolysis.

The oxidation of radicals 1 and 2 by tetranitromethane was also studied by pulse radiolysis with optical and conductometric detection. The use of the latter technique allowed us to monitor the release of protons. The rate of the reaction with tetranitromethane with 1 and 2 is ~$2 \times 10^9$ $dm^3$ $mol^{-1}$ $s^{-1}$, as has also been observed for other α-alkoxyl radicals [35]. First a short-lived adduct may be formed [e.g. 6, reaction (9)] which subsequently hydrolyses [reaction (10)] yielding the carbocation and nitroform anion which has been detected by its strong absorption at 350 nm. The carbocation is also very short-lived and a proton is released [cf. reaction (7)] which leads to the observed conductivity increase.

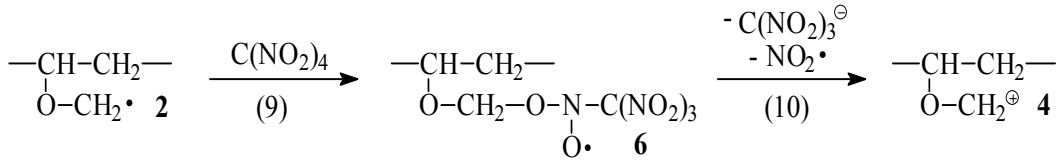


Decomposition of hemiacetal 5 leads to the formation of formaldehyde [reaction (8)] (analogous reaction was observed for the model compound, [23]). The formaldehyde yield in the presence of the oxidants tetranitromethane or $IrCl_6^{2-}$, a measure of the yield of radicals 2, is $G = 2.4 \times 10^{-7}$ mol $J^{-1}$, i.e. ~40% of initial yield of $^{\bullet}OH$ [using $Fe(CN)_6^{3-}$ gives rise to only $G(CH_2O) = 1.3 \times 10^{-7}$ mol $J^{-1}$; much lower $G(CH_2O)$ have also been observed for the radicals derived from 2,4-dimethoxypentane and dimethyl ether, [23] i.e. side reactions must occur with this oxidant]. Having established the yield of radical 2 at ~40% and the sum of 1 + 2 at ~72%, the yield of radical 1 is calculated at ~32%, and the remaining ~28% then must be attributed to radical 3. Based on the number of hydrogen atoms available for abstraction (random H-abstraction) one calculates 17% 1, 50% 2 and 33% 3. Thus there seems to be some preference for the formation of the tertiary radical 1. On the other hand, the formation of the primary radical 2, although stabilized by an alkoxyl group, seems not much favoured over that of the secondary radical 3. A substantial preference for abstraction of the tertiary hydrogen has also been noted in our model compound 2,4-dimethoxypentane (35% vs. 12.5% for random attack) [23] or diisopropyl ether (78 % vs. 14% for random attack) [30].

Previously, data have been reported where the yield of radicals 1 plus 2 have been determined at only 26% by following their oxidation by thionine [20, 21]. However, repeating this experiment with our purified sample led to a yield of about 70%, in good agreement with the value obtained with the other oxidants. Here, the error might have arisen from the high scavenging capacity of low-molecular-weight contaminations (cf. also spectral differences). We therefore believe that the values reported previously [20, 21] are on the low side.

We also have to correct our own preliminary data, where the yield of radicals 1 plus 2 was estimated at ~54% [22]. There were probably two sources for errors that may have contributed to this underestimate; a different (and probably less efficient) purification technique, and dosimetry problems due to a relatively poor long-time stability of the electron beam parameters when the ELU-6 linear

accelerator (a machine different from the one used in the present study) was operated in the untypical low dose mode.

### 2.3. Decay of the PVME radicals

The radicals derived from the PVME model compound 2,4-dimethoxypentane decay with an overall bimolecular rate constant of $2k = 1 \times 10^9$ dm$^3$ mol$^{-1}$ s$^{-1}$ [23]. In contrast, the bimolecular decay of PVME radicals cannot be described by simple second-order kinetics. Similar effects have been described for a number of other polymers and their low-molecular-weight models [36–40].

When the reciprocal of the radical concentration ([R$^\bullet$]) is plotted *vs.* the time, a straight line is obtained if simple second-order kinetics are followed. For PVME, however, such a plot is strongly curved (Fig. 1), and the observed momentary second-order rate constant decreases with time.

Bimolecular rate constants calculated from the slopes of curves of the type shown in Fig. 1 (main graph) are shown in the inset as a function of the average number of radicals present on each polymer chain ($Z_R$). The three data sets represent different irradiation conditions (dose per pulse and polymer concentration), i.e. three different *initial* average numbers of radicals per chain $Z_{R0}$. The polymer concentrations in our experiments are lower than the critical hydrodynamic concentration (for our sample ~0.5 mol dm$^{-3}$ at 25ºC as estimated by viscometry and multi-angle laser light-scattering); i.e. the polymer coils do not overlap.

For understanding why the momentary termination rate constant decreases in the course of the reaction, one has to recall that in pulse radiolysis many radicals are formed at each macromolecule. This implies that, at least in the first stages, recombination is mainly *intra*molecular. Radicals at a polymer chain cannot move freely and independently, as in homogeneous, diffusion-controlled reactions. Instead, a distribution of distances and possibly of activation energy exists, which implies different reactivities. Moreover, in the course of termination new C-C bonds are formed between the segments. This decreases segment mobility, and slows down the rate of the subsequent termination event. Two more sources of deviation from the homogeneous kinetics may be mentioned. The initial spatial distribution of the radicals within the macromolecule is not random, but rather reflects the fact that $^\bullet$OH radicals are formed in spurs. Those radicals formed in a close vicinity are expected to recombine fast. At a later stage, when the average $Z_R$ is close to one, many macromolecules bear only one radical. These radicals have to terminate *inter*molecularly, i.e. the termination mechanism now changes. In addition to segmental diffusions, *inter*molecular termination requires the diffusion of macromolecules as a whole, and therefore is slower than the *intra*molecular termination.

When the three data sets in the inset of Fig. 1 are compared, it becomes evident that the momentary rate constant of termination depends not only on the momentary number of radicals per chain $Z_R$, but also on the *initial* number of radicals per chain, $Z_{R0}$. In fact, when we compare data for equal $Z_R$ but different $Z_{R0}$, we compare recombination at different stages. A sample which starts with a low $Z_{R0}$ is at a relatively early stage, i.e. it has only some radical pairs for recombination and no or only a few internal crosslinks. On the other hand, a sample which starts with a high $Z_{R0}$ is, at the same $Z_R$, at a later stage, with no more fast-reacting pairs and a higher number of internal crosslinks. As a consequence of this, the momentary termination rate constant, if compared for two samples of the same $Z_R$, is lower for the sample of higher $Z_{R0}$.

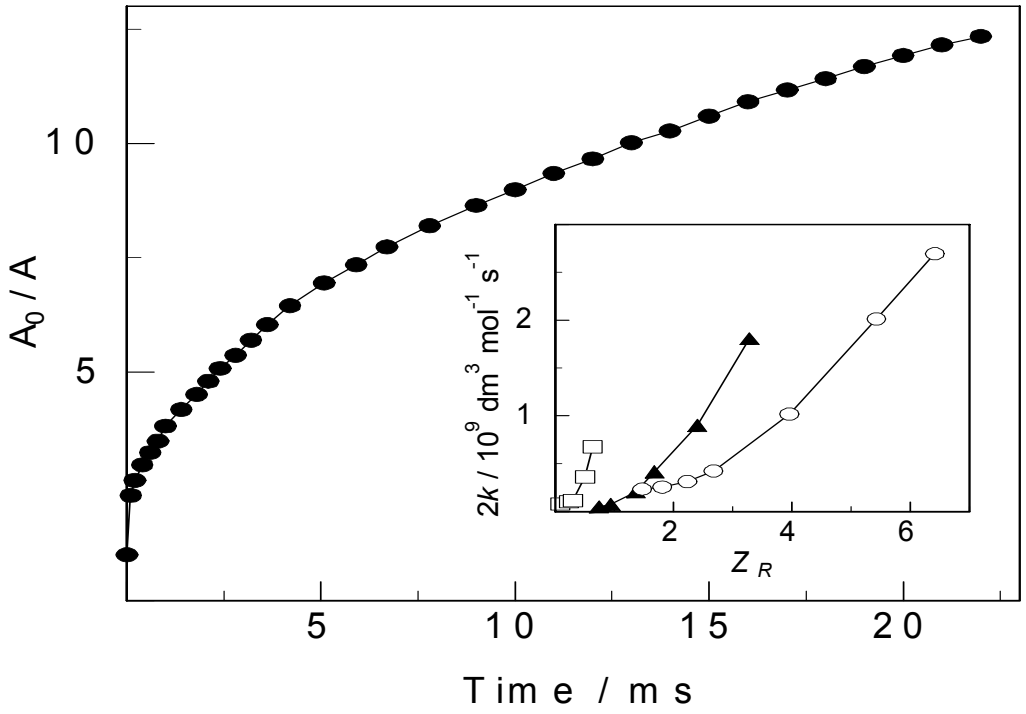


*FIG. 1. Pulse radiolysis of PVME (1 × $10^{-3}$ mol dm$^{-3}$) in $N_2O$ saturated aqueous solution. The ratio of the absorbance at 290 nm directly after pulse ($A_0$) to the absorbance (A) observed at a given time after the pulse. Inset: momentary second-order rate constants as a function of concentration of radicals per macromolecule $Z_R$. Polymer concentration: 2 × $10^{-3}$ mol dm$^{-3}$ (○), 1 × $10^{-2}$ mol dm$^{-3}$ (▲) and 1 × $10^{-1}$ mol dm$^{-3}$ (□).*

**Crosslinking of PVME chains**

Under dioxygen-free conditions, the resulting molecular weight depends on the ratio of the rate constants of radical recombination and chain scission. Unimolecular chain scission resulting from β-fragmentation of polymer radicals is typically a slow process [e.g. for poly (acrylic acid) $k$ = 0.025 s$^{-1}$, [39], for poly (methacrylic acid) [41, 42] $k$ = 1.8 s$^{-1}$] and only plays a role when the competing recombination reactions are slow as well. This is especially the case with radicals derived from polyelectrolytes such as poly(acrylic acid) and poly(methacrylic acid), where, due to the repulsive electrostatic forces between the charged chains, the termination rate constants are <100 dm$^3$ mol$^{-1}$ s$^{-1}$ [41, 42]. With the exception of polysaccharides, for the irradiation of uncharged polymers, where the termination rate constants are typically in the order of $10^7$ – $10^9$ dm$^3$ mol$^{-1}$ s$^{-1}$, no decrease in the molecular weight of the polymer has been reported.

When termination dominates over scission, the extent of the increase in average molecular weight depends on two more factors: the proportion between recombination and disproportionation and the ratio between inter- and intramolecular recombination.

The data on the model compound, 2,4-dimethoxypentane, indicate that β-fragmentation reactions must be of little importance and that recombination and disproportionation occur with equal probability [23]. Thus, one may expect that chain scission is also negligible in the case of PVME. Assuming a similar ratio of recombination to disproportionation would thus set the total (intra- plus intermolecular) crosslinking yield close to 1.5 × $10^{-7}$ mol J$^{-1}$.

The increase in weight-average molecular weight of PVME upon γ-irradiation in $N_2O$-saturated solutions is shown in Fig. 2.

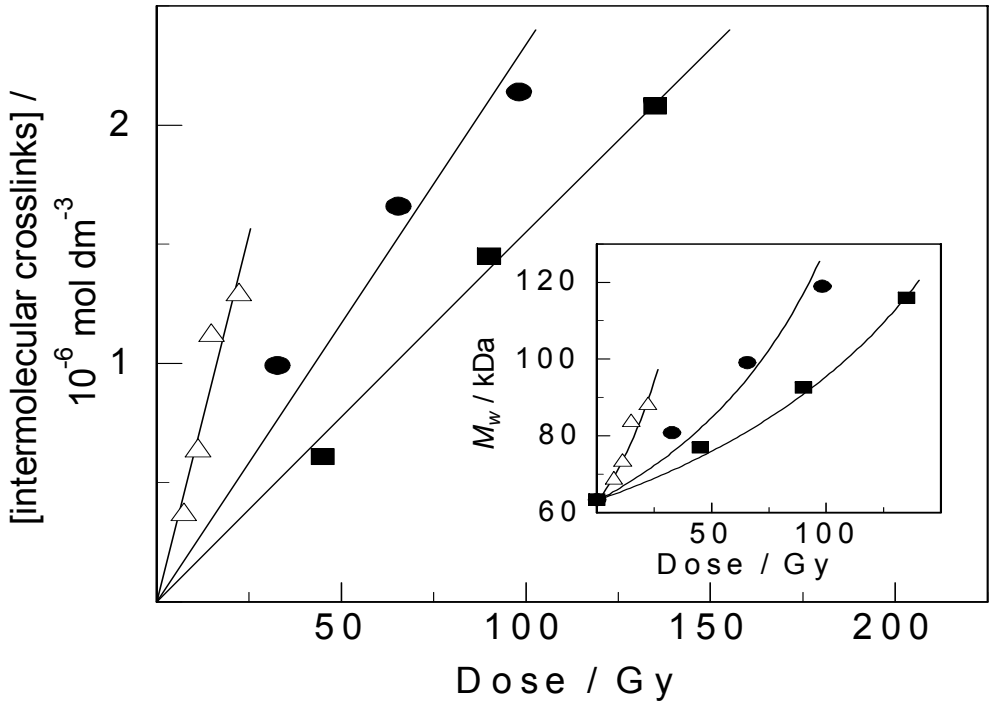


*FIG. 2. Radiolysis of PVME (1 × $10^{-2}$ mol $dm^{-3}$) in $N_2O$-saturated aqueous solutions. Concentration of intermolecular crosslinks (main graph) and weight-average molecular weight (inset) as a function of dose. Dose rates: 0.15 Gy $s^{-1}$ (■), 0.013 Gy $s^{-1}$ (●) and 0.0015 Gy $s^{-1}$ (Δ).*

Based on equation (11) [45, 46], where $M_{w0}$, $M_w$ (in g $mol^{-1}$) are the weight-average molecular weights before and after irradiation and $c_{PVME}$ is the polymer concentration (in g $dm^{-3}$), the concentration of intermolecular crosslinks was calculated.

$$[\text{intermolecular crosslinks}] = 0.5 \times (M_{w0}^{-1} - M_w^{-1}) \times c_{PVME} \qquad (11)$$

The linear plots of the concentration of intermolecular crosslinks *vs*. the dose allowed us to calculate *G*(intermolecular crosslinks) for three different dose rates, 0.150 Gy $s^{-1}$, 0.013 Gy $s^{-1}$ and 0.0015 Gy $s^{-1}$, at 0.15 × $10^{-7}$ mol $J^{-1}$, 0.23 × $10^{-7}$ mol $J^{-1}$ and 0.62 × $10^{-7}$ mol $J^{-1}$, respectively.

The observed yields of *inter*molecular crosslinks are significantly lower than the expected total yield of crosslinking. This fact, along with the observed dependence of *G*(intermolecular crosslinks) on the dose rate, indicates the importance of *intra*molecular recombination under our experimental conditions. This process does not change the average molecular weight of the polymer but leads to changes in coil dimensions and flexibility [40, 47]. As expected, the lower dose rate favours an intermolecular recombination due to a lower probability for the presence of two or more radical sites on a single polymer chain in the steady state.

The existence of hydrophobic sites on the PVME chain that tend to associate in the inner part of the polymer coil leads to a kind of ordered structure, less flexible than expected for a random coil, i.e., as mentioned above, to a very compact conformation of the PVME coils. This effect must slow down segmental diffusion and should lead to a reduced mobility of a radical located inside such a structure, nearly preventing this radical from intermolecular recombination. It seems probable that some of these single radicals trapped inside the coils undergo termination when, during further irradiation, another radical is formed within the same coil. This mechanism would enhance the yield of intramolecular at the expense of intermolecular crosslinking.

## 3. CONCLUSIONS

Due to its compactness in aqueous solutions, PVME has properties that enables reactions to occur that may also be undergone by other polymers, but to a lesser extent. For example, there is now evidence that intramolecular crosslinking can be of much greater importance than intermolecular crosslinking even at very low radical steady-state concentrations. Thus conditions can be chosen easily that favour e.g. nanogel formation. This raises the question, whether compaction of other water-soluble polymers, e.g., by the addition of salt or by lowering the temperature could be beneficial if nanogel formation is desired.

Irradiation at low aqueous polymer concentrations ($c < c^*$) does not result in the formation of macroscopic networks. Depending on the irradiation parameters (radiation dose, dose rate, polymer concentration, irradiation temperature) molecules with different structures can be obtained (long-chain branches, nanogels, microgel or microgel particles). Irradiation of the collapsed structure of PVME in diluted aqueous solutions above LCST leads to temperature-sensitive microgel particles [48]. These particles have a porous structures that serves as a template of emulsion polymerization of poly(pyrrole) to needle-like conductive polymer structures [49].

Increasing the dose rate (e.g. electron beam irradiation) increases the number of radicals at the polymer chain and changes the properties of the products. Irradiation of diluted aqueous solutions with pulsed electron beams (generation of a large number of radicals on each separate polymer chain in a short time) leads to the intramolecular combination of the produced radicals. In diluted homogeneous solutions (each macromolecule is separated) the formation of nanogels occurs [40, 47, 50, 51].

The aim of the work was the pulsed electron beam irradiation of diluted aqueous PVME solutions in different concentrations to obtain internal crosslinked macromolecules (nanogels). These polymeric materials were characterized with respect to their molecular weight, dimension, viscosity, and temperature-sensitive behavior. Experiments at temperatures above the LCST were be performed to obtain temperature-sensitive microgels. Their size can be varied by irradiation at different polymer concentrations and different radiation doses. They are characterized with respect to their dimension and temperature-sensitivity.

### 3.1. Pulsed electron beam irradiation and measurements

Pulse irradiations were performed in a closed-loop flow system (Fig. 3) consisting of a solution reservoir, Tygon tubing, a peristaltic pump and a quartz irradiation cell (effective volume, $V = 0.7\ cm^3$). Prior to and during the irradiation, polymer solution in the reservoir was being continuously saturated with Argon. The solution, flowing through the cell at a rate of $1\ cm^3\ s^{-1}$, was pulse-irradiated with 6 MeV electrons generated by an ELU-6 linear accelerator (Eksma, Russia). Pulse frequency of 0.5 Hz and pulse duration of 3 μs were applied. The average dose absorbed per single pulse was determined by ferrocyanide dosimetry [52–54] to 0.96 kGy. The average dose for the whole solution volume was calculated based on the number of pulses applied as well as the known volume of the solution ($500\ cm^3$) and the irradiation cell ($0.7\ cm^3$).

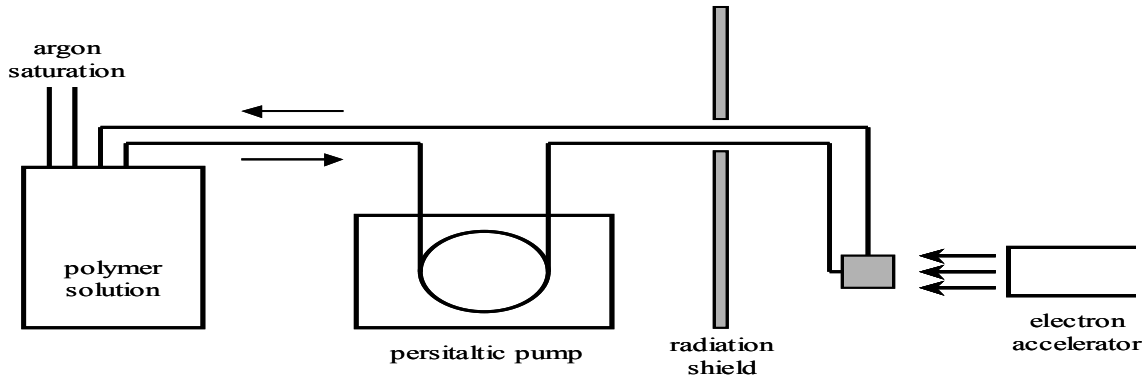


*FIG. 3. Scheme of the irradiation setup (closed-loop system).*

The same irradiation facility was used for the synthesis of PVME microgels. Diluted aqueous PVME solutions ($c_p$ = 0.05, 0.1, 0.5 g/l) were irradiated under phase-separated conditions. The temperature of the solution reservoir was adjusted to T = 50±2°C. Pulse frequency of 5 Hz and pulse duration of 3 µs were applied. The volume of the cuvette V was 1.0 ml.

The molecular weight $M_w$ and the values of the hydrodynamic radius $R_h$ were measured by the static and dynamic laser light scattering method based on a multi-angle Brookhaven Instruments setup consisting of a Lexel 95E argon ion laser (514.5 nm, typical output power 100±200 mW) and a BI-200SM goniometer. Measurements were performed using triple-distilled water as solvent.

By using static light scattering the angle and concentration dependence of the scattered light was measured at 25°C. ZIMM plot algorithm was used to evaluate the scattering data.

$$\frac{K' c_B}{R(q)} = \frac{1}{M_w}\left(1 + \frac{1}{3}\left\langle r^2 \right\rangle_z^{1/2} q^2\right) + 2A_2 c_B \qquad (12)$$

where $K' = 4\pi^2 n^2 / N_A \lambda_0^2 \, (dn/dc_B)^2$, the optical constant, $c_B$ the polymer concentration, R(q) the RAYLEIGH ratio, $M_w$ the weight average of the molecular weight, $\langle r^2 \rangle_z^{1/2}$ the radius of gyration, q the scattering angle and $A_2$ the second virial coefficient.

The time correlation function of the scattering intensity, obtained by dynamic light scattering, was analyzed by using CONTIN fit.

$$\tau = \frac{1}{D \cdot q^2} \qquad (13)$$

With the diffusion coefficients D the hydrodynamic radius $R_h$ was calculated (STOKES-EINSTEIN equation, equ. 13). For dynamic light scattering no extrapolation of $\vartheta \to 0$ and $c_p \to 0$ was done. An apparent hydrodynamic radius $R_{h,app}$ was determined.

$$R_h = \frac{k_B T}{6\pi\eta D} \qquad (14)$$

The samples were filtered through filters of 0.45 µm pore size directly before the measurement.

### 3.2. Molecular characterization

In dependence on the polymer concentration and the dose rate two different crosslinking reactions can be obtained: inter- and intramolecular crosslinking (see Fig. 4). If the numbers of radicals per single chain $z_R$ is low ($z_R < 1$) the intermoleculare combination of the formed radicals is observed. Increasing the dose rate (dose D per time t) leads to increased amount of radicals per chain ($z_R > 1$). In diluted solutions these radicals crosslink intramolecularly. The additional crosslinks in these macromolecules lead to reduction of the dimension of the molecule. This kind of polymers are more resistant to degradation processes because a degradation of C-C main chain bonds do not reduce the molecular weight.

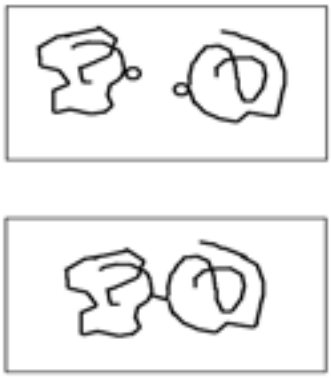

a) intermolecular crosslinking

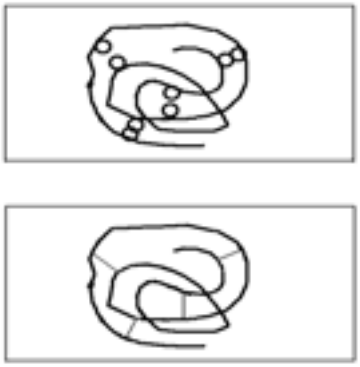

b) intramolecular crosslinking

*FIG. 4. Scheme of the synthesis of PVME nanogels by radiation techniques. a) Single polymer chains with a low number of radicals crosslink intermolecularly. b) An increasing number of radicals per chain leads to an intramolecular crosslinking. Polymeric nanogels are formed.*

By using static light scattering in water the molecular weights of the PVME nanogels were measured versus radiation dose D and polymer concentration cp. The results are shown in Fig. 5.

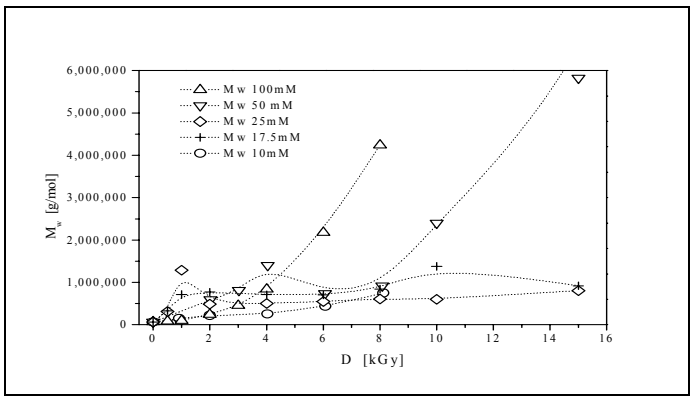


*FIG. 5. Molecular weight $M_w$ determined by static light scattering of the pulsed irradiated aqueous, de-oxygenated PVME solutions in dependence on the radiation dose D and the polymer concentration $c_p$ (○ - 10 mM, + - 17.5 mM, ◇ - 25 mM, ▽ - 50 mM, △ - 100 mM).*

With increasing radiation dose the molecular weights of the PVME nanogels increase. A strong increasing $M_w$ value was observed at high concentrations $c_p > 25$ mM.

The values of the radius of gyration $\langle r^2 \rangle_z^{1/2}$ were not evaluated because of the fact that at low polymer concentrations ($c_p < 25$ mM) the values are not realistic. The explanation of the reduction of the dimension of the internally crosslinked macromolecules was discussed by using the data of dynamic light scattering. The results are shown in fig. 6.

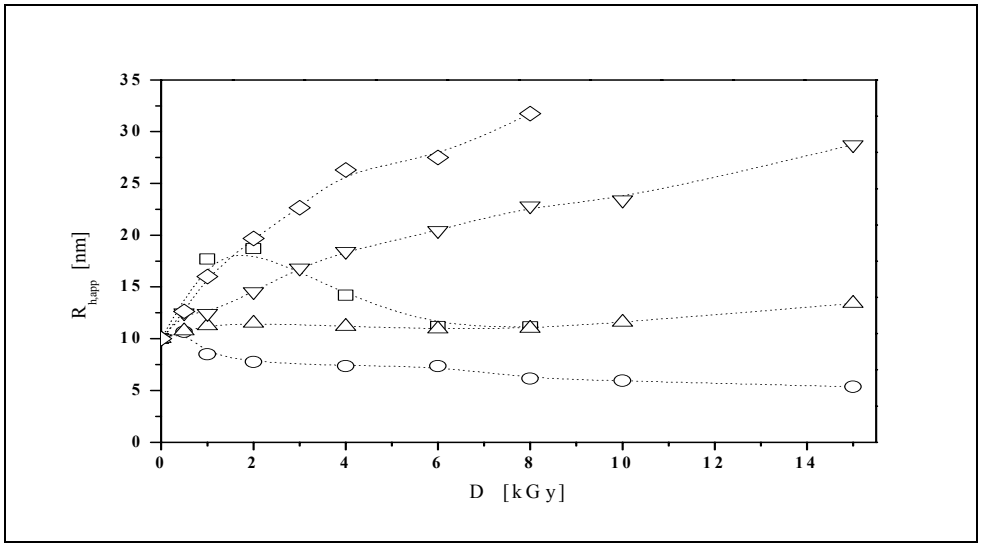


*FIG. 6. Apparent hydrodynamic radius $R_h$ ($\vartheta = 90°$) determined by dynamic light scattering of the pulsed irradiated aqueous, de-oxygenated PVME solutions versus the dependence of the radiation dose D and the polymer concentration $c_p$ (□ - 10 mM, ○ - 17.5 mM, △ - 25 mM, ▽ - 50 mM, ◇ - 100 mM).*

At high polymer concentrations the value of $R_{h,app}$ increase with increasing radiation dose due to the intermolecular crosslinking process. At $c_p = 25$ mM the radius is nearly constant at the initial value. At lower concentrations $R_{h,app}$ decreases with increasing D. The macromolecules crosslink intramolecularly and form nanogels.

### 3.3. PVME of high molecular weight

Vinyl ether monomers can not be polymerized in a radical way, only cationic. Cationic polymerized polymers (like in general vinyl ethers) have low molecular weights due to side reactions during the polymerization. Cation transfer reactions to already formed macromolecules lead to a long-chain branching of this polymer. The molecular weight of these polymers is relatively low ($M_w \approx 10^5$ g/mol) and the polydispersity is relatively high ($M_w/M_n > 2$).

That is why it is difficult to obtain vinyl ether polymers with high molecular weight. One possibility to increase the molecular weight of such polymer is the irradiation of their concentrated aqueous solutions with low doses below the gelation dose $D_g$. The crosslinking reaction of these polymers is intermolecularly and polymers with higher molecular weight are formed. However, they are long-chain branched.

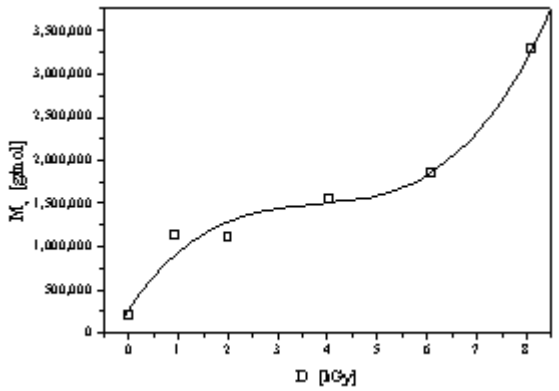


a)

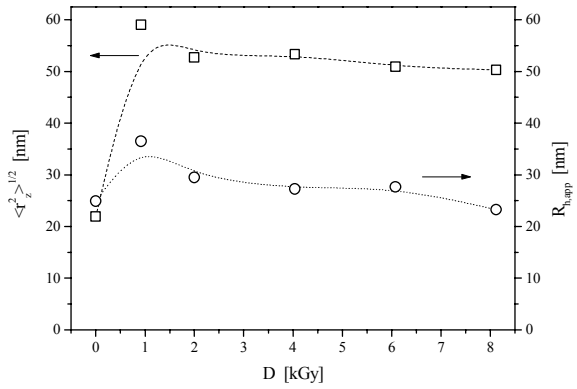


b)

*FIG. 7. Molecular weight $M_w$ (fig. 7a), radius of gyration $\langle r^2_z \rangle^{1/2}$ (fig. 7b), and apparent hydrodynamic radius $R_h$ ($\vartheta = 90°$) (fig. 7b) of the pulsed irradiated aqueous, de-oxygenated PVME ($\gamma$-irradiated, ca. 30 kGy) solutions versus the radiation dose D.*

Irradiation of this sample in the range of radiation dose D = 0-8 kGy leads to a small increasing of molecular weight and decreasing of dimensions (radius of gyration and hydrodynamic radius). In the range of very low doses the molecular weight and the dimension increase, again. Between 1 kGy and 6 kGy $M_w$ ranges between 1,000,000 g/mol and 2,000,000 g/mol. Above 1 kGy the dimensions of the crosslinked PVME molecules decrease.

### 3.4. Intermolecular crosslinking

In dependence on the radiation dose structural changes were obtained by different processes. The crosslinking and degradation reaction strongly depend on dose. At low dose values and at low polymer concentrations crosslinking is favored and main chain scission occurs rarely. Crosslinking of polymers by irradiation can occur on two different ways: intra- and intermolecular. The concentration of intermolecular crosslinks can be calculated using equation (eq. 11), where $M_w^0$ denotes the $M_w$ of the non-irradiated polymer and $c_P$ the polymer concentration of the irradiated aqueous solution. The calculated $n_C$ values in dependence on the radiation dose are shown in fig. 8.

The value of the intermolecular crosslinks decreases with decreasing polymer concentration. At $c_p < 50$ mM and $D > 2$ kGy no significant changes in these values could be observed. The crosslinking reaction occurs on the intramolecular way. Polymeric nanogels are formed.

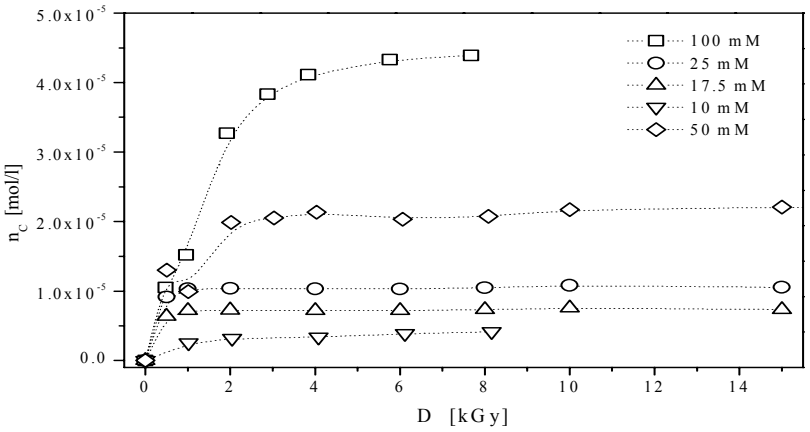


*FIG. 8. Numbers of intermolecular crosslinks $n_C$ calculated by using equation (11) in dependence on the radiation dose D and on the polymer concentration $c_p$ (▽ - 10 mM, △ - 17.5 mM, ○ - 25 mM, - 50 mM, □ - 100 mM).*

### 3.5. Characterization of PVME microgels

It was found [48] that PVME molecules form globular particles in diluted aqueous solutions above the LCST (scheme of the synthesis is shown in fig. 9). These phase-separated aggregates have been crosslinked by electron beam irradiation to form temperature-sensitive microgels. The advantage of this method is the synthesis of such materials starting from the polymer and without the use of any additives (e.g. monomer, initiator, crosslinker, etc.). However, one can see that not all PVME molecules are crosslinked by the 'static' method (irradiation of heated solutions in Petri dishes). Sol molecules remain in the microgel solution, which they have to be separated from [55].

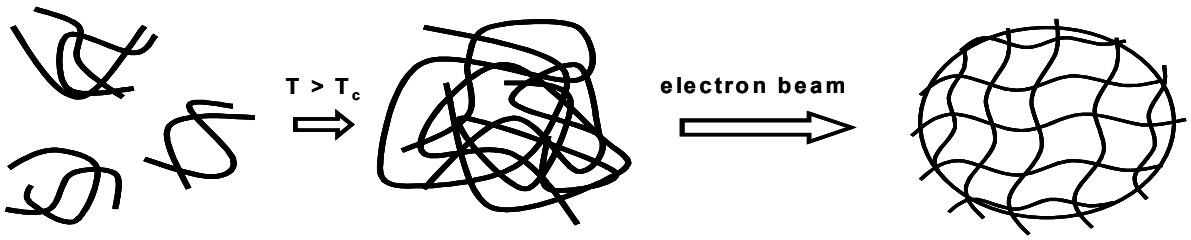


*FIG. 9. Scheme of the synthesis of PVME microgels by radiation techniques. The associated polymer chains collapse at $T > T_c$ to globular aggregates [48]. This phase-separated structure of PVME is fixed by electron beam irradiation and temperature-sensitive microgels particles are formed.*

Applying the closed-loop system under the same conditions ($c_p < c^*$, $T > T_{cr}$) can reduce the amount of sol molecules because of the irradiation in several steps (several loops). Experiments were performed at different polymer concentrations ($c_p$ = 0.05–0.5 g/l) and different radiation doses (D = 10–80 kGy). Irradiation experiments at higher concentrations lead to the precipitation of the polymer.

The results of static light scattering measurement in the swollen (T = 25°C) and in the shrunken (T = 50°C) state are shown in fig. 10.

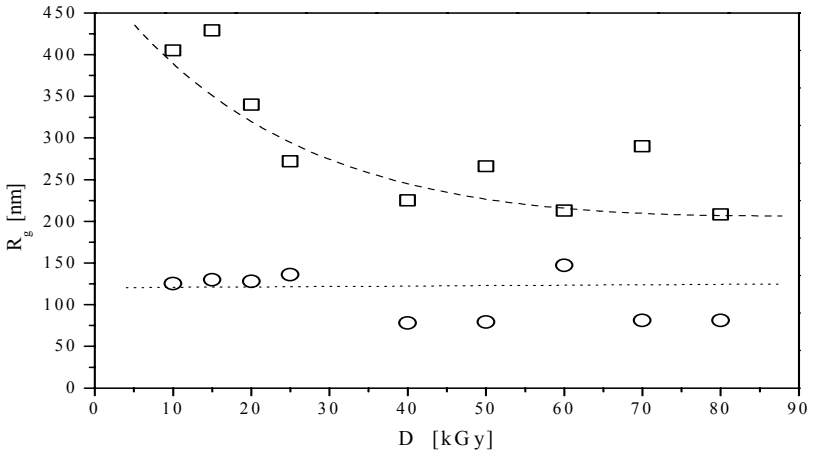


*FIG. 10. Dose dependence of the radius of gyration $R_g$ below (□ - 25°C) and above $T_{cr}$ (○ - 50°C) of PVME microgels synthesized by pulsed electron beam irradiation (D/pulse = 850 Gy) of a diluted PVME solution ($c_p$ = 0.115 g/l) at T = 50±2°C.*

Increasing the radiation dose D leads to decreasing of radii of gyration in the swollen state. The crosslinking density of the microgels increases and their swelling degree decreases. The radii in the shrunken state are nearly constant at $R_g$ = 120 nm. The crosslinked phase-separated structure of PVME aggregates has always the same size.

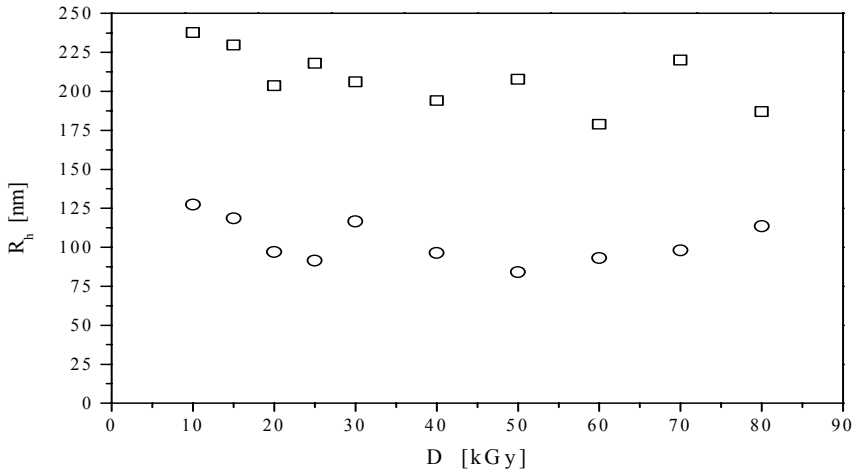


*FIG. 11. Dose dependence of the hydrodynamic radius $R_h$ ($c_p \approx 10^{-3}$ g/l, $\vartheta$ = 20°) below (□ - 25°C) and above $T_{cr}$ (○ - 50°C) of PVME. Nanogels synthesized by pulsed electron beam irradiation (D/pulse = 850 Gy) of a diluted PVME solution ($c_p$ = 0.115 g/l) at T = 50±2°C.*

Dynamic light scattering measurements show the same tendency of the radii with increasing radiation dose. At low temperatures the value of the hydrodynamic radius decrease with increasing D. In the shrunken state the radii at low doses (D < 25 kGy) and at high doses (D < 60 kGy) are higher than the radii in medium range of dose. In former measurements it could be shown, that additional polymer in microgel solution collapse at the surface of these microgels (no separate aggregates are formed). At low doses still un-crosslinked sol molecules are in the microgel solution. These molecules collapse and increase the radius of the microgels observed at T = 50°C.

## 4. CONCLUSIONS

It was shown, that various polymeric structures can be formed by applying pulsed electron beam irradiation of aqueous de-oxygenated PVME solutions. Irradiation experiments at room temperature lead to the formation of PVME nanogels due to an intramolecular crosslinking reaction. At low radiation doses the molecular weight of PVME increases because of intermolecular crosslinking the relatively low Mw. With further increasing of the radiation dose at low polymer concentrations (cp < 25 mM) no further increasing of molecular weight can be observed – intramolecular crosslinking reaction occurs. The hydrodynamic radii decrease with increasing dose. The dimension and the intrinsic viscosity of the internally crosslinked nanogels decrease.

Pulsed electron beam irradiation at temperatures above the LCST of PVME leads to the formation of temperature-sensitive microgel particles. Applying the closed-loop system reduces the amount of sol molecules. At low doses (D < 25 kGy) the sol content s < 10%. For this purpose no further purification steps are necessary.

## REFERENCES


[1] P. MOLYNEUX, Water-Soluble Synthetic Polymers. Properties and Applications, CRC Press, Boca Raton, 1987.
[2] H. MAEDA, J. Polym. Sci. B, 1994, 32, 91.
[3] H. SCHAFER-SOENEN, R. MOERKERKE, H. BERGHMANS, R. KONINGSVELD, K. DUSEK, and K. SOLC, Macromolecules, 1997, 30, 410.
[4] F. MEEUSSEN, Y. BAUWENS, R. MOERKERKE, E. NIES, and H. BERGHMANS, Polymer, 2000, 41, 3737.
[5] O. HIRASA, S. ITO, A. YAMAUCHI, S. FUJISHIGE, and H. OCHIJO, in Polymer Gels, ed. D. De Rossi, Plenum Press, New York, 1991, p. 247.
[6] B.G. KABRA, M. K. AKHTAR, and S. H. GEHRKE, Polymer, 1992, 33, 990.
[7] J. ED. DUSEK, Responsive Gels: Volume Transitions, Springer, Berlin, 1993.
[8] R. MOERKERKE, F. MEEUSSEN, R. KONINGSVELD, and H. BERGHMANS, Macromolecules, 1998, 31, 2223.
[9] N.A. PEPPAS and J. J. SAHLIN, Biomaterials, 1996, 17, 1553.
[10] M.C. BONFERONI, S. ROSSI, F. FERRARI, and C. CARAMELLA, Pharm. Dev. Technol., 1999, 4, 45.
[11] A.D. WOOLFSON, D.F. MCCAFFERTY, and G. P. Moss, Int. J. Pharm., 1998, 169, 83.
[12] R. KISHI, H. ICHIJO, and O. HIRASA, J. Intel. Mater. Syst. Struct., 1993, 4, 533.
[13] H. ICHIJO, R. KISHI, O. HIRASA, and Y. TAKIGUCHI, Polym. Gels and Networks, 1994, 2, 315.
[14] M. HIRAIDE and A. MORISHIMA, Anal. Sci., 1997, 13, 829.
[15] H. ICHIJO, O. HIRASA, R. KISHI, M. OOWADA, E. KOKUFUTA, and S. OHNO, Radiat. Phys. Chem., 1995, 185.
[16] J. M. ROSIAK and P. ULANSKI, Radiat. Phys. Chem., 1999, 55, 139.
[17] J. M. ROSIAK, in Radiation Effects on Polymers, ed. R.C. Clough and S.W. Shalaby, Am.Chem.Soc., Washington, 1991, p. 271.

[18] J. M. ROSIAK, J. Controlled Release, 1994, 31, 9.
[19] X.D. LIU, R. M. BRIBER, and B. J. BAUER, J. Polym. Sci. B: Polym. Phys., 1994, 32, 811.
[20] S.SABHARVAL, H.MOHAN, Y. K. BHARDWAJ, and A.B. MAJALI, J. Chem. Soc. Farad. Trans., 1996, 92, 4401.
[21] S. SABHARVAL, H. MOHAN, Y.K. BHARDWAJ, and A.B. MAJALI, Radiat. Phys. Chem., 1999, 54, 643.
[22] I. JANIK, P. ULANSKI, and J.M. ROSIAK, Nucl. Instr. Meth. Phys. Res. B, 1999, 151, 318.
[23] I. JANIK, P. ULANSKI, J. M. ROSIAK, and C. VON SONNTAG, submitted to J. Chem. Soc. Perkin Trans 2.
[24] C. VON SONNTAG and H.-P. SCHUCHMANN, Methods Enzymol., 1994, 233, 3.
[25] G.V. BUXTON and C.R. STUART, J. Chem. Soc. Faraday Trans., 1995, 91, 279.
[26] D. VELTWISCH, E. JANATA, and K.-D. ASMUS, J. Chem. Soc. Perkin Trans. II, 1980, 146.
[27] F. LIPARI and S.J. SWARIN, J. Chromatogr., 1982, 247, 297.
[28] A.O. ALLEN, C.J. HOCHANADEL, J.A. GHORMLEY, and T.W. DAVIS, J. Phys. Chem., 1952, 56, 575.
[29] P. DOWIDEIT and C. VON SONNTAG, Environ. Sci. Technol., 1998, 32, 1112.
[30] M.N. SCHUCHMANN and C. VON SONNTAG, Z. Naturforsch., 1987, 42b, 495.
[31] C. NESE, M. N. SCHUCHMANN, S. STEENKEN, and C. VON SONNTAG, J. Chem. Soc. Perkin Trans. 2, 1995, 1037.
[32] G.V. BUXTON, C.L. GREENSTOCK, W.P. HELMAN, and A.B. ROSS, J. Phys. Chem. Ref. Data, 1988, 17, 513.
[33] H.-P. SCHUCHMANN and C. VON SONNTAG, Radiat. Phys. Chem., 1988, 32, 149.
[34] C. VON SONNTAG, E. BOTHE, P. ULANSKI, and A. ADHIKARY, Radiat. Phys. Chem., 1999, 55, 599.
[35] J. EIBENBERGER, D. SCHULTE-FROHLINDE, and S. STEENKEN, J. Phys. Chem., 1980, 84, 704.
[36] I.A. RAAP and U. GRÖLLMANN, Macromol. Chem., 1983, 184, 123.
[37] P. ULANSKI, E. BOTHE, J.M. ROSIAK, and C. VON SONNTAG, Makromol. Chem., 1994, 195, 1443.
[38] P. ULANSKI, ZAINUDDIN, and J.M. ROSIAK, Radiat. Phys. Chem., 1995, 46, 917.
[39] P. ULANSKI, E. BOTHE, K. HILDENBRAND, J.M. ROSIAK, and C. VON SONNTAG, J. Chem. Soc. Perkin Trans. 2, 1996, 13.
[40] P. ULANSKI, I. JANIK, and J. M. ROSIAK, Radiat. Phys. Chem., 1998, 52, 289.
[41] P. ULANSKI, E. BOTHE, and C. VON SONNTAG, Nucl. Instr. Meth. Phys. Res. B, 1999, 151, 350.
[42] P. ULANSKI, E. BOTHE, K. HILDENBRAND, and C. VON SONNTAG, Chem. Eur. J., 2000, 6(21), 3922
[43] P. ULANSKI, E. BOTHE, K. HILDENBRAND, C. VON SONNTAG, and J. M. ROSIAK, Nukleonika, 1997, 42, 425.
[44] B.G. ERSHOV, Russ. Chem. Rev., 1998, 67, 315.
[45] A. CHARLESBY, Atomic Radiation and Polymers, Pergamon Press, Oxford, 1960.
[46] W. SCHNABEL, Polymer Degradation. Principles and Practical Applications, Hanser, München, 1981.
[47] P. ULANSKI and J. M. ROSIAK, Nucl. Instr. Meth. Phys. Res. B, 1999, 151, 356.
[48] ARNDT, K.F., SCHMIDT, T., REICHELT, R., Polymer 2001; 42, 6785.
[49] PICH, A., LU Y., ADLER, H.J.P., SCHMIDT, T., ARNDT, K.F., Polymer 2002, 43, 5723.
[50] ULAŃSKI P, KADŁUBOWSKI S, ROSIAK JM., Rad. Phys. Chem. 2002, 63, 533.
[51] KADŁUBOWSKI, S., GROBELNY, J., OLEJNICZAK, W., CICHOMSKI, M., ULAŃSKI, P., Macromolecules , 2003, 36, 2484.
[52] RABANI J., MATHESON MS., J. Phys. Chem. 1966, 70, 761.
[53] BROSZKIEWICZ, R., Chemical Methods of Dosimetry of Ionising Radiation, Warsaw: WNT, 1971.
[54] SCHULER, R.H., HARTZELL, A.L., BEHAR, B., J. Chem. Phys., 1981, 85, 192.
[55] SCHMIDT, T., QUERNER, C., ARNDT, KF., Nucl. Instrum. Methods. Phys. Res. B, 2003, 208, 331.

# RESEARCH AND DEVELOPMENT IN THE NANOTECHNOLOGY FIELD IN MALAYSIA, ROLE OF RADIATION TECHNIQUE

KHAIRUL ZAMAN HJ. MOHD DAHLAN, JAMALIAH SHARIF, NIK GHAZALI NIK SALLEH, MEOR YAHAYA RAZALI
Radiation Processing Technology Division,
Malaysian Institute for Nuclear Technology Research (MINT),
Kajang, Malaysia

**Abstract**

Nanotechnology is a strategic area of research and it is an emerging technology that Malaysia together with other countries in the world wishes to exploit for the benefits of mankind. The use of radiation technique to process nanostructured materials or to produce nanostructured materials have been shown technically superior as alternative and viable techniques for further commercial exploitation. Research on radiation processing of nanocomposites have been initiated at the Radiation Processing Technology Division of MINT in the past three years. The main focus of these research are to utilize indigenous natural polymers for production of nanocomposites materials. Natural rubber/clay composites and thermoplastic natural rubber/clay composites are the important materials that under studied. On the other hand, specialty products such as high abrasion and high scratch resistance materials have many industrial applications and its involved the usage of nano-sized silico-organic particles. In this area, palm oil acrylate is seen to have potential to be utilized in the formation of nano-sized silico-organic hybrids

## 1. INTRODUCTION

In recent years there is a wide spread interest in development of nanostructured materials. The vast commercial potential of nanostructured materials has attracted the interest of the industry, academic institutions and government laboratories. The term nanostructured materials usually refer to "solids or thin film in which either the fundamental building block or the microscopic order are nanostructured". Generally, nanostructured material is defined as particles, grains, functional structures or devices with dimensions of ≤100 nanometer. Increasing interest in this kind of particles size is attributed to the high surface to volume ratio. These kinds of materials are expected to demonstrate a unique mechanical, optical, electronic and magnetic property.

The approach to produce nanostructured materials and devices are categorized by many scientists as 'top-down' and 'bottom-up' approached. Bottom-up means building larger objects from smaller building blocks. It involves the initial formation of the nanostructured molecules and atoms and their assembly into the final materials. Self-assembly is one of the most important bottom-up ways of creating nanostructures. Self-assembly consists of the spontaneous integration of the components bouncing in a solution, gas phase or interface until a stable structure is reached. Bottom-up approaches usually take place and inspired by chemical and biological systems.

The other important approach is still now vigorously promoted by scientists is 'top-down'. Top-down refers to the approach that begins with appropriate starting materials (or substrate) that is then 'sculpted' to achieve the desired functionality. This method is similar to that used by the semiconductor industry in fabricating devices out of a substrate by the methods of electron beam lithography and reactive ion etching. Another typical top-down approach is the 'ball-milling' technique, which involves the formation of nanostructure building blocks via controlled, mechanical erosion of the bulk starting substance. Those nano-building blocks are then subsequently assembled into a new bulk material.

## 2. NANOTECHNOLOGY IN MALAYSIA

Malaysia is amongst the countries in the Asia and Pacific region that have initiated program on nanotechnology. Governments in the Asia and Pacific region have started planning and have placed

nanotechnology as one of the priorities areas in Science and Technology research program. Countries like Japan, South Korea and China are the leading countries in the Asia and Pacific region that allocated substantial budgets for nanotechnology initiatives. Japan is the second world leader in nanotechnology initiatives just after USA. Table I summarizes the nanotechnology government funding in the Asia for 2003–2007.

TABLE I. SUMMARY OF NANOTECHNOLOGY GOVERNMENT FUNDING IN ASIA FOR 2003–2007 [1].

| Country | Population (million) | Funding 2003-2007 (US$, million) | Priority | Policy Characteristic |
|---|---|---|---|---|
| China | 2000 | +300 | M, ME | National and regional centres |
| India | 1000 | 20 | M, MEMS | Un-coordinated |
| Thailand | 62.0 | 25 | M, MEMS | National centers |
| South Korea | 48.3 | 1000 | M, E | National centers |
| Malaysia | 24.0 | 23 | M, E, Bio | Un-coordinated |
| Taiwan | 21.5 | 500 | M, E, Bio | Stress on education |
| Singapore | 4.2 | 60 | M, E | Bottom up |

Note: M=Materials, MEMS=Microelectromechanical System, E=Electronic, Bio=Biomedical

In the past 10 years, under the 6th and 7th Malaysian Plans, several research projects on nanotechnology have been initiated by Malaysian scientists and supported by government research funds, Intensification of Priority Research Area (IRPA), administered by MOSTE. This has provides the necessary infrastructure and human resources for Malaysian scientist to further intensify efforts in nanotechnology. In the 8th Malaysian Plan, 2001–2005, nanotechnology has been included as one of 14 priorities research areas, and is categorized under "Strategic Research" (SR). The SR projects are for a maximum period 60 months, with potential for enhancing future competitive socio-economic development or new breakthroughs with commercial potential. Additionally, the projects must be multidisciplinary, and have industrial linkages, with potential for commercialization. A sum of RM1.0 billion (RM3.8=US$1.0) is allocated for the IRPA program under 8th Malaysian Plan and out of this amount, RM350 million is allocated for the SR projects that include nanotechnology.

However, under the current 8th Malaysian Plan, several nanotechnology based projects have been initiated under the priorities research areas [1]. In the area of material and manufacturing, 8 research projects totaling RM94.5million in relation to development of catalyst and usage of palm oil to produce high value added oleochemicals have been approved. In the area of electronic and telecommunication, a budget of RM113.6 million has been allocated for 6 projects in relation optics and electronics for telecommunication, automotive and photonic. Whereas in life sciences and medicine area, 9 projects with budget totaling RM81.4 million has been allocated.

Under the Malaysian National Science and Technology Policy II, nanotechnology is included in the strategy of building competence for specialization in key emerging technologies, and has been identified as a key technology area to support local industry. The areas for nanoscience and technology research include, amongst others, nanostructured materials, nanophotonics, nanoparticles, nanoelectronics, nanomedicine and nanobiotechnology. Some recent developments of Malaysia in nanotechnology are:

a) Establishment of well-equipped nanoscience research centers at several research institutions and universities

b) Increased number of postgraduates in nanoscience/advanced materials

c) Increase number of journal publications

d) Organization of national seminars in nanoscience and nanotechnology

e) Categorization of nanotechnology as priority area under IRPA program

f) Collaboration with international research organization.

## 3. RADIATION PROCESSING OF NANO-STRUCTURED MATERIALS ACTIVITIES IN MALAYSIA

In Malaysia, radiation processing of nanostructured materials is still at infancy and it was started three years ago. At present the applications of electron beam and gamma irradiation are for cross-linking and grafting of nanostructed materials in particular for producing crosslinked or grafted nanosize materials in a polymeric matrix or onto backbone of polymer chain respectively. Radiation processing is also used for curing of coating of nanosized silica acrylate. Work is in progress to produce nanosize magnetic particle embedded in radiation crosslinked natural rubber or natural rubber blend matrices for industrial applications.

### 3.1. Radiation processing of polymer and polymer blend/clay nanocomposites

Among the large number of inorganic layered materials that exhibit intercalation capabilities, layered silicates are one of the most typical because of the versatility of the reactions. In particular, the smectite group of clay minerals such as montmorillonite, sponite and hectorite has mainly been used because they have excellent intercalation abilities. The combination of clay silicate layers and polymer matrices at nanoscale level constitutes the basis for preparing an important class of inorganic-organic nano-structured materials.

The clay such as montmorillonite consists of a dioctahedral aluminum sheet sandwiched between two silica tetrahedral sheets in a layer structure that is ~ 1 nm thick (Figure 1). Stacking of the layers leads to a regular Van der waal's space between the layers called interlayer. Clay has the ability to undergo extensive interlayer expansion or swelling, exposing a large active surface area, permitting guest molecules to enter into the interlayer. Interlayer cations such as Na+, Ca++, and K+ exist on the internal surfaces but can be exchanged with alkyl ammonium cations to give surfaces that are less ionic or polar [2]. Such organically modified interlayers are more easily penetrated by polymers (either in the molten state or in solution) or by monomers that are subsequently crosslinked or polymerized chemically or by using radiation. In the process of polymer-clay nanocomposite synthesis, it is important to ensure the compatibility of the entering polymer/monomer (hydrophobic) with the clay surface interlayer (ionic) by using intermediate such as exchangeable organic based cations, intercalation agent or compatibilizer. Figure 2 shows the overall process of preparing nanocomposites based on clay and polymer/monomers.

The entering polymer molecules into the interlayer can either simply increase the distance between the still-parallel layers in an intercalation process or randomly disperse the separate layers entirely in an exfoliation. In conventional composites, the registry of the clay nanolayers is retained when mixed with the polymer, but there is no intercalation of the polymer into the clay structure. Consequently, the clay fraction in conventional clay composites plays little or no functional role and acts mainly as a filling agent for economic considerations.

An improvement in modulus is normally achieved in conventional clay composite, but this reinforced benefit is usually accompanied with a sacrifice in other properties such as strength or elasticity.

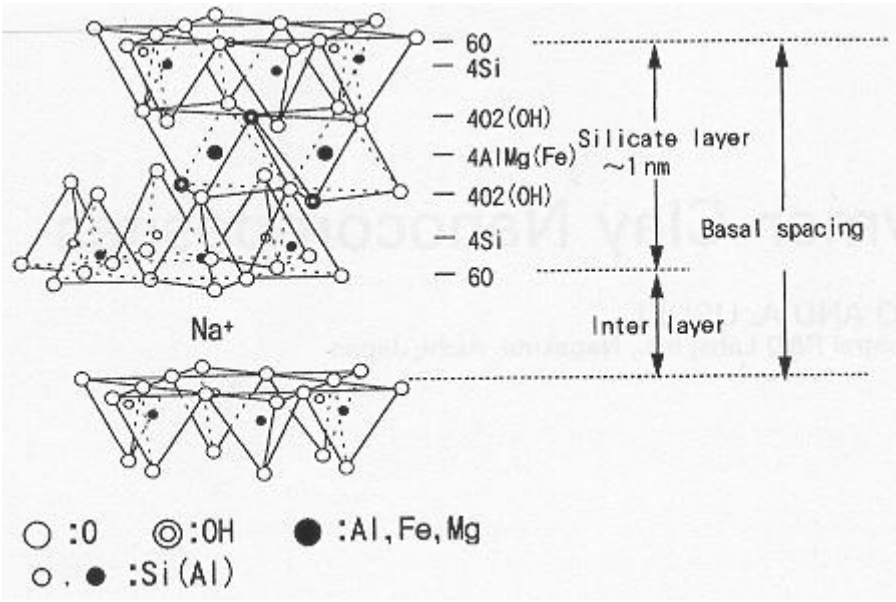


*FIG. 1. Structure of montmorillonite [3].*

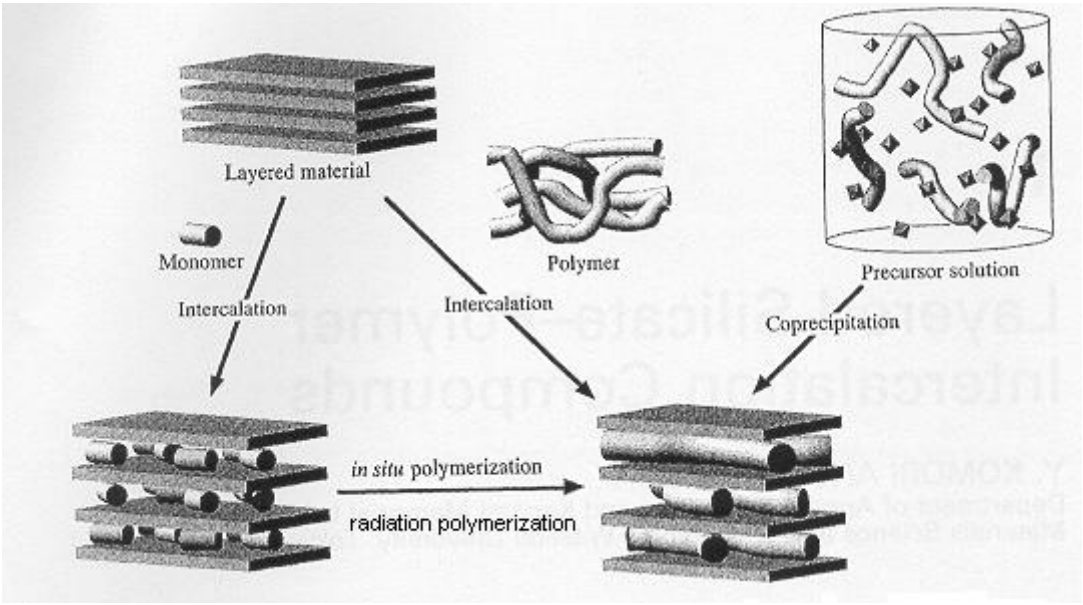


*FIG. 2. Schematic view of preparation of methods for polymer intercalation compounds [4].*

Two types of polymer-clay nanocomposites are possible, i.e. intercalated nanocomposites and exfoliated nanocomposites. Intercalated nanocomposites are formed (Figure 3) when one or a few molecular layers of polymer are inserted into the clay interlayer with fixed interlayer spacing. Exfoliated nanocomposites are formed when the silicate nanolayers are individually dispersed in the polymer matrix, the average distance between the segregated layers being dependent on the clay loading. The separation between the exfoliated nanolayers may be uniform or non-uniform. Exfoliated nanocomposites show greater phase homogeneity than intercalated nanocomposites. More importantly each nanolayer in an exfoliated nanocomposites contribute fully to interfacial interaction with the matrix.

This structural distinction is the primary reason why the exfoliated clay state is especially effective in improving the reinforcement and other performance properties of clay composite materials.

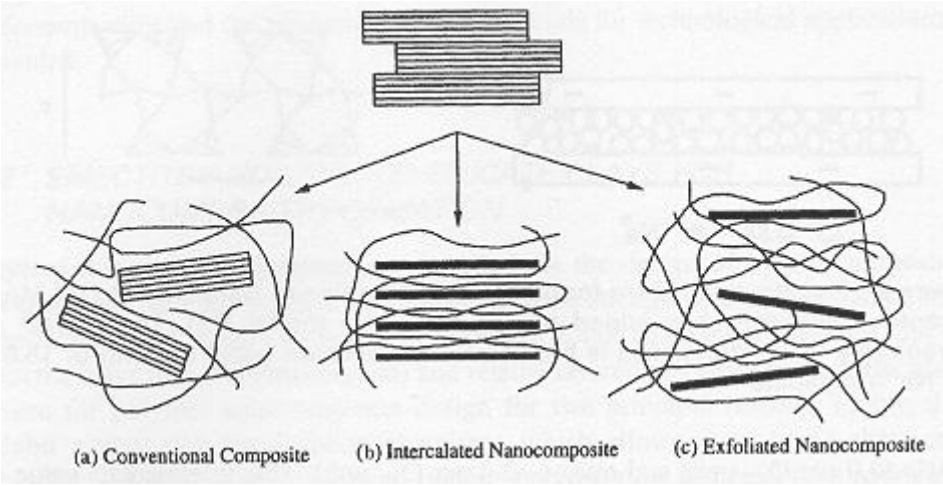


*FIG. 3. Schematic illustration of the structure (a) conventional (b) intercalated and (c) exfoliated [5].*

In Malaysia research on polymer and polymer blend/clay nanocomposites have attracted many researches at Universities and Research Institutes. Polymer and polymer blend that of interest are natural rubber/clay, epoxidised natural rubber/PVC blend/clay, LDPE/clay, fibers reinforced polymer/clay nanocomposites. Study at MINT indicates that radiation processing has great potential to be utilized in the processing of nanocomposites materials via crosslinking of the polymer matrix or grafting of the nanoparticles onto the backbones of the polymer molecules. The blend of natural rubber with thermoplastic and nanosized particles (clay or magnetic particles) will add further dimension to the study of radiation processing of nanocomposites based on natural rubber. Other workers have studied in situ intercalative polymerization for poly (methyl methacrylate)/clay nanocomposite by gamma radiation [6].

The selection of alkyl cation or surfactants that of having acrylate functional group at the end of the hydrocarbon chain such as N,N, dimethyacyloamide is expected to improve further the properties of the nanocomposite when expose to electron beam radiation.

### 3.2. Radiation processing of nano-sized particles – organic polymer composites

The preparation of nanosized materials can be either 'top down' or 'bottom up' approached. In the case of top down, there are many nanosized particles that are available and being used as fillers, reinforced materials or other specific functions for composites. The use of nanosized silica as fillers for radiation crosslinked polyacrylates is one of the area that has been shown of great sucess [7,8]. In our laboratory, with the cooperation of IOM, Germany, work on development of radiation curing of silico-organic nanoparticle is in progress. The purpose of this research is to develop coating materials of high abrasion and scratch resistance. Several acrylates and AEROSIL OX50 based nanocomposites were synthesized in the laboratory by the heterogeneous hydrolytic condensation of the silane to silanol groups of the AEROSIL particles. The insitu reaction is proton catalysed and efficiently proceeds at $70^0$C.

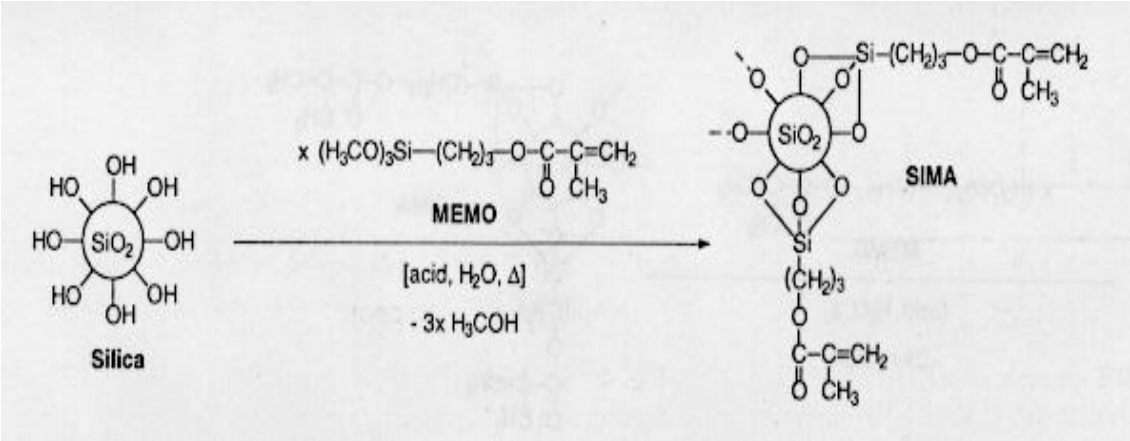


*FIG. 4. Acid catalyzed condensation of methacryloxypropyl trimethoxysilane to form silica modified acrylate (SIMA) [7].*

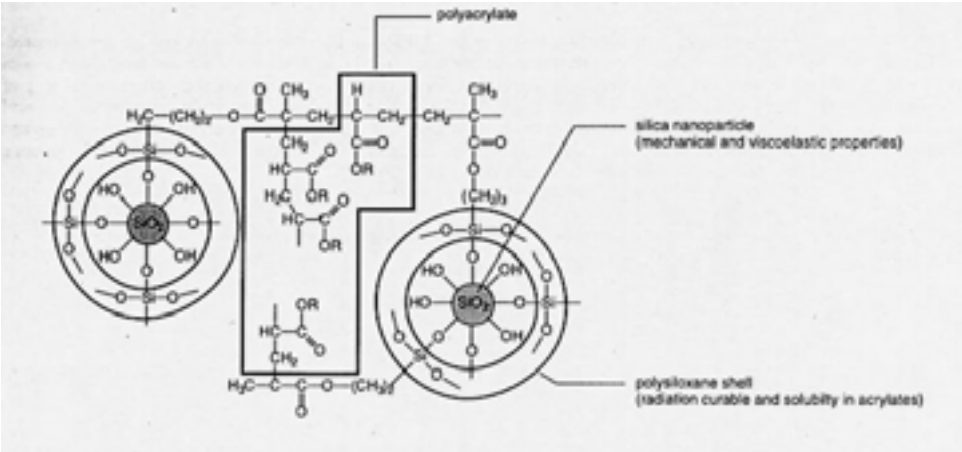


*FIG. 5. UV or EB curing of SIMA to produce polyacrylate.*

The study indicates the significant improvement of the abrasion resistance of nanocompsoites coating materials compared to pure acrylate based coatings. For the UV curing of nanocomposites, the higher the number of acrylate functional groups, the higher will be the abrasion resistance, tetra-functional > tri-functional > di-functional.

At a relatively high nanopowder content of nanodispersion, UV induced polymerization proved to be an efficient alternative to EB curing. However, the scratch resistance of the nanocomposites are comparable to the pure acrylate coating materials.

This work has been expanded into the development of sol gel nanostructured organic – inorganic hybrid materials from palm oil acrylate. Currently, palm oil acrylate such as epoxidised palm oil acrylate (EPOLA) and Palm Oil based Urethane Acrylate (POBUA) are being synthesized in our laboratory.

### 3.3. Radiation processing of nanosized electromagnetic polymer composites

The existing of elastomeric microwave absorbers, also known as MAGRAM and Polyiron (micron sized magnetic particles), are commonly used for EMC (or sometimes is called Electromagnetic Interference (EMI) reduction), and for radar cross section (RCS) reduction or Stealth. The absorbers can be tuned to specific frequencies, multiple frequencies, or used for broadband

surface wave attenuation. Typical formulation consists of rubber and high volume fractions of fillers (up to 60%). Typical fillers include carbonyl iron, iron silicide, ferrites, and carbon. As mentioned above, with the use of magnetic nanoparticles/fillers, it will reduce the amount of fillers used due to its high surface area to volume ratio - as compared to bulk, and at the same time, increase the rubber content.

Three methods can be used to produce the magnetic nanoparticles:-

- Sonolysis of iron pentacarbonyl in decalin.
- Thermal degradation of iron acetylacetonate in dioctyl ether,
- Radiation-reduction of $Fe^{2/3+}$ and radiation-polymerization of natural rubber latex simultaneously with γ-rays.

Methods (i) & (ii) followed by compounding with Natural Rubbers using two-roll-mill to produce elastomeric-magnetic nanocomposites, and then to be exposed to radiation (electron beam or/and γ-rays). The function of radiation is to enhance the physical and mechanical properties of the matrix (elastomeric component). Method (iii) is a direct method of producing elastomeric-magnetic nanocomposites using radiation (γ-rays).

## REFERENCES


[1] SHARIFAH BEE ABD HAMID AND MOHD AMBAR YARMO, Perspective and Challenges in Nanotechnology: A National Strategy for Malaysia, *National Symposium on Science and Technology*, Kuala Lumpur, 28–30 July (2003).

[2] THENGTH, B.K.G. Formation and properties of polymer clay complexes, Elsevier, Amsterdam, (1979).

[3] KATO, M., USUKI, A., Polymer-clay nanocomposites: Polymer Clay Nanocomposites, Edited by T.J. Pinnavaia and G.W.Beall, John Wiley & Sons, Ltd. (2000) 97–109

[4] KOMORI, Y., AND KURODA, K., Layered silicate-polymer intercalation compounds: Polymer-Clay Nanocomposites, Edited by T.J. Pinnavaia and G.W.Beall, John Wiley & Sons, Ltd. (2000) 3–18.

[5] WANG, Z., MASSAM, J., AND PINNAVAIA, T.J., Epoxy-Clay Nanocomposites: Polymer-Clay Nanocomposites, Edited by T.J. Pinnavaia and G.W.Beall, John Wiley & Sons, Ltd. (2000) 127–149.

[6] WEI'AN ZHANG, YU LI, LUO WEI AND YUE'E FANG. In situ intercalative polymerization of poly(methyl methacrylate)/clay nanocomposites by γ-ray irradiation. *Materials Letters*, 4342 (2003) 1–5.

[7] BAUER, F., ERNST, H., DECKER, U., FINDEISEN, M., GLASEL,H-J., LANGGUTH, H., HARTMANN, E., MEHNERT, R., AND PEUKER, C., Preparation of scratch and abrasion resistance polymeric nanocomposites by monomer grafting onto nanoparticle, I. FTIR and multi-nuclear NMR spectroscopy to the characteristic of methyl grafting, *Macromol. Chem. Phys*., 201 (2000) p. 2654.

[8] GLASEL, H.–J., BAUER, F., ERNST, H., FINDEISEN, M., HARTMANN, E., LANGGUTH, H., MEHNERT, R., SCHUBERT, R., Preparation of scratch and abrasion resistance polymeric nanocomposites by monomer grafting onto nanoparticle, 2. Characterization of radiation curable polymeric nanocomposites, *Macromol. Chem. Phys*., 201 (2000) p. 2765.

# PROPERTIES OF RADIATION CROSSLINKING OF NATURAL RUBBER/CLAY NANOCOMPOSITES

JAMALIAH SHARIF[1], KHAIRUL ZAMAN HJ. MOHD DAHLAN[1], WAN MD ZIN WAN YUNUS[2], MANSOR HJ. AHMAD[2]
[1] Malaysian Institute for Nuclear Technology Research (MINT), Bangi, Kajang
[2] Universiti Putra Malaysia, Serdang, Selangor

**Abstract**

The properties of radiation cured natural rubber/clay nanocomposites were studied. The natural rubber used in this work is of grade SMRL (Standard Malaysian Rubber) and the clay used was sodium montmorillonite modified with various types of cationic surfactants in order to make the galleries hydrophobic and thus more compatible with the elastomer. The natural rubber /clay nanocomposites were prepared by melt mixing at 120°C in an internal mixer Haake for 10 minutes. The compound was then irradiated with electron beam at optimum dose. X-ray diffraction results indicated intercalation of the natural rubber into silicate interlayers. Upon irradiation at 250 kGy, the tensile strength of the NR/Na-MMT nanocomposites constantly reduced slightly with increasing clay loading. Whereas the tensile strengths of NR/DDA-MMT and NR/ODA-MMT increases to optimum levels, 12.1 MPa and 9.5 MPa respectively at 3 phr clay contents before decreasing and remain constant up to 10 phr clay content. On the other hand, the elongation of NR/DDA-MMT nanocomposites is less affected with increasing clay content up to 3 phr after which the elongation drop drastically. TGA studied showed that NR/DDA-MMT and NR/ODA-MMT nanocomposites have higher decomposition temperatures in comparison with the NR/Na-MMT.

## 1. INTRODUCTION

Clay has been used as natural rubber filler for many years but the reinforcing ability of clay is poor due to its large particle size and low surface activity. The clay particles could only be dispersed on the microscale in the polymer matrix even though the clay comprised of silicate layers having a 1 nm thick planar structure. The layers cannot be separated from each other through general polymer processing methods. Recent way of improving the reinforcing ability of clay is by changing the hydrophilic nature of clay to organophilic. This is done by ion exchange the clay interlayer cations with organic cations such as alkylammonium or alkylphosphonium. By using the modified clay many researchers have succeeded in intercalating various polymer in the clay interlayer to prepare clay/polymer nanocomposites. The first such clay-based nanocomposites were synthesized by a Toyota research group [1,2] using a polyamide as the polymer matrix. The work was expanded with various polymers and these include polypropylene [3–5], ethylene propylene diene monomer (EPDM) [6], styrene [7], poly(methyl methacrylate) [8], Ethylene vinyl acetate [9] and many others. The nanocomposites showed major improvements in physical and mechanical properties, heat stability, reduce flammability and provide enhanced barrier properties at low clay contents.

Study on synthetic rubber and natural rubber/clay composites cured by sulfur or peroxide have been carried out by several researchers. Okada et al. [10] showed for acrylonitrile butadiene rubber (NBR) cured by sulfur only 10 phr organoclay were necessary to achieve tensile strength comparable to compounds loaded with 40 phr carbon black. Changwoon et al. [11] observed totally different tear morphology for acrylonitrile-butadiene rubber/clay nanocomposites cured with peroxide. Usuki et al. [12] study ethylene-propylene-diene (EPDM)/clay hybrids by a vulcanization process using several vulcanization accelerators. Silicate was exfoliated and uniformly dispersed but the gas permeability of the hybrid reduced 30% as compared to pristine EPDM. Arroyo et al. [13] showed that the blending of 10 phr octadecyl amine modified montmorillonite with natural rubber is enough to obtain the same mechanical behavior as the compound with 40 phr carbon black. Vu et al. [14] found organic modification of clay facilitated the intercalation of the synthetic cis 1,4, polyisoprene and ENR into the clay gallery thus increased the tensile and modulus properties of the compound cured by sulfur.

To our knowledge there is no report on radiation curing of natural rubber/clay nanocomposites. The objective of this work is to prepare naturally occur cis-1,4 -polyisoprene, natural rubber/clay

nanocomposites and study the properties of compounds cured by radiation method. NR that will be used in this work is SMRL grade. This is a light colored rubber prepared from field latex by adding formic acid. The coagulum is left matured for 6–12 hours and then converted to granular form. Drying of the crumbs is carried out in deep-bed through circulation driers at 100°C for 4–5 hours [15].

## 2. EXPERIMENTAL

### 2.1. Materials

Natural rubber (NR) of SMRL grade was purchased from Guthrie Corp. (M) Bhd., Malaysia. Sodium Montmorillonite (Kunipia F) with a cation exchange capacity of 119 meq/100 g was purchased from Kunimine Ind. Co. Japan. Dodecyl, and octadecylamine were purchased from Merck.

*Preparation of organophilic clay*

Organophillic clay MMT was prepared by cationic exchange process in an aqueous solution by vigorously stirring 20 g of sodium montmorillonite which was dispersed in 800 ml of distilled water at 80°C with 50 mmol Dodecyl ammonium chloride which was prepared by stirring 50 mmol dodecyl amine with 50 mmol concentrate HCl in 200 ml distilled water. The precipitate was filtered and washed with distilled water until no chloride was detected with 1N $AgNO_3$ solution. It was then dried at 60°C for 24 hours. The organophilic montmorillonite was ground with a mortar and particles with the size less than 75μm were collected for the preparation of nanocomposites. The product was marked as DDA-MMT. For the preparation of octadecyl ammonium-montmorillonite (ODA-MMT), 50 mmol octadecyl amine was stirred with 50 mmol HCl to form octadecyl ammonium chloride.

*Preparation of nanocomposites*

Natural rubber/clay nanocomposites with different contents of the organically modified clays were prepared by melt mixing using Haake internal mixer W50E at 120°C. The rotor speed was set at 60 rpm and the mixing time was 10 minutes. The compounds were compression moulded at 120°C and pressure 110 kg/cm$^2$ to produce samples sheet with the dimension of 150x150x1 mm.

### 2.2. Irradiation of samples

Irradiation was carried out in air using a Cockroft Walton type electron beam accelerator (Manufactured by Nissin High voltage, Japan) at an acceleration voltage of 2 MeV and beam current of 5 mA. The dose rate was 50 kGy/pass. The sample was irradiated at 250 kGy.

### 2.3. Characterization techniques

XRD was performed at room temperature by a Shimadzu XRD 600 X-Ray diffractometer. The X-ray beam was nickel filtered CuKα (λ=1.542A) radiation operated at 40 kV and 30 mA Data were obtained from 2θ, 2° to 10° at a rate of 1°/min

The gel content was determined by soxhlet extraction with toluene for 24 hours. The extracted samples were vacuum dried to constant weight for 16 hours. The gel content was calculated as the ratio of weight of dried sample after extraction to weight of the sample before extraction.

Tensile properties were measured using an Instron 4032 tester on dumbell shaped samples having thickness 1 mm. The crosshead speed was 500 mm/min. Five specimens were tested and the average of the values was taken with an error less than 10%.

The thermogravimetric analysis was performed with Perkin Elmer instrument using 15 mg samples. The samples were heated at 10°C/min from 50 to 700°C in dynamic nitrogen atmosphere.

## 3. RESULTS AND DISCUSSION

### 3.1. X-ray diffraction studies for the clay and nanocomposites

The dispersion of the silicate layer in NR matrix was measured with the X-ray diffractometer. The XRD results show on the regular arrangements of silicate layers in both pristine or intercalated forms and the irregular arrangements in the case of complete exfoliation of the layers [16].

Fig 1 shows the XRD pattern for Na-MMT and the corresponding pattern of the NR/Na-MMT nanocomposites with various amount of unmodified clay in the range of the diffraction angle $2\theta = 2–10°$.

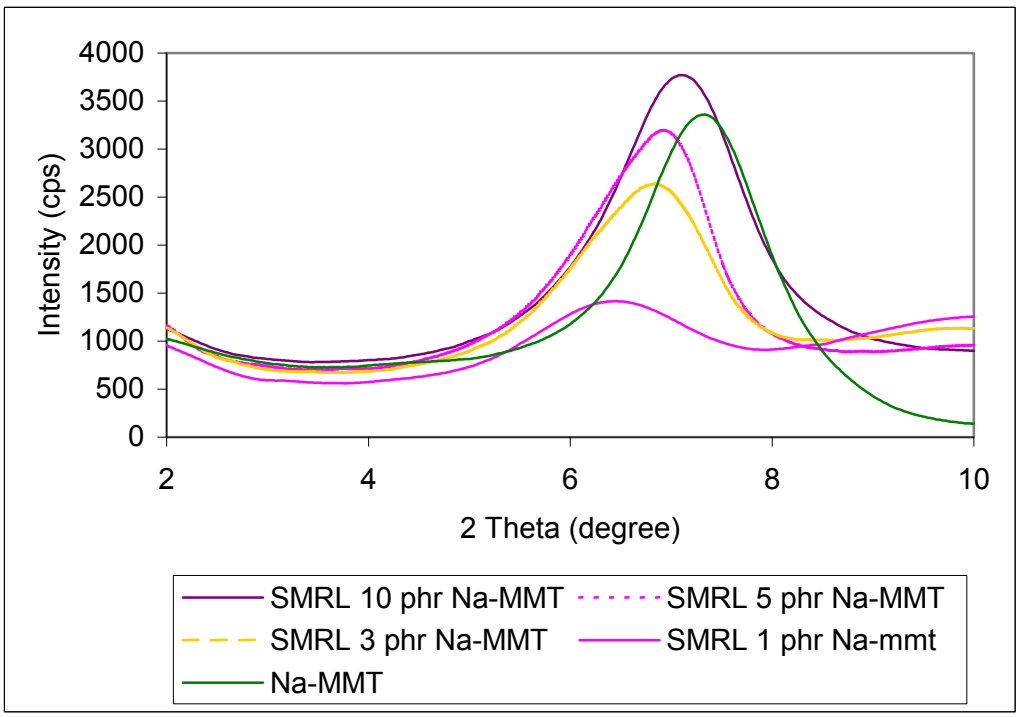


*FIG. 1. XRD pattern of Na-MMT and NR/Na-MMT nanocomposites.*

The Peak of Na-MMT (1.22 nm) shifts slightly to 1.38, 1.32, 1.31 and 1.25 nm for NR containing 1, 3, 5 and 10 phr Na-MMT. As expected the hydrophilic nature of the Na-MMT is hardly intercalated by the natural rubber. The unmodified Na-MMT particles are simply incorporated into the NR matrix in an agglomerated state resulting an opaque appearance of the natural rubber sheets.

Fig. 2 shows the XRD pattern for DDA-MMT and the corresponding pattern of the NR/DDA-MMT nanocomposites with various amount of modified clay in the range of the diffraction angle $2\theta = 2–10°$.

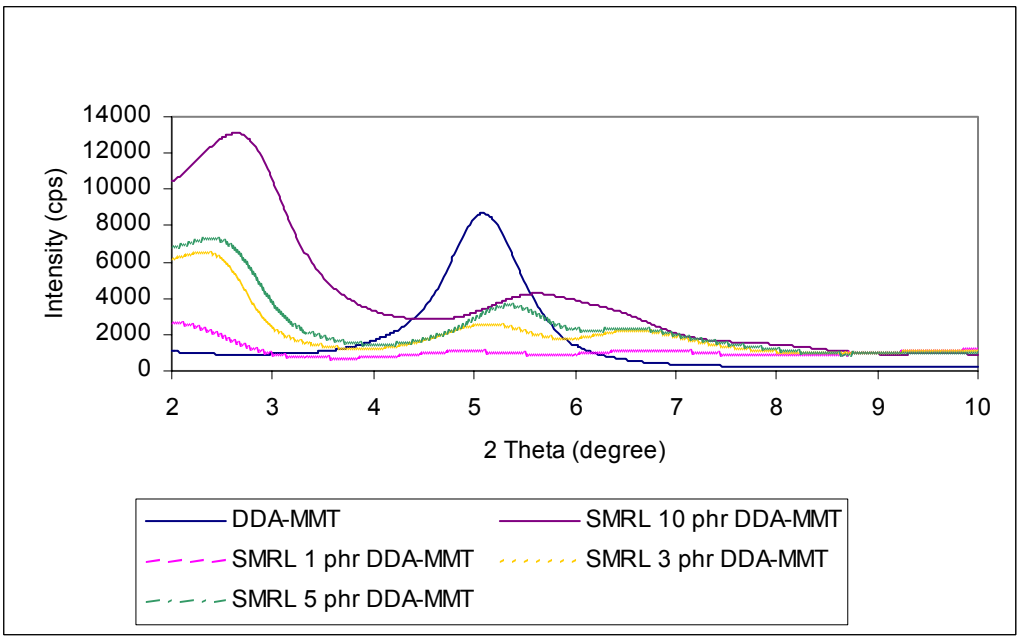


*FIG. 2. XRD pattern of DDA-MMT and NR/DDA-MMT nanocomposites.*

For all concentration of DDA-MMT, three peaks appeared at around 3.29–3.90, 1.50–1.70 and 1.20–1.30 nm. Two of them are below the initial value of DDA-MMT (1.73 nm). The peak corresponding to 1.50–1.70 is probably due to the re-aggregation of the silicate layers during the melt mixing process. While the peak corresponding to 1.20–1.30 may be attributed to unmodified part of the DDA-MMT. On the other hand, the peak at $d_{001}$= 3.29–3.90 nm demonstrates the pronounced intercalation of NR into the hydrophobic silicate layers.

The XRD patterns of NR mixed with ODA-MMT are shown in Fig. 3.

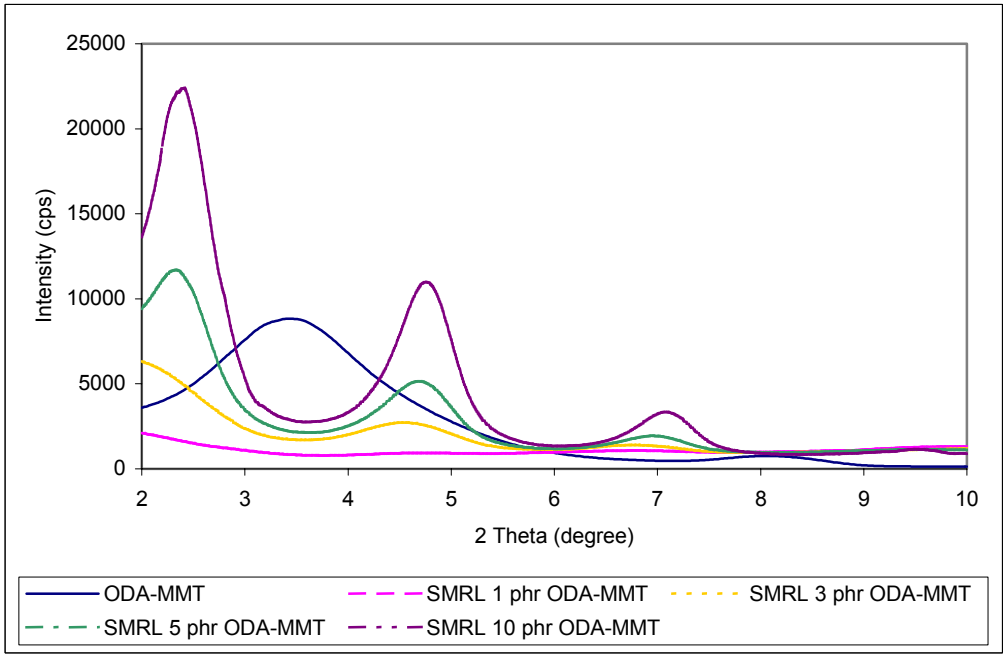


*FIG. 3. XRD pattern of ODA-MMT and NR/ODA-MMT nanocomposites.*

It is apparent from the spectrum that for nanocomposites with 3, 5 and 10 phr ODA-MMT, three peaks appeared at around 4.0–3.60, 1.80–1.90 and 1.25–1.31 nm. Two of them are below the initial value of ODA-MMT (2.90 nm). This is probably due to the re-aggregation of the silicate layers during the melt mixing process and the presence of unmodified part of the organoclay. On the other hand, the peak at $d_{001}$ = 3.80 nm demonstrates the pronounced intercalation of NR into the hydrophobic silicate layers. The XRD pattern clearly show that the interlayer distance reduce with the increase of organoclay content. The extent of intercalation depends on the polymer transport processes through the agglomerate micro pores, the agglomerate size, the diffusion of elastomer chains within the silicate layers and the nature of the elastomer itself [14].

The summary of the intercalated silicate clay layer ($d_{001}$, nm) obtained from the above XRD analysis is given in Table I.

TABLE I. XRD ANALYSIS OF NR/MODIFIED MMT NANOCOMPOSITES

| Organoclay composites /clay content | $d_{001}$ spacing (nm) | | | | |
|---|---|---|---|---|---|
| | 0 phr | 1 phr | 3 phr | 5 phr | 10 phr |
| Na-MMT | 1.22 | | | | |
| DDA-MMT | 1.73 | | | | |
| ODA-MMT | 2.90 | | | | |
| NR/Na-MMT | - | 1.38 | 1.32 | 1.31 | 1.25 |
| NR/DDA-MMT | - | 3.99, 1.74, 1.31 | 3.60, 1.70, 1.35 | 3.47, 1.64, 1.35 | 3.29, 1.50, 1.20 |
| NR/ODA-MMT | - | 1.87, 1.31 | 4.07, 1.94, 1.29 | 3.69, 1.89, 1.27 | 3.64, 1.86, 1.25 |

### 3.2. Gel content

In order to study the efficiency of radiation crosslinking on the natural rubber/organo-clay nanocomposites, the gel content of NR/Na-MMT, NR/DDA-MMT and NR/ODA-MMT nanocomposites irradiated at 250 kGy were determined and the results are plotted in Fig. 4.

The figure shows that the gel content of NR/DDA-MMT and NR/ODA-MMT is almost unchanged with the increase of clay content up to 5 phr and it starts to decrease with further addition of clay. However, the gel content is still high and above 90% for clay content up to 10%.

These results indicate that the presence of DDA-MMT and ODA-MMT up to 10 phr in NR does not affect significantly the formation of the radiation induced crosslinking network. The relationship between gel content and radiation-induced crosslinking is well described by Charlesby (1960) [17], who found natural rubber form crosslinking network upon irradiation. The formation of crosslink is via the free radical process-the same free radical process when peroxide is in use (van Gisbergen and Overbergh, 1992 [18]; Akiba and Hashim, 1997 [19]).

Fig. 4 also shows that the gel content of NR/Na-MMT is much lower than NR/DDA-MMT and NR/ODA-MMT which indicate that the presence of Na-MMT in the rubber matrix inhibits to some extent the formation of rubber crosslinking network. The agglomeration structure of Na-MMT in rubber matrix acts as incompatible particle fillers that may reduce the radiation effects or scavenge the NR-radicals network formation.

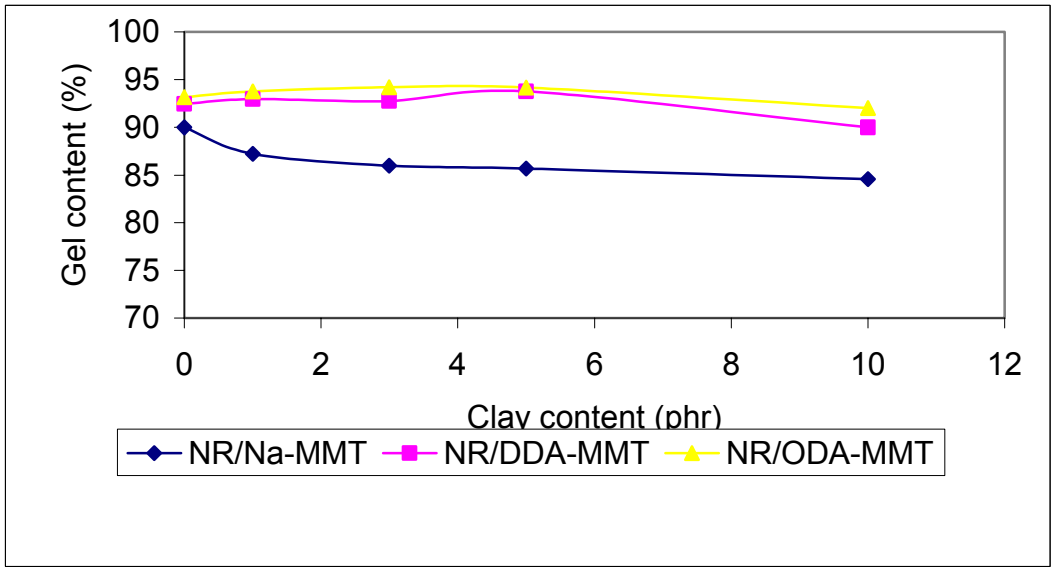


*FIG. 4. Gel content of NR/clay nanocomposites irradiated at 250 kGy.*

### 3.3. Mechanical properties

The relationship between tensile strength with the clay content for NR/Na-MMT composites and NR/DDA-MMT, NR/ODA-MMT nanocomposites irradiated at 250 kGy are shown in Fig. 5 & 6. The tensile strengths of irradiated NR/DDA-MMT and NR/ODA-MMT nanocomposites as showed in Fig. 5 exhibit the same trend with the increasing clay contents.

It is apparent from Fig 6 that upon irradiation the tensile strength of natural rubber decrease slightly with the addition of Na-MMT up to 10.0 phr. The poor compatibility between Na-MMT and natural rubber lead to poor adhesion between the matrix and the reinforcing materials thus no improvement in tensile strength was observed (Nielsen, 1974) [20].

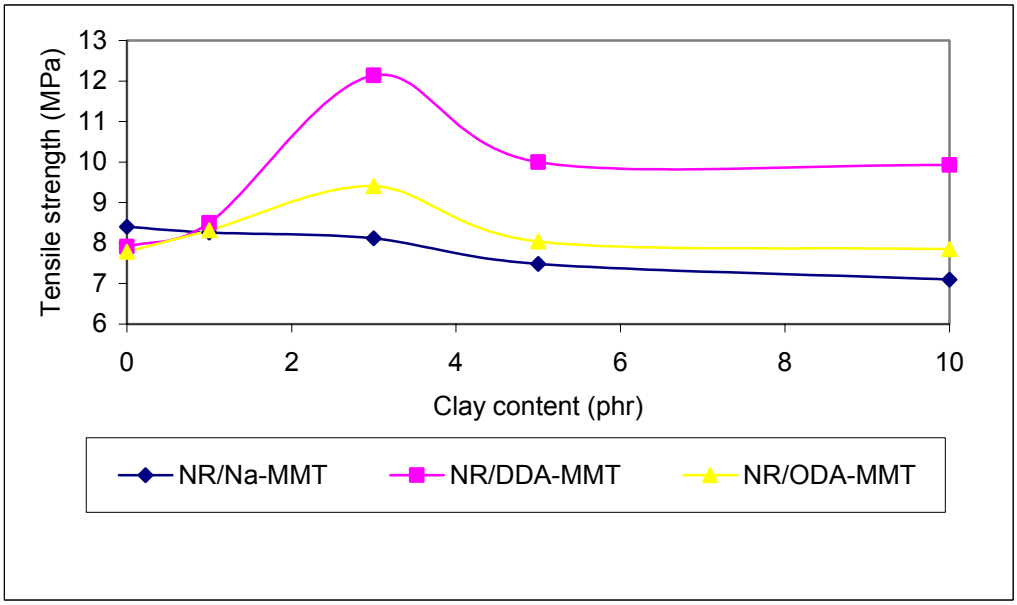


*FIG. 5. Tensile strength of NR/clay nanocomposites irradiated at 250 kGy.*

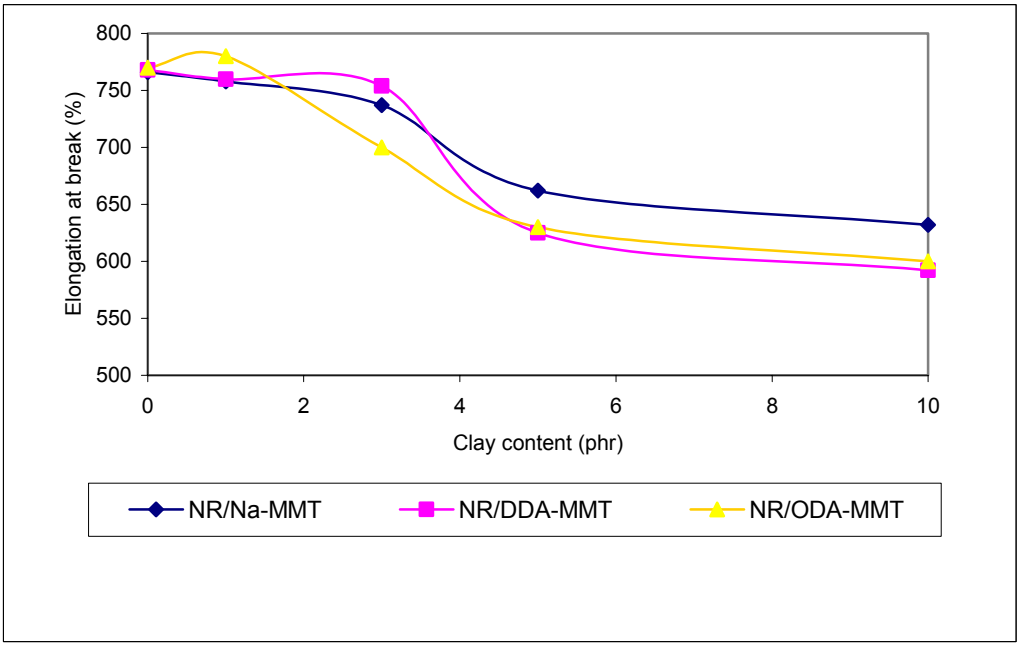


*FIG. 6. Elongation at break for NR/Clay nanocomposites irradiated at 250 kGy.*

Both composites show optimum tensile strengths at around 3.0 phr clay content. This clearly indicates that the intercalation of NR into the clay silicate layers has improved the compatibility of the two materials that resulted in increase in tensile strength. However, at higher clay content, i.e. >3.0 to 10.0 phr, the tensile strengths slightly decrease and remain constant with increasing clay content. The drop in tensile strength at higher concentration of DDA-MMT and ODA-MMT may be due to the aggregation of the clay as indicated in the XRD analysis, which lead to the formation of weak point in the natural rubber matrix consequently reduce the elastomer strength [20, 21]. However, the effects of clay aggregation may be offsets by the crosslinked natural rubber matrix that are able to keep the strength of the composites constant.

The optimum tensile strength of NR/DD-MMT nanocomposite was 12.1 MPa whereas 9.5 MPa for NR/ODA-MMT in comparison with 8.5 MPa for NR/Na-MMT.

As the tensile strength increases for both NR/DDA-MMT and NR/ODA-MMT nanocomposites, the elongations are expected to drop as shown in Fig. 6. However, the elongation of NR/DDA-MMT nanocomposites seems to have less impact up to 3 phr clay content compare to NR/ODA-MMT and after which the elongation drop drastically.

From the above testing, it shows that the mechanical properties of NR/DDA-MMT are better than NR/ODA-MMT.

### 3.4. Thermogravimetric analyses

Themogravimetric analyses were done on NR/DDA-MMT nanocomposites in order to determine the effect on the thermal properties of layered silicate distribution in NR matrix. The results of TGA were shown Fig. 7.

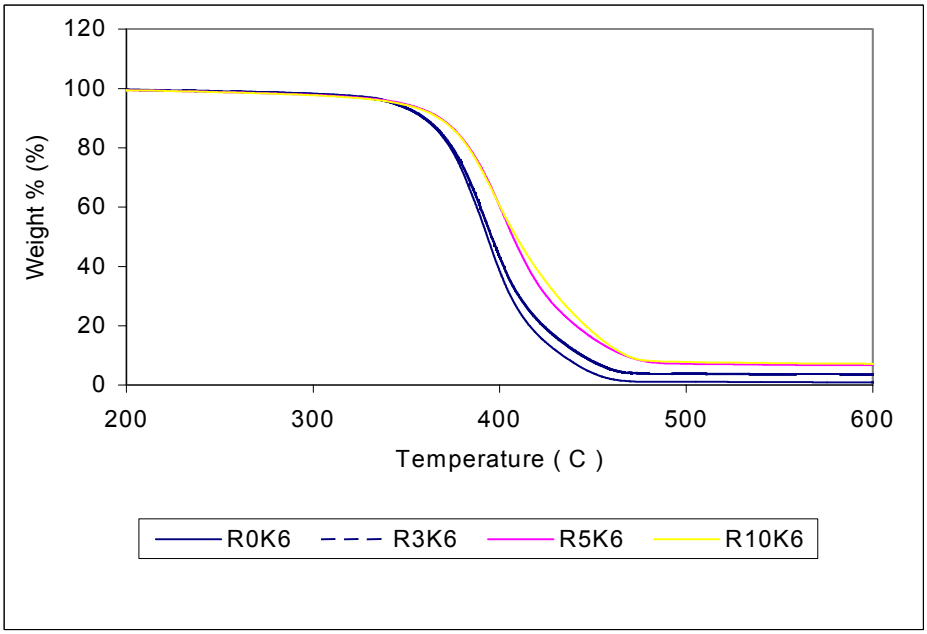


*FIG. 7. TGA results of irradiated NR/DDA-MMT nanocomposites*

The onset of the degradation of the nanocomposites was slightly faster in the presence of the DDA-MMT due to the initial decomposition of the organic intercalating agent used for surface treatment of MMT. However the initial decomposition of the nanocomposites occurred at the same temperature range as NR/Na-MMT i.e. at 255°C. The results also show that thermal stability increase by 20% with the increase of clay loading. According to Bolland and Orr [22] in the temperature range 200–270°C both scission and crosslinking occur though no loss of unsaturation of the bulk rubber. The decomposition of natural rubber is accompanied by the volatilization 39% isoprene, 13.2%dipentene and small amounts of p-menthene as reported by Madorsky and coworkers [23, 24]. The presence of silicate layers disperse homogeneously in natural rubber sheet hinders the permeability of volatile degradation products out from the material and help delay the degradation of the nanocomposites.

## 4. CONCLUSION

The natural rubber/organo-clay intercalated nanocomposites were successfully prepared via melt mixing method as proven by the XRD pattern. NR/DDA-MMT and NR/ODA-MMT cured by EB irradiation at 250 kGy, show excellent improvement in tensile strength. The formation of radiation induce crosslinking does not affected by the filler content. The thermal stability of NR/clay nanocomposites improves with the increase of clay content. The irradiated NR/Na-MMT composites do not show improvement in tensile strength and elongation at break due to the size of clay that in the agglomeration states act as week points in the composites.

## REFERENCES

[1] KOJIMA, Y., USUKI, A., KAWASUMI, M., FUKUSHIMA, Y., OKADA, A., KARAUCHI, T., KAMIGATO, O., J Mater Res 1993, 8, 1185–1189

[2] USUKI, A., KOIWAI, A., KOJIMA, Y., KAWASUMI, M., OKADA, A., KURAUCHI, T., KAMIGATO, O., J Appl Polym Sci 1995, 55, 119

[3] KATO, M., USUKI, A., OKADA, A., Synthesis of polypropylene oligomer-clay intercalation compounds, J Appl Polym Sci 1997, 66, 1781–1785

[4] HASEGAWA, N., KAWASUMI, M., KATO, M., USUKI, A., OKADA, A., Preparation and mechanical properties of Polypropylene-clay hybrids using a maleic anhydride-modified polypropylene oligomer, J Appl Polym Sci 1998, 67, 87–92.

[5] SAUJANYA, C., RADHAKRISHNAN, S., Structure development and crystallization behaviour of PP/nanoparticulate composite, Polymer, 2001, 42, 6723–6731.
[6] USUKI, A., TUKIGASE, A., KATO, M., Preparation and porperties of EPDM-clay hybrids, Polymer, 2002, 43, 2185–2189.
[7] FU, S., QUTUBUDDIN, S. Polymer-clay nanocomposites:exfoliation of organophilic montmorillonite nanolayers in polystyrene, Polymer 2001, 42, 807–813.
[8] OKAMOTO, M., MORITA, S., KIM, H. Y., KOTAKA, T. AND TATEYAMA, H. Dispersed structure change of smectic clay/poly(methyl methacrylate) nanocomposites by copolymerization with polar comonomer, Polymer 2001, 42(3), 1201–1206.
[9] ZANETTI, M., CAMINO, G., THOMANN, R. AND MULHAUPT, R. Synthesis and thermal behaviour of layered silicate-EVA nanocomposites, Polymer, 2001, 42(10), 4501–4507.
[10] OKADA, A., USUKI, A., KURAUCHI, T., KAMIGAITO, O., 1995, In Mark JE, Lee CYC, Bianconi PA, editors. Hybride organic-inorganic composites. ACS Symp Ser.
[11] CHANGWOON NAH, HYUNE JUNG RYU, SANG HYUB HAN, JOHN M. RHEE AND MYONG-HOON LEE, 2001, Fracture behaviour of acrylonitrile-butadiene rubber/clay nanocomposite, Polym Int, 50, 1265–1268.
[12] USUKI, A., TUKIGASE, A., KATO, M., Preparation and porperties of EPDM-clay hybrids, Polymer, 2002, 43, 2185–2189.
[13] ARROYO, M. LOPEZ-MANCHADO, M. A., HERRERO, B., 2003, Organo-montmorillonite as substitute of carbon black in natural rubber compounds, Polymer 44, 2447–2453.
[14] VU, Y.T., MARK, J.E., PHAM, L.H., ENGELHARDT, M., Clay Nanolayer Reinforcement of cis-1,4-Polyisoprene and epoxidized Natural Rubber, J Appl Plym Sci 2001, 82, 1391–1403.
[15] SUBRAMANIAM, A., Natural Rubber (1987) in Rubber Technology (ed. Morton, M.) Van Nostrand Reinhold Co. N. York, p 187.
[16] THENGTH, B.K.G., Formation and properties of Polymer clay complexes, Elsevier, Amsterdam 1979
[17] CHARLESBY, A., 1960. Atomic radiation and polymers. Pergamon Press, Oxford, pp. 198–283.
[18] VAN GISBERGEN, J.G.M., OVERBERGH, N., 1992. Radiation effect on polymer blends. In: Singh, A., Silverman, J. (Eds.), Radiation Processing of Polymers. Hanser, Munich, pp. 51–69.
[19] AKIBA, M., HASHIM, A.S., 1997. Vulcanization and crosslinking in elastomers. Prog. Polym. Sci. 22, 471–521.
[20] NIELSEN, L.E., editor,1974, Mechanical properties of polymers and composites, 2. New York: Marcel Dekker.
[21] AGAG, T., KOGA, T., TAKEICHI, T., 2001, Polymer, 42,3405
[22] BOLLAND, J.L. ORR, W.J.C., Trans Inst Rubber Ind 1945, 21:133
[23] STRAUS S., MADORSKY, S.L., J Res Natl Bur Std 1953, 50 165
[24] MADORSKY, S.L., STRAUS, S., THOMPSON, D., WILLIAMSON, L., J Res Natl Bur Std 1949, 42, 499.

# CHEMICAL MODIFICATION OF NANOSCALE PORES OF ION TRACK MEMBRANES

Y. MAEKAWA,[a,*] Y. SUZUKI,[b] K. MAEYAMA,[b] N. YONEZAWA,[b] M. YOSHIDA[a]
[a] Japan Atomic Energy Research Institute,
Takasaki Radiation Chemistry Research Establishment,
Takasaki, Gunma, Japan
[b] Department of Organic and Polymer Materials Chemistry,
Tokyo University of Agriculture and Technology, Koganei, Tokyo, Japan

**Abstract**

Chemical modification of the pore internal surfaces with sub-micrometer in diameter in poly(ethylene terephthalate) (PET) was examined using the reaction of the carboxylic acids on the surfaces with alkylbromides as an electrophile with catalytic potassium fluoride. The reaction condition for the chemical modification of the pore internal surfaces was estimated from the change in the contact angles and fluorescent spectra of PET surfaces using alkylation reagents, 2-bromomethylaphthalene (BrNP) and 4-(bromomethyl)-6,7-dimethoxy-coumarin (BrCU). In the reactions of PET surfaces with both reagents, the contact angle of the surfaces increased with the increases of reaction time; furthermore, in alkylation with BrCU, which was a reagent bearing a coumarin fluorophore, the change in fluorescent emission intensity is in good agreement with the increases of the contact angles. The DMF solution of BrCU with catalytic KF was introduced into the pores of ion track membranes with a constant pressure. The membranes reacting with BrCU showed emission maximum at 436 nm and excitation maximum at 345 nm, which were not observed in the membranes without alkylation reaction. The linear relationship between the emission and excitation intensities of fluorescence spectra and the pore surface areas were observed, indicating that the alkylation reaction also proceeded on the pore internal surfaces. The fluorescent spots of about 300 nm in diameter can be observed in the fluorescence microscope image of the membrane with pores of 210 nm in diameter. The fluorescent spots were located at the position of the pores observed in the optical image, indicating that a highly concentrating fluorescent probe attaches chemically on the internal surfaces of the cylindrical pores with 210 nm in diameter in the membranes.

## 1. OBJECTIVE OF THE RESEARCH

Porous materials on nanometer scale such as ion track membranes and porous alumina have attracted much attention for applying to separation membranes, electronic and optic devices, and the like because nanoscopic pores can be made with thick films having more than 1 μm in thickness.

Our objective of this paper focuses on the chemical modification of pore inner surfaces in PET ion track membranes since the well-controlled properties of pore inner sufaces should be very important from the view point of synthetic chemistry of polymer surfaces as well as designing materials for application such as separation membranes and nanoscopic electronic devices.

Porous materials on nanometer scale such as ion track membranes and porous alumina have attracted much attention for applying to separation membranes, electronic and optic devices, and the like because nanoscopic pores can be made with thick films having more than 1 μm in thickness [1–7]. Ion track membranes, which are prepared by heavy ion beam radiation followed by alkaline etching, possess cylindrical pores with narrow distribution of pore diameter in a wide range of pore sizes (Figure 1) [8–11]. The fabrication of ion track membranes made of PET have been reported to develop selective membranes for the separation of toxic metal ions, biomolecules, and biological cells because of the advantages to control the pore size and the properties of the internal surfaces of the pores [9, 12–14].

The methods of modifying polymeric surfaces, such as corona [15], plasma [16] and radiation [17] treatments and graft polymerization, are very important for improving surface functionalities [18]. However, these methods are not suitable for the precise control of surface properties, i.e., the transformation of the chemical structure on the surface on a molecular level, of the inner pore surfaces of separation membranes. In grafting polymerizations [19, 20], surface properties can be controlled by

the various functional groups introduced from the corresponding monomers; nevertheless, this method does not meet the need for the precise control of surface properties because it causes morphological changes on polymer surfaces.

SCHEME I The alkylation reaction of the carboxylic acid of PET with the reagent bearing naphthalene and a coumarine fluorophore.

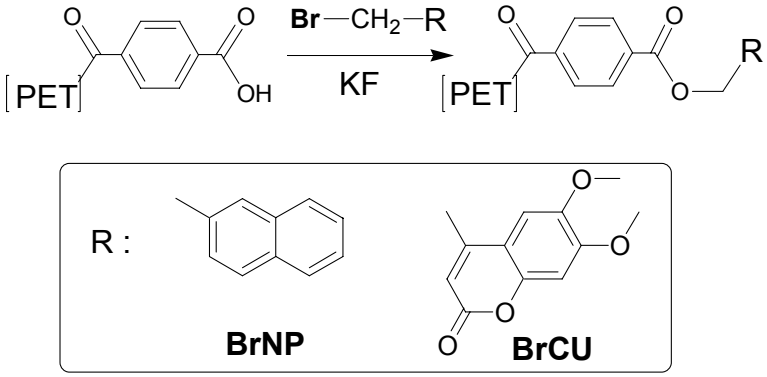


On the other hand, chemical modification, in which chemical reactions of functional groups of polymers modify surface properties, is considered a suitable method for the precise control of not only surface hydrophilicity and charges but also of the quantitative introduction of functional properties, without causing surface deformations [21–23]. Since hydrolysis of PET films, which is the ion track formation condition, provides hydrophilic carboxyl and hydroxyl groups on the surface, these groups might provide suitable functionality for subsequent chemical reactions [24, 25].

Conventional condensation reagents are not useful for selective alkylation of carboxyl groups because re-esterification with the hydroxyl group in the polymer is competitive with the alkylation reagents. Recently, we reported that the hydrophilic surface of PET films was chemically modified by the selective alkylation of the carboxyl groups on the surface using acyl bromide alkylation reagents with catalytic KF and the chemical incorporation of the electrophiles was confirmed by fluorescence spectroscopy measurements.[26,27] Thus, we applied the alkylation method to the chemical modification of the internal surfaces of sub-micron cylindrical pores using a fluorescence reagent and confirmed its incorporation onto the surfaces by fluorescence microscopy.

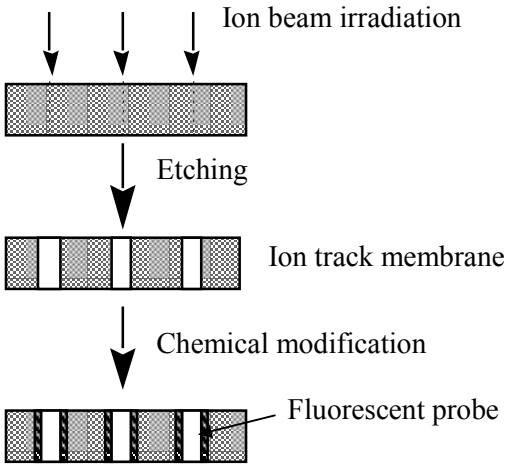


*FIG. 1. Schematic illustration for the preparation of ion track membranes and the modification of the pore internal surfaces.*

## 2. MATERIALS AND METHODS

### 2.1. Materials

PET films with 12 μm and 38 μm in thickness were purchased from Hoechst Japan Co, Ltd. and cut into pieces of 2.0 x 2.0 $cm^2$. 2-(Bromomethyl)naphthalene (BrNP) and 4-(bromomethyl)-6,7-dimethoxycoumarin (BrCU) were purchased from Aldrich Chemical Co., Inc. (U.S.A.) and used without any purification. N,N-Dimethylformamide (DMF), potassium fluoride (KF), and sodium hydride (NaOH) were purchased from Wako Pure Chemical Industries, Ltd. (Osaka, Japan). DMF was dried over molecular sieves 4A. KF was used without any purification.

### 2.2. Measurement

Water contact angles on PET surfaces were measured at room temperature using a Kyowa contact-angle meter CA-X (Kyowa Kaimen Kagaku Ltd., Japan). A constant volume (1 μL) of water was placed on film surfaces from the tip of a 1 mL syringe. Each value reported here is the average of 6 measurements with standard deviations. The rate constants ($K$) of contact angle change of hydrolyzed PET were fitted to the pseudo-first order kinetics using a Table Curve 2D v5 (ALSN Software) installed on a SGI 320 workstation. Fluorescent measurement was performed with a Hitachi F-4500 Fluorescence Spectrophotometer. PET films treated with BrCU were attached on a solid sample holder. The emission and excitation spectra of PET films were measured with excitation and emission wavelengths, 350 nm and 430 nm, respectively. Fluorescence micrographs were observed using a CCD camera set on an optical microscope (Olympus; BX-60). Excitation of the fluorescence was achieved with a mercury lamp through an excitation filter (BP 330-385, Olympus), which allows light of wavelengths of 330–385 nm to pass and the absorption filter (BA420, Olympus), allows light of wavelengths longer than 420 nm to pass. The surface of the films was coated with gold using a Giko IB-3 ion coater and observed with a JEOL JXA-733 scanning electron microscopy (SEM).

### 2.3. Ion beam irradiation and ion track membrane preparation

Six sheets of film samples were set on the turntable-type film-carrier in a vacuum chamber for the formation of ion-track pores in the film, which was connected to the Azimuthally Varying Field (AVF) cyclotron on the Takasaki Ion Accelerators for Advanced Radiation Application (TIARA), Japan Atomic Energy Research Institute (JAERI), Japan. $^{129}Xe$ ion beams with energy of 3.5 MeV/n were used with fluxes of 3 x $10^6$ or 3 x $10^7$ ions/$cm^2$. The irradiated films were illuminated by UV light at wavelengths longer than 310 nm for 6 hours and, in consequence, etched in a 0.5 M NaOH aqueous solution at 40°C without stirring. The specimens were washed with a large amount of water and dried at room temperature. The clear hole patterns with 210–750 nm in diameter were observed in the SEM image of the films.

### 2.4. Ion beam irradiation and ion track membrane preparation

Clean (non-hydrolyzed) PET surfaces were prepared by washing with ethanol at reflux for 2 hours using Soxhlet equipment. The PET films with pure surfaces were immersed in a 1 M NaOH aqueous solution at 40°C for 2 hours. The films were taken out and washed with running water for 30 minutes followed by distilled water on a shaking bet for 30 minutes at room temperature. The films were dried under vacuum (0.1 mmHg) at 0°C for 2 hours to prepare the hydrolyzed PET films. For reaction with BrNP, hydrolyzed PET films were put into suspension of KF of 23.2 mg (0.400 mmol) in a solution of BrNP of 221 mg (1.00 mmol) in 20 mL of DMF on a shaking bet at a room temperature [28]. The films were taken out and washed with DMF to remove the reagents and dried under vacuum (0.1 mmHg) at 0°C for 2 hours. For other surface reactions of hydrolysed films, BrCU of 299 mg (1.00 mmol) was used instead of BrNP in the same reaction condition as mentioned above [29].

Since the contact angle of solid surfaces ($\theta$) are related with the surface tension ($\gamma_S$) by Young's equation ($\gamma_S = \gamma_{SL} + \gamma_L cos\theta$), the changes in $cos\theta$ of the surfaces as a function of reaction time were evaluated. The contact angle data are fitted by the following equation,

$$\cos\theta = a \exp(-kt) + b,$$

where a and b are the total change in $\cos\theta$ and the $\cos\theta$ at the final time. Then, the initial change rate ($K$) in $\cos\theta$ should be expressed by the equation,

$$K = (d\cos\theta / dt)_{t=0} = a \times k.$$

### 2.5. Chemical modifications of cylindrical pore surfaces of PET

We employed BrCU as a fluorescent probe because it possesses an acyl bromide moiety, which reacts with carboxyl groups of PET, and shows an excitation maximum at 350 nm, at which there is no absorption in PET films. According to the condition of alkylation on the hydrolyzed PET surfaces, in which the selective alkylation of the carboxyl groups on PET surface using alkylation reagents has completed for 2 hours judging from the change in the surface contact angles, the pore internal surfaces of ion track membranes with 210, 540 and 750 μm in diameter were modified with the DMF solution of 20.0 mM BrCU with 50.0 mM KF at room temperature. The DMF solution was loaded into a glass syringe, which was connected to a stainless syringe holder (ADVANTEC). Then, the solution was introduced into the pores of ion track membranes in the holder with a constant pressure (5.3 kPa).

## 3. RESULTS AND DISCUSSION

### 3.1. Alkylation of film surfaces

The alkaline etching of PET films irradiated with heavy ions provides hydrophilic carboxyl and hydroxyl groups on the pore inner walls. Since alkaline hydrolysis of the PET film provides the same hydrolyzed structure on the film surface, the alkylation reaction of the film surfaces was conducted as the model reaction to determine the reaction condition for the chemical modification of the pore internal surfaces. Clean (non-hydrolyzed) PET surfaces, which were prepared by ethanol washing, showed a water contact angle of 82.5 ± 1.1°. As the clean films were hydrolyzed in 1M NaOH at 40 °C, the water contact angles of the surfaces quickly decreased and after 1.5 hours reached an almost constant angle of 58.1 ± 1.1°. Since the modification of the hydrolyzed surfaces with alkylation reagents (BrNP and BrCU) makes the surfaces more hydrophobic (probably similar to the hydrophilicity on the non-hydrolyzed PET surface), we first monitored the extent of alkylation reactions on the hydrolyzed PET surfaces using a contact angle measurement.

When the hydrolyzed PET films were immersed in DMF solutions of BrNP with the concentrations ranging from 10 to 80 mM each in 10.0 mM KF, the contact angles of the PET surfaces increased rapidly within 30 min; after 2 hours, it reached the constant values ranging from 63 to 75°. The rate of hydrophobic change of the surfaces during the reaction can be evaluated by the initial change rates ($K$) in $\cos\theta$, as described in Experimental Section. Figure 2a shows the change in $K$ as a function of the concentration of BrNP. The initial change rate increased with the increases of the concentration and reached the constant value (0.4) at the concentration higher than 50 mM. Likewise, in order to examine the effect of KF concentration the on the contact angle change on the film surfaces, the hydrolyzed PET films were treated in DMF solutions of 50.0 mM BrNP with KF of the concentration ranging from 2.5 to 50 mM. As shown in Figure 2b, the initial change rate, $K$, increased with the increases of the concentration of KF and reached the constant value (1.2) at the concentration higher than 20 mM. According to the above experiments, further chemical modification of the film surfaces as well as the pore internal surfaces of ion track membranes were treated by 50.0 mM alkylation reagents with 20.0 mM KF at room temperature.

We applied this substitution reaction to the electrophilic reagent containing a fluorescent unit, in order to monitor the alkylation reactions of the hydrolyzed films by fluorescent spectroscopy [30, 31]. We employed BrCU as a fluorescent probe for two reasons. 1) BrCU can be expected to have similar electrophilic reactivity with the acid salt to that of BrNP, because these reagents have a similar structure to each other, except that the former has an allyl group instead of a naphtyl group at the

carbon atom of reaction center; 2) BrCU shows an excitation maximum at 350 nm, at which there is no absorption in PET films [32]. When the hydrolyzed films were immersed in a DMF solution with 50.0 mM BrCU, the contact angle of the film surfaces increased to ca. 76° in the same manner as did the cases with BrNP. Therefore, BrCU possesses almost the same electrophilic reactivity to the acid salt of the surface as those of the other alkylation reagents.

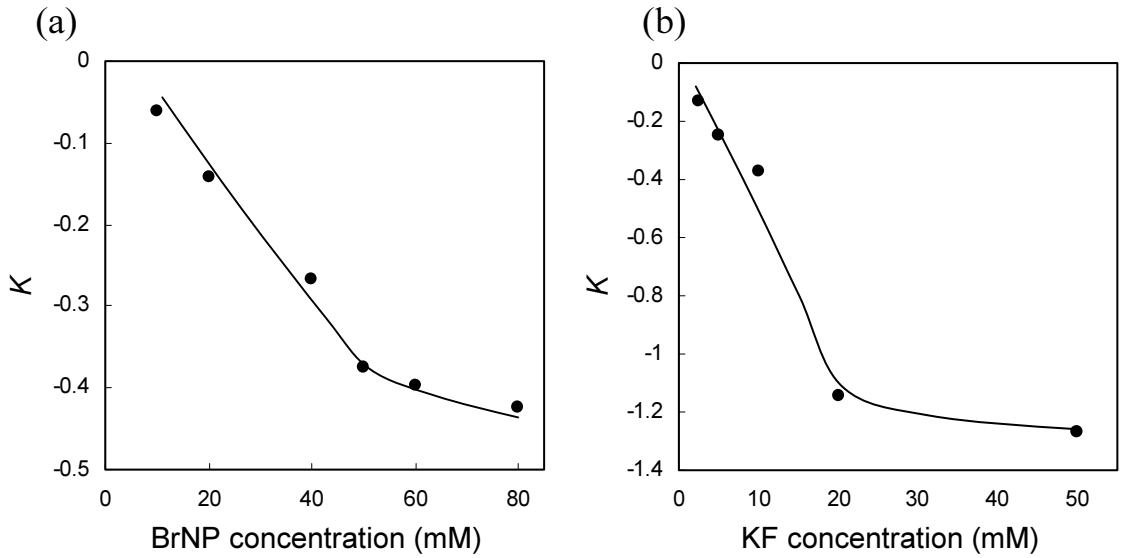


*FIG. 2. (a) Plots of initial change rates of the contact angle (K) of hydrolyzed PET films as a function of BrNP concentration (10 - 80 mM) with KF (10 mM) in a DMF solution. (b) Plots of K of hydrolyzed PET films as a function of KF concentration (2.5 - 100 mM) with BrNP (50 mM) in a DMF solution.*

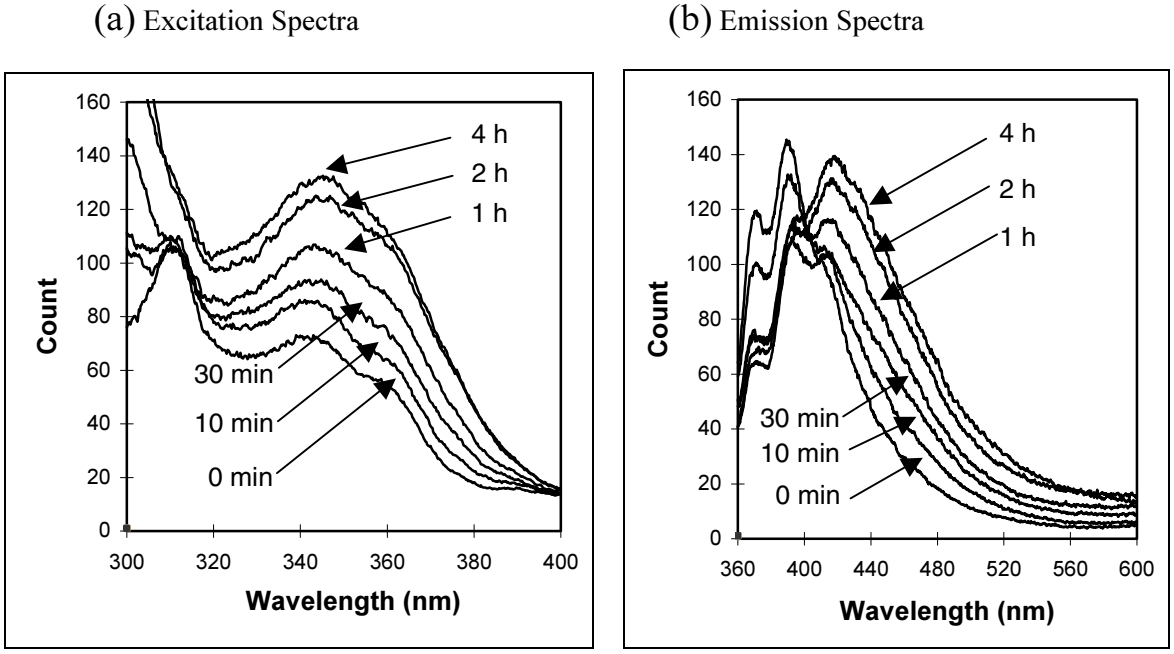


*FIG. 3. (a) The emission spectrum of the films with excitation at 350 nm (a) and the excitation spectrum obtained by monitoring the emission at 430 nm (b) at the different reaction times of the hydrolyzed films in the DMF solution of 50.0 mM **BrCU** and 20.0 mM KF.*

Figure 3 shows the emission spectrum with the excitation at 350 nm (a) and the excitation spectrum by monitoring the emission at 430 nm (b) at different reaction times of the hydrolyzed film with 50.0 mM BrCU with 20.0 mM KF. As the reactions proceeded, the intensities of both the emission and excitation spectra of the films increased, with sufficient sensitivity to monitor the alkylation reactions on the PET surfaces. In Figure 4, the emission and excitation intensities of the PET films at 350 and 430 nm are plotted as functions of the reaction time of the hydrolyzed film with BrCU, together with these contact angles. The intensity of excitation spectra overlapped well with that of the emission spectra throughout the course of the reactions. The proportional increases in these intensities indicated that neither the absorption of the polymer nor the change in the film surfaces interfered with the excitation and emission spectra throughout the course of the reaction.

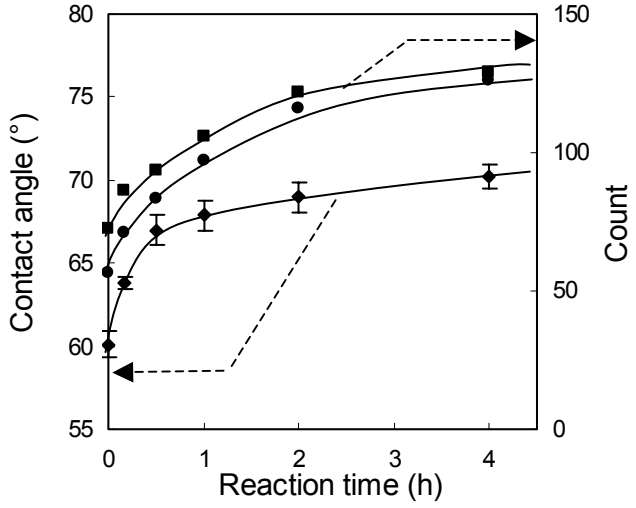


*FIG. 4. The emission (●) and excitation (■) intensities of the PET films at 350 and 430 nm plotted as a function of the reaction time of the hydrolyzed PET films with **BrCU**, together with the contact angles of the films (□).*

### 3.2. Alkylation of pore internal surfaces

PET films with 12 μm in thickness were irradiated by $^{129}Xe$ ion beams with energy of 3.5 MeV/n with ion beam fluxes of 3.0 x $10^6$ or 3.0 x $10^7$ ions/cm$^2$. The irradiated films were illuminated by UV light at wavelengths longer than 310 nm for 6 hours to enhance the dissolution rates in only ion tracks and, in consequence, etched in 0.5 M NaOH aqueous solution at 40°C for 12,14, and 24 hours to dissolve the ion tracks. The clear hole patterns with 210, 540, and 750 nm in diameter were observed in the SEM images of these films (210, 540, and 750 nm-pore membranes).

The DMF solution of 50.0 mM BrCU with 20.0 mM KF was loaded into a glass syringe, which was connected to a stainless syringe holder, as shown in Figure 5. Then, the solution was introduced into the pores of ion track membranes with a constant pressure (5.3 kPa) to make sure the contact of the reaction solution to the internal surfaces of the pores during the whole courses of the reaction. The flow rate of the solution through the 210, 540, and 750 nm-pore membranes were 15, 75 and 13 μL/min, respectively. FIG. 6 shows the emission spectra of the BrCU-modified PET membranes with the excitation at 350 nm and the excitation spectrum monitored with the emission at 430 nm. The emission spectra of PET are shown as a reference in the same figure. The 210 nm-pore membrane showed emission maximum at 440 nm and excitation maximum at 375 nm, which were not observed in the membranes without the alkylation reaction. The 540 and 750 nm-pore membranes showed similar fluorescence spectra with different intensity compared to the 210 nm-pore membrane.

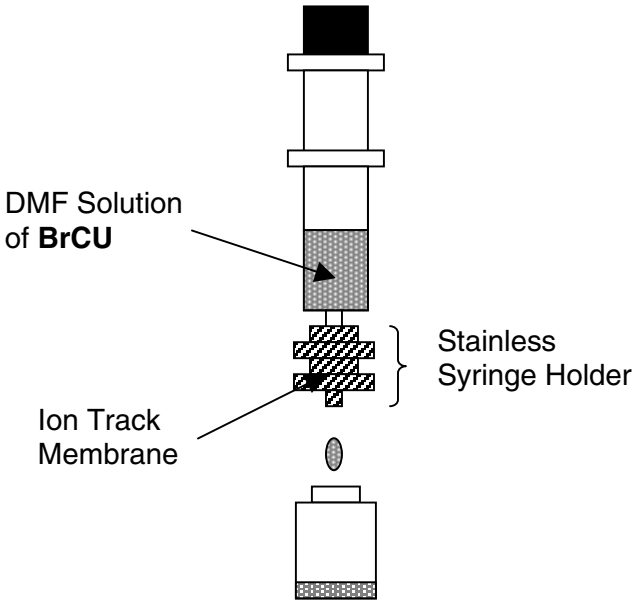


*FIG. 5. Schematic illustration for the chemical modification reactor of the pore internal surfaces in ion track membranes.*

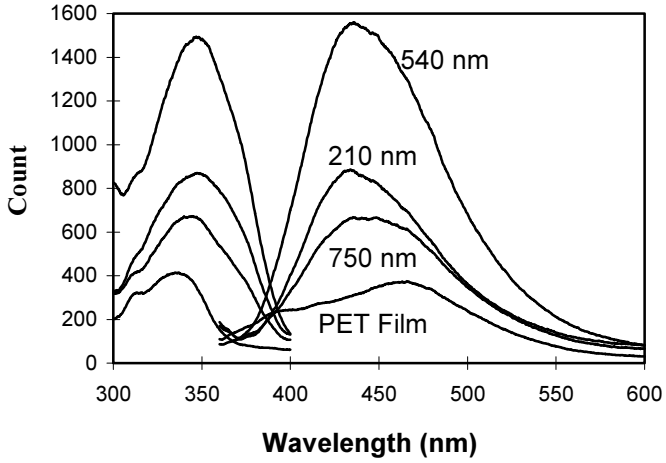


*FIG. 6. Schematic illustration for the chemical modification reactor of the pore internal surfaces in ion track membranes.*

TABLE I. PORE DIAMETERS, ION FLUXES AND SURFACE AREAS OF PET ION TRACK MEMBRANES.

| Pore diameter (nm) | Ion flux (ions/cm$^2$) | Film surface (cm$^2$) | Pore surface (cm$^2$) | Total surface (cm$^2$) | Excitation Intensity (350nm) | Emission Intensity (430nm) |
|---|---|---|---|---|---|---|
| 210 | 3 x 10$^7$ | 1.88 | 2.38 | 4.26 | 864 | 876 |
| 540 | 3 x 10$^7$ | 1.76 | 6.13 | 7.89 | 1480 | 1530 |
| 750 | 3 x 10$^6$ | 1.87 | 0.85 | 2.72 | 649 | 646 |

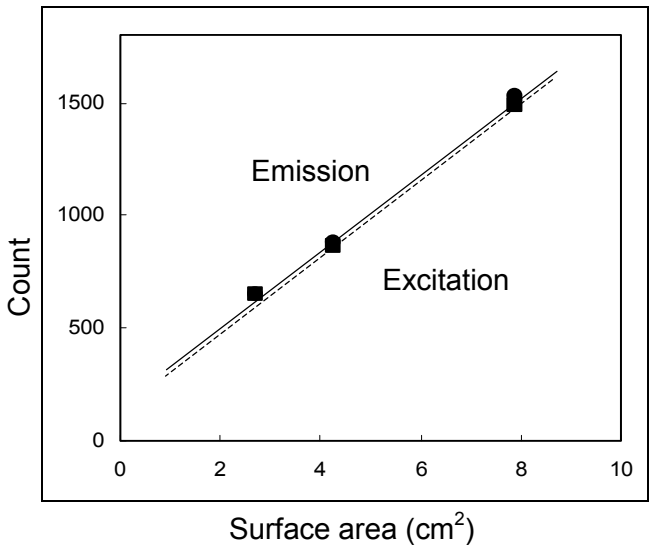


*FIG. 7. The emission intensities at 430 nm (excitation at 350 nm) (●) and the excitation intensities at 350 nm (monitoring at 430 nm) (■) plotted as a function of the surface area of the **BrCU**-modified PET membranes.*

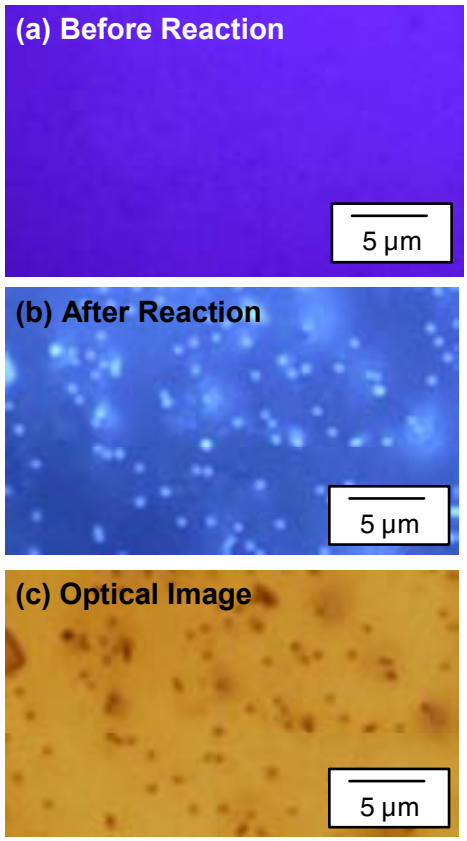


*FIG. 8. Fluorescence microscope photographs of the ion track membrane (pore diameter : 210 nm, hole density 3 x $10^7$ $cm^{-2}$) (a) before and (b) after the reaction with **BrCU**. (c) Optical microscope photograph at the same area of the corresponding membrane.*

Since the alkaline etching of irradiated PET films provides hydrophilic carboxyl and hydroxyl groups on the film surface as well as the pore inner walls, the fluorescent probe should be also attached onto the film surfaces. Thus, the different intensities should be qualitatively related to the total surface area of the film surface and pore inner wall of the membranes (Table 1). As shown in Figure 7, the excitation and emission spectra of the membranes are linearly related to the total surface area of the membranes. When the 210 nm-pore membrane was placed in the DMF solution of BrCU without KF as a control experiment, there was no change in the excitation and emission spectra of the film. The control experiment indicates that the observed fluorescence results from the chemical incorporation but not physical adsorption of the coumarin fluorophore.

The fluorescent images of the 210 nm-pore membrane were taken using a microscope with a standard CCD digital camera. The images were observed with the fluorescence at wavelengths longer than 420 nm (excitation 380 nm). No fluorescence microscope image was observed on the membranes without alkylation reaction (Figure 8a). Whereas, in the same measurement condition, one can clearly observe the fluorescent spots of about 300 nm in diameter in the image of the membrane with BrCU, as shown in Figure 8b. The fluorescent spots were located at the pore position, which was determined from the optical image of the membrane at the same area (Figure 8c). Although the fluorescent probe should be also attached onto the film surfaces, the fluorescence was observed only at the pore position with a good contrast. Namely, one can observe the emission from the fluorescent probes accumulated along the pore inner surfaces perpendicular to the film surfaces. From these observations, it is obvious that the fluorescent probe attaches chemically on the internal surfaces of the cylindrical pores with 210 nm in diameter.

## 4. CONCLUSION

Chemical modification of the pore internal surfaces with sub-micrometer in diameter in PET could be achieved using the reaction of the carboxylic acids on the surfaces with alkylbromides of 20 mM as an electrophile with KF of 50 mM in a DMF solution. The contact angle of the surfaces increased by the alkylation with BrNP and BrCU, which was an alkylation reagent bearing a coumarin fluorophore. The change in fluorescent emission intensity is in good agreement with the increases of the contact angles.

By the introduction of DMF solution of BrCU into the pores of ion track membranes with a constant pressure, the membranes showed emission and excitation spectra, which are attributed to those of BrCU attaching onto the internal pore surfaces. The linear relationship between the emission and excitation intensities of fluorescence spectra and the pore surface areas were observed, indicating that that the alkylation reaction also proceeded on the pore internal surfaces.

The fluorescent spots of about 300 nm in diameter can be observed in the fluorescence microscope image of the membrane with pores of 210 nm in diameter. The fluorescent spots were located at the position of the pores observed in the optical image, indicating that a highly concentrating fluorescent probe attaches chemically on the internal surfaces of the cylindrical pores with 210 nm in diameter in the membranes. Well-characterized chemical modification of pore inner surfaces in polymer membranes should be very important from the view point of synthetic chemistry of polymer surfaces as well as designing materials for application such as separation membranes and nanoscopic electronic devices.

## REFERENCES


[1] M. YOSHIDA, M. ASANO, A. SAFRANJ, H. OMICHI, R. SPOHR, J. VETTER, AND R. KATAKAI, Macromolecules, 29, 8987 (1996).
[2] S.B. LEE AND C. R. MARTIN, Chem. Mater., 13, 3236 (2001).
[3] C.R. MARTIN, Science, 266, 1961 (1994).
[4] T.M. WHITNEY, J. S. JIANG, P.C. SEARSON, AND C.L. CHIEN, Science, 261, 1316 (1993).

[5] M.E.T. MOLARES, V. BUSCHMANN, D. DOVREV, R. NEUMANN, R. SHOLZ, I.U. SCHUCHERT, AND J. VETTER, Adv. Mater., 13, 62 (2001).
[6] L.D. PRA, E. FERAIN, R. LEGRAS, AND S. DEMOUSTIER-CHAMPAGNE, Nucl. Instru. Meth., B196, 81 (2002).
[7] S. SEKI, K. MAEDA, S. TAGAWA, H. KUDOH, M. SUGIMOTO, Y. MORITA, AND H. SHIBATA, Adv. Mater. 13, 1663, (2001).
[8] R.L. FLEISHER, P.B. PRICE, AND R.M. WALKER, "Nuclear Tracks in Solids: Principles and Applications," ed. by R. L. Fleisher, University of California Press, Berkley (1975).
[9] R. SPOHR, Ion tracks and Microtechnology, Principles and Applications, Vieweg & Sohn Verlagsgesellschaft mbH: Braunschweig (1990).
[10] Y. SUZUKI, Y. MAEKAWA, M. YOSHIDA, K. MAEYAMA, AND N. YONEZAWA, Chem. Mater., 14, 4186 (2002).
[11] Y. MAEKAWA, Y. SUZUKI, M. YOSHIDA, K. MAEYAMA, AND N. YONEZAWA, Polymer, 44, 2307 (2003).
[12] N. REBER, R. SPOHR, A. WOLF, H. OMICHI, M. TAMADA, M. YOSHIDA, J. Membr. Sci., 140, 275 (1998).
[13] R. SPOHR, N. REBER, A. WOLF, G. ALDER, V. ANG, C.L. BASHFORD, C.A. PASTERNAK, H. OMICHI, M. YOSHIDA, J. Contr. Rel, 50, 1 (1998).
[14] C. SAMMON, J. YARWOOD, N. EVERALL, Polym. Degrad. Stabil, 67, 149 (2000).
[15] S. SAPIEHA, J. CERNY, J.E. KLEMBERG-SAPIEHA, L. MARTINU, J. Adhes., 42, 91 (1993).
[16] H. YASUDA, A.K. SHARMA, T. YASUDA, J. Polym. Sci., Polym. Phys. Ed., 19, 1285 (1981).
[17] G. FISCHER, A. HAGEMEYER, J. DEMBOWSKI, H. HIBST, J. Adhes. Sci. Technol., 8, 151 (1994).
[18] B.D. RANTNER, D.G. CASTNER, " Surface Modification of Polymeric Biomaterials", Plenum Press, New York and London, 1997.
[19] K. SUGIYAMA, K. KATO, M. KIDO, K. SHIRAISHI, K. OHGA, K. OKADA, O. MATSUO, Macromol. Chem. Phys., 199, 1201 (1998).
[20] E. UCHIDA, Y. IKADA, Macromolecules , 30, 5464 (1997).
[21] D.S. EVERHART, C.N. REILLY, Anal. Chem., 53, 65 (1981).
[22] A.Y. FADEEV, T.J. MCCARTHY, Langmuir, 14, 5586 (1998).
[23] W. CHEN, T.J. MCCARTHY, Macromolecules , 31, 3648 (1998).
[24] A. LAUNAY, F. THOMINETTE, J. VERDU, Polym. Degrad. Stabil., 46, 325 (1994).
[25] C. SAMMON, J. YARWOOD, N. EVERALL, Polym. Degrad. Stabil, 67, 149 (2000).
[26] J. LI, Y. MAEKAWA, T. YAMAKI, AND M. YOSHIDA, Macromol. Chem. Phys., 203, 2470 (2002).
[27] Y. MAEKAWA, Y. SUZUKI, K. MAEYAMA, N. YONEZAWA, M. YOSHIDA, Chem. Lett., 2004, 150-151.
[28] J.H. CLARK, J.M. MILLER, Tetrahedron Lett., 7, 599 (1977).
[29] V.L. MCGAFFIN, R.N. ZARE, Proc. Natl. Acad. Sci. USA, 82, 8315 (1985).
[30] J.R. RASMUSSEN, E.R. STEDRONSKY, G.M. WHITESIDES, J. Am. Chem. Soc., 31, 4736 (1977).
[31] T. MATSUNAGA, Y. IKADA, ACS Symp. Ser.,. 121, 391 (1980).
[32] I. OUCHI, Polymer Journal, 15, 225 (1983).

# USE OF IONIZING RADIATION FOR AND IN THE ELECTRONIC INDUSTRY

P.G. FUOCHI
Institute for the Organic Synthesis and Photoreactivity (ISOF),
National Research Council (CNR),
Bologna, Italy

**Abstract**

Ionizing radiation has been found to be a useful tool for modifying the structures and properties of many materials both in the bulk and on surface in order to improve and tailor their performances. This paper is intended to provide a brief survey of radiation processing methods of interest for the electronic industry, ranging from technologies already commercially well established, through innovative applications at R&D stage for preparation and production of micro and nanostructures for which an exciting future for commercial use is foreseen. Radiation-processing technologies reported here cover the following fields: production of nanoparticles, nanoaggregates and metal semiconductors/polymer nanocomposites, ion-track membranes and lithography for nanodevice production, carrier lifetime control by electron and ion beam irradiation of semiconductor devices. Besides the conventional gamma and e-beam sources, a number of promising new applications make use of novel radiation types like ion beams, focused e-beams and soft X rays, and coherent X rays from a synchrotron.

## 1. INTRODUCTION

The discovery of ionizing radiation more than 100 years ago by W.C. Röntgen [1], H. Becquerel [2] and the Curies [3] opened new fields of research. The basic studies of S.C. Lind in 1910 [4], using radium and its decay products, and the applied research of W.D. Coolidge [5], using an electron beam accelerator, blazed the path that, years later after the World War II, led to the development of almost all the practical applications of ionizing radiation. These applications have grown enormously particularly over the past 50 years thanks to the development of nuclear reactors, that made available radioisotopes in much larger quantities at a lower cost, and to the development of radar during the war, which made possible to build more reliable high-power, high-energy particle accelerators at reasonable costs and now they are an essential part of industrial practice all over the world. The use of radiation in medicine, agriculture and industry is one of the major benefit brought to mankind through a greater industrial productivity, better and more abundant food production, and improved health.

The electronic industry too has benefited from the use of ionizing radiation both as a tool for non-destructive analysis and to test electronic components, and in the production process of these devices. Objective of this paper is to provide a brief, and for that not exhaustive, review of the well established radiation technologies and related commercial products as well as emerging applications of ionizing radiation which are under development in research laboratories as far as electronics and related fields (optoelectronics, photonics, sensors, etc.) are concerned. The following radiation-processing technologies will be presented:

- Production of compounds and materials like metal chalcogenide semiconductors/polymer nanocomposites, that can be used for nano-/microfabrication of electronic devices,
- Electron beams, ions and X rays to perform lithography based nanofabrication of electronic circuits,
- Ion track membranes used as templates for preparation of semiconductors, metal-semiconductors, micro- and nanostructures like nanotubes and nanowires,
- Proton and electron beam irradiation of power devices for lifetime control.

## 2. PRODUCTION OF METAL CHALCOGENIDE SEMICONDUCTORS/POLYMER NANOCOMPOSITES AND NANOPARTICLES

### 2.1. Implantation of metal ions

Ionizing radiation has been and is widely used at R&D stage for preparation of different types of materials and structures. Oxide glasses doped with nanosized metallic inclusion are considered with attention because of their peculiar optical properties potentially useful for integrated optics applications [6]. The size, shape, concentration and spatial distribution of the dopant particles within the composite determine these properties. To obtain dispersion of these metallic particles in dielectric matrices, ion exchange and ion-implantation techniques are mainly used.

Low-energy (30–100 keV) implantation of metal ions, like Cu, Ag and Au ions, at concentration $\leq$1016 ion/cm$^2$ to avoid nucleation, has been used to modify at the nm level the surface of amorphous insulators such as $SiO_2$, $Al_2O_3$ and soda-lime silicate glasses [7] to obtain optically non-linear materials which may be integrated with electronic devices on a single insulator semiconductor chip.

The implantation of MeV Cu, Ag, and Au ions into silica glasses and crystalline materials, like $LiNbO_3$ or MgO, followed by heat treatment produces metal nanoclusters near the implanted surface that form a planar light-guiding layer with changes in both the linear and non-linear optical properties. These changes, which are due to modification of the refractive index of the implanted region, make the glasses and crystals useful for fabrication of photoreactive devices such as ultrafast photonic switches and modulators. The techniques used to form nanoclusters may be summarized as follows: (a) room temperature implantation, followed by high temperature annealing [8, 9]; (b) room temperature implantation at doses above the threshold for spontaneous nanocluster formation (over-dose implantation) [9, 10]; (c) room temperature ion implantation and post-implantation irradiation with Si ions to reduce the threshold implantation dose [9, 11–13]; (d) ion implantation at elevated temperatures; (e) co-deposition of Au and silica followed by annealing or by MeV Si ion bombardment [14].

There is a growing interest on the synthesis and characterization of wide band gap materials due to the many possible applications that they have in optical and/or electronic devices [15]. Nanoaggregates of GaN and $In_2O_3$ wide band gap materials have been synthesized by sequential ion implantation into dielectric substrates, followed by thermal annealing of the samples in either reducing or oxidizing atmosphere which promoted cluster growth. $SiO_2$ and $Al_2O_3$ dielectric substrates were sequentially implanted with 120 keV Ga and 30 keV N ions, or 100–320 keV In and 20–50 keV N ions. Annealing treatments at 900°C in $NH_3$ atmosphere gave rise to the formation of metallic In and $In_2O_3$ nanocrystals and to GaN nanoclusters [16].

### 2.2. Metal and inorganic semiconductor/polymer nanocomposites

A great amount of scientific and technological research has been devoted to hybrid inorganic semiconductor/polymer nanocomposites because they frequently show special properties, which are combinations of those of their original semiconductor and polymer materials. Thus the addition of inorganic nanoparticles to polymers can enhance conductivity and mechanical toughness useful for application in such areas as organic batteries, microelectronics, non-linear optics and sensors. Only few methods have been used to prepare the composites. In general two basic steps are needed: (a) metal ions are introduced into the polymer by copolymerization of an organic monomer and the metal ions, or by an ion-exchange process; (b) a chalcogen source is introduced for the preparation of nanocrystalline chalcogenide. In these methods, the polymerization of organic monomer and formation of nanocrystalline metal chalcogenide particles are performed separately, and thus it is very difficult to control the dispersion of metal chalcogenide in the polymer matrix. Moreover most of the products prepared by these routes at room temperature are amorphous, and post-treatment under high temperature or pressure is often necessary. Synthesis of semiconductor/polymer nanocomposites at room temperature and in a single step is an ideal method for material chemists and alternative routes have been investigated in various laboratories.

Since many monomers can polymerize upon exposure to γ rays, and γ irradiation methods have been developed to prepare nanocrystalline materials [17, 18], a novel strategy to synthesize semiconductor/polymer nanoassemblies in a single step at room temperature by γ irradiation has been devised. In general the metal ion source, chalcogen salt and organic monomer are mixed homogeneously in the deaerated aqueous solution with an appropriate amount of alcohol, as hydroxyl radical scavenger. The resulting mixture is then subjected to γ irradiation (irradiation dose ≥104 Gy) leading to the simultaneous formation of nanocrystalline metal chalcogenide particles and polymerization of monomer. By precipitation reaction of the metal ion attached onto the surface or inside the polymer microspheres and the chalcogen ion, released from the decomposition of the salt upon γ irradiation, a homogeneous dispersion of nanocrystalline metal chalcogenide particles in the microsphere polymer matrixes is thus formed at room temperature and ambient pressure without pollution of chemical initiators. In this way quasi-spherical CdS, PbS, Ni, and Ag particles having diameters of 5 to 25 nm, homogeneously dispersed in polyacrylonitrile [19, 20], polyacrylamide [21, 22], and polystyrene [23] matrixes have been prepared. By appropriate control of experimental conditions the γ irradiation method may be extended to the preparation of a variety of spherical assemblies of metals and semiconductors/polymer nanocomposites in aqueous system.

Analogously several kinds of semiconductor/polymer nanowires have been synthesized in a heterogeneous solution system. In this system, an organic monomer with polar groups can self-organize into amphiphilic supramolecules (micelles, microemulsions, vesicles and monolayers on surfaces), utilizing the difference in solubility of different fragments in the monomer. Such supramolecules can polymerize to a pre-organized polymer tubule with a hydrophilic core and a hydrophobic sheath under γ irradiation. The polymer tubule acts as both template and nanoreactor for the following growth of inorganic semiconductor nanowires in the hydrophilic cores from various water soluble sources. Thus, a nanocable with semiconductor wire in a polymer sheath can be obtained. Several kind of inorganic nanowires have been prepared by using this method at room temperature and ambient pressure. For instance a CdSe/poly(vinyl acetate) (PVAc) nanocable with 6 nm core and an 80 nm diameter sheath has been successfully synthesized in a heterogeneous system with an upper layer of vinyl acetate (VAc) monomer and a lower layer of aqueous solution of isopropanol (isopropanol is used as a scavenger for the hydroxyl radicals generated in water by radiation), cadmium sulfate (CdSO4·8/3H2O), and sodium selenosulfate (Na2SeSO3). Under γ irradiation at low dose rate (20.3 Gy/min), to make sure there is enough time for the self-organization of the VAc monomer into supramolecules, the self-assembled supramolecules polymerize forming a solid tubular structure. The PVAc tubules, because of their greater density than the water, drop into the lower water layer, and the water soluble CdSO4 and NaSeSO3 will automatically distribute in the favourable hydrophilic cores of the PVAc tubules. Further irradiation will form CdSe, as Cd2+ ions combine with Se2– released from the radiation induced decomposition of NaSeSO3, and nanowires grow within the inner hollow of PVAc, which act as both nanoreactor and template [24]. Similar nanowires of CdSe, CdS, ZnS with diameter of 5–6 nm and lengths from 200 nm to 1.2 μm in different organic polymer matrixes have been synthesized [25–27]. These nanowires are also able to keep their structures after removing the templates and it has been observed that they could pack into bundles with ordered hexagonal packings.

### 2.3. Nanosized metals and semiconductors

γ Irradiation has been successfully used to prepare nanocrystalline metals, alloys, II–VI semiconducting materials, metal oxide and glass-metal. Deaerated aqueous solutions, with an appropriate amount of ethanol or isopropanol as scavenger of hydroxyl radical, containing metal ions and a surfactant have been irradiated at doses of the order of 104 Gy. The products have been obtained in the form of precipitates that, after washing with ethanol and distilled water to remove by-products, have been dried in vacuum at 50–60°C. In this way nanocrystalline CuX (X = Cl, Br, I), Co, Sb powders and $MoO_2$ of little nm size have been synthesized [see for instance 28, 29] and by employing chalcogen sources, in the presence of ammonia, nanocrystalline ZnE and CdE (where E = S, Se, Te) have been also obtained [30, 31].

All these nanoparticles have great potential technological application in many fields; the semiconducting materials can serve as sputtering target to produce photoconductive films, infrared filters and phosphors for cathode ray tubes [32]. They are also used for LEDs, in electrochromic devices, solar cells, as switches in optical computers [33], and as detectors in nuclear medicine diagnostic applications [34] while the nanocrystalline powders are expected to have possible application as electrolytes for solid state batteries, as catalysts [35], in optical nonlinear devices, optical memory devices [36] and recording materials.

## 3. LITHOGRAPHY

Lithography is that part of the collective procedures for manufacturing silicon integrated circuits which involves the fabrication of specific regions (patterns) of the silicon with the electrical characteristics required by the circuit. Ultraviolet light is generally used to create the patterns, but the move of semiconductor industry towards the downsizing of integrated circuits has pointed out the limits of photolithography as technique for the fabrication of structures with dimensions on the submicron to nanometer scale. In fact, due to diffraction effects, the resolution of the process is limited to few microns. In order to continue shrinking features on chips and making, for instance, computers even more powerful and economical, it has been necessary to go to radiation-based technology using X rays, e-beams and ion beams in order to approach submicronpatterning [37, 38]. Here a brief description of basic principles of X ray and e-beam lithography is reported.

A silicon substrate is first oxidized to form a layer of silicon dioxide ($SiO_2$) several nanometers thick, which is then spin-coated with a uniform layer of polymer (the resist) that is sensitive to ionizing radiation. A soft-bake of the resist is necessary to remove the solvent in which the resist has been dissolved. Selected areas of the resist are then exposed to a radiation source, often through a mask so that to outline the desired pattern. Upon sufficient exposure, the polymer chains in the resist are either broken (positive resist), or become cross-linked (negative resist) thus forming a positive or a negative image of the mask. By choosing the right developer (a solvent), temperature and developing time, the more soluble material is removed and a pattern in the resist is obtained that can be a straight, round-off or undercut depth profile. Pattern transfer from the resist to the unpatterned $SiO_2$ film is realized by wet or dry etching. Wet etching uses chemical or electrochemical processes to dissolve and remove the exposed areas of $SiO_2$. In dry etching, either ion bombardment (sputter etching) or plasma etching with active species (ions, atoms, free radicals) is used to remove the unwanted materials. These dry etching processes can produce straight and sharp pattern edges with a better resolution, therefore they are more useful for patterning ultrafine nanostructures. At the end of the process, the remaining resist is stripped away. The most widely used materials for patterning technologies are polymers with high G values for cross-linking or degradation upon irradiation. Chloromethylated polystyrene and poly(glycidyl methacrylate) cross link on irradiation and behave as negative resists (less soluble upon exposure to radiation). Polymethyl methacrylate and its derivatives and poly(1-butene sulfones) are degraded by irradiation and act as positive resists (more soluble upon exposure).

The e-beam lithography technique uses an electron beam from a scanning or transmission electron microscope (SEM or TEM respectively) to expose an electron-sensitive resist. The beam is controlled by a computer through a position generator interface that allows writing any computer-defined patterns on the resist. X ray lithography is done by using X rays from a synchrotron radiation facility [39] or from a laser-induced plasma. Similarly to the e-beam lithography method the sample is covered by a resist layer with high sensitivity to X rays and then exposed to the synchrotron radiation. Between the radiation source and the sample, at few micrometers above the resist layer, a mask, with the same feature sizes as what is being created, is placed to define the pattern. The X ray masks are usually made of very thin (about 2 μm) silicon carbide films, covered by a metallic pattern, made of high-Z absorber material to prevent unwanted X ray exposure of the sample, with the desired geometry. After irradiation the resist undergoes development to form the desired structure, which, through an etching process is then transferred on the substrate. Both e-beam and X ray lithography are capable of patterning all the way down to lines and spaces well under 70 nm.

The use of ion beams for patterning of micro and nanocircuits or structures instead of using e-beams or X rays is also being investigated. As with e-beams it is possible to use ion beams for direct

writing the pattern nanostructure on a surface under processing. Both the electron and ion beams can be easily focused down to a narrow size, using electromagnetic lenses, as small as few nanometers. Once focused, they can also be scanned across a surface with great precision. Hence, focused beams can be computer controlled to reproduce a digitally stored image by rastering across the substrate without the need of resists or masks. This technique is useful in producing masks with high feature fidelity.

## 4. ION TRACK MEMBRANES

The creation of microporous and nanoporous membranes having highly uniform geometry and precisely determined structures is an exciting example of industrial application of ionizing radiation. These materials, called track membranes (TMs) were first made by irradiation of polymeric sheets, micas, and glasses with fragments from the fission of heavy nuclei such as californium or uranium (nuclear track etch method) [40]. This technique presents a great limitation due to contamination of the foil with radioactive products so that "cooling" of the irradiated material, before using, is needed; this usually takes a few months. The second method makes use of heavy ion beams, usually of energy on the order of several MeV, from accelerators [see for instance 40, 41] and presents quite a few advantages over the former one which are: (a) no induced radioactivity in the irradiated material when ion energy is below the Coulomb barrier; (b) all tracks show the same etching properties; (c) higher energy of particles = deeper penetration in the material; (d) higher density (>109 $cm^2$) track arrays; (e) easier control of the impact angle and production of arrays of parallel tracks. Widely used polymers for ion track membranes are polyethylene therephthalate (PET) and polycarbonate (PC). By bombarding PET or PC sheets or films with swift heavy ions (e.g. Ar+, N+ or Xe+) latent radiation damage linear tracks are created through the samples. Following etching with an alkali solution (NaOH for instance), uniform cylindrical, conical, tunnel-like, or cigar-like pore have been obtained at will. Pore sizes or dimensions depend upon various factors, viz. the nature and energy of incident particles, the target material, etch conditions, e.g. temperature, nature of etchant, pre-etch storage conditions, etc. and are controllable. Cylindrical channel 0.02–5.0 μm in diameter with lengths of 10–50 μm, 10–100 nm pores, membranes containing anywhere from a single pore up to 109 pores/$cm^2$ have been produced and thin film polymer membranes having highly uniform pore size and a wide variety of porosities in well-distributed areas of the template (patterning) are already commercially available. A number of modification methods have been devised for creating TMs with special properties and functions (see references in [37, 42, 43]). These nanoporous membranes are used as template materials for the synthesis of micro- and nanostructures.

The template-base method consists of filling a host porous medium with one or more desired materials. Three main processes are used for the synthesis of various combination of polymers and/or metals: (a) electrodeposition (see for instance [44]), where one side of the template, coated with a metallic layer, or the template support itself, is used as a cathode for electroplating; (b) chemical polymerization [44] where a solution of the desired monomer and initiator, in which the template membrane is dipped, is left to diffuse through the pores of the templates leading to a polymerization reaction in these pores; (c) electroless plating (see for instance [45]) where a catalyst to the pore walls is applied which facilitates the deposition of metal on the activated pores of the template. The micro- or nanomaterials so produced take the form of wires or tubules. Magnetic, conducting and superconducting nanowires and nanotubules in array or isolated mode possessing special properties have been manufactured in this way (see references in [42, 43]). Potential applications in devices such as microwave filters for shielding microwave ovens and mobile phones, or in chemical detectors and biosensors with conductive polymer nanotubules are also being seriously considered.

## 5. LIFETIME CONTROL IN SEMICONDUCTOR DEVICES BY ELECTRON AND PROTON IRRADIATION

The carrier lifetime in power semiconductors plays a major role in determining the switching performances of these devices and on its reduction depends their electrical behaviour, in particular their commutation behaviour.

The carrier lifetime is strongly affected by the presence of deep levels (induced by the presence of impurity atoms and/or lattice defects inside the silicon crystal), which act as recombination centres. It was found that electron irradiation of these devices, at relatively high energy (> 3–4 MeV), was an efficient mode [46, 47] to introduce lattice defects into the silicon crystal in a controllable manner. Since then this technique has replaced the traditional thermal diffusion of heavy metal impurities and has become an integral part of the industrial fabrication process of fast switching power devices [47]. This technique offers several advantages; a drawback is, however, that the electrons affect the entire bulk, since they pass straight through the devices, creating defects all along the way. By the use of light, high energy ions, this drawback can be overcome [48]. In fact protons are stopped inside the bulk of the device at a depth determined by their energy; they create most of the lattice damage towards the end of their range, enabling a localization of regions of high defect concentration while most of the silicon bulk is left relatively unaffected. By using proton implantation, it is then possible to introduce deep levels in a reproducible way at a controlled depth in the active device region (for instance the p-i junction in p-i-n diodes or the n-base layer in GTO) by varying the energy of the incident particles. But the range straggling sets a limit as to how narrow the lifetime reduced regions may be and the skewness of the distribution implies that a "tail" of recombination centres appears along the ion track increasing the forward voltage drop. Experiments performed on thyristors and power diodes [49, 50] have shown that a better trade-off between dynamic and static properties of the devices has been achieved by a combination of low fluence proton and electron irradiation. Similar treatments gave promising results on ultra high-power p-i-n diodes for high frequency applications (PoSeICo, Italy); ion implantation was carried out at IMM-CNR Institute while electron irradiation was carried out at the 12 MeV Linac at ISOF-CNR Institute [51]. The production of proton-irradiated devices is very limited because of high costs and it is reserved to very specialized niches.

## 6. CONCLUSIONS

It has not been feasible to review the field comprehensively in this paper and some areas are not covered at all, most notably non destructive analysis and radiation tolerance tests. We have focused on highlighting some of the more specialized areas that both provide information and illustrate the techniques available. Some of the above technologies are already generating revenue; others are attractive for future commercial application. We can be confident that ionizing radiation can be a valuable tool for solving fundamental problems in material sciences and can provide additional opportunities in the nanoscience and nanotechnology fields as a tool for the development and production of new nanostructured materials with interesting morphologies for different applications, for examples, in photonics, electronics, catalysis, and microsensors.

## REFERENCES


[1] RÖNTGEN, W.C., Sitzungsberichte der Phys. Mediz. Gesellschaft zu Würzburg 137 (1895) 132; Nature 53 (1986) 274.
[2] BECQUEREL, H., C.R. Acad. Sci. Paris 122 (1896) 420–422.
[3] CURIE, P., CURIE, M., C.R. Acad. Sci. Paris 127 (1898) 1215.
[4] LIND, S.C., Monatsh. Chem. 33 (1912) 295; Am. Chem. J. 47 (1912) 397; J. Phys. Chem. 16 (1912) 564.
[5] COOLIDGE, W.D., Phys. Rev. II (1913) 409.
[6] NANAHASKI, I., MANABE, Y., ET AL., J. Appl. Phys. 79 (1976) 1244.
[7] STEPANOV, A.L., HOLE, D.E., TOWNSEND, J., Non-Cryst. Solids 244 (1999) 275.
[8] ZIMMERMAN, R.L., ILA, D., ET AL., Nucl. Instr. and Meth. B 148 (1999) 1064.
[9] ILA, D., WILLIAMS, E.K., ET AL., Nucl. Instr. and Meth. B 141 (1998) 289.
[10] SARKISOV, S., CURLEY, M.J., ET AL., Nucl. Instr. and Meth. B 166 (2000) 750.
[11] ILA, D., WU, Z., ET AL., Nucl. Instr. and Meth. B 127 (1996) 570.
[12] ILA, D., WILLIAMS, E.K., ET AL., Nucl. Instr. and Meth. B 148 (1999) 1012.
[13] ILA, D., WILLIAMS, E.K., ET AL., Nucl. Instr. and Meth. B 166 (2000) 845.
[14] ILA, D., ZIMMERMAN, R.L., ET AL., Nucl. Instr. and Meth. B 191 (2002) 416.
[15] MRS Bulletin, August 2000.

[16] BORSELLA, E., DE JULIÁN FERNÁNDEZ, C., ET AL., Nucl. Instr. and Meth. B 191 (2002) 447.
[17] ZHU, Y.J., QIAN, Y.T., ET AL., Mater. Res. Bull. 29 (1994) 377.
[18] ZHU, Y.J., QIAN, Y.T., ET AL., Chem.Commun. (1997) 1081.
[19] XIE, Y., ET AL., J. Mater. Chem. 9 (1999) 1001.
[20] QIAO, Z.P., XIE, Y., ET AL., Mater. Res. Bull. 35 (2000) 1355.
[21] QIAO, Z.P., XIE, Y., ET AL., J. Mater. Sci. 35 (2000) 285.
[22] LIU, H.R., GE, X.W., ET AL., Mater. Lett. 46 (2000) 205.
[23] WU, D.Z., GE, X.W., ET AL., Mater. Lett. 57 (2003) 3549.
[24] XIE, Y., QIAO, Z.P., ET AL., Adv. Mater. 11 (1999) 1512.
[25] XIE, Y., QIAO, Z.P., ET AL., Nanostruct. Mater. 11 (1999) 1165.
[26] CHEN, M., XIE, Y., ET AL., J. Mater. Chem. 10 (2000) 329.
[27] JIANG, X., XIE, Y. ET AL., Chem. Mater. 13 (2001) 1213.
[28] ZHU, Y.J., QIAN, Y.T., ET AL., Mater. Sci. Eng. B 57 (1999) 247, and references therein.
[29] LIU, Y.P., ZHU, Y.J., ET AL., J. Mater. Chem. 7 (1997) 787.
[30] QIAO, Z.P., XIE, Y., ET AL., Mater. Chem. Phys. 62 (2000) 88.
[31] YANG, Q., TANG, K.B., ET AL., Mater. Lett. 57 (2003) 3508.
[32] CELIKKAYA, A., AKINC, M., J. Am. Ceram. Soc. 73 (1990) 2360.
[33] KORNOWSKI, A., EICHBERGER, R., ET AL., J. Phys. Chem. 100 (1996) 12467.
[34] SCHEIBER, C., Nucl. Instr. and Meth. A 448 (2000) 513.
[35] ROUSSELET, G., CAPDEVIENE, P., ET AL., Tetrahedron Lett. 34 (1993) 6395.
[36] OKAMOTO, S., MASUMOTO, Y., ET AL., Jpn. J. Appl. Phys. Part 1 34 (1995) 128.
[37] CLOUGH, R.L., Nucl. Instr. and Meth. B 185 (2000) 8, and references therein.
[38] MARTIN, J.I., NOGUÉS, ET AL., J. Magn. Magn. Mater. 256 (2003) 449, and references therein.
[39] SILVERMAN, J.P., J. Vac. Sci. Technol. B 15 (1997) 2117.
[40] FLEISCHER, R.L., PRICE, P.B., ET AL., Nuclear Tracks in Solids: Principles and Applications. University of California Press, Berkeley, 1975, and references therein.
[41] FLEROV, G.N., APEL, P., ET AL., At. Energy 67 (1989) 274 (see Engl. Transl.).
[42] APEL, P., Radiat. Meas. 34 (2001) 559.
[43] FERAIN, E., LEGRAS, R., Nucl. Instr. and Meth. B 208 (2003) 115.
[44] PIRAUX, L., DUBOIS, S., ET AL., J. Mater. Res. 14 (1999) 3042.
[45] DEMOUSTIER-CHAMPAGNE, S., DELVAUX, M., Mater. Sci. Eng. C 15 (2001) 269.
[46] CARLSON, R.O., SUN,Y.S., ET AL., IEEE Trans. Electron Dev. 24 (1977) 1103.
[47] FUOCHI, P.G., Radiat. Phys. Chem. 44 (1994) 431.
[48] MOGRO-CAMPERO, A., LOVE, R.P., ET AL., IEEE Trans. Electron Dev. 33 (1986) 1667.
[49] HALLÉN, A., BAROWSKI, M., Solid-State Electron. 32 (1989) 1033.
[50] BRAMMER, R., HALLÉN, ET AL., IEEE Trans. Electron Dev. 40 (1993) 2089.
[51] PORTESINE, M., ZANI, P.E., ET AL., INFM-III Silicon Workshop, 6-8 February 2002 Genova (Italy), Paper VIII-1, Book of Abstracts.

# NEW ISSUES IN RADIATION EFFECTS ON SEMICONDUCTOR DEVICES

A. PACCAGNELLA, A. CESTER
Dipartimento di Elettronica e Informatica, Università di Padova,
Padova, Italy

**Abstract**

We have briefly reviewed the most important degradation mechanisms affecting ultra-thin gate oxides after exposure to ionizing irradiation. The increase of the gate leakage current seems the most crucial issue for device lifetime, especially for non-volatile memory and dynamic logic. The build-up of positive charge in the oxide and the subsequent threshold voltage shift, which was the major concern for thicker oxide, are no longer appreciable in today's devices due to the reduced oxide thickness permitting a fast recombination of trapped holes with electrons from interfaces. Among the leakage currents affecting thin oxides we have considered here the Radiation Induced Leakage Current (RILC) and the Radiation Soft Breakdown (RSB). RILC is observed after irradiation with a low Linear Energy Transfer (LET) radiation source and comes from a trap-assisted tunneling of electrons mediated by the neutral traps produced by irradiation. RILC depends on the applied bias during irradiation and the maximum is measured when devices are biased in flat band. Contrarily to RILC, RSB is observed after irradiation with high LET ions and derives from the formation of several conductive paths across the oxide corresponding to the ion hits. Finally, we present some preliminary results, which indicate that although the direct effects of irradiation (in terms of gate leakage current increase) are small for oxide thinner than 3nm, it is possible that these devices may experience an accelerated wear-out and/or breakdown after subsequent electrical stress relative to a fresh (not irradiated) device.

## 1. INTRODUCTION

It is well known that exposure to ionizing radiation degrades the electrical properties of solid-state electronics. The effects of γ-rays, X rays, electron, proton, heavy ion exposure on MOS devices characteristics have been the topic of several works, books, and review articles over the past two decades [1-4]. In principle, the main effect of an ionizing particle is the generation of electron-hole pairs along the particle track, in a number and density depending on the particle type and energy and on the material characteristics. In irradiated MOS structures, carriers generated in the silicon substrate may produce transient phenomena possibly leading to soft error but also to catastrophic consequences such as Latch Up, mainly due to charge collection at reverse biased junctions: these phenomena will not be considered in this work. Instead we will examine the radiation effects on the gate oxide layers, where the majority of the radiation generated carriers are promptly recombined shortly after thermalization. Some are left behind: while electrons can be rapidly swept out by the oxide field owing to their high mobility, slow residual holes may be trapped in pre-existing defects or in radiation induced defects inside the oxide. The resulting positive charge trapped in the gate oxide has been the main reliability concern in irradiated MOS along with the radiation induced $Si/SiO_2$ interface defects, related as well to radiation induced hole trapping and defect generation. As a consequence substantial threshold voltage ($V_T$) shift and transconductance ($g_m$) reduction have been measured as the typical results of exposing MOSFETs to ionizing radiation. CMOS hardening technologies were developed ad hoc to prevent or limit the occurrence of these degradation phenomena, permitting the use of hardened MOS IC's in radiation harsh environments.

In parallel, Moore's law itself was playing an underground role in enhancing the radiation tolerance of CMOS components, a role appeared only in recent years. In fact, shrinking the device dimensions following Moore's law can be accomplished only by the parallel thinning of the gate oxide to preserve the transistor current driving capability [5,6]. Being the electron tunneling distance around 3 nm in $SiO_2$, when the oxide thickness reaches 6 nm or less the radiation induced oxide positive charge is easily recombined or neutralized by electrons tunneling from the gate and/or Si substrate. This oxide thickness was approximately reached at the CMOS technological node of 0.25μm. Following the CMOS technological evolution the gate oxide thickness has now reached 2 nm or so, becoming even less sensitive to positive charge trapping problems.

If radiation induced charge trapping problems have been overcome owing to the gate oxide transparency to electrons, this characteristic has become the weak point from a reliability viewpoint. Ionizing radiation (as well as electrical stresses) can in fact produce defects acting not as trapping centers but as the agents of leakage paths across the gate oxide driving an excess gate current. Gate leakage adversely affects the overall circuit power consumption, which has been often taken as the key parameter for reliability predictions. Different leakage currents developed depending on the oxide thickness and radiation LET. In this work, we have reviewed the main issues of Radiation Induced Leakage Current (RILC) and Radiation Soft-Breakdown (RSB), as well as the long term wear out of irradiated oxides. In section 2 we have analyzed the RILC conduction mechanism, its dependence on the applied bias during irradiation and the growth kinetics with the total dose. In section 3 we summarize the main aspects of RSB: the conduction mechanism, the dependence on applied bias during irradiation, the gate current noise, and the temperature dependence. Finally, in section 4 we present the radiation induced wear-out and breakdown of gate oxides, which derives from the combined effect of irradiation plus a successive electrical stress.

## 2. RADIATION INDUCED LEAKAGE CURRENT

In the following of this section, we will address various issues concerning RILC [7-9]: First of all, we will analyze the RILC conduction mechanism, aiming to better understand the tunneling process mediating the electron transport across the oxide. Secondly, the RILC intensity will be studied as a function of the oxide field during irradiation, in order to evaluate the origin and the distribution of the neutral traps mediating the tunneling conduction. Finally,we'll present the RILC kinetics as a function of the total cumulative radiation dose, and compared with that found for SILC.

### 2.1. RILC conduction mechanism

The current density – oxide field characteristics ($J_g$-$E_{ox}$) of a 6-nm oxide are shown in Fig. 1a, before and after a high dose irradiation with 8 MeV electrons produced by a pulsed LINAC accelerator. The main effect of irradiation is represented by the increase of the low-field gate current, observed between $E_{ox}$=3 MV/cm and $E_{ox}$=6 MV/cm. The oxide trapped charge in the stressed capacitors is negligible, as deduced from the overlap of the high-field characteristics of irradiated and unirradiated devices, corresponding to the FN tunneling regime. RILC can be evaluated as the excess current $J_e$ arisen after stress:

$$J_e = J_g - J_0 \qquad (1)$$

$J_g$ and $J_0$ are the gate current density after and before the stress, respectively.

RILC appears quite similar to the Stress Induced Leakage Current (SILC) observed after high oxide field electrical stress in thin gate oxides. SILC is generally considered as the result of a trap-assisted tunneling across the oxide, mediated by neutral traps created by the stress [10–12]. Owing to the similar $J_g$-$E_{ox}$ characteristics of RILC and SILC, even RILC can be correlated to a trap-assisted tunneling where traps are generated by irradiation. It has been shown that the experimental results are not consistent with an elastic tunneling model for RILC. An anelastic trap-assisted tunneling process (see Fig. 1b) has been experimentally demonstarted more suitable for RILC conduction mechanism [7]. Again, an analytical model of RILC has been developed for ultra-thin oxides submitted to ionizing radiation, based on the analytical solution of the Schrödinger equation for a simplified oxide band structure [8]. Here RILC occurs through a two-step process: first, an electron tunnels into the oxide defect from the cathode conduction band edge. Then, the electron tunnels out the trap after having lost approximately 1.5 eV, in agreement with previous findings for SILC. The mathematical support of the model is quite heavy and even the final analytical expression of the tunneling current is pretty complex. They show that the RILC is definitely field dependent and that the same trap parameters (energy position, cross section) can be used independently of the total dose, indicating that similar defects are generated at the beginning of, during, and at the end of irradiation.

Noticeably, only defects close to the center of the oxide thickness can contribute to the excess gate leakage, owing to the decrease of the cumulative tunneling probability for defects near to the interfaces.

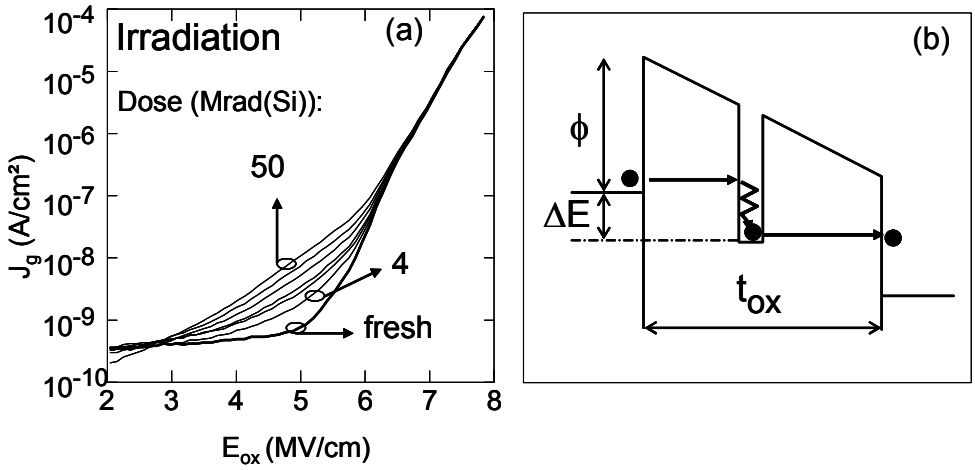


*FIG. 1. $J_g$-$E_{ox}$ a) curves measured before (fresh) and after irradiation for various doses ranging from 4 to 50 Mrad(Si); b) Simplified band structure for the inelastic trap assisted tunneling mediating RILC.*

### 2.2. RILC dependence on applied bias during irradiation

In this section we investigate how the distribution of neutral traps responsible for RILC is affected by the bias applied during irradiation. To this purpose the capacitors were irradiated by using a 8 MeV electron beam and were biased at different oxide fields during and after irradiation. In Fig. 2a ($t_{ox}$=4 nm) and Fig. 2b ($t_{ox}$=6 nm) we have reported RILC as a function of the oxide field applied during irradiation. The 6-nm capacitors have been subjected to a radiation dose 10 times higher than the 4-nm devices, to enhance the measured current and the corresponding experimental precision. The obtained results are similar on both device types. Positive RILC is higher than the negative one in devices negatively biased during irradiation. The opposite holds true on devices positively biased when irradiated. Such difference disappears and RILC is the maximum when the oxide field is close to zero during irradiation, while RILC decreases for increasing oxide field applied during irradiation.

These results show that the trap distribution is controlled by the oxide field during irradiation. This result cannot be explained, if neutral traps are directly generated by the impinging 8-MeV electrons, as in case of knock-on displacement damage of the oxide lattice, for instance. Such defects should be homogeneously generated in the oxide layer, and any effect due to the oxide field should be negligible. Instead, the RILC-assisting defects result from microstructural transformations of charged defects generated by irradiation, which are field-sensitive. Neutral defects could result from the neutralisation of an E' centre after capturing a hole [13]. In short, a neutral electron trap could result from a hole capture at a weak Si-Si covalent bond, which may relax into a $Si:^{-}$ $Si^{+}$ neutral amphoteric defect after the hole compensation. Even though holes appear as the first candidate for generating neutral defects, the possible role of hydrogen cannot be neglected [14].

In fact, ionizing radiation can easily break the weak bonds of bonded H atoms, which can migrate under an electric field and be trapped in different sites, possibly generating again neutral defects in the oxide and/or leaving electron traps in the original site.

RILC intensity grows with the defect density, but it is strongly dependent on the defect position in the oxide layer. Results indicate that RILC is maximum for a homogeneous distribution of traps (zero-field irradiation), and it decreases when traps are pushed toward one interface ($E_{ox} \neq 0$), even though the trap density is likely higher in the latter case.

Differences between positive and negative RILC result from this asymmetric trap distribution, indicating that traps are less effective when close to the cathodic interface during measurement, in full agreement with simulations that identify traps close to the middle of the oxide thickness as the most affective for RILC [8].

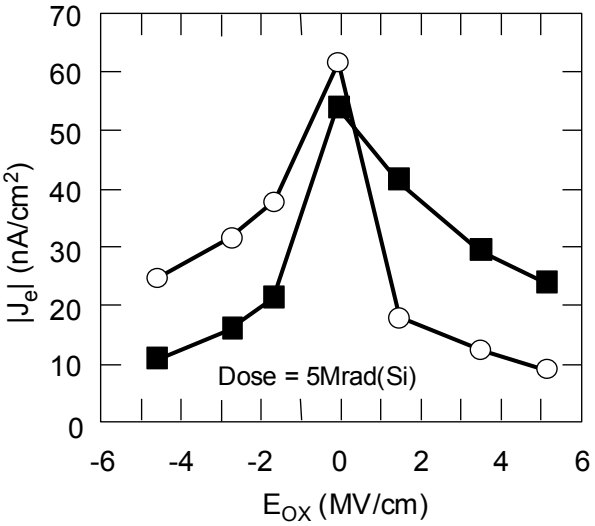


a)

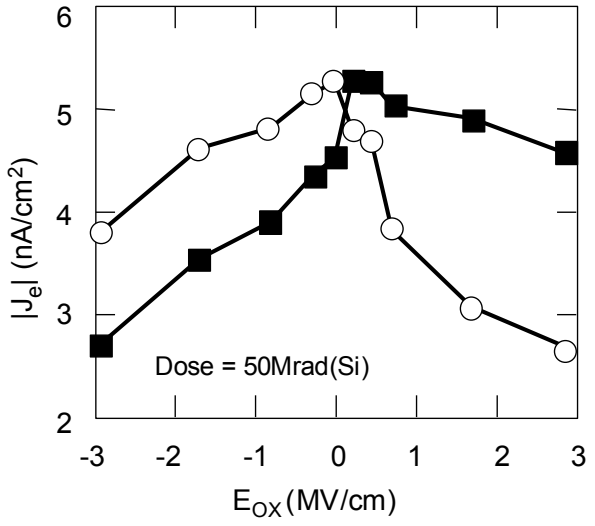


b)

*FIG. 2. Excess current read at $|E_{OX}|$ = 5MV/cm for different gate voltages applied during 8 MeV electron irradiation for: a) $t_{ox}$ = 4nm and b) $t_{ox}$=6nm (○ = positive RILC; ■ = negative RILC).*

Note: 1 Gy = 100 rad

**RILC growth kinetics**

We show in Fig. 3a the RILC variation with the total cumulative dose. RILC has been measured at an oxide field $E_{ox}$ = 6 MV/cm on both 4-nm and 6-nm oxides. For a given radiation dose, the excess current is much higher in the 4-nm oxides, owing to the higher tunneling probability across the barrier, which is thinner than in the 6-nm oxide. RILC data can be well fitted by using the following relation:

$$J_e = K_R \cdot \text{Dose}^{\beta} \qquad (2)$$

Here $\beta \cong 0.9$ for $t_{ox} = 6$ nm and $\beta \cong 0.94$ for $t_{ox} = 4$ nm, while $K_R$ is a constant that depends from the read-out gate voltage and oxide thickness. Approximately, RILC grows linearly with the radiation dose, indicating that the oxide defect density follows a linear growth rate as well. In Fig. 3b SILC is plotted versus the injected charge ($Q_{inj}$) during a CCS with $J_{str} = -10 mA/cm^2$ for both 4-nm and 6-nm devices. At least at high stress levels, SILC follows the empirical law [15]:

$$J_e = J_{sat} \cdot \exp\left(-\frac{DJ_{stress}^{\gamma}}{Q_{inj}^{\alpha}}\right) \qquad (3)$$

where $\alpha \cong 0.31$ for $t_{ox} = 6$ nm, $\alpha \cong 0.18$ for $t_{ox} = 4$ nm, $\gamma \cong 0.04$, $J_{sat}$ is the saturation SILC level, and D is a constant depending on the oxide thickness and quality.

RILC and SILC can be attributed to holes trapped in the oxide. Despite this correspondence, SILC shows a saturating behavior for those current levels, which still correspond to a linear growth rate of RILC. Moreover, $\alpha$ is lower in 4-nm than in 6-nm oxides, indicating that SILC saturates faster in thicker oxides. This basic difference between RILC and SILC should be related on one side to the defect distribution within the oxide layer, which results from uniform generation of holes across the oxide (RILC) or high field injection from the anode (SILC). On the other hand, many more electron are injected by CCS than by radiation for the same gate leakage level, suggesting that electrons may effectively passivate/anneal part of the stress induced defects for electrically stressed devices.

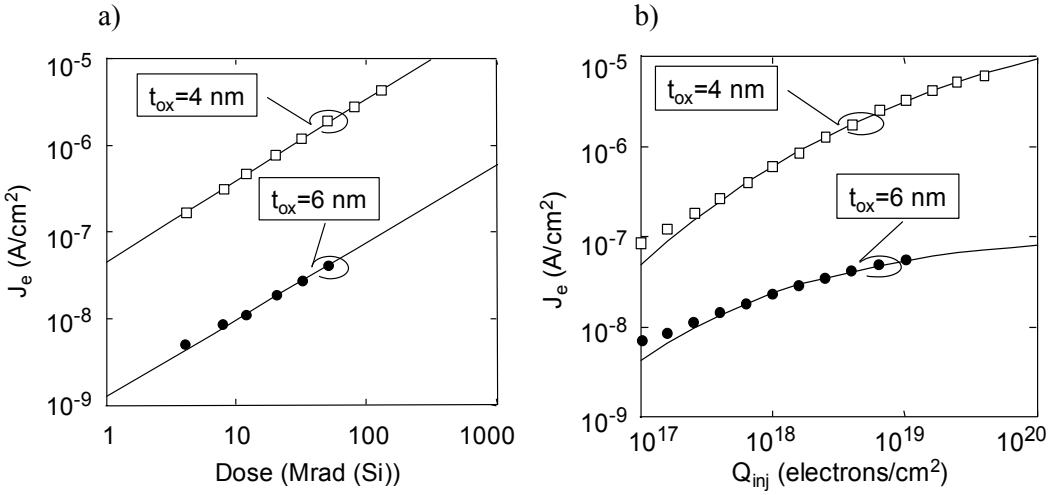


*FIG. 3. RILC (a) and SILC (b) kinetics (negative excess current) for $t_{ox}$ = 4 nm (□) and $t_{ox}$ = 6 nm (●). $V_g$=0V during 8 MeV electron irradiation.*

## 3. RADIATION INDUCED SOFT BREAKDOWN

The relative increase of the gate current due to RILC is much reduced in oxide thinner than 3-4nm, due to the increased tunneling current even in a fresh device. A large impact on the gate current is measured instead when a SB or HB event occurs [16–2].

The first reports of Radiation induced Soft Breakdown (RSB) appeared during SEGR studies in 1998 [19, 21]. RSB was detected as a sudden, large increase of the gate current, much larger than in case of RILC (see Fig. 4), but still smaller than in case of HB. In contrast with RILC, which is associated to a tunneling process across a single trap, RSB conduction is activated when one or more regions with high defect density are produced in the oxide layer. Physical models can describe some (if not all) of the RSB current characteristics as in case of SB. For instance, in a percolation picture, these defects produce different conduction paths for electrons across the oxide [23]. In the Quantum Point Contact (QPC) approach, a single one-dimensional quantum path is activated across the oxide, where electrons are spatially confined [24, 25].

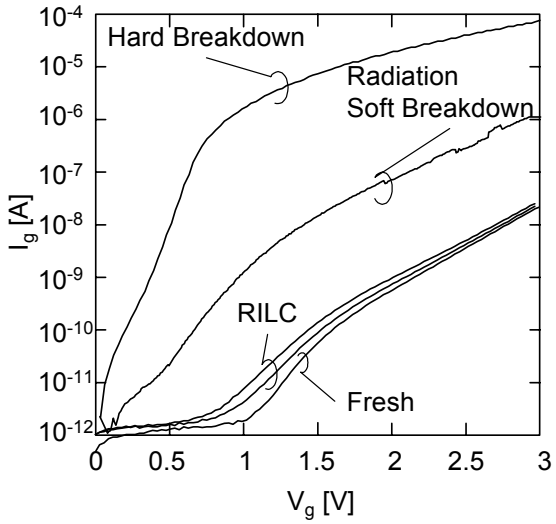


*FIG. 4. Gate Current vs. Gate Voltage ($I_g$-$V_g$) measured before and after irradiation on a 3-nm oxide. Ig The two curves referring to RILC have been measured after irradiation with $5.8 \cdot 10^{10}$ and $1.5 \cdot 10^{11}$ Si ion/cm$^2$. The RSB has been obtained after irradiation with $10^7$ I ions/cm$^2$.*

### 3.1. Quantum point contact modeling

In contrast with RILC, which is associated to a tunneling process across a single trap, RSB conduction can be successfully explained on the basis of the Quantum Point Contact (QPC) model [18, 26]. The QPC model has been firstly introduced for electrically induced oxide Hard Breakdown and SB. [24, 25]. The basic idea beyond the QPC picture is that the conduction is strongly localized and electrons flow through a single conductive path. In the case of radiation, each ion crossing the oxide has a non-zero probability of generating a RSB leakage path. Based on the QPC model, the lateral dimension of the breakdown paths is so small that the momentum in the direction perpendicular to propagation is quantized. If the path is narrow enough, the ground sub-band E0 is above the Fermi level at the cathode, and the conduction can only take place by tunneling across an effective 1-dimensional potential barrier (see Fig. 5), whose height is just $E_0$.

This barrier is not material-related, but its height cannot be larger than that of the $Si/SiO_2$ system because electrons would be otherwise no longer laterally confined [25]. This model leads to the exponential relation for the gate current across a single SB spot [18]:

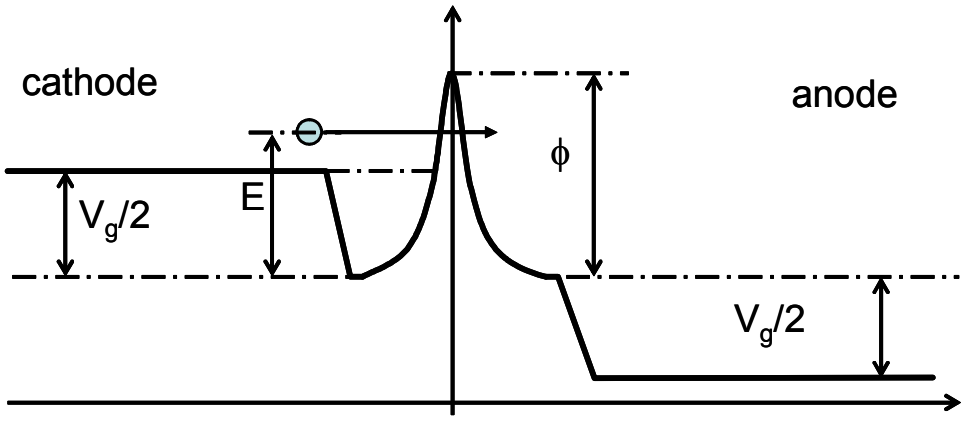


*FIG. 5. Schematic drawing representing the band structure associated to the QPC spot.*

$$I_g \quad A \ \exp(\qquad) \ \exp(B \ V_g) \qquad (4)$$

The parameters A and B have been related to the height and thickness of the local barrier in the breakdown path. The offset voltage $V_0$ is due to some potential drop in the substrate. In case of RSB, where several spots can be activated after irradiation, Eq. 4 should be modified accordingly as [26]:

$$I_g \quad N \ A \ \exp(\qquad) \ \exp(B \ V_g) \qquad (5)$$

N being the number of active spots.

The A end B coefficient are given by:

$$A = \frac{4q}{\alpha \cdot h} \qquad B = \frac{\alpha q}{2}$$

with *q* the electron charge and *h* the planck constant.

The two main parameters associated with the model are $\phi$, the barrier height of the quantum point contact, and $\alpha$, which is correlated to the shape or thickness of the contact. In the RSB regime, $\phi$ is saturated to the value of the oxide/silicon barrier height, while $\alpha$ decreases with the fluence increase due to the increase of the RSB spot number [18].

### 3.2. RSB current noise

In Fig. 6 we have plotted the gate current measured in a 3-nm oxide after irradiation with 257 MeV I ions. The gate voltage applied during the measurement was $V_g$ = -2.7V, and the sampling frequency was $F_S$ = 64Hz.

The RSB current approximately behaves as a multi-level Random Telegraph Noise (RTN). Such fluctuations correspond to the activation/deactivation of conductive paths (inside the radiation induced weak spots) across the oxide, occurring after irradiation [27]. By focusing on a small portion of the gate current response a “small” RTN appears superimposed on the main “large” fluctuations (see inset of Fig. 6), pointing to the complex nature of the weak spots. Remarkably, the average current flowing across the oxide after irradiation is much larger than in a fresh device, indicating that despite the large fluctuations some regions in the oxide layer are irreversibly damaged permitting a large current to constantly flowing.

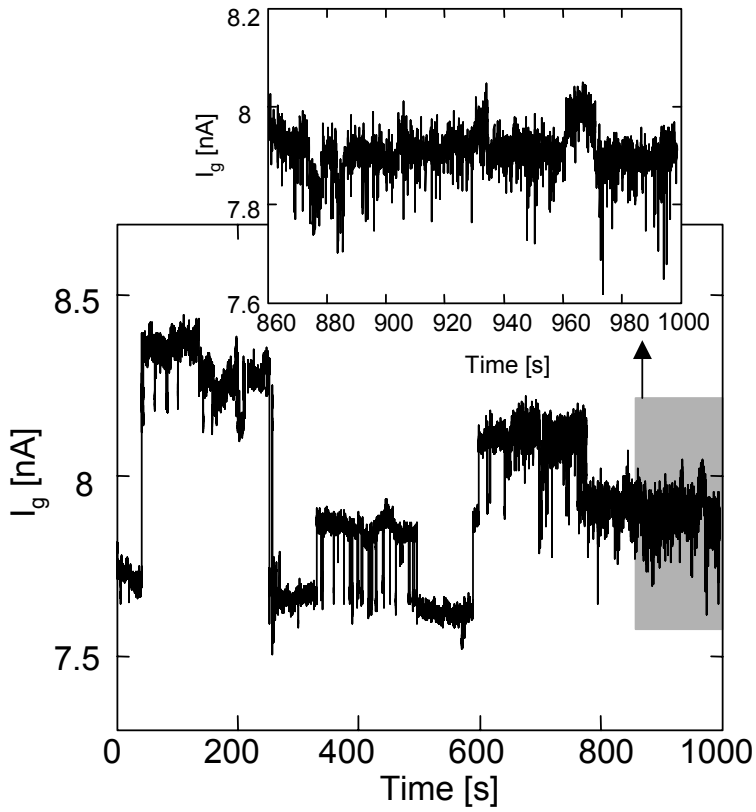


*FIG. 6. Gate current measured at $V_g$=-2.7 V as a function of measurement time in a 3-nm oxide after $7 \cdot 10^6$ I ions/cm$^2$. Sampling frequency was 64 Hz.*

Mixed "large" and "small" RTN fluctuations have been observed for different values of oxide thickness, radiation dose, measurement polarity, and sampling frequency. In Fig. 7 we have plotted the post-irradiation gate current measured in a 4-nm oxide at $V_g$ = –2.7V and at a sampling frequency FS = 4kHz. Noticeably, the RSB current is larger in 4-nm than in 3-nm oxides, due to the random nature of the RSB phenomenon. Also in the 4-nm oxide a clear multi-level RTN appears, characterized by "large" and "small" fluctuations, as found also in Fig. 6. Noticeably, "small" fluctuations occur much more frequently than "large" ones, and both are usually attributed to an electron trapping/detrapping process. The correlation between switching frequency and fluctuation amplitude may help understanding the microscopic nature of the RSB spot. In fact, fast fluctuations can be attributed to electron trapping/detrapping in shallow traps, hence characterized by fast trapping/detrapping kinetics. On the contrary, deep traps could be responsible for the slow fluctuations due to their longer capturing and emitting time. Experiments show that the current fluctuations are either "slow and large" or "fast and small" [27]. This suggests that shallow electron traps should modify the conductance of the RSB spot much less than slow deep traps. In a simple view, deep traps could reside in a central region of the RSB spot, which can be effectively clogged by a trapped electron resulting in larger RSB current variations. Instead, shallow traps should be located peripherally with respect to the RSB spot, where their impact on the driven current is relatively modest.

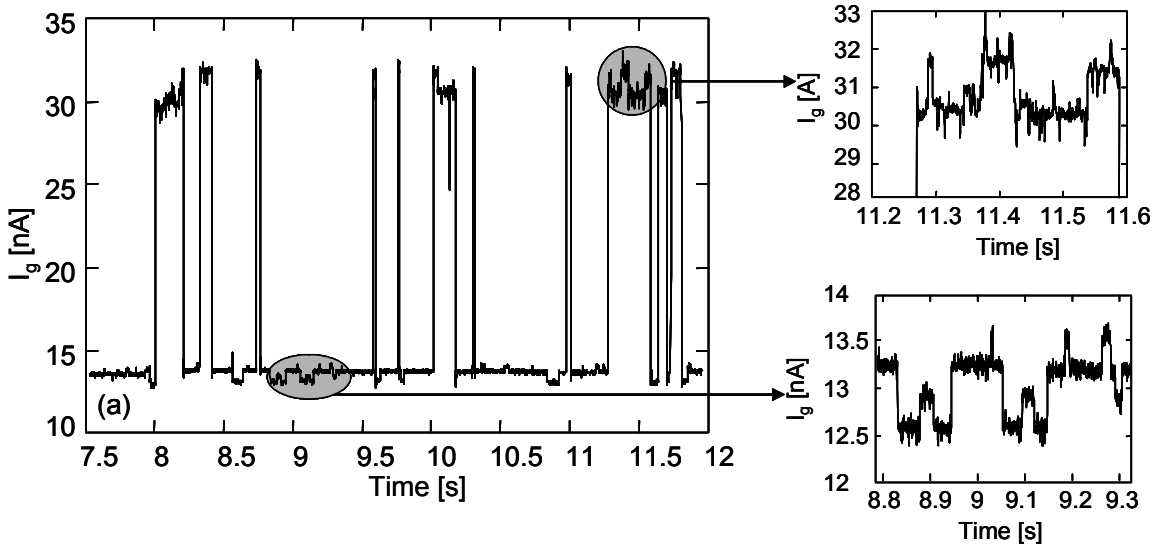


*FIG. 7. Gate current measured at $V_g$ = -2.7 V as a function of measurement time in a 4-nm oxide after $7 \cdot 10^6$ I ions/cm$^2$. Sampling frequency was 4 kHz.*

### 3.3. Temperature dependence of gate current noise

In Figs. 8a and 8b we show the gate current measured at 300 K and 77 K, respectively, in the same irradiated device. The RSB exhibits a RTN behavior in both cases, but the switching frequency of the current noise decreases with the temperature. This result is in agreement with the role attributed in producing RTN to electron trapping/detrapping, which decreases at low temperature. Recently, discrete RTN has also been observed in the drain voltage of MOSFET's (with 18-nm gate oxide) operating in strong inversion with a constant drain current [28]. The authors attributed these RTN fluctuations to the trapping/detrapping at interface defects and found that trapping events are quite strongly activated by temperature. This seems consistent with RSB results: in fact, it is possible that these near-interfacial defects in thicker oxides (laying at approximately 2–3 nm from the interface [29]) might have similar nature, i. e., similar trapping characteristics, to the "bulk" defects in oxides thinner than 4–5 nm.

In Figs 8a and 8b the RSB current was measured at 2 different gate voltages, that is, $V_g = -1.2$V and –2.6V, respectively, aiming to keep similar RSB current values at different temperatures. In fact, the RSB current at 77 K was almost 3 orders of magnitude smaller than at 300 K and current fluctuations were almost undetectable at $V_g = -1.2$V. In that case, the electron-trapping rate on the RSB related defects was also reduced due the decrease of the electrons available for trapping, owing to the small gate current.

Even though the switching frequency increases with the gate voltage, still it is much slower at 77 K than at 300 K, as illustrated also in Fig. 9 where the corresponding Power Spectral Density (PSD) is plotted at $F_S = 64$Hz and $F_S = 4$kHz. We observe a general decrease of the noise power and a leftward shift of the switching frequencies by decreasing the temperature. The power spectral density follows a $1/f^{\alpha}$ law in both curves with the same $\alpha$ coefficient. In general (as found in all irradiated samples), the exponent $\alpha$ is between 1 and 2, which derives from the superposition of some lorentzian curves, each of them describing a RTN with a particular switching frequency and amplitude [30]. In particular, 3 lorentzian curves at 300 K and 2 lorentzian curves at 77 K are sufficient to obtain good agreement with experimental data.

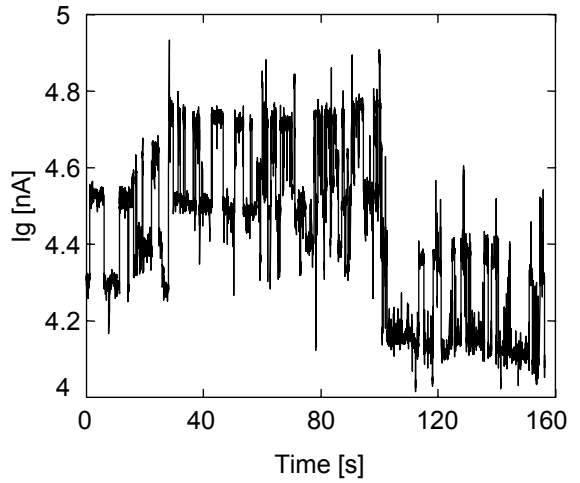


a)

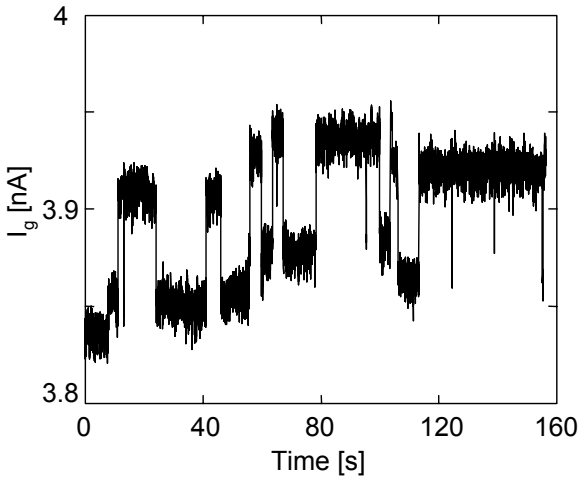


b)

*FIG. 8. Gate current measured in a 3-nm oxide after $7 \cdot 10^6$ I ions/cm$^2$: a) at 300 K, $V_g$=-1.2V, $F_S$ = 64 Hz; b) at 77K, $V_g$ = –2.6V, $F_S$ = 64 Hz.*

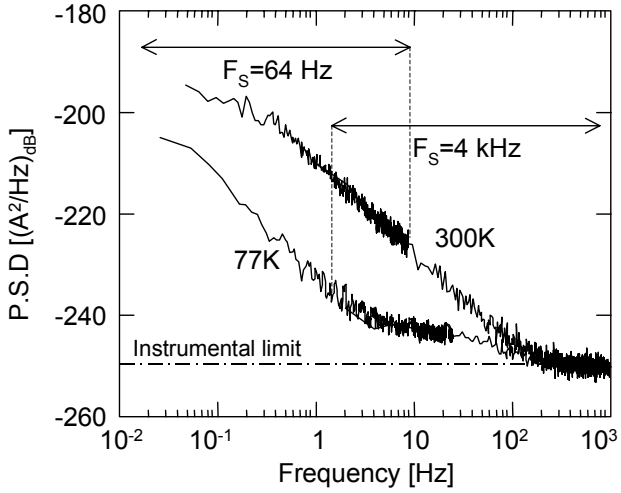


*FIG. 9. Power Spectral density of the RSB current in a 3-nm oxide at 77K and 300 K after $7 \cdot 10^6$ I ions/cm$^2$.*

## 4. RADIATION INDUCED WEAR-OUT

In the two previous sections we showed that different leakage current can affect thin irradiated oxide. RILC and RSB represent the most important degradation phenomena affecting ultra-thin oxides. Both RILC and RSB are characterized by a current increase, which is much smaller than in Hard Breakdown (HB) regime. RILC and, mainly, RSB have been demonstrated not to be an enhanced failure mode of significance for digital Very Large Scale Integration (VLSI) [31]. Those observations were based on the assumption that the device operation integrity is basically preserved owing to the small gate leakage, with few possible exceptions (such as floating gate memories or analog circuits). Further, the RSB probability appears extremely low in space missions.

When considering long term device reliability radiation is not the only concern, as gate oxides are subjected to high electric fields during normal circuit operations. Oxide wear-out due to the applied oxide fields is usually investigated on large area MOS capacitors through accelerated electrical stresses at fields higher than those of normal device operation. The cumulative effect of ionizing radiation and accelerated electrical stresses has been considered a few times in literature [9, 32–35], mainly for oxides irradiated with low Linear Energy Transfer (LET) radiation (γ-rays, electrons, X rays). It was found that radiation damage does not significantly impact the oxide reliability parameters, such as time-to-breakdown and time-zero-breakdown, at least for relatively high oxide thickness' (>12nm). In case of RILC, a modification due to irradiation was reported for the growth kinetics of the excess current during electrical stresses after γ-irradiation [9].

Only recently some works have been devoted to the combined effects of heavy ion irradiation and electrical stresses on ultra-thin oxides [36–9]. In the following we present the results of electrical stresses on large area MOS capacitors previously irradiated with heavy ions, showing that oxide breakdown occurs faster in irradiated devices.

### 4.1. Experimental evidence of Radiation Induced Wear-Out

Low LET radiation, such as gamma rays from Co60, produce no detectable effect on the Time-To-Breakdown (TTB) measured during accelerated electrical stresses (CVS) after high dose irradiation [39]. Similar results were observed in thick gate oxides, as the radiation induced point defects in the gate oxide are not effective in promoting the development of a breakdown path. However, when oxides are exposed to heavy ions a dramatic decrease of TTB was measured in the Weibull plot due to the radiation induced damage in the oxide [39]. In all irradiated devices an increase of the leakage current was also observed after irradiation, mainly after heavy ion exposure that lead to RSB in some cases.

However, radiation effects may be even silent after irradiation, appearing only during a subsequent electrical stress, as illustrated by the $I_g$-$V_g$ curves in Fig. 10a before and after CVS at $V_g$ = –2 V, i. e., close to the normal bias conditions VDD = 1.8 V [36]. The device was hit by only 10 I ions on the gate oxide owing to the small gate area. Only the first Ig-Vg measurement taken immediately after irradiation exhibited a very unstable behavior featuring several jumps, whereas the second and the third measurements were stable, overlapping each other, and are very close to the fresh curve. In this case the effective damage induced by the ion irradiation is apparently negligible, since the current increase is very modest.

The large instabilities featured by the first measurement could be related to an unstable cluster of oxide defects produced by irradiation, likely being the signature of a single ion induced localized weak spot. This cluster is stabilized by the current injected during the first measurement, as a consequence of some electron trapping or electron-hole recombination at the radiation induced oxide defects.

The electrical stress on this device demonstrates that the rearrangement of the ion damaged oxide region after the first measurement does not restore the pre-irradiation condition. In fact, CVS at $V_g$ = –2V produced SB in just 400s (see Fig. 10b). For comparison, CVS at $V_g$ = –2V produced no measurable effect on $I_g$-$V_g$ curves in fresh (unirradiated) samples even after 105–106s. Noticeably, this

result shows that even a single ion hit may effectively reduce the oxide life-time when considering SB or HB as the failure criterion.

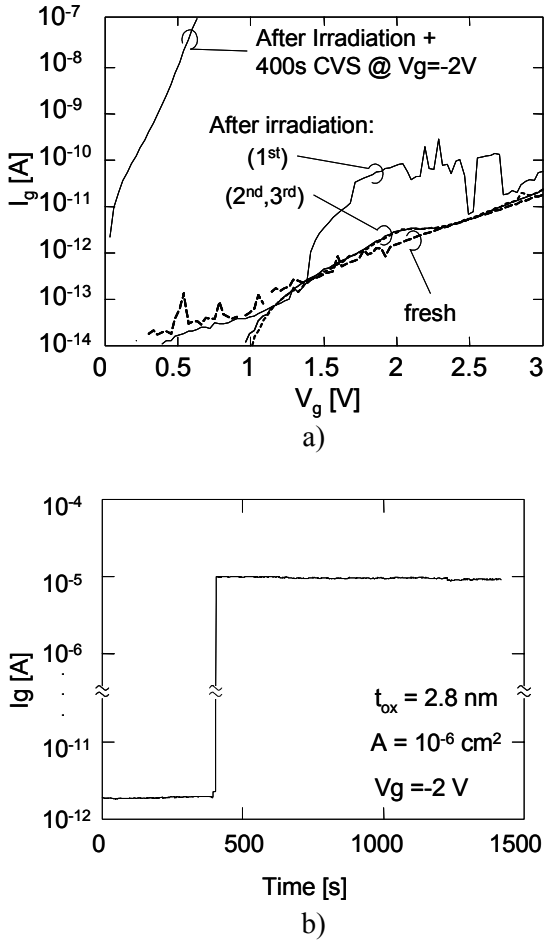


*FIG. 10. a) $I_g$-$V_g$ curves before irradiation (fresh), after irradiation (1st, 2nd and 3rd measurements), after irradiation + CVS on a MOS capacitors with gate area = $10^{-6}cm^2$ and $t_{ox}$ = 2.8 nm. The radiation fluence was $10^7$ I ions/$cm^2$, i.e., approximately 10 ions hit the gate oxide. b) gate current during the CVS performed after irradiation in the device of Fig. 10a.*

SB and HB may appear in parallel on irradiated samples, as indicated by curves A and B, respectively, in Fig. 11a. The abrupt increase of the gate current (marked by A) in Fig. 11b indicates the formation of a single SB path across the oxide, produced even in this case in a short time (1800s) and at low CVS voltage ($V_g$ = –2V). By applying a second CVS at $V_g$ = –3.5V the same capacitor underwent HB after only 360s (marker B in Fig. 11c). Remarkably, a CVS at $V_g$ = –4.5V applied to unirradiated devices needed more than 105s to generate a breakdown event. That the first SB event was not the precursor of the subsequent HB has been demonstrated by using the Light Emission Microscopy (LEM) technique on some devices with poly-Si gate without any overlying metal [32].

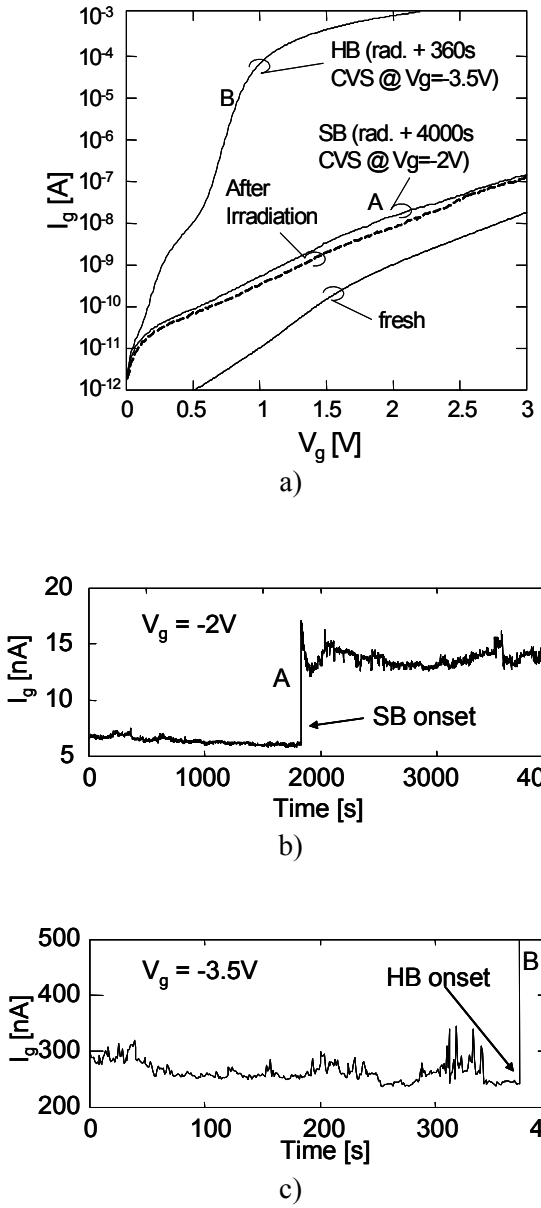


*FIG. 11. a)$I_g$-$V_g$ curves before (fresh) and after irradiation with $10^7$ I ions/cm$^2$, and after two subsequent CVS's (curves A and B) in a MOS capacitors with gate area = $10^{-3}$cm$^2$ and $t_{ox}$ = 2.8 nm. b) Gate current during CVS at $V_g$ = –2V for the same irradiated device of Fig. 11a; c) Gate current during the CVS at $V_g$ = –3.5V, for the same device of Figs. 11a and 11b.*

Figure 12 shows the evolution of the SB and HB spot of the sample of Fig. 11 as observed by the LEM. After irradiation (frame (a)) no light spot appeared, indicating that RSB conduction took place across several weak spots, each being too weak to be observed by LEM. The first SB occurred during CVS (mark A in Figs. 11a and 11b) can be clearly observed in the frame (b) and zoom (A) of Fig. 12. The subsequent HB occurred on a different position from SB, as shown in frame (c) and zoom (B) of Fig. 12, indicating that SB and HB are independent phenomena. After CVS the gate current flows through preferential paths generated by the electrical stress itself in those regions more damaged by heavy ions.

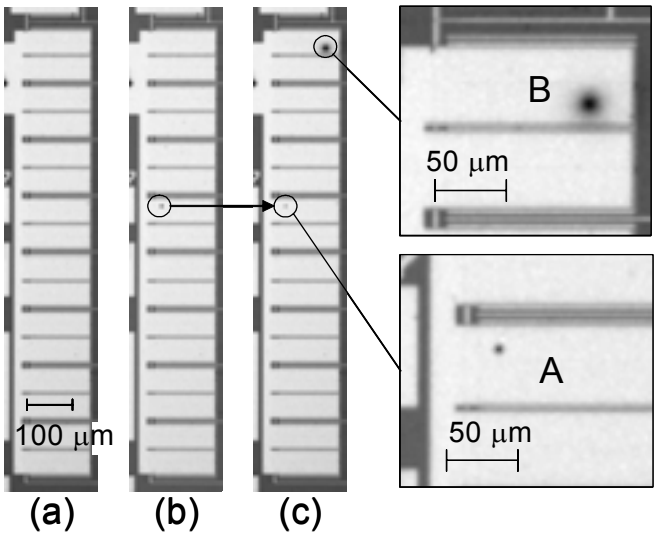


*FIG. 12. Light Emission Microscope observations of the device of Fig. 6.37 (reverse images) taken by biasing the capacitors at $V_g = -1V$ The white areas corresponds to the gate regions, divided in 16 rectangular sections, while the dark lines are proper of isolation: a) immediately after irradiation; b) after the 1st CVS at $V_g = -2V$; c) after the 2nd CVS at $V_g = -3.5V$. Dark spots A and B are associated to the gate current increase observed in curves A (SB) and B (HB) in Fig. 11, respectively.*

### 4.2. LET dependence of radiation induced wear-out

The dependence of the oxide degradation from the heavy ion LET coefficient has been studied for different ions at a fluence of $6.5 \cdot 10^7$ ions/cm$^2$ [37] and is clearly illustrated in Figs. 13a and 13b. Irradiated and unirradiated samples were submitted to electrical stress with different gate voltage until HB occurrence.

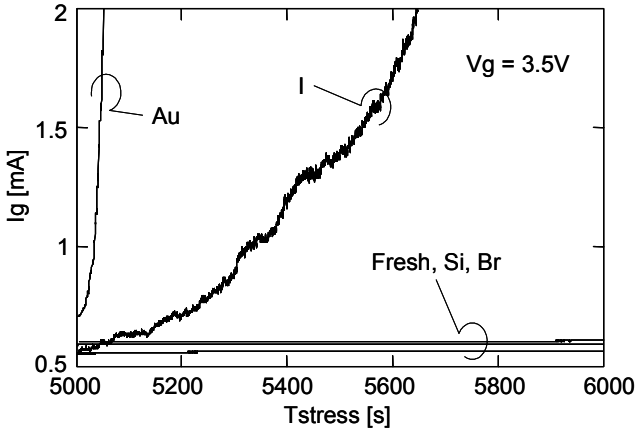


a)

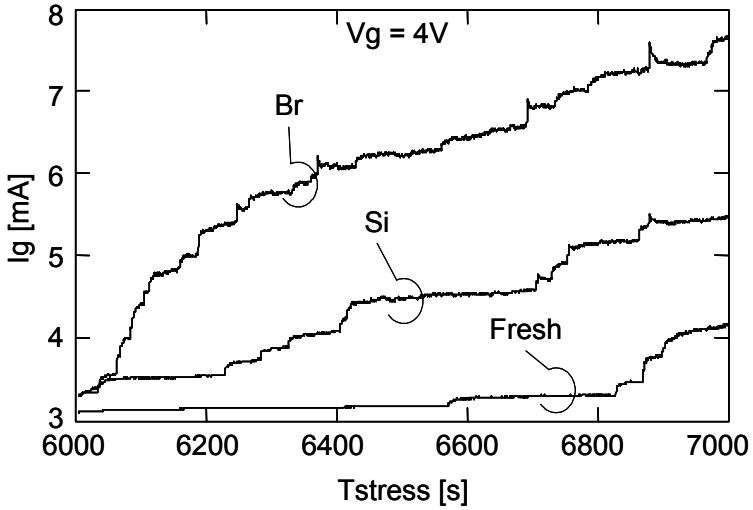


b)

*FIG. 13. Gate current evolution for few selected devices during: a) the 5th step of SVS for 311 MeV Au and 276 MeV I irradiated samples (Tstress = 5000s–6000s, $V_g$,stress = 3.5V); b) the 6th step of SVS for 241 MeV Br, 257 MeV Si, and unirradiated samples (Tstress = 6000s–7000s, $V_g$,stress = 4V).*

## 5. RADIATION EFFECT ON MOSFET

Traditionally, oxide Hard Breakdown (and to a less certain degree, Soft Breakdown) marks the end of the MOSFET lifetime [31]. The increase of the gate current, which is quite modest in the RSB regime (1nA - 1μA), produces a small increase of the corresponding power consumption in the broken MOSFET (~1μW or less). In most analog and digital applications, where the power budget is hundreds mW or more, such an increase is relatively small and does not significantly affect the total power consumption, unless many breakdown events take place in different transistors. On the other hand, the large noise characterising the RSB current could have a deleterious impact on the signal/noise ratio of analog circuits, even when the power consumption does not exceed the circuit specifications. Digital applications appear much more robust to RSB noise, as long as it remains smaller than the digital gate noise margins. Some authors have stated that threshold voltage and transconductance do not significantly change after Soft Breakdown (SB), so that the soft broken transistors can be still switched on and off, at least in those devices with large aspect ratio [31].

Radiation (but also electrical) stresses are often performed on large area MOS capacitors, to address the reliability problem over gate areas comparable to those of large chips. Very few results are available on the effect of ionizing radiation (and also electrical stresses) on MOSFET's with ultra-thin gate oxide and small W/L aspect ratio, proper of contemporary CMOS technologies. Recent results are rising the issue that only tests on small area devices are significant to evaluate the impact of the oxide degradation on the MOSFET electrical characteristics at least in case of minimum size devices or so, as we'll show in the following.

We consider here two MOSFETs with gate area A = 3 $\mu m^2$ and aspect ratio W/L = 0.3μm/10μm or W/L = 10 μm/0.3 μm (drawn), irradiated with 65·106 I ions/$cm^2$ [40]. In this case only 1 or 2 ions hit the gate oxide surface owing to the small gate area. No increase in the gate leakage current is observed after irradiation independent on the transistor aspect ratio W/L (Figs. 14a and 14b), as expected. Figs. 15 and 16 show the effect of heavy ion irradiation on the drain current of the same MOSFETs of Fig. 14. In the W/L = 10 μm/0.3 μm device gm slightly decreases (Fig. 15a), with an almost negligible variation of the drain saturation current (Fig. 6.15b). Even the threshold voltage and the subthreshold drain current are practically unchanged after irradiation, as illustrated in Fig. 15c. But when W/L = 0.3 μm/10 μm both transconductance and drain saturation current collapse as shown in

Figs. 16a and 16b, respectively. Large variations also appear in the logarithmic $I_{ds}$-$V_{gs}$ plot of Fig. 16c. For Vgs>0.1–0.2V the decrease of drain current is much larger than in the case of the large W/L transistor of Fig. 16c. In addition only a 20–30 mV shift of the threshold voltage is observed after irradiation, accompanied by a large increase of the subthreshold current for $V_{gs}$<0.1V (4–5 decades with respect to the fresh device).

These results point to the formation of a damaged oxide region produced by the ions striking the gate oxide. The current peak appearing for Vgs near 0V (Fig. 16c) is similar to the excess current of a gated diode after irradiation, clearly indicating the presence of $Si/SiO_2$ interface traps under the gate oxide.

The small positive shift of the MOSFET threshold voltage (~20–30mV, Figs. 15c and 16c) is an evidence that oxide trapped charge is negligible. Furthermore, the positive charge trapping usually observed in thick oxide and commonly addressed as the main cause of MOSFET failure after irradiation can not give rise of this phenomena, being the threshold shift opposite to that generated by a positive trapped charge.

The physical mechanism controlling the drain current collapse has no impact on the gate leakage current. In fact, the defect distribution is not sufficient to drive a substantial gate current (Fig. 14), but high enough to pinch the channel below it. The radiation induced defects form no RSB conductive path but must be distributed over a channel portion with dimension comparable with the transistor W (0.25–0.3 μm). Hence, the ion microdose effect spans over an oxide region much wider than the electron-hole generation volume of a single ion in the oxide (3–4 nm in radius), but similar to its size in Si (around 100 nm). This suggests that electron-hole pairs generated in the Si substrate close to the oxide interface may effectively contribute to the defect generation in the oxide layer, for instance by ionizing the Hydrogen atoms passivating the oxide interface defects.

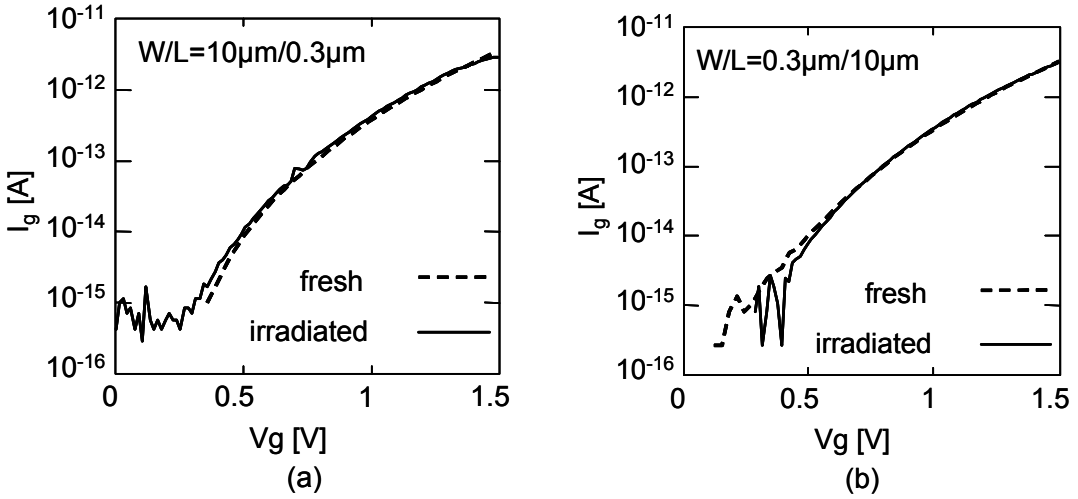


*FIG. 14. $I_g$-$V_g$ curves taken before and after irradiation with $65 \cdot 10^6$ I ions/cm$^2$ in two MOSFETs with the same gate area A = 3 μm$^2$ and oxide thickness $t_{ox}$ = 2.5 nm and different aspect ratios: a) W/L = 10μm/0.3μm; b) W/L = 0.3μm/10μm. Approximately 1–2 ions hit the gate oxide.*

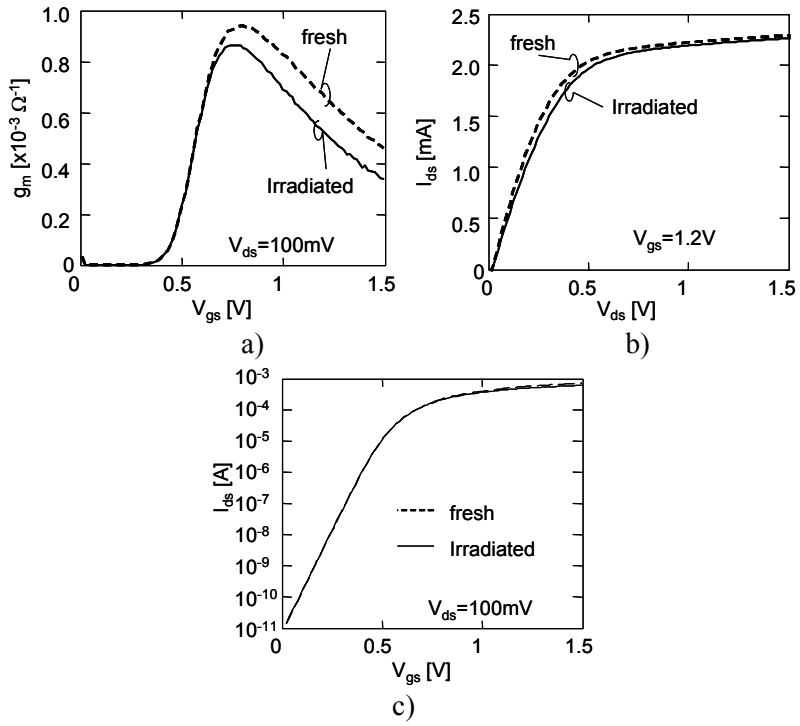


*FIG. 15. a) MOSFET transconductance ($g_m$) as a function of gate-source voltage ($V_{gs}$) measured in the device of Fig. 6.42a with W/L=10μm/0.3μm, before and after irradiation with 65·10$^6$ I ions/cm$^2$. b) Drain current (Ids) as a function of drain-source voltage ($V_{ds}$) measured in the same device of Fig. 6.42a. c) Subthreshold drain current (Ids) as a function of gate-source voltage ($V_{gs}$) measured in the same device of Fig. 6.42a.*

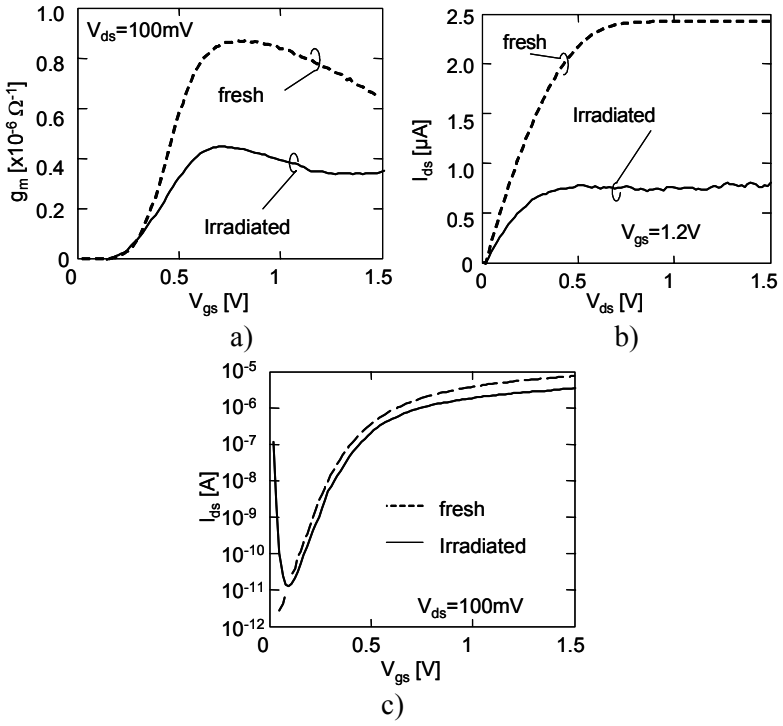


*FIG. 16. a) MOSFET transconductance ($g_m$) as a function of gate-source voltage ($V_{gs}$) measured in the same device of Fig. 6.42b with W/L = 0.3 μm/10 μm, before and after irradiation with 65·10$^6$ I ions/cm$^2$. b) Drain current (Ids) as a function of drain-source voltage ($V_{ds}$) measured in the same device of Fig. 6.42b, before and after irradiation with 65·10$^6$ I ions/cm$^2$. c) Subthreshold drain current ($I_{ds}$) as a function of gate-source voltage ($V_{gs}$) measured in the same device of Fig. 6.42c, before and after irradiation with 65·10$^6$ I ions/cm$^2$.*

These results demonstrate that a single heavy ion can significantly reduce the MOSFET drive current capability in small W devices. In very narrow (small aspect ratio) MOSFET's the damaged oxide region may span over a large portion of the gate width, effectively hampering the channel formation and increasing the effective channel resistance. In large W devices, this effect becomes less important as W becomes larger than the damaged region.

All these considerations lead to the conclusion that a MOSFET with small W may fail due to a single ion hit producing a collapse of the drain current well before the oxide breakdown condition is reached. RSB or SEGR may occur a long time after the device has lost most of its current driving capability and is, therefore, failed. In this case the device lifetime cannot be evaluated by considering the breakdown onset but, instead, its sensitivity to microdose effects such as those produced by high LET particles. Remarkably, the effect we measured must not be confused with the well-known single-event microdose effect observed by Oldham and McGarrity [41] in thick gate oxides and reported in several subsequent works. In that case, the ion induced microdose effect produced a localized trapping of positive charge, leading to increased drain leakage, which is the opposite of these experimental observations.

## REFERENCES


[1] MA, T.P., DRESSENDORFER, P.V., Ionizing radiation effects in MOS devices and circuits, John Wiley & Sons, (1989).

[2] HOLMES-SIEDLE, A. ADAMS, L., Handbook of radiation effects – 2nd Edition, Oxford University Press (2002).

[3] OLDHAM, T.R., Ionizing radiation effects in MOS oxides, World Scientific (2000).

[4] IEEE – Trans. Nuclear Science - Special issue on single-event effects and space radiation environment, April 1996.

[5] DAVARI, B., DENARD, R.H., SHAHIDI, G., "CMOS Scaling for high performance and low power – The next ten years", Proc. of IEEE 83 (1995) 595-606.

[6] FRANK, D.J., DENNARD, R.H., NOWAK, E., SOLOMON, P.M., TAUR, Y., WONG, H.-S.P., "Device scaling limits of Si MOSFETs and their application dependencies", Proc. of IEEE 89 (2001) 259-288.

[7] CESCHIA, M., PACCAGNELLA, A., CESTER, A., SCARPA, A., GHIDINI, G. "Radiation Induced Leakage Current and Stress Induced Leakage Current in Ultra-Thin Gate Oxides", IEEE Trans. on Nucl. Sci., 45 (1998) 2375-2382.

[8] LARCHER, L., PACCAGNELLA, A., CESCHIA, M. GHIDINI, G., "A Model of Radiation Induced Leakage Current (RILC) in Ultra-Thin Gate Oxides", IEEE Trans. on Nucl. Sci., 45 (1999) 1553-1561.

[9] SCARPA, A., PACCAGNELLA, A., MONTERA, F., GHIBAUDO, G., PANANAKAKIS, G., GHIDINI, G., FUOCHI, P.G., "Ionising Radiation Induced Leakage Current on Ultra-Thin Gate Oxides", IEEE Trans. on Nucl. Sci., 44 (1997) 1818-1825.

[10] ROSENBAUM, E., REGISTER, L.F. "Mechanism of stress induced leakage current in MOS capacitors", IEEE Trans. on Electron Device 44 (1997) 317-322.

[11] RUNNION, E.F., GLADSTONE, S.M., SCOTT, R.S., DUMIN, D.J., LIE, L., MITROS, J.C., "Thickness dependence of stress-induced leakage currents in silicon oxide" IEEE Trans. Electron. Devices. 44 (1997) 993-1001.

[12] TAKAGI, S., YASUDA, N., TORIUMI, A., "Experimental Evidence of Inelastic Tunneling in Stress-Induced Leakage Current", IEEE Trans. on Electron Devices, 46, (1999) 335-341.

[13] WALTERS, M., REISMAN, A., "Radiation-Induced Neutral Electron Trap Generation in Electrically Biased Insulated Gate Field Effect Transistor Gate Insulators", J. Electrochem. Soc. 138 (1991) 2756

[14] DIMARIA, D.J., CARTIER, E., "Mechanism for stress-induced leakage currents in thin silicon dioxide films", J. Appl. Phys, vol. 78, pp. 3883-3894, 1995.

[15] SCARPA, A., GHIBAUDO, G., PANANAKAKIS, G., PACCAGNELLA, A., "Reliability extrapolation model for stress induced leakage current in thin silicon oxides", Electronic Letters 33 (1997) 1342-1344

[16] CESCHIA, M., PACCAGNELLA, A., SANDRIN, S., GHIDINI, G., WYSS, J., LAVALLE, M., FLAMENT, O., "Low Field Leakage Current and Soft Breakdown in Ultra-Thin Gate Oxides After Heavy Ions, Electrons or X ray Irradiation", IEEE Trans. on Nucl. Sci. 47 (2000) 566-573.
[17] CESCHIA, M., PACCAGNELLA, A., TURRINI, M., CANDELORI, A., GHIDINI G., WYSS, J., "Heavy ion irradiation of thin oxides" IEEE Trans. Nucl. Sci. 47 (2000) 2648-2655
[18] CONLEY, J.F., SUEHLE, J.S., JOHNSTON, A.H., WANG, B., MIYAHARA, T., VOGEL, E.M., BERNSTEIN, J.B., "Heavy ion induced Soft Breakdown of thin gate oxides", IEEE Trans. on Nucl. Sci. 48 (2001) 1913-1916
[19] JOHNSTON, A.H., SWIFT, G.M., MIYAHIRA, T., EDMONDS, L.D., "Breakdown of Gate Oxides During Irradiation with Heavy Ions", IEEE Trans. Nucl. Sci. 45 (1998) 2500-2508
[20] MASSENGILL, L.W., CHOI, B.K., FLEETWOOD, D.M., SCHRIMPF, R.D., GALLOWAY, K.F., SHANEYFELT, M.R., MEISENHEIMER, T.L., DODD, P.E., SCHWANK, J.R., LEE, J.R., JOHNSON, R.S. LUCOVSKY, G., "Heavy-ion-induced breakdown in ultra-thin gate oxides and high-k dielectrics", IEEE Trans. Nucl. Sci., vol. 48, p. 1904-1912, 2001
[21] SEXTON, F.W., FLEETWOOD, D.M., SHANEYFELT, M.R., DODD, P.E., HASH, G.L., SCHANWALD, L.P., LOEMKER, R.A., KRISCH, K.S., GREEN, M.L., WEIR, B.E., SILVERMAN, P.J., "Precursor Ion Damage and Angular Dependence of Single Event Gate Rupture in Thin Oxides", IEEE Trans. Nucl. Sci., vol. 45, p. 2509-2518, 1998
[22] TITUS, J.L., WHEATLEY, C.F., VAN TYNE, K.M., KRIEG, J.F., BURTON, D.I., CAMPBELL, A.B., "Effect of Ion Energy Upon Dielectric Breakdown of the Capacitor Response in Vertical Power MOSFETs", IEEE Trans. on Nucl. Sci., Vol. 45, pp. 2492-2499, 1998
[23] HOUSSA, M., NIGAM, T., MERTENS, P.W., HEYNS, M.M., "Model for the current-voltage characteristics of ultrathin gate oxide after soft breakdown", J. Appl. Phis. 84 (1998) 4351-4355
[24] MIRANDA, E., SUÑE, J., NAIFRÍA, M., AYMERICH, X., "Point Contact Conduction at the Oxide Breakdown of MOS Devices", Proc. IEEE – IEDM 1998, 191-194
[25] CESTER, A. BANDIERA, L. SUÑE, J., PACCAGNELLA, A., BOSCHIERO, L., GHIDINI, G. "A Novel Approach to Quantum Point Contact for post Soft Breakdown conduction", Proc. of IEEE – IEDM, 2001
[26] CESTER, A., PACCAGNELLA, A., SUÑE, J., MIRANDA, E., "Post-radiation-induced soft breakdown conduction properties as a function of temperature", Appl. Phys. Lett., 70 (2001) 1336
[27] CESTER, A., BANDIERA, L., CESCHIA, M., GHIDINI, G., PACCAGNELLA, A., "Noise characteristics of radiation induced Soft Breakdown Current in ultra-thin gate oxides", IEEE Trans. on Nucl. Sci. 48 (2001) 2093-2100
[28] SCOFIELD, J.H., BORLAND, N., FLEETWOOD, D.M., "Temperature-Independent switching rates for a random telegraph signal in a silicon metal-oxide-semiconductor field –effect transistor at low temperatures", Appl. Phys. Lett. 76, (2000) 3248-3250
[29] FLEETWOOD, D.M., ""Border traps" in MOS devices", IEEE Trans. Nuclear Science, 39 (1992) 269-271.
[30] KIRTON M.J., UREN, M.J., "Noise in solid state microstrucures: A new perspective on individual defects, interface states and low frequency (1/f) noise", Advances in Physics, 38 (1989) 367-468.
[31] WEIR, B.E., SILVERMAN, P. J., MONROE, D., KRISCH, K.S., ALAM, M.A., ALERS, G.B., SORCH, T.W., TIMP, G.L., BAUMANN, F., LIU, C.T., MA, Y., HWANG, D., "Ultra-Thin Gate Dielectrics: They Break Down, But Do They Fail", Proc. IEEE –IEDM 1997 73-76.
[32] ANDERSON, S.R., SCHRIMPF, R.D., GALLOWAY, K.F., TITUS, J.L., "Exploration of heavy ion irradiation effects on gate oxides reliability", Microelectron. Reilab. 35 (19950 603-608.
[33] BROZEK, T., WISNIEWSKI, R., BECK, R.B., JAKUBOWSKI, A., "Effect of radiation on breakdown of electrically pre-degraded oxides in MOS structures", Microelectron. Eng. 28 (1995) 349-352.

[34] KIM, S., LEE, H., HAN, C., LEE, K., CHOI, S., JEON, Y., DI FABRIZIO, E., GENTILI, M., "The effects of X ray irradiation induced damage on reliability in MOS strucures", Solid-St. Electron., 38 (1995) 95-99.
[35] PACCAGNELLA, A., CANDELORI, A., MILANI, A., FORMIGONI, E., GHIDINI, E., PELLIZZER, F., DRERA, D., FUOCHI, P. G., LAVALE, M., "Breakdown properties of irradiated MOS capacitors", IEEE Trans. Nucl. Sci. 43 (1996) 2609-2616.
[36] CESTER, A., "Wear-out and breakdown of ultra-thin gate oxides after irradiation", IEE-Electronics Letters 38, (2002) 1137-1139.
[37] CESTER, A., CIMINO, S., PACCAGNELLA, A. GHIBAUDO, G., GHIDINI, G., WYSS, J., "Accelerated Wear-out of Ultra-thin Gate Oxides After Irradiation", IEEE – Trans. Nucl. Sci. 50 (2003) 729-734.
[38] CESTER, A., CIMINO, S., MIRANDA, E., CANDELORI, A., GHIDINI, G. Paccagnella, A. "Statistical Model for Radiation Induced Wear Out of Ultra-Thin Gate Oxide after Exposure to Heavy Ion Irradiation", IEEE – Trans. Nucl. Sci. 50 (2003) 2167-2175.
[39] SUEHLE, J.S., VOGEL, E.M., CONLEY, J.F., JOHNSTON, A.H., WANG, B., BERNSTEIN, J.B., WEINTRAUB, C.E., "Observation of latent reliability degradation in ultrathin oxides after heavy-ion irradiation", Appl.Phys. Lett. 80 (2002) 1282-1284.
[40] CESTER, A., CIMINO, S., PACCAGNELLA, A., GHIDINI, A., GUEGAN, G., "Collapse of MOSFET Drain Current After Soft Breakdown and its Dependence on the Transistor Aspect Ratio W/L", Proc. IEEE – IRPS 2003 189-195.
[41] OLDHAM, T.R., MCGARRITY, J.M., "Ionization of SIO2 by heavy charged particles" IEEE Trans. on Nucl. Sci. 28 (1981) 3975-3980.

# NEW CHALLENGE ON LITHOGRAPHY PROCESSES FOR NANOSTRUCTURE FABRICATION

L. SCALIA
STMicroelectronics, DSG Division R&D Pilot Line,
Catania, Italy

**Abstract**

Currently, and for the last several decades, optical projection lithography has been the lithographic technique used in the high-volume manufacture of integrated circuits. In order to keep pace with the demand for the printing of ever smaller features and to increase speed and performance of the chip, lithography tool manufacturers have found it necessary to gradually reduce the wavelength of the light used for imaging and to design imaging systems with ever larger numerical apertures. As the minimum printable size is reduced, speed and performance in chips increases as does substantially the cost of the optical lithography tool. Fortunately, a number of strategies have been developed to extend the usefulness of any optical lithography generation. Resolution enhancement techniques (RET) such as phase-shift masks (PSM), modified illumination schemes, and optical proximity correction (OPC) can be used to enhance resolution while increasing the effective Depth of focus (DOF). Owing to the physical limits of optical lithography, over the next several years it will be necessary for the semiconductor industry to identify a new lithographic technology that will carry it into the future, eventually enabling the printing of lines as small as 30 nm. Potential successors to optical projection lithography are being aggressively developed. These are known as "Next-Generation Lithographies" (NGLs). Extreme ultraviolet lithography (EUVL) is one of the leading NGL technologies; others include X ray lithography, ion-beam projection lithography, and electron-beam projection lithography.

## 1. INTRODUCTION

Lithographic processes have been leading the way to miniaturization in semiconductor technology. Any lithographic process is characterized by its power (resolution) to resolve the smallest dimension. Currently, and for the last several decades, optical projection lithography has been the lithographic technique used in the high-volume manufacturing of integrated circuits (ICs). In order to keep pace with the demand for the printing of over smaller features, for increase speed and performance of the chip, lithography tool manufacturers have found it necessary to gradually reduce the wavelength of the light used for imaging and to design imaging systems with ever larger numerical apertures. The reasons for these changes can be understood from the following equations that describe two of the most fundamental characteristics of an imaging system: its resolution (RES) and depth of focus (DOF). These equations, called Reyleigh, are usually expressed as

$$RES=K_1 \lambda / NA$$

and

$$DOF = K_2 \lambda /(NA)^2$$

where $\lambda$ is the wavelength of the radiation used to carry out the imaging, and NA is the numerical aperture of the imaging system (or camera). These equations show that better resolution can be achieved by reducing $\lambda$ and increasing NA.

The strategy to meet the continued demands for higher resolution and larger depth of focus was to migrate from visible light (436 and 365 nm) to deep UV (248 and 193 nm) wavelengths for resist exposure and this trend is continuing to wavelengths of 157 nm. As the minimun features size is reduced, speed and density in chip increase, as substantially does the cost of the optical lithography tool. Fortunately, a number of strategies have been developed to extend the usefulness of any optical lithography generation. Resolution enhancement techniques (RET) such as phase-shift masks (PSM), modified illumination schemes, and optical proximity correction (OPC) can be used to enhance resolution while increasing the effective DOF.

Over the next several years it will be necessary for the semiconductor industry to identify a new lithographic technology that will carry it into the future, eventually enabling the printing of lines as

small as 30 nm. Potential successors to optical projection lithography are being aggressively developed. These are known as "Next-Generation Lithographies" (NGLs). EUV lithography (EUVL) is one of the leading NGL technologies; others include X ray lithography, ion beam projection lithography, and electron beam projection lithography [1].

## 2. EVOLUTION IN OPTICAL LITHOGRAPHY

From the late 1960s, when integrated circuits had linewidths of 5 μm, until today, when minimum linewidths have reached 70 nm, optical lithography has been used ubiquitously for manufacturing. The modern lithography started at the beginning 1980s with the spectral line of 436 nm (g-line) capable of resolving 1μm of feature size. By mid-80s the first stepper which printed at 365 nm became available, permitting a dimension of 0.35 μm. Presently, the most advanced lithographic tools used in high-volume manufacture employ deep ultraviolet (DUV) radiation with a wavelength of 248 nm and 193 nm to print features that have line widths, respectively, as small as 130 nm and 90 nm. Recent DUV tools, which are in an advanced stage of development, employ radiation that has a wavelength of 157 nm. They will be enable optical lithography to print features as small as 65 nm.

A lithographic system includes exposure tool, mask, resist, and all of the processing steps to accomplish pattern transfer from a mask to a resist and then to devices. Transition from one wavelength to another employs changes to photoresist chemistry as well as the optical system material, such as lenses and masks.

Any photoresist must offer three fundamental properties: high transparency at the exposure wavelength, etch resistance during subsequent process and the ability to undergo efficient photochemical transformations. Transition from one wavelength to another necessitates the change in photoresist chemistry in order to fulfil above-mentioned requirements [2, 3]. The near UV (436–365 nm) technology is dominated by diazonapthaquinone-novolac based resists. But their excessive unbleachable absorption and low sensitivity at DUV wavelengths make them unsuitable for use in DUV region. In order to circumvent this intrinsic sensitivity limitation and to increase resist sensitivity, concept of chemically amplified (CA) resists was introduced by Ito and Wilson in 1982 [4]. In CA resists, an additional photoactive compound commonly called photo acid generator (PAG) is added to the polymer matrix and photosensitizer. The PAG produces a small amount of acid, when exposed to light by photochemical decomposition. During post-exposure bake (PEB), the acid activates a cascade of subsequent chemical transformations in the resists causing a polarity change in the polymer from lipophilic to hydrophilic, making exposed regions soluble in basic developers like tetra-methyl ammonium hydroxide (TMAH). Thus, the previously generated acid acts as a catalyser during PEB and is hardly consumed by the reaction. This results in a dramatic increase in quantum efficiency and sensitivity of the exposure.

248 nm CA resists are based on hydroxystyrene polymers, alone or in combination with other monomers such as *t*-butyl acrylate. Acrylic polymers are the new basis for 193 nm resist design because of their excellent optical transparency. Acrylic polymers provide good resolution but lack in etch resistance. New polymers, called cyclo olefin maleic anhydrides (COMA) found improved etch resistance but lacked the needed resolution. This led to a dual approach that is still playing out, in which resist chemists improve etch resistance in acrylic resists without decrease in resolution, or enhance resolution in COMA resists without sacrificing etch resistance. Besides tremendous improvement in 193 nm resist technology, significant developments are going on with 157 nm CA resists [5] to keep pace with ITRS roadmap. However, designing high-resolution photoresist for 157 nm poses a difficult challenge, since, air and most hydrocarbons are strongly absorbing at this wavelength. Spectroscopic studies lead to the observation that highly fluorinated hydrocarbons and silicon based siloxanes offer the best hope for the transparency that is necessary for the design of an effective 157 nm photoresist, and these classes of materials have quickly become the prominent platforms for a variety of research activities in this field. The main challenge in developing a siloxane resist is achievement of a sufficiently high glass transition temperature.

In Table I are summarized the kind of source light, mask and lens material utilized in near UV and in DUV lithography.

TABLE I. SOURCE LIGHT, MASK AND LENS MATERIALS FOR NEAR UV AND DUV LITHOGRAPHY

| *Wavelength (nm)* | *Source* | *Lens material* | *Mask material* |
|---|---|---|---|
| 436 (g-line) | Hg arc lamp | Quartz | Quartz |
| 365 (i-line) | Hg arc lamp | Quartz | Quartz |
| 248 | KrF excimer laser | Fused silica | Fused silica |
| 193 | ArF excimer laser | $CaF_2$ | Fused silica |
| 157 | $F_2$ excimer laser | $CaF_2$ | Modified fused silica(*) |

(*) Fused silica is not transmissive enough at 157 nm; transmission improvements have been obtained by preparing fused silica with low OH content and by incorporating fluorine into the glass network.

## 3. RETICLE ENHANCEMENT TECHNIQUE (RET)

The semiconductor industry pushed lithography tools to the point where the minimum feature size of the circuits are smaller than the wavelength of light that can be projected through the mask to create them. Thus a number of strategies have been developed to extend the usefulness of any optical lithography generation. Printing that close to the resolution limit of an exposure tool results in severe optical proximity effect, caused by the absence of higher diffraction orders during image formation. These effects can severely limit the control of Critical Dimension (CD). For deep subwavelength designs, the increasing gap between the exposure wavelength and minimum feature CD is partially bridged using reticle enhancement technique (RET) applied to drawn layout.

RET generally includes three distinct variations, each targeted at one of the physical properties of a wavefront on the mask. Wave direction is controlled by designing special illuminator (off axis illumination, OAI), wavefront amplitude is controlled by changing aperture sizes and shapes (optical and process correction, OPC) and local wavefront phase is controlled by changing material properties or etching structures into the surface of the mask (Phase Shifting Mask, PSM). The aim of OAI is to direct light onto the reticle at certain angles so as to obtain a shift of the diffraction pattern and thus eliminate the zero order of diffraction. PSM works by destructive optical interference to enhance image contrast [6]. Two types of PSM are commonly used in lithography: they are the alternating aperture PSM and the embedded attenuating PSM. While there are many types of PSM, they all employ the same basic concept, which is well illustrated by the original version introduced by Levenson [7,8] and it is used here to introduce the subject. The shifter material that is added to the mask is able to change the phase of light by 180° in adjacent patterns leading to destructive interference rather than constructive interference. Unfortunately this kind of masks is difficult to make and repair.

Printing of the layout on wafer, near resolution limit, is affected by the same phenomena such as iso-dense bias, corner rounding and end of line shortening. These phenomena are due to the optical proximity effect that can be significantly reduced by applying OPC [9, 10]. The goal of OPC is to provide the smallest nominal deviation of silicon image from the drawn layout, especially in critical areas. OPC provides a revision on mask layout to achieve the target layer on the wafer to compensate for process distortions. This approach complicates the design flow for mask generation as it-requires definition of multiple OPC features and their extensive characterization by process, CAD and design. The most common approach involves rule-based OPC, i.e. edge, corner, or line end corrections defined by a set of width and spacing proximity rules. However, such corrections not only rely on a limited set of test geometries, but they are not adjustable to the actual process condition. In contrast, model based OPC features are generated for the actual layout environment and can be changed

depending on the adopted photolithography process. In model-based OPC, the flow for generation of the mask layout itself contains a process simulation step, which predicts the final result on the wafer, and adapts the layout until convergence between the final image and the original physical design intent is achieved.

Both of these methods add complexity to the design of the mask. A 90 nm microprocessor, for instance, already requires 200 gigabytes of data to describe its 22 to 25 masks. Another problem is due to the inspecting and repairing of defects in the masks. With masks that are more complex, finding and repairing a significant defect is like hunting for a basketball in an area the size of California.

## 4. EUV LITHOGRAPHY

EUVL appears a natural extension to optical lithography with the use of shorter wavelengths instead of increasing NA. EUV lithography (EUVL) [11] is a relatively new form of lithography that uses extreme ultraviolet (EUV) radiation with a wavelength in the range from 10 to 14 nm to carry out projection imaging. EUVL is capable of printing features of 45 nm and smaller, while achieving a DOF of 0.5 μm and larger.

EUV radiation is strongly absorbed in all materials, even gases; therefore EUV imaging must be carried out under vacuum. Absorption also rules out the use of refractive optical elements, such as lenses and transmission masks, thus EUVL imaging systems are entirely reflective. An all-reflective condenser optical system collects this EUV radiation and projects it onto a resonant-reflective reticle. The reflected radiation carries the IC pattern on the mask to wafer via an optical system comprised of multilayer optical surfaces. In the process a demagnification of 4/5X is achieved. The entire reticle is exposed onto the wafer by synchronously scanning the mask and the wafer, i.e., a step-and-scan exposure. Thus the main components of this system are: a source of soft X rays, a condenser optics (to transfer illumination to the mask plane), a reflective mask, i.e. an absorber pattern over a multilayer stack, an optical system, and a photo-resist coated wafer.

Illumination at EUV wavelengths (soft X rays) can be produced by a variety of sources including laser-produced-plasmas (LPP), synchrotron radiation, discharge pumped X ray lasers and electron beam driven radiation devices. However the required output of 30–60W of EUV source power can be achieved, to date, by the first two. The LPP sources are formed by focusing a pulsed laser beam onto a solid, liquid or gas target to produce a bright “spark” which has a broad emission from the visible to the EUV.

Masks consist of a patterned absorber of EUV radiation placed on top of a multi-layer reflector deposited on a robust and solid substrate, such as a silicon wafer. Reflective mask and multilayer mirrors are made by alternating layers of Mo and Si with prescribed thicknesses, also known as Bragg reflectors. A large number of layers are needed in order to improve the reflectivity of these mirrors. Pellicle masks are not required because of the undesirable absorption that would be encountered. The mirrors, that comprise the camera, will be required to exhibit an unprecedented degree of perfection in surface figure and surface finish in order to achieve diffraction-limited imaging.

A resist acceptable for high volume manufacture must exhibit high contrast for printing in combination with a sensitivity that will yield an acceptable throughput. The main problem to be confronted in developing a satisfactory photoresist for EUVL is the strong absorption of EUV radiation by all materials. The absorption depth in standard organic resists used today is less than 100 nm. EUV resists will most likely be structured so that printing occurs in a very thin imaging layer at the surface of the resist. Resist types, being actively worked on, include silylated single-layer resists, refractory bi-layer resists, and tri-layer resists. A resist sensitivity of 10 $mJ/cm^2$ is our goal since it represents a good compromise between the need for high throughput and the desire to minimize the statistical fluctuations due to photon shot noise.

Much work remains to be done in order to determine whether or not EUVL will ever be ready for the production line. There are a number of serious problems to be solved:

- a source will be required that provides sufficient power to yield adequate wafer throughput in a manufacturing tool,
- because EUV absorption in optical photoresists is very high, new resists and processing techniques will be required for application in EUV,
- there are no known methods for repairing defects in an ML coating, since masks must be free of defects,
- a technique must be developed for depositing defect-free ML reflectors, the challenge for a fabricator of optics for EUVL is to achieve the desired levels of figure accuracy and surface roughness simultaneously.

## 5. E-BEAM LITOGRAPHY

Electron beam lithography (EBL) is a technique derived from the early scanning electron microscopes; in brief the technique consists of scanning a beam of electrons across a surface covered with a resist film sensitive to those electrons [12]. This the technology is capable of very high resolution, almost to the atomic level, is a flexible technique that can work with a variety of materials and an almost infinite number of patterns, but it is slow, being one or more orders of magnitude slower than optical lithography.

The part of the EBL system that forms the electron beam is normally referred to as the column. An EBL column typically consists of an electron source, two or more lenses, a mechanism for deflecting the beam, a blanker for turning the beam on and off, a stigmator for correcting any astigmatism in the beam, apertures for helping to define the beam, alignment systems for centring the beam in the column, and finally, an electron detector for assisting with focusing and locating marks on the sample. Underneath the column is a chamber containing a stage for moving the sample around and facilities for loading and unloading it. Associated with the chamber is a vacuum system. A computer, which may be anything from a personal computer to a mainframe, controls the system. Electrons may be emitted from a conducting material either by heating it, thermionic sources (Tg or LaB6), or by applying an electric field (field emission sources). Three key parameters of the source are the virtual source size, its brightness (expressed in $A \cdot cm^{-2} \cdot sr^{-1}$), and the energy spread of the emitted electrons (measured in eV). As the electrons penetrate the resist, some of them are subjected to small angle forward scattering events, which tend to broaden the initial beam diameter. As the electrons penetrate through the resist into the substrate, they occasionally undergo large angle scattering events (backscattering). The backscattered electrons cause the proximity effect, where electrons scattering from other features nearby affect the dose that a pattern feature receives. During this process the electrons are continuously slowing down, producing a cascade of low voltage electrons, called secondary electrons, with energy from 2 to 50 eV. These are responsible for the bulk of actual resist exposure process. Since their range in resist is only a few nanometers, they contribute little to the proximity effect.

In the simplest positive resists, electron irradiation breaks polymer backbone bonds, leaving fragments of lower molecular weight. A solvent developer selectively washes away the lower molecular weight fragments, thus forming a positive tone pattern in the resist film (PMMA, EBR-9, PBS, ZEP). In the negative resists, instead, electron irradiation cross-links the polymer chains, rendering them less soluble in the developer. Negative resists tend to have less bias (often zero) than positive resists. However, they tend to have problems with scum (insoluble residue in exposed areas), swelling during development, and bridging between features. Polymethyl methacrylate was one of the first materials developed for e-beam lithography. It is the standard positive e-beam resist and remains one of the highest resolution resists available.

Currently, electron beam lithography is used mainly in support of the integrated circuit industry, where it has three niche markets. The first is in mask making, typically the chrome-on-glass masks

used by optical lithography tools. It is the preferred technique for masks because of its flexibility in providing rapid turnaround of a finished part described only by a computer CAD file. An emerging market in the mask industry is a mask for X ray lithography. These masks typically have features ranging from 0.25 μm to less than 0.1 μm and will require placement accuracy and linewidth control of 20 nm or better. The second application is direct write for advanced prototyping of integrated circuits and manufacture of small volume specialty products, such as gallium arsenide integrated circuits and optical waveguides. Finally, EBL is used for research into the scaling limits of integrated circuits and studies of quantum effects and other novel physics phenomena at very small dimensions. Here the resolution of EBL makes it the tool of choice. Other applications include devices to study ballistic electron effects, quantization of electron energy levels in very small structures, and single electron transistors.

Any tool for microscopy - optical, electron, or scanning probe - may be adapted to work in reverse; that is, for writing instead of reading. Converted electron microscopes suffer the same limitations as light microscopes used for photolithography, namely, a small field of view and low throughput. Nevertheless, for a subset of research and R&D applications, converted SEMs offer a relatively inexpensive solution.

## 6. CONCLUSIONS

Over the last several years optical lithography has been used ubiquitously for manufacturing. This dominance of optical lithography in production has been the result of a worldwide effort to improve optical exposure tools and resists. Improvements in this technology will allow it to remain the semiconductor industry's workhorse through the 70 nm generation of devices.

Owing to the physical limits of optical lithography potential successors to optical projection lithography are being aggressively developed. These include EUV technique that can be considered a “bridge technology below 50nm, before next generation lithography systems”.

## REFERENCES


[1] McCORD, M.A., ROOKS, M.J., Handbook of Microlithography, Micromachining and Microfabrication, Vol. 1, Ed. P. Rai-Choudhury.

[2] KUBIAK, G.D, KANIA, D.R., Extreme Ultraviolet Lithography, Eds. OSA Trends in Optics and Photonics, Vol. 4, Optical Society of America, Washington, DC (1996).

[3] SAHOO, P.B., VYAS, R., WADHWA, M., VERMA, S., “Progress in deep-UV photoresists”, Bull. Mater. Sci., 25 (2002) 553-556.

[4] ITO, H., WILSON, C.G, Proc. of SPIE, Regional Technical Conference on Photopolymers, Tokio, Japan (1982).

[5] BATES, A.K., ET AL., Review of technology for 157 nm lithography, IBM J. Res. & Dev., Vol. 45 n. 5, September 2001.

[6] GARCIA, P.F., HUGHES, G., FRENCH, R.H., TORARDI, C., REYNOLD, G., DICU, I., Thin film for phase-shift masks, DuPont Co. Central Research and DuPont Photomasks Inc., Published in Vacuum and Thin Film, THS Publishing Group, 14-21 September 1999.

[7] LEVENSON, M.D., Phase-Shifting Mask Strategies: Line-Space Patterns, IBM Research Division, Almaden Research Center, San Josè, California.

[8] LEVENSON, M.D., Phase-Shifting Mask Strategies: Isolated Dark Lines, IBM Research Division, Almaden Research Center, San Josè, California.

[9] SCHELLENBERG, F.M., CAPODIECI, L., SOCHA, B., Adoption of OPC and the impact on design and layout, Mentor Graphics.

[10] DRIESSCHE, V.V., FINDERS, J., TRITCHKOV, A., RONSE, K., VAN DEN HOVE, L., TZVIATKOV, P., Feasibility of 250 nm gate patterning using i-line with OPC, IMEC and Olin, Microelectronic Materials.

[11] BJORKHOLM, J.E., “EUV Lithography-The successor to opticle lithography?”, Advanced Lithography Department, Technology and Manufacturing Group, Intel Corp.,Santa Clara, CA.
[12] Handbook of Microlithography, Micromachining and Microfabrication, Vol. 1, Ed. P. Rai-Choudhury.

# NANOTECHNOLOGY AND NANOLITHOGRAPHY USING RADIATION TECHNIQUE IN JAPAN

Y. MAEKAWA
Japan Atomic Energy Research Institute,
Takasaki Radiation Chemistry Research Establishment,
Takasaki, Gunma, Japan

**Abstract**

Radiation technique is essential to nanotechnology with high resolution and a high aspect ratio because radiation beams can be focused into a few nanometer or less and scanned with quite high speed. There have been many attractive reports about radiation processes to fabricate nanoscale structures of organic and inorganic materials. In this paper, several examples of such newly developed radiation techniques for nanotechnology using electron beams (EB), focused ion beams (FIB), heavy ion beams (cyclotron), and X rays in Japan are summarized. The fabrication with resolution lower than 10 nm requires EB, FIB, and X ray processes. The developed EB lithography system enables the fabrication of extremely small structures in micro/nanometer scale such as the world's smallest globe with about 60 μm in diameter, strong SiC micro tubes with 5 and 24 μm in inner and external diameters, and nanoscopic colour imaging of the polymer films with the resolution of 300 nm. Using low energy ion beams, a 3D nanostructure fabrication process with FIB-CVD enables to prepare a microwine glass with 2.75 μm external diameter and 12 μm height. In contrast, nanostructure formation with aspect ratios higher than 1000 requires heavy ion beam processes. Heavy ion beam processes enable the fabrication of anisotropically conducting membranes possessing copper wires with less than sub-micron in diameter and Si based nanowires with 170 nm in length and 30 nm in width. Furthermore, LIGA processes for mass production of plastic, ceramics or other materials of high aspect ratio micro/nano structures can be achieved by exposing Synchrotron Radiation to the resist through X ray mask and formation of Ni micromold by electroplating.

## 1. INTRODUCTION

In lithographic technology, the energy of light sources is getting higher; namely, the energy of light sources of the generation after a F2 laser possess beyonds the ionization potential of organic materials such as photo-acid generators. Therefore, we must consider radiation chemistry of these compounds rather than photochemistry when we use these high energy light sources for preparing nanoscale architectures [1–5]. At the moment, there are many competitive methods even except radiation technique in nanotechnology. Photo processes (current lithography system) and near field optics are promising candidates for a conventional bottom down method. A bottom up method is more intensively investigated as a new nano fabrication technique; soft lithography using X ray and EB, cantilever such as AFM and STM tips, and dip pen lithography should be used in future. Although there are many tools for nano-fabrication, radiation technique must play a crucial role for both bottom down and bottom up methods.

Figure 2 shows the aspect ratios and resolution limit (line width) of optical and radiation processes. It is clear that radiation methods are essential to nanotechnology with high resolution and high aspect ratios. Especially, nanofabrication with resolution lower than 10 nm requires EB and X ray processes; in contrast, fabrication with aspect ratios higher than 1000 requires heavy ion beam processes [6]. Therefore, X ray, EB, and low energy ion beams such as EB scanning devices and focused ion beam (FIB) should be useful for future nanolithography, and 3D nano fabrication. On the other hand, heavy ion beam processes can be useful for fabrication of nanopores and nanowires owing to its ability to give high aspect ratio patterns.

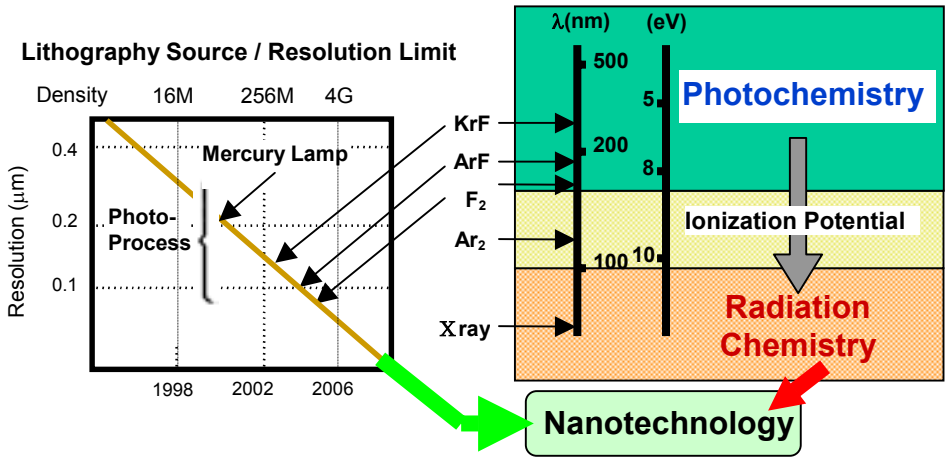


*FIG. 1. Optical and radiation sources for nanotechnology.*

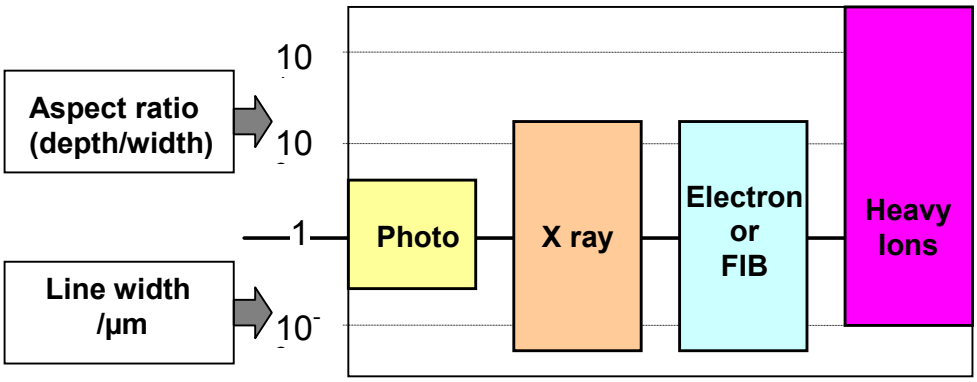


*FIG. 2. Aspect ratio and resolution limit of various lithographic methods.*

The followings are the examples of nanostructure fabrication, presented in this paper, using EB, ion beam, and X rays.

1Nano-fabrication using EB
(1) 3D EB lithography
(2) SiC Tubes
(3) Colour Imaging of Polymer Films

2. Nano-fabrication using Ion Beam
(1) Focused Ion Beam Fabrication (FIB)
(2) Heavy Ion Beams : Anisotropically Conducting Films (3) Heavy Ion Beam : Si Nanowires

3. Nano-fabrication using SOR-LIGA Process

2. NANO-FABRICATION USING ELECTRON BEAM

The electron beam (EB) radiation possesses several advantages such that the beams can be focused into nanometer scales and scanning at a high speed [1]. Therefore, EB irradiation has attracted much attention in recent years as a promising technique for nanolithography and fabrication of future nanodevices in a variety of fields such as electronics and photonics [1, 4, 5].

### 2.1. 3D EB lithography [7]

The first example of nano-fabrication using EB is developed by Nippon Telegraph and Telephone Corporation (NTT). The developed EB lithography system enables the fabrication of extremely small three-dimensional (3D) structures in nanometer scale (FIG. 3a). The 3D nanopatterning and nanofabrication can be conducted by exposing a small sphere to the EB to form the world's smallest globe (FIG. 3b).

The new technique consists of a special drive to rotate a sample and EB nanolithography, which has resolution 100 times higher than that obtained by the methods using an optical or X rays. This enables reasonably fast 3D fabrication and patterning. One key technique is the ability to rotate a 3D sample in such a way that any of its faces can be exposed to the EB. Another key technique is EB focusing on a 3D sample. This requires an ability to determine the height (Z coordinate) and horizontal position (X and Y coordinates) of any point on a sample. To measure the height, they developed a new height measurement system that uses a confocal laser microscope. The system makes a height map of a sample, thus enabling the height of any point on the sample to be determined, even if the sample is rotated.

The world's smallest globe was made by writing a map of the world on a micro-sphere made of resin. This nano-globe has a diameter of about 60 μm. The smallest pattern is about 10 nm in size, which corresponds to 2 km on the actual earth.

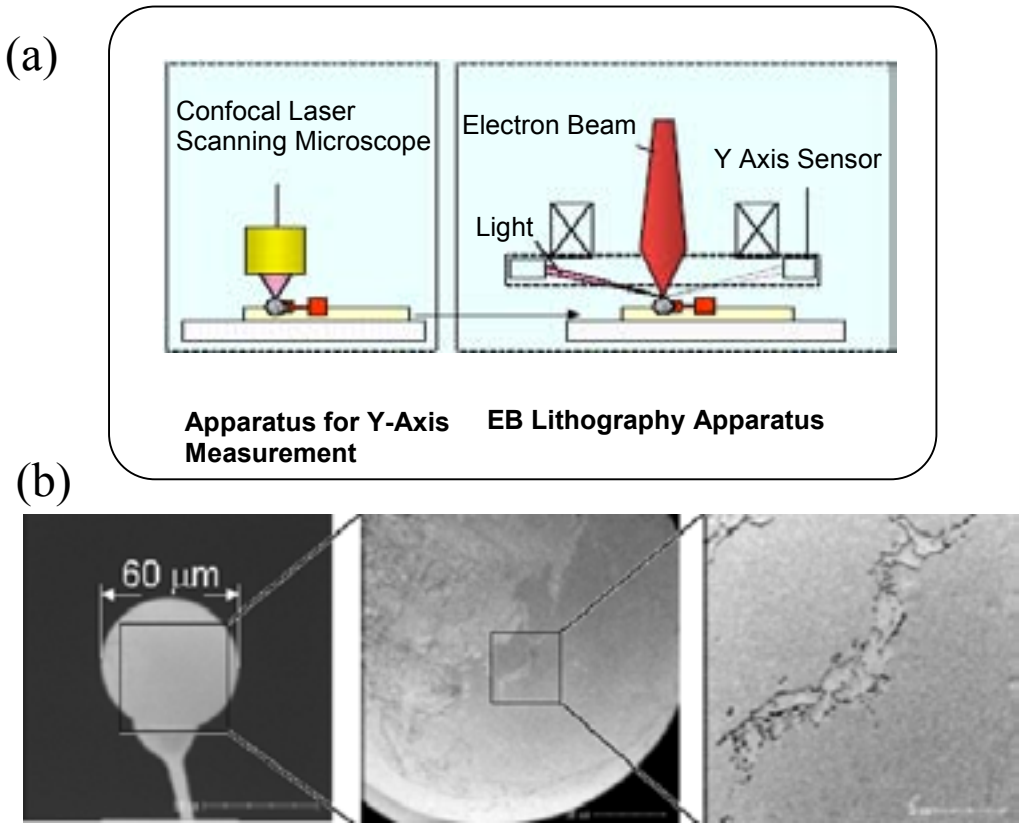


*FIG. 3. (a) Apparatus for 3D EB lithography (b) A terrestrial globe prepared by 3D EB lithography.*

### 2.2. SiC Tubes [8, 9]

A new technique for producing soft and strong SiC fibers has been developed by irradiation of polycarbosilane (PCS) in oxygen followed by heat treatment. PCS fibers are well oxidized by EB irradiation in air to produce free radicals. The free radicals react preferably with oxygen, and react with each other to form cross-linking. In the case of EB irradiation, the oxidation takes place only at surface layer of the PCS fiber and the inside of the PCS fiber is not crosslinked by oxygen. The oxidized surface layer is not dissolved by the solvent of tetrahydrofuran (THF), but the inside is well dissolved (FIG. 4).

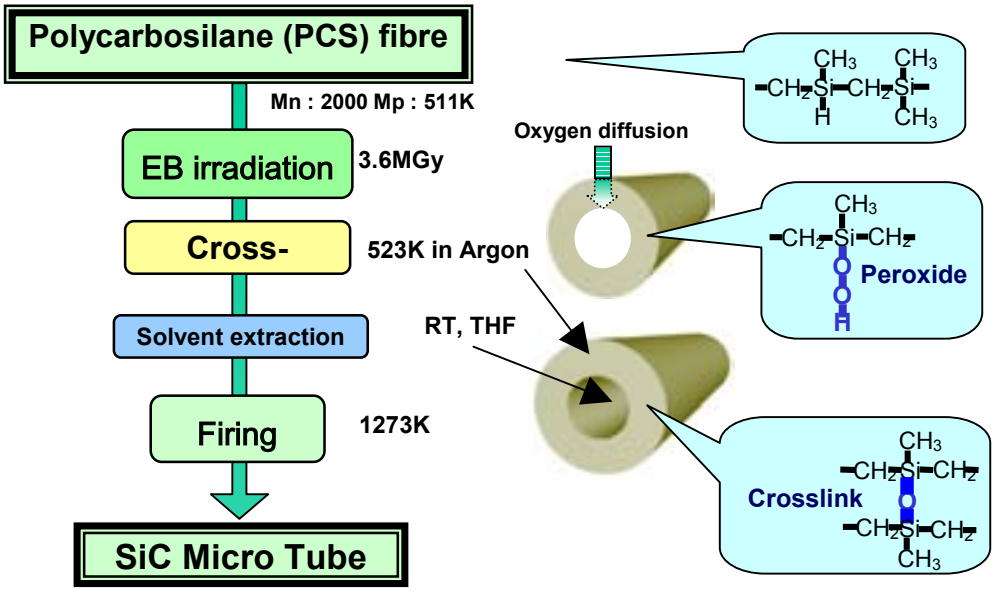


*FIG. 4. Fabrication process for SiC Tubes.*

Using the EB oxidation process, PCS tubes in micrometer scale can be prepared by extracting the un-crosslinked part inside of the interstices of fiber through the surface layer swelled by THF, which is ideally crosslinked by EB irradiation for extracting. The PCS tube is converted to the SiC tube by pyrolysis in Ar gas at a temperature over 1300K. As shown in FIG. 5, the synthesized SiC tubes have dimensions with 5 and 24 μm in inner and external diameters. The spinnability of PCS is not so good and it would be difficult to make polymer tube by special spinning method like polypropylene or polyethylene fiber. Therefore, this new technique is important technique to make ceramic tubes and wide range of application is expected.

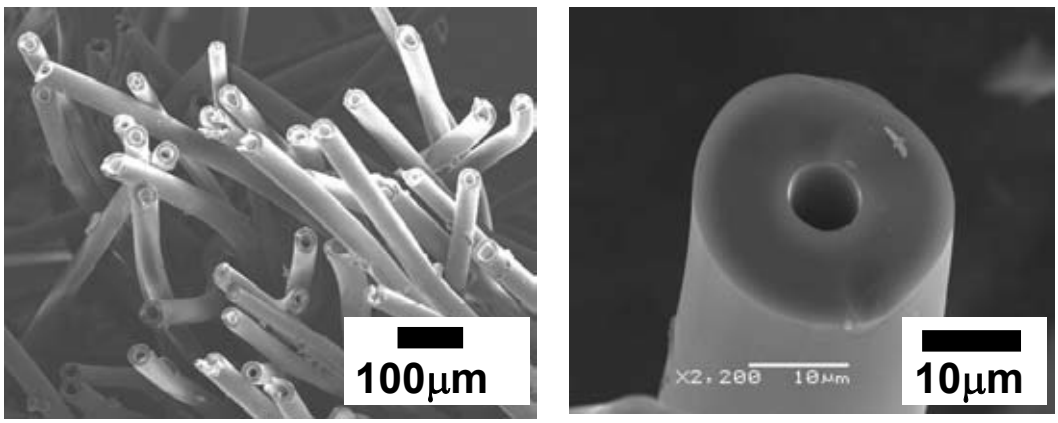


*FIG. 5. Synthesis of SiC tubes using EB oxidation process.*

### 2.3. Colour imaging of polymer film

The transformation of functional groups in a molecular level in polymer matrix is required for optical storage media. If radiation technique can be used for recording of optical memory, the density of memory increases by several orders of magnitude, compared with a conventional optical system because radiation beams such as EB and X rays are focused into less than 10 nm. Therefore, the molecular level transformation has been conducted using an EB scanning device to develop EB induced colour formation of polymer films, which should be applied for high density optical storage systems.

There have been few reports on the useful EB-sensitive polymer materials although a number of studies on the resist materials for EB-lithography have been conducted. Recently, we examined the EB induced reactions of photosensitive compounds such as cinnamic acid derivatives4 sulfonium salt5, and sulfonic acid derivatives in the crystalline state, together with comparison with the corresponding photoreactions. Among these compounds, the EB irradiation of sulfonamides underwent the Fries rearrangement and scission to yield the aniline derivatives; whereas, the corresponding carboxylic acid derivatives did not give rise to any rearrangement or scission products. It is notable that these reactions accompany transformation of an acidic sulfonamide to basic aniline groups.

A polymer consisting of sulfonamide (PSA) and copolymers consisting of sulfonamide and carbonyl amide units were prepared by polycondensation of benzene-1,3-disulfonyl chloride and isophthaloyl dichloride with bis(4-aminophenyl)ether. Since the EB-induced reaction of these polymers yielded aniline groups inside and at the terminal of polymer chains, the EB irradiation of these polymers can be applied for nanoscale colour imaging by using the colour forming reactions of Ehrlich reagents (4-N,N-dimethylaminobenzaldehyde, DAPA) with the aniline groups.

Upon EB irradiation with the dose of 10 MGy, PSA proceeded fries rearrangement and scission of sulfonamide groups to form amino groups in the main chain and at the polymer terminal. The 1H-NMR spectra of the irradiated samples revealed that EB irradiation of copolymers induced the chemo-selective reaction of the sulfonamide group, but not amide group. By the treatment of the irradiated films with DAPA, the terminal aniline group but not amino groups of the main chain resulting from Fries rearrangement reacted with DAPA in the film state to give aromatic imines, which exhibited yellow-orange colour ( max = 454 nm).

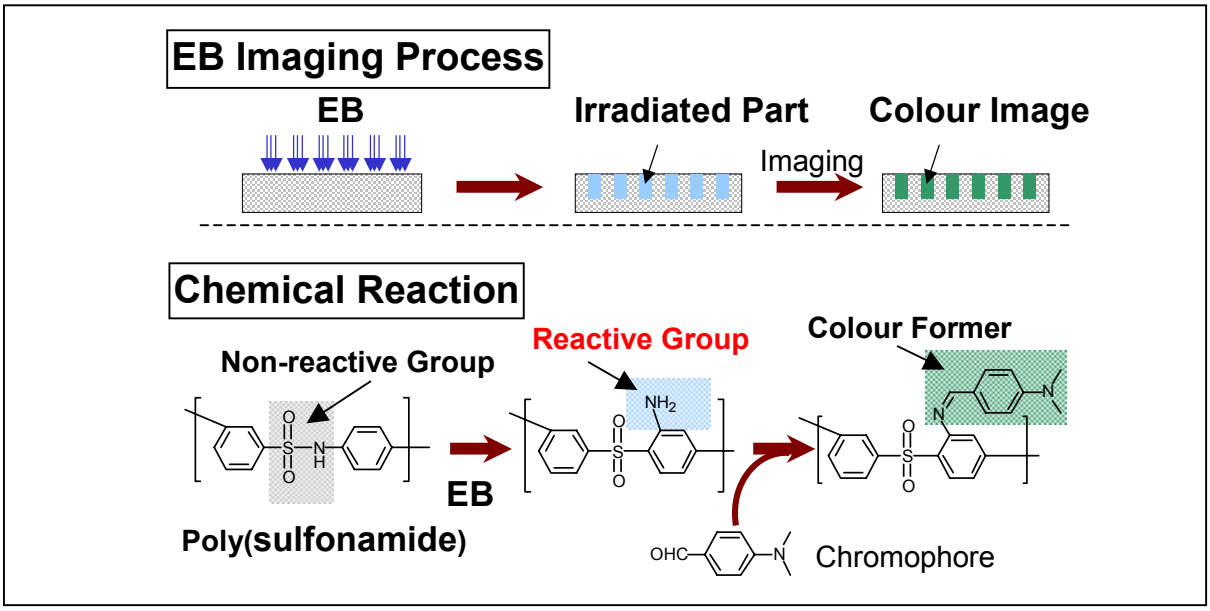


*FIG. 6. EB Induced Colour Imaging of Polymer Film.*

Then, nanoscopic colour imaging of the polymer films was performed using an EB imaging device. EB irradiation of PSA with the dose of 500 C/cm$^2$ provided the colour imaging of dot patterns with the resolution of 500 nm and line/space patterns with the resolution of 300 nm.

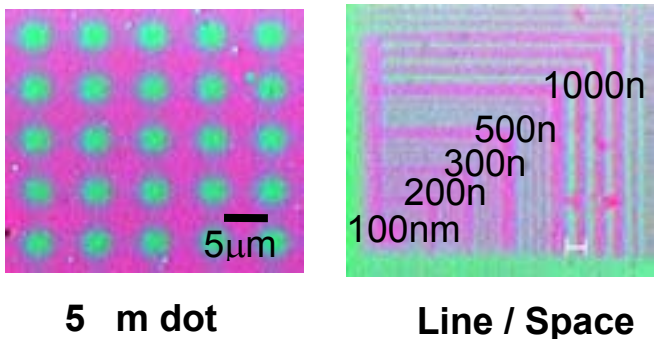


*FIG. 7. Dot and line / space patterns of EB induced colour Images.*

## 3. NANO-FABRICATION USING ION BEAM

Even in the same ion beams, low and high energy ion beams have totally different characteristics for nano fabrication of materials. Low energy ion beams such as FIB is very useful for surface fabrication like EB with resolution less than 10 nm; in contrast, heavy ion beams is a very powerful tool for nano structure formation with aspect ratios higher than 1000.

### 3.1. Focused Ion Beam Fabrication (FIB) [10]

The first example of nano fabrication using ion beams is developed by the groups of Ritsumeikan University using FIB. Three-dimensional (3D) nanostructure fabrication has been demonstrated by 30 keV Ga focused ion beam with a aromatic hydrocarbon precursor gas. 3D structure fabrication process by FIB CVD is illustrated in FIG. 8. In FIB CVD processes, the beam is scanned at digital mode. First, a pillar of diamond-like amorphous carbon is deposited on the substrate by fixing a beam position (position 1). After that, the beam position is moved within a diameter of pillar (position 2) and then fixed until the deposited terrace becomes thick enough to exceed an ion range of a few nanometers. This process is repeated to make 3D structures. A microwine glass with 2.75 μm external diameter and 12 μm height was created, as shown in FIG. 9. Furthermore, a microcoil with 0.6 μm coil diameter, 0.7 μm coil pitch, and 0.08 μm linewidth can be formed by the same FIB method.

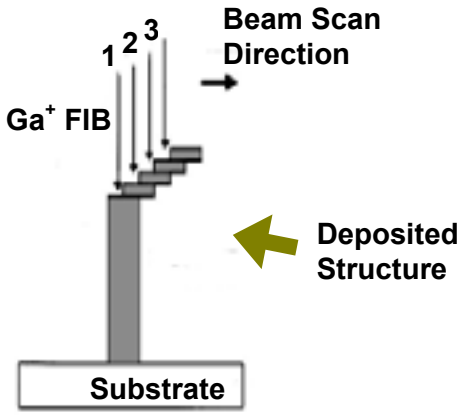


*FIG. 8. Nano Fabrication Process using FIB.*

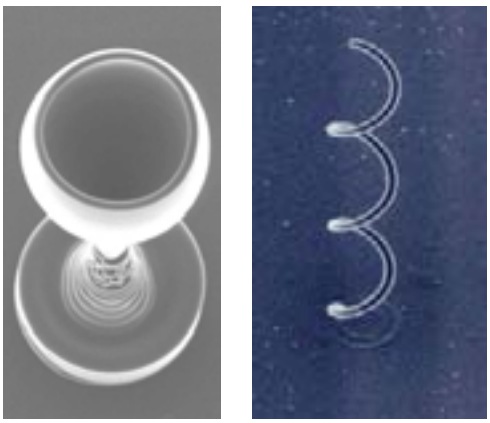

*FIG. 9. (a) Nano Wine Glass. (b) Nano Coil.*

### 3.2. Heavy Ion Beams: anisotropically conducting film [11]

A heavy ion beam with acceleration energy of more than 1 MeV/n deposits its energy to a substrate in a region < 10 nm in diameter (an ion track); the depth of the affected region can be regulated by changing the energy or replacing species of ion particles.

There are two distinct nano fabrication processes using heavy ion beams; one is nano-hole formation due to the damage of ion beam path, and the other is nano-wire formation due to cross-linking of polysilane, which is also caused by heavy ion beams.

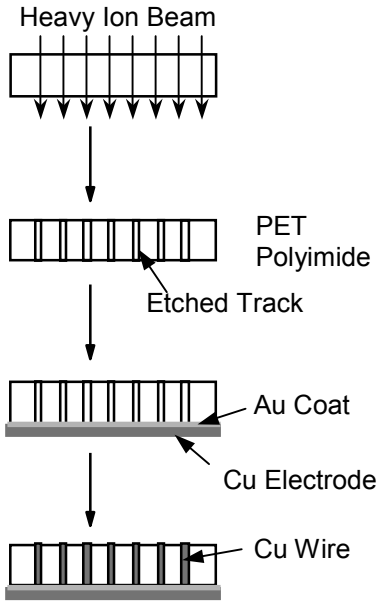


*FIG. 10. The preparation of an ion track membranes and electroplating of copper wires within the pores of ion track membranes.*

When organic polymer films are used as a substrate, the materials around the ion track have been damaged enough to be etched out in alkaline solutions because of scission of the polymer main chains. Thus, "ion track membranes", which possess cylindrical through-holes with diameter ranging from 10 nm to 1 μm, are prepared by ion beam irradiation followed by etching out of the damaged part of the material (FIG. 10) [12-17].

There have been many reports for manufacturing metallic wires by electrochemical template synthesis in the pores of ion track membranes for technological applications, such as electron field emitters, solar absorbers, vertical magnetic materials, and optical fibers [18–22]. Among them, copper wires have been prepared by electrochemical template synthesis mainly using the ion track membranes made of polycarbonate (PC); then, the PC membranes were removed after copper preparation for investigating structural and physical properties of copper wires. However, there has been no attempt for applying the electroplating with ion track membranes to fabricate conductive and insulating hybrid membranes. Therefore, we report herein the application of the ion track membranes to the fabrication of anisotropically conducting films consisting of copper wires of a diameter, which is 100 times smaller than those of commercially available films (FIG. 10).

PET films with 12 μm in thickness, which were irradiated by $^{129}Xe^{23+}$ ion beams, were etched in 0.2M NaOH aqueous solution, resulting in the clear hole patterns with 200 nm in diameter, as shown in FIG. 11 (a).

The copper wires were deposited into the pores with 200 nm in diameter by electroplating method. After removing the PET film from the copper electrode, the geometry of the copper wires was confirmed to be 200 nm in diameter and 12 μm in height, which were in good agreement with the size of the pores as shown in FIG. 11 (b). This observation confirms the successful formation of the hybrid membranes consisting of insulating PET film and perpendicularly aligned cylindrical copper wires with high aspect ratio (height/diameter = 50).

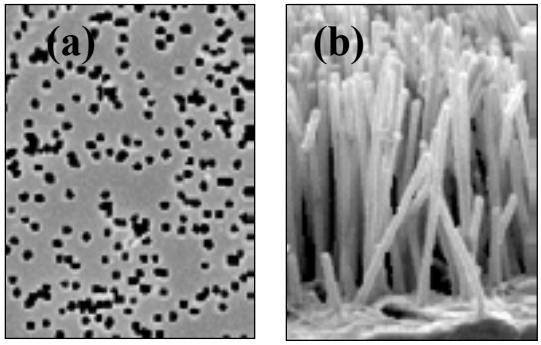


*FIG. 11. SEM photographs of (a) the surface of the PET ion track membrane possessing through-holes with 200 nm in diameter, (b) copper wires with 12 μm in height and 200 nm in diameter on copper electrode after removing the PET film.*

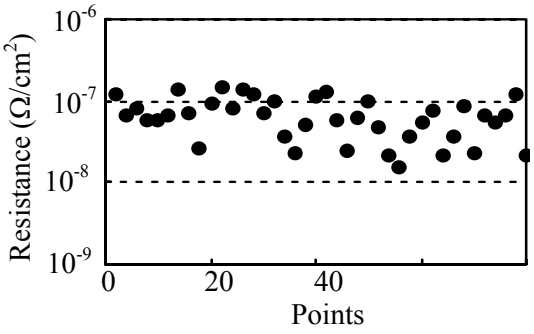


*FIG. 12. The resistances of the hybrid membranes consisting of PET film with cylindrical copper wires in the directions perpendicular to the surfaces by a four terminal resistance method. Copper wires with 12 μm in height and 200 nm in diameter.*

The conductivity of the PET/Cu hybrid membranes consisting of PET with 12 μm in height and 200 nm in diameter was evaluated by the measurement of the membrane resistance in the directions perpendicular and parallel to the surfaces by a four terminal resistance method. As shown in FIG. 12, the membrane showed the average resistance is estimated to be $6.9 \pm 3.7 \quad 10^{-7}$. This average resistance of the membrane is about three times higher than the theoretical resistance (2.1 $10^{-7}$ σ/cm$^2$). Such lower conductivity of the PET/Cu hybrid membranes compared with the calculated value is likely to result from the defects in copper wires during the electroplating preparations, influence of the interfaces between copper wires and the pore surfaces of PET, and/or the contact resistances between the needle probe and the top of copper wires. In contrast, the resistance of the membrane parallel to the surfaces were zero at any points. From these results, it is evident that anisotropically conducting membranes possessing copper wires with less than sub-micron in diameter are prepared by electroplating of copper into the cylindrical pores in the ion track membrane made of PET.

### 3.3. Heavy ion beams: Si nanowires [23]

Next ion beam induced nano fabrication is the reverse tone of the fabrication of ion track membranes, ie., negative type patterning of organosilane polymers using heavy ion beams. FIG. 14 shows a schematic procedure to obtain isolated nanowires. An incident ion deposits its energy within a limited area along the ion projectile where cross-linking of polysilanes occurred. The uncrosslinked part of a film is washed with solvent, resulting in isolated nanowires of crosslinked polysilanes.

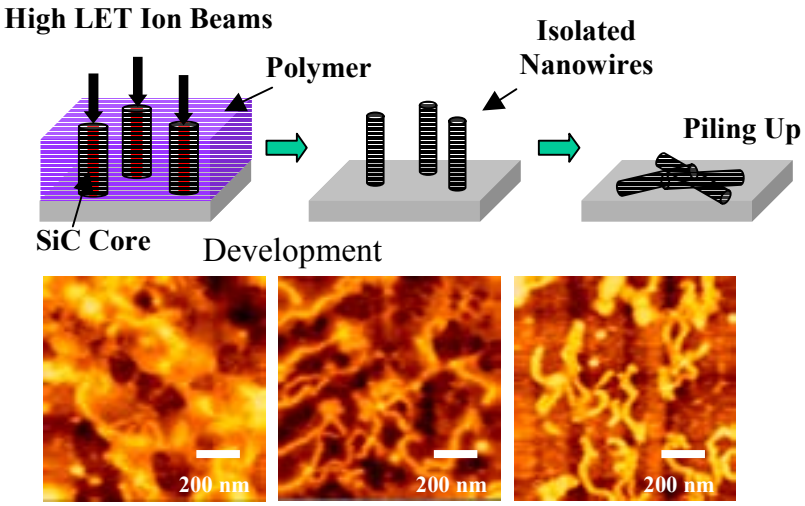


*FIG. 13. Formation process of Si based nanowires.*

As shown in the AFM images of FIG. 14, nanowires formed on a Si substrate can be clearly observed in AFM images. The number of observed nanowires in a unit area shows good agreement with that of incident particles. In spite of a development procedure in a solvent, the wires adhere to the Si substrate and the nanowires remain isolated from each other. This indicates that one end of the wire is chemically connected the substrate. Surface treatment of Si substrates give a number of –Si-OH groups on the top surface; thus, Si-O-Si bridges form between the substrate and the nanowires. The images in FIG. 14 were obtained using a film of 170 nm initial thickness. Since the mean length of the nanowires is 180 nm, the length of a wire should be well controlled by simply changing the thickness of the target film.

## 4. NANO-FABRICATION USING SOR-LIGA PROCES[24]

SOR light is used for a LIGA process for mass production of plastic, ceramics or other materials of high-aspect ratio micro/nano structures. Based on a compact synchrotron light source, a dedicated X ray beam line and a new exposure device has been constructed, which can work in the exposure environments of vacuum or helium gas. The deep X ray exposure system mainly includes an X ray beam line and the exposure device, which is shown in FIG. 14. Based on a compact synchrotron light source, the dedicated X ray beam line has been constructed. It is mainly made up of beam shutter, Be window, Kapton window, exposure shutter, exposure chamber, vacuum system and measurement & control system.

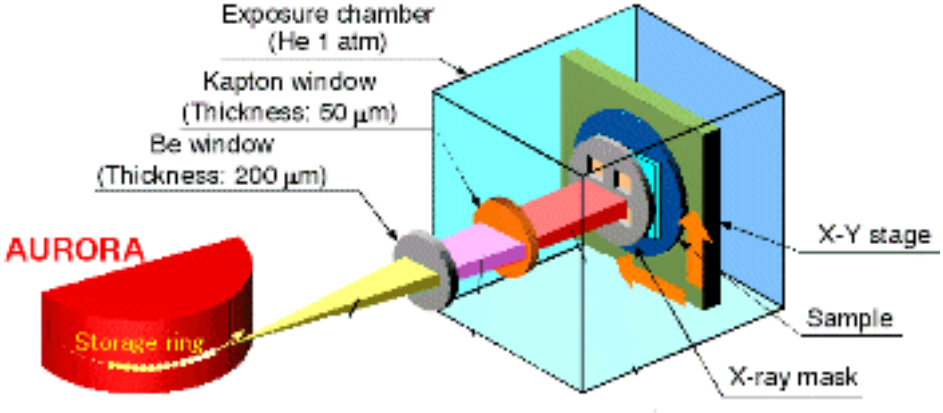


*FIG. 14. X ray beam line and the exposure device.*

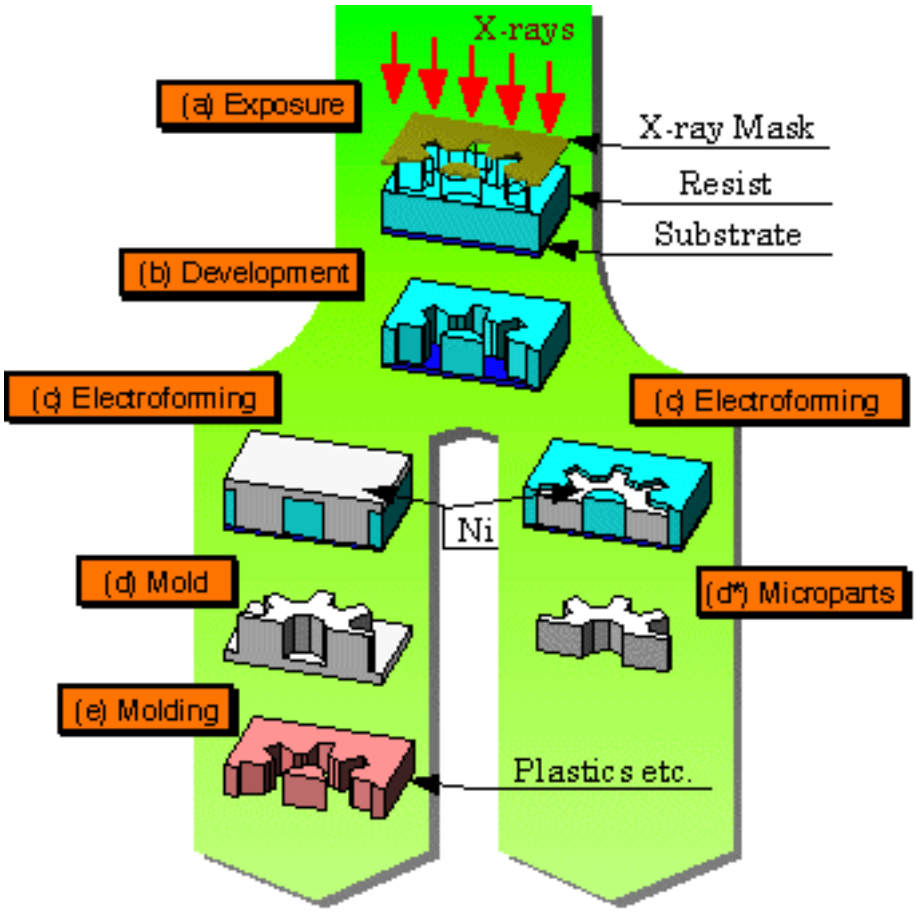


*FIG. 15. LIGA process using SOR.*

LIGA process is an effective technology for reaching high-aspect ratio micro/nano structures (FIG. 15). By exposing Synchrotron Radiation to the resist through X ray mask, the resist will be shaped by X ray lithography. Micromold will be formed by electroplating metals. The mold will finally be used for batch fabrication of plastic, ceramics or other materials of micro/nano structure.

Poly (methyl metacrylate) (PMMA), which is a conventional X ray resist, can be transformed to microsized patterns by SOR exposure and a solution development, as shown in FIG. 16a.

Using the microscopically patterned PMMA as a template, nickel molds are fabricated on Si wafer, which acts as a conducting layer, by electroplating. The nickel micro-molds can be used for mass production of polymer micro-parts.

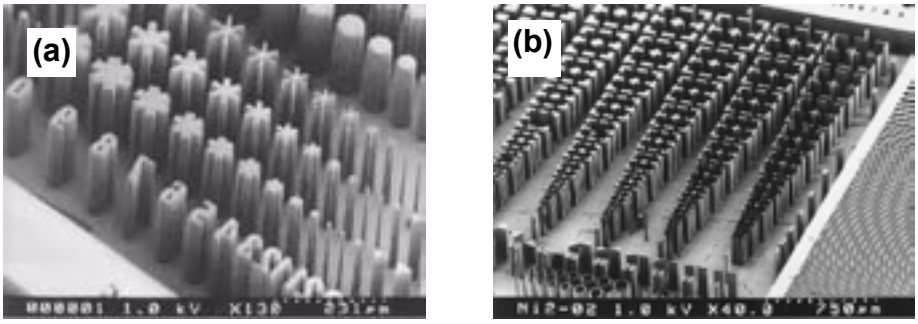


*FIG. 16. Nano-fabrication using SOR-liga Process. (a) PMMA X ray resist. (b) Electroplating Nickel onto PMMA.*

## 5. CONCLUSION

Recent development of radiation techniques such as EB, Ion beam, and X rays for nanotechnology in Japan are summarized in this paper. The fabrication with resolution lower than 10 nm requires EB, FIB, and X ray processes. The developed EB lithography system enables the fabrication of extremely small structures in micro/nanometer scale such as the world's smallest globe with about 60 m in diameter, strong SiC micro tubes with 5 and 24 m in inner and external diameters, and nanoscopic colour imaging of the polymer films with the resolution of 300 nm. Using low energy ion beams, a 3D nanostructure fabrication process with FIB-CVD enables the preparation of a microwine glass with 2.75 m external diameter and 12 m height. In contrast, nanostructure formation with aspect ratios higher than 1000 requires heavy ion beam processes, which enable the fabrication of anisotropically conducting membranes possessing copper wires with less than sub-micron in diameter and Si based nanowires with 170 nm in length and 30 nm in width. Furthermore, LIGA processes for mass production of plastic, ceramics or other materials of high-aspect ratio micro/nano structures can be achieved by exposing Synchrotron Radiation to the resist through X ray mask and formation of Ni micromold by electroplating. Accordingly, X ray, EB, and low energy beams such as EB scanning devices and FIB should be useful for future lithography and 3D fabrication. On the other hand, heavy ion beam can be useful for fabrication of nanopores and nanowires owing to its ability to give high aspect ratio patterns.

## REFERENCES

[1] J.R. SHEATS, B.W. SMITH, Microlithography, Science and Technology; Marcel Dekker: New York, 1998.

[2] K. SUZUKI, S. MATSUI, Y. OCHIAI, Sub-Half-Micron Lithography for ULSIs; Cambridge University Press: Cambridge, 2000.

[3] Y. TABATA, Y. ITO, S. TAGAWA, CRC Handbook of Radiation Chemistry; CRC Press: Boca Raton, FL, 1991.
[4] Y. MAEKAWA, T. INABA, H. HOBO, T. NARITA, H. KOSHIKAWA, S. MOON, J. KATO, M. YOSHIDA, Chem. Commun. 2002, 2088.
[5] S. MOON, Y. MAEKAWA, M. YOSHIDA, Chem. Lett. 2001, 408.
[6] R. SPOHR, Ion tracks and Microtechnology, Principles and Applications, Vieweg & Sohn Verlagsgesellschaft mbH: Braunschweig (1990).
[7] NTT News Release, Feb. 2, 2004.
[8] M. NARISAWA, S. KITANO, A. IDESAKI, K. OKAMURA, M. ITOH, J.Mater.Sci., 33, 2663–2666 (1998).
[9] R.IDESAKI, M.NARISAWA, K.OKAMURA, M.SUGIMOTO, TANAKA, Y.MORITA, T.SEGUCHI, M. ITOH, J.Mater.Sci., 36, 5565–5569 (2001).
[10] S. MATSUI, T. KAITO, M. KOMURO, K. KANDA, Y. HARUYAMA, J. Vac. Sci. Technol. B18, 3181–3184 (2000).
[11] Y. MAEKAWA, H. KOSHIKAWA, M. YOSHIDA, Polymer, 45, 2291–2295 (2004).
[12] N. REBER, R. SPOHR, A. WOLF, H. OMICHI, M. TAMADA, M. YOSHIDA, J. Membr. Sci. 140, 275 (1998).
[13] C. SAMMON, J. YARWOOD, N. EVERALL, Polym. Degrad. Stabil., 67, 149 (2000).
[14] H.G. CRAIGHEAD, Science, 290, 1532 (2000).
[15] A. DUTTA, S.P. LEE, Y. HAYAFUNE, S. ODA, J. Vac. Sci. Technol. B18, 2857 (2000).
[16] Y. SUZUKI, Y. MAEKAWA, M. YOSHIDA, K. MAEYAMA, N. YONEZAWA, Chem. Mater., 14, 4186 (2002).
[17] Y. MAEKAWA, Y. SUZUKI, M. YOSHIDA, K. MAEYAMA, N. YONEZAWA, Polymer, 44, 2307 (2003).
[18] S.B. LEE. C.R. MARTIN, Chem. Mater., 13, 3236 (2001).
[19] C.R. MARTIN, Science, 266, 1961 (1994).
[20] T.M. WHITNEY, J.S. JIANG, P.C. SEARSON, C.L. CHIEN, Science, 261, 1316 (1993).
[21] M.E.T. MOLARES, V. BUSCHMANN, D. DOVREV, R. NEUMANN, R. SHOLZ, I.U. SCHUCHERT, J. VETTER, Adv. Mater., 13, 62 (2001).
[22] L.D. PRA, E. FERAIN, R. LEGRAS, S. DEMOUSTIER-CHAMPAGNE, Nucl. Instru. Meth., B196, 81 (2002).
[23] S. SEKI, K. MAEDA, S. TAGAWA, H. KUDOH, M. SUGIMOTO, Y. MORITA, H. SHIBATA, Adv. Mater. 13, 1663–1665 (2001).
[24] N. NISHI, T. KATOH, H. UENO, S. SUGIYAMA, Microsystem Technologies, 9, 1-4, Springer (2002).

# PLASMA-FOCUS BASED RADIATION SOURCES FOR NANOTECHNOLOGY

V.A. GRIBKOV
Institute of Plasma Physics and Laser Microfusion,
Warsaw, Poland

**Abstract**

Between soft X ray sources fitted to demands of nanotechnology and, in particular, to the goals of proximity X ray lithography and micromachining a dense plasma focus (DPF) device has its own niche. We developed new principles of design and operation of this device confronted the technology specifications. It is a collection of a new component base (DPF chambers, capacitors, pseudosparks as switching elements, firing system, etc.), special regimes of the systems operation, geometry of the systems arrangement, and some other means. We manufactured several samples of this design and tested them in a single and in a repetitive mode of operation as well as with various gas and gas mixtures. Optimization of its operation gave us a possibility to reach soft X ray power circa 300 W with its efficiency 1…10% from the mains. Samples of photoresists irradiated with these devices are presented.

## 1. OBJECTIVE OF THE RESEARCH

Because of the importance of a higher degree of miniaturization in electronics and micromachining the adequate sources of photon radiation are under current interest. In particular, in the technology of proximity lithography and micromachining (especially of microelectromechanical structures – MEMS) fabrication X ray sources have the first priority. Only a few of present day devices can fit the corresponding demands. Dense plasma focus (DPF) is between them. But in spite of the fact that this set up is known for more than 40 years, its design and characteristics are very far from performance objectives. That is why the development and optimization of the device fitted to the microelectronics and micromachining operation requirements is a very important goal.

Our objective focuses on the design development of a proper DPF and its tests and optimization in different conditions. Furthermore, we also used it for demonstration experiments in the above mentioned fields of technology.

The most common source of soft X rays used in procedure employed in the production of chips with the characteristic size $\leq 0.1$ μm and in micromachining with a few μm elements is synchrotron. Yet this excellent facility has a number of drawbacks. Between them the most important are the following two.

First one is connected with the fact that a modern specialized synchrotron normally provides circa 20 technological beams. Namely in that case this rather expensive device economically sounds. But in an emergency situation all these 20 factories producing chips become out of operation simultaneously. It is not so with any single-beam inexpensive device.

Second issue results from the fact that all these 20 beams propagate in a horizontal plane. And it is principally impossible to change this feature of the synchrotron. It means that this facility has to use the same number of X ray steppers, moving in a vertical plane. But the steppers of such a kind are much more expensive in comparison with those ones, moving in a horizontal plane. And these micromechanical devices preserve almost the same price for years. Contrary to it an X ray exposure hole of a single-beam device may be oriented in any direction.

One of the most convenient single-beam devices is DPF. The problem with its application in microelectronics and micromachining is usually related to its repetition rate, life-time, and size of the X ray source and efficiency of the soft X ray production. We have elaborated a new design, which as it seems fits the respective demands.

2. APPARATUS, MATERIALS, AND METHODS

## 2.1. DPF devices

We have manufactured several installations with bank energy 2 to 6 kJ (Fig.1 – PF-6). All of them are based on the following elements [1]: 4 capacitors of the KMK-7 type (7 μF, 30 kV, 8 nH), switches of the pseudospark type, namely TDI1-150k/25 (150 kA, jitter less than 4 ns), and DPF chambers of the special design [2] (see Fig. 1). All of them except chambers as well as other systems like master spark, current collector etc. were developed to have a life-time circa $10^6$ "shots" and to work with a repetition rate in the range of 3…15 cycles per second. X ray beam propagates in the upward direction through the anode. The chambers have a cooling system and can be replaced during a very short period of time.

*FIG. 1. Photo of the PF-6 device.*

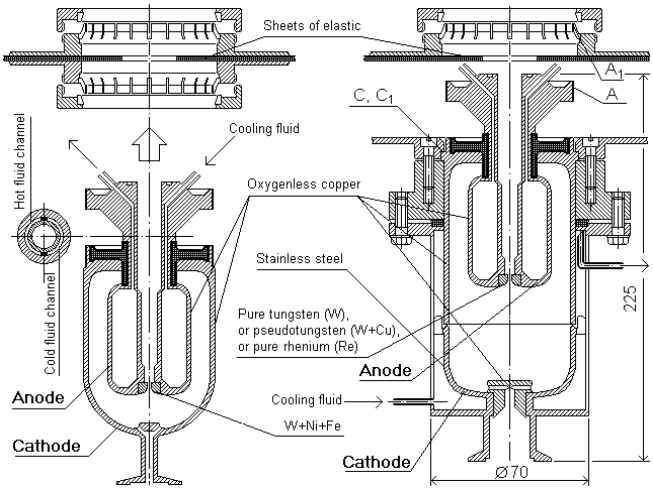


*FIG. 2. Sectional drawing of DPF chambers with cooling anode and with complete chamber cooling.*

### 2.2. Materials

These devices have been optimized for two tasks. The first one – X ray lithography – demands X ray photons of the energy of ~1 keV. For this purpose we used Ne as a working gas for the DPF chamber filing [3]. We expected here to produce resonance lines of H- and He-like ions of Ne.

For the micromachining where 3D structures should be formed the photon energy must be higher to penetrate deeper inside the resist. In this work we have used Ar or Ar-Kr mixture as a working gas of DPF (same types of Ar ions line emission) [4]. In a case of success this gas should give us X ray photons of the energy in the range ~3-4 keV. In all these experiments we used different types of resists – usual positive and negative resists (e.g. simple PMMA) with sensitivity ~1 J/cm$^2$ as well as two types of resists with chemical amplification (CAR) having sensitivity 100 mJ/cm$^2$ to 10 mJ/cm$^2$ (SU-8).

### 2.3. Methods

For diagnostics of the devices operation and measuring of plasma and X ray characteristics we used Rogowski coil, X ray crystal spectrograph, a set of five BPX65 p-i-n diodes with different foils, the pin-hole camera with a diaphragm 50 μm in diameter, Hewlett Packard Logic Analysis System 16 500A or TDS-3052 oscilloscope connected to a PC and a printer for recording our signals. Our resists were placed 20 to 40 cm from the source. During the irradiation process we might abrupt it at a predetermined moment (at any dose deposited).

## 3. RESULTS

### 2.4. Device and X ray beam characteristics

We have investigated our devices in different regimes (with variation of geometry of electrodes, applying voltage, initial gas pressure and percentage of gases composition). Examples of current derivative waveform (NX1 device), pulses of soft X rays (NX1, Ne filling, and RNX2, Ar+Kr filling), and pin-hole soft X ray images of the source (pinch and hot-spot regimes) are shown on Fig. 3 – 6.

Current derivative of NX1 device

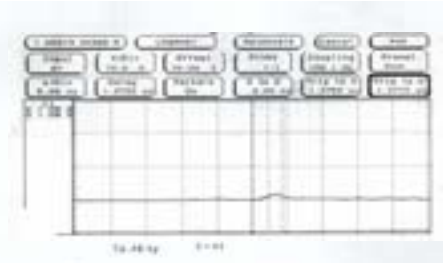

*FIG. 3. Soft X ray pulse ($E_{h\nu}$≅1 keV) of NX1 device (Ne chamber filling).*

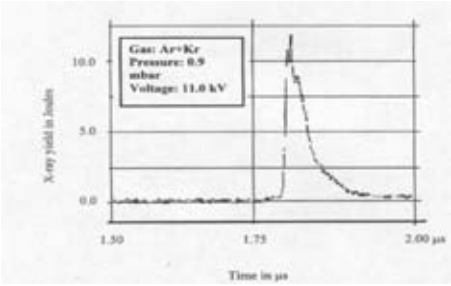


*FIG. 4. Soft X ray pulse ($E_{h\nu} \cong 1$ keV).*

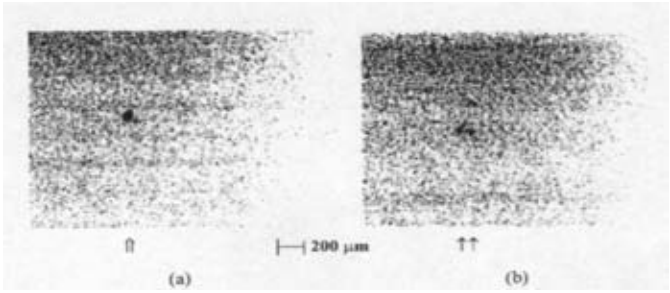


*FIG. 5. Soft X ray pin-hole pictures of X ray source in cases of RNX2 device (Ar+Kr filling) of pinch (a) and hot-spot (b) regimes.*

After optimization we have compared the *average* figures received on our devices (NX1 and retrofit NX2 [3] – RNX2 [4]) with the same ones for usual laboratory set up (see table I).

TABLE I. SUMMARY OF PLASMA FOCI PERFORMANCE

| Device | Energy (kJ) | Voltage (kV) | Current (kA) | Rep rate (Hz) | Gas or gas mixture | Soft X ray yield per shot (J) | Efficiency (%) | Neutrons (n/shot) |
|---|---|---|---|---|---|---|---|---|
| NX1 | 2.0 | 12 | 300 | 3.5 | Ne | 100 | 5 | - |
| RNX2 | 2.0 | 11 | 350 | 15 | Ar | 1 | 0.05 | - |
| | | | | | Ar+Kr | 10 | 0.5 | - |
| PF-6 | 3.0 | 14 | 525 | single | $D_2$ | - | - | $>10^8$ |
| UNU/ICTP | 2.9 | 14 | 170 | single | Ne | 5 | 0. | $<10^8$ |

The best result reached on the NX1 with chamber filled by Ne was 200 J per shot, which gives 10% of the device efficiency from the mains. One may see that the power on the order of 300 W for 1 keV photons and 30 W for 3–4 keV photons has been reached. Our device NX1 to the moment is in operation for more than 200,000 shots, and its operation is perfect.

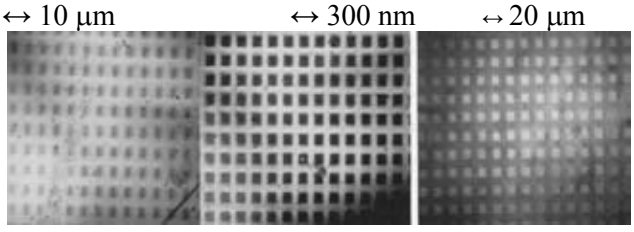


*FIG. 6. Test exposure, NX1, 200…400 shots.*

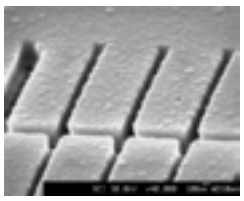

*FIG. 7. Test exposure, NX1, 500 shots, resist US-8.*

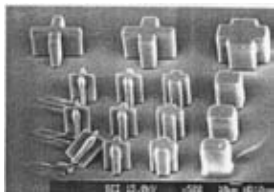

*FIG. 8. 3-keV photons, sensitivity of the resist is 100 mJ/cm$^2$.*

### 3.2. Resists irradiation

Fig. 7, 8 gives scanning electron microscope pictures of resists exposed by 1-keV photons, whereas Fig. 9 – the same for the 3-keV photons. The most interesting feature of these experiments is that the necessary exposure (the number of DPF shots), calculated beforehand and verified by a conventional X ray tube, appeared to be several times lower than expected in the case of 1-keV photons. We explained it on the base of *"flash radiation chemistry"* in a perfect sense of this term [5], when various *synergetic effects* take place provided that the effective interaction spheres (in this case – micro volumes filled with 280-eV photoelectrons) overlapped *during the interaction time* (soft X ray pulse duration).

## 4. CONCLUSION

These experiments have demonstrated opportunities provided by DPF of new design, which uses advantages of modern pulsed power technology. It seems that these devices can be effectively used in proximity X ray lithography and micromachining.

## REFERENCES


[1] BOGOLYUBOV, E.P., BOCHKOV, V.D., VEKHOREVA, L.T., GRIBKOV, V.A., DUBROVSKY, A.V., IVANOV, YU.P., LEE, S., ZHANG, G.X., et al. "A powerful soft X ray source for X ray lithography based on plasma focusing", Physica Scripta 57 (1998) 488 –494.

[2] DUBROVSKY, A.V., GRIBKOV, V.A., IVANOV, Yu.P., LEE, P., LEE, S., LIU, .M.H., SAMARIN, V.A., "0.2-kJ and 2-kJ high rep rate dense plasma foci: their design, technology and applications", Nukleonika 46 (2001) Supplement 1: S107–S111.

[3] LEE, S., LEE, P., ZHANG, G.X., FENG, X., GRIBKOV, V.A., LIU, M.H., SERBAN, A., WONG, T.K.S., "High rep rate high performance plasma focus as a powerful radiation source", IEEE Transactions on Plasma Science 26 (1998) 1119–1126.

[4] GRIBKOV, V.A., SRIVASTAVA, A., LEE, P.Ch.K., KUDRYASHOV, V., LEE, S., "Operation of NX2 dense plasma focus device with argon filling as a possible radiation source for micro-machining", IEEE Transactions on Plasma Science 30 (2002) 1331–1338.

[5] GRIBKOV, V.A., "New possibilities in pulsed radiation physics and chemistry with the use of a Dense plasma focus device", Dense plasma interaction with materials, Proc. of the Tallinn University of Social and Educational Sciences, ed. by U. Ugaste, B2, Tallinn (2003) 57–68.

## LIST OF PARTICIPANTS

| | |
|---|---|
| Angelucci, R | CNR-IMM Institute, Bologna, Italy |
| Baccaro, S. | FIS/ION-ENEA, C.R. Casaccia, Roma, Italy |
| Buttafava, A. | Dipartimento di Chimica Generale,<br>Universita di Pavia, Pavia, Italy |
| Camaioni, N | CNR-ISOF Institute, Bologna, Italy |
| Chmielewski, A.G. | International Atomic Energy Agency |
| Credi, A. | Dipartimento di Chimica "G. Ciamician", Universita di Bologna,<br>Bologna, Italy |
| Di Marco, P. | CNR-ISOF Institute, Bologna, Italy |
| Dahlan, K.Z.H. | Division of Radiation Processing,<br>Malaysian Institute for Nuclear Technology (MINT),<br>Bangi, Kajang, Malaysia |
| Fuochi, P. | Istituto per la Sintesi Organica e la Fotoreattivita (ISOF),<br>CNR, Bologna, Italy |
| Gribkov, V. | Institute of Plasma Physics and Laser Microfusion (IPPLM),<br>Warsaw, Poland |
| Jones, D. | CNR-ISOF Institute, Bologna, Italy |
| Maekawa, Y. | Department of Material Development,<br>Takasaki Radiation Chemistry Research Establishment,<br>Japan Atomic Energy Research Institute (JAERI),<br>Watanuki, Takasaki, Gunma 370-1292, Japan |
| Marletta, G. | Dipartimento di Scienze Chimiche, Universita di Catania,<br>Catania, Italy |
| Meisel, D. | Radiation Laboratory and Department of Chemistry,<br>University of Notre Dame,<br>Notre Dame, IN 46556, U.S.A. |
| Paccagnella, A. | DEI-Universita di Padova,<br>Padova, Italy |
| Rizzoli, R. | CNR-IMM Institute, Bologna, Italy |
| Rosiak, J. | Institute of Applied Radiation Chemistry,<br>Technical University of Lodz, Lodz, Poland |
| Samori, P. | CNR-ISOF Institute, Bologna, Italy |
| Scalia, L. | R&D Process Development,<br>ST Microelectronics, Catania, Italy |
| Spadaro, G. | Dipartimento di Ingegneria Chimica dei Processi e dei Materiali,<br>Universita di Palermo, Palermo, Italy |
| Tondelli, L. | CNR-ISOF Institute , Bologna, Italy |